ISSN 2074-272X

науково-практичний журнал

2026/3

Електротехніка і Електромеханіка

Electrical Engineering & Electromechanics

Електричні машини та апарати
Електротехнічні комплекси та системи
Промислова електроніка
Електричні станції, мережі і системи

Журнал включено до найвищої категорії «А» Переліку фахових видань України

З 2019 р. журнал індексується у Scopus

З 2015 р. журнал індексується у Web of Science Core Collection: Emerging Sources Citation Index

Electrical Engineering & Electromechanics

Scientific Journal was founded in 2002
Co-founders: National Technical University «Kharkiv Polytechnic Institute» (Kharkiv, Ukraine);
Anatolii Pidhornyi Institute of Power Machines and Systems of NAS of Ukraine (Kharkiv, Ukraine)

From no. 1 2019 Journal «Electrical Engineering & Electromechanics» is indexing in **Scopus**
and from no. 1 2005 Journal is indexing in **Web of Science Core Collection: Emerging Sources Citation Index (ESCI)**
Also included in DOAJ (Directory of Open Access Journals), in EBSCO's database, in ProQuest's databases – Advanced Technologies & Aerospace Database and Materials Science & Engineering Database, in Gale/Cengage Learning databases.

Editorial office address:
National Technical University «Kharkiv Polytechnic Institute», Kyrpychova Str., 2, Kharkiv, 61002, Ukraine
phone: +380 67 3594696, **e-mail:** a.m.grechko@gmail.com (**Grechko O.M.)**
ISSN (print) 2074-272X
ISSN (online) 2309-3404

Approved for printing on 28 April 2026. Format 60 × 90 ⅛. Paper – offset. Laser printing. Edition 50 copies.
Printed by Printing house «Madrid Ltd» (18, Gudanova Str., Kharkiv, 61024, Ukraine)

Electrical Engineering & Electromechanics
Scientific Journal

no. 3, 2026

Table of Contents

Electrical Machines and Apparatus

Electrotechnical Complexes and Systems

Industrial Electronics

Power Stations, Grids and Systems

UDC 621.318 https://doi.org/10.20998/2074-272X.2026.3.01

O. Belguet, R. Mehasni, A. Belounis, M. Ouili

Effects of friction on the efficiency of open gradient magnetic separation in dry granular materials

Introduction. *Magnetic separation is one of the most effective and widely used techniques for the purification and enrichment of materials. It plays a crucial role in mineral processing, recycling, and environmental applications, where the separation efficiency depends on both the magnetic field characteristics and the physical properties of the treated materials.* ***Problem.*** *A major limitation of existing studies is that the frictional drag force is often neglected in magnetic separation, although it can sometimes completely prevent the separation process.* ***Goal.*** *To estimate and experimentally verify the effect of frictional drag force on the performance and operational limits of open gradient magnetic separation (OGMS) under dry conditions.* ***Methodology.*** *An integrated analytical, numerical, and experimental approach was used. The granular medium was modeled as a complex fluid where friction acted as a drag force. The coupled magnetic and dynamic equations were solved using Finite Element (FE) – Runge–Kutta (RK4) methods, and results were validated experimentally with a permanent magnet drum separator.* ***Results.*** *To verify the obtained results experiments were carried out on samples of a mixture of sand and iron particles with different components sizes (iron particles and sand grains) in a permanent magnet drum separator. Limited to fine granulometries, the experiments carried out confirmed the results obtained theoretically.* ***Scientific novelty****. The study introduces a coupled FE–RK4 model that explicitly integrates the frictional drag force into the particle dynamic equations, enabling accurate prediction of trajectories and operational thresholds. This provides a realistic description of dry magnetic separation behavior, which has been largely overlooked in previous models of dry magnetic separation.* ***Practical value.*** *The findings provide engineers with a framework for optimizing dry OGMS performance. The developed model defines the threshold separating efficient from inhibited particle capture and clarifies how frictional drag controls the operational range of magnetic separators. These insights support improved design, process adjustment, and greater reliability in dry magnetic separation.* References 41, tables 7, figures 12.

Key words: **finite element method, fine particle, frictional drag force, granular material, magnetic field, magnetic separation, particle dynamics.**

Вступ*. Магнітна сепарація – один з найбільш ефективних і широко використовуваних методів очищення та збагачення матеріалів. Вона відіграє важливу роль у переробці мінералів, вторинній переробці та охороні навколишнього середовища, де ефективність поділу залежить як від характеристик магнітного поля, так і від фізичних властивостей оброблюваних матеріалів.* ***Проблема****. Основним обмеженням існуючих робіт є те, що сила тертя часто не враховується при магнітній сепарації, хоча іноді вона може заважати поділу.* ***Метою*** *роботи є оцінка та експериментальна перевірка впливу сили тертя на продуктивність та експлуатаційні межі відкритої градієнтної магнітної сепарації (OGMS) у сухих умовах.* ***Методика****. Використовувався інтегрований аналітичний, чисельний та експериментальний підхід. Гранульоване середовище моделювалося як складна рідина, де тертя діяло як сила опору. Зв'язані магнітні та динамічні рівняння розв'язувались з використанням методів скінченних елементів (FE) – Рунге–Кутта (RK4), а результати були експериментально підтверджені за допомогою барабанного сепаратора з постійними магнітами.* ***Результати****. Для перевірки отриманих результатів проведені експерименти на зразках суміші піску та частинок заліза з різними розмірами компонентів (частинки заліза та піщинки) у барабанному сепараторі з постійними магнітами. Експерименти з дрібнозернистим складом підтвердили теоретично одержані результати.* ***Наукова новизна****. У дослідженні представлена зв'язана модель FE–RK4, яка явно інтегрує силу тертя в рівняння динаміки частинок, що дозволяє точно прогнозувати траєкторії та робочі граничні значення. Це забезпечує реалістичний опис поведінки сухої магнітної сепарації, яка значною мірою ігнорувалась у попередніх моделях сухої магнітної сепарації.* ***Практична значимість****. Отримані результати надають інженерам основу оптимізації роботи сухих магнітних сепараторів. Розроблена модель визначає граничне значення, що розділяє ефективне і ускладнене захоплення частинок, і пояснює, як сила тертя контролює робочий діапазон магнітних сепараторів. Ці дані сприяють поліпшенню конструкції, коригування процесу та підвищенню надійності сухої магнітної сепарації.* Бібл. 41, табл. 7, рис. 12.

Ключові слова: **метод скінченних елементів, дрібнодисперсні частинки, сила тертя, гранульований матеріал, магнітне поле, магнітна сепарація, динаміка частинок.**

Introduction. Magnetic separation is a powerful process widely used in the mining industry notably for beneficiation and concentration of iron ores [1–5]. It is based on the application of magnetic field that allows the separation and recovery of the ferrous component in a desired site. The ore is initially extracted in form of rocks containing several minerals (iron, phosphor, zinc etc) with different concentrations. Before proceeding with magnetic separation which can be conducted in dry or wet ways [6–10], the constituting minerals are firstly dissociated by the grinding of the ore. The finer the grains, the better the dissociation.

Considering the water penury in arid regions on one hand and to avoid the pollution of the environment that can be caused by the ejection of water used in this process on the other hand, dry separation is favored in which permanent magnet drum separators are commonly used [11–13]. In these separators where open gradient magnetic field is used, the granular material to be treated is generally fed through a conveyor belt.

In fact, the separation process results from the action of applied forces that depend directly on the size of the constituent components (particles and grains). The fineness of the latter, which is advantageous for the dissociation of the material constituting minerals, can be a disadvantageous factor for the separation. In granular materials, the main forces acting on the particle to be separated are magnetic, gravity and frictional drag forces.

Numerous studies have investigated dry magnetic separation in granular media and various separators were designed without considering the frictional drag force that, in some cases, can have dominant effect [13–16].

The **goal of the work** is to estimate and experimentally verify the effect of frictional drag force on the performance and operational limits of open gradient magnetic separation (OGMS) under dry conditions.

The generator of the magnetic field is itself the capture element [14, 16–19].

The friction of solid object in non-cohesive granular media was studied in several works related to other problems. It was found that the domination of the frictional force depends on the object shape, velocity, depth and the medium specifications notably the packaging rate. To calculate the dynamics of the object, different models of the friction force were used, where the coefficients are determined experimentally according to the specifications of each problem [20–30].

Because in our application there are other conditions where the particles to be separated move randomly in a free-falling granular material (the material is not fed by conveyor belt but ejected vertically from a container under the effect of gravity), such models cannot be applied. Therefore, the moving granular material is modeled as a complex fluid in which the frictional force is approached to the fluid drag force for which an analytical model is used [31].

To estimate the effect of the frictional drag force on the separation efficiency and so on the use limits of the OGMS, we compared between the particle trajectories computed with and without considering such a force. For this purpose, and in order to take into account the coupling of the magnetic and particle dynamics phenomena in a study domain of complex geometry, a numerical resolution of the separation problem based on the coupling of Finite Element (FE) and Runge–Kutta (RK4) methods was carried out [16–19]. In such configurations, finite element methods are commonly employed for their robustness in dealing with irregular geometries and strongly coupled field–particle interactions [32, 33].

To verify the obtained results experiments were carried out on mixtures of sand and iron particles with different sizes and concentrations. For this purpose, a horizontal permanent magnets drum separator producing an open gradient magnetic field was used. The obtained results confirmed qualitatively what was found theoretically. They showed that the friction have significant effect that, in some cases of material granulometry and applied field, can even prevent the separation.

Modeling of the separation problem in dry granular medium. To separate the magnetic particles a static magnetic field is used. Because the permanent magnet drum is driven at a constant speed (Fig. 1), the spatial distribution of the magnetic field is computed at each rotation step by solving the equation given by [34]

$$\nabla\times\left(\frac{1}{\mu}\nabla\times\boldsymbol{A}\right)=\frac{1}{\mu}\nabla\times\boldsymbol{B}_r\,, \tag{1}$$

where $\boldsymbol{A}$ is the magnetic vector potential; $\boldsymbol{B}_r$ is the residual magnetic flux density of the magnets; μ is the magnetic permeability.

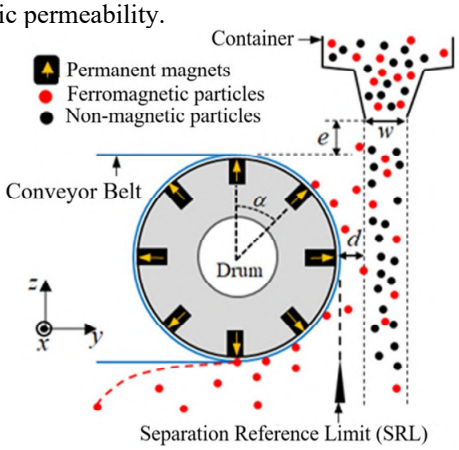

Fig. 1. 2D view of the considered dry drum separator

To compute the magnetic force applied on a magnetized particle, different approaches can be applied [35, 36]. In order to know the distribution of the magnetic force $\boldsymbol{F}_m$ and its nature in the environment of the separator, it is preferable to apply locally the formula given by [16, 18, 19, 37]:

$$\boldsymbol{F}_m=\mu_0\int_{V_p}(\boldsymbol{M}\cdot\nabla)\boldsymbol{H}\mathrm{d}V\,, \tag{2}$$

where $\boldsymbol{H}$ is the magnetic field strength; μ_0 is the magnetic permeability of vacuum; $\boldsymbol{M}$ is the particle magnetization; V_p is the particle volume.

The major disadvantage of (2) resides in its high sensitivity to the quality of the FE meshing of the study domain. The existence of FEs of bad quality can lead to singularities which generate significant errors. Such errors may significantly propagate during the computation process, particularly when successive spatial gradients are evaluated. For this reason, and given that the particles are rigid bodies, the Maxwell stress tensor method is applied. For an elementary surface $\mathrm{d}\boldsymbol{\Gamma}$ of the rigid particle, the force is given by [36]

$$\mathrm{d}\boldsymbol{F}_m=-\frac{1}{2}\mu_0\boldsymbol{H}^2\mathrm{d}\boldsymbol{\Gamma}+\mu_0(\boldsymbol{H}\cdot\mathrm{d}\boldsymbol{\Gamma})\boldsymbol{H}\,, \tag{3}$$

where $\mathrm{d}\boldsymbol{\Gamma}=\mathrm{d}\Gamma\boldsymbol{n}$, where $\boldsymbol{n}$ is the unitary vector normal to the surface of the particle body.

When the particle displaces in the granular medium, it enters in collision with the medium grains. Such collision results in a drag force that prevents its motion. To take into account this effect in the study of the particle dynamics, the granular medium is considered as a complex fluid for which the drag force $\boldsymbol{f}_D$ is approached analytically by [31]

$$\boldsymbol{f}_d=3\pi\eta_g D_p\boldsymbol{v}_{rel}\left(1+0.15R_e^{\,0.687}\right), \tag{4}$$

where η_g is the granular medium viscosity; D_p is the particle diameter, $\boldsymbol{v}_{rel}$ is the relative velocity between the particle and the medium; R_e is the Reynolds number of the particle.

The Reynolds number of the particle is given by [31]

$$R_e=\rho_e|v_{rel}|D_p/\eta_g\,, \tag{5}$$

where ρ_e is the effective density of the granular material; $\rho_e=\rho_s\cdot\varphi$, where ρ_s is the mass density of medium grains; φ is the packing fraction of the granular medium.

To distinguish the effect of the granular drag force on the particle behavior, it is necessary to study its motion without considering such a medium. In this case, one of the acting forces that merits to be considered is the drag force of air (fluid) given by [14]

$$\boldsymbol{f}_D=\frac{1}{2}A_p\rho_a C_D|\boldsymbol{v}_{rel}|\boldsymbol{v}_{rel}\,, \tag{6}$$

where A_p is the surface of the particle; ρ_a is air density; $\boldsymbol{v}_{rel}$ is the relative velocity between the particle and air (continuum phase); $C_d=24\left(1+0.15R_e^{\,0.687}\right)/R_e$ is the coefficient of drag of the particle. The Reynolds number is given by the following formula [14]

$$R_e=\rho_a|v_{rel}|D_p/\eta\,, \tag{7}$$

here η is the fluid (air) viscosity.

The other significant force applied on the particle is the gravitational force:

$$\boldsymbol{f}_g=m_p\boldsymbol{g}\,, \tag{8}$$

where $\boldsymbol{g}$ is the gravity acceleration; m_p is the particle mass.

According to the 2nd Newton's law, the computation of the particle motion requires the resolution of the dynamic equation given by [16–19],

$$m_p\frac{\mathrm{d}\boldsymbol{v}_p}{\mathrm{d}t}=\boldsymbol{f}_g+\boldsymbol{f}_D+\boldsymbol{F}_m\,, \tag{9}$$

here $\boldsymbol{v}_p$ is the particle velocity.

Resolution method and obtained results. To solve the separation problem, we have coupled the FE and RK4 numerical methods. Before proceeding to such a resolution, we firstly verified the accuracy of the magnetic modeling equations and the reliability of the developed FE computing tools. Such verification was based on the computation of the distributions of the magnetic field and force in the environment of the drum.

Applied magnetic field and generated force. To compute the distribution of the magnetic field in the geometrically complex domain, a 3D FE program was developed and used as in [38, 39]. To facilitate the interpretation and understanding of the results, we considered the case where the drum is static. The resolution of (1) and the exploitation of (2) for a drum of diameter D_d=0.1 m with 8 identical NdFeB magnets of B_r=1.1 T, cross sectional area S_M=0.01×0.012 m^2 and depth d_M=0.1 m arranged periodically with a spacing angle α=45° (see Fig. 1) have given the results presented in Fig. 2. Figure 2,*a* shows a periodic distribution of the magnetic vector potential that corresponds exactly to the chosen magnets polarity and arrangement; Fig. 2,*b* shows that a field of attractive magnetic force is obtained around the drum (to obtain the zoom, we presented only the force vectors in elements located out of the circle of radius 8·10^{-2} m).

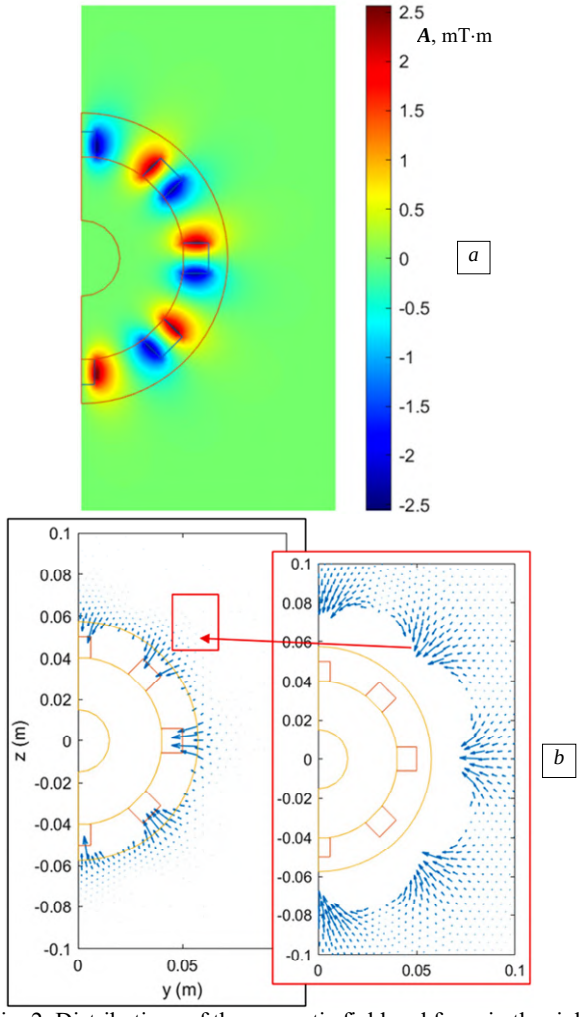

Fig. 2. Distributions of the magnetic field and force in the right side of the drum (plane (y, z)): *a* – magnetic vector potential; *b* – magnetic force density

To know quantitatively the specifications of the spatial distribution of the generated magnetic force, we computed the variations of its components following the 3 space directions x, y, z represented respectively by line 1 (x, D_d/2+75·10^{-4} m, 0), line 2 (0, y>D_d/2+75·10^{-4} m, 0) and line 3 (0, D_d/2+75·10^{-4} m, z) (see Fig. 3).

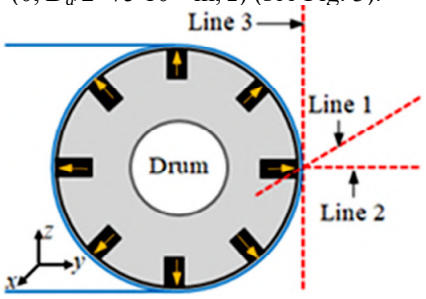

Fig. 3. Chosen lines for the representation of the variations of the magnetic force according to the 3 space directions respectively x, y, z

For the shown position of the drum magnets, we obtained the results presented in Fig. 4. Figure 4,*a* shows that along the length of line 2, only the component F_{my} can have effect. It is high near the drum surface and decreases sharply when we move away from it. Along the length of line 3, F_{mx} is negligible and only the components F_{my} and F_{mz} can have effect (see Fig. 4,*b*). The domination of each component depends on the evaluation position in relation to the magnets. Figure 4,*c* shows that on line 1, except weak effect of the component F_{mx} at the drum edges, there is a clear domination with quasi homogeneity of F_{my} along the length of the magnet.

When we move along the perimeter of the drum, we find the same result for F_{mx} with a decreasing of F_{my} and increasing of F_{mz}. The two components can have the same value near the immediately following magnets. At the lowest and highest magnets, it is F_{mz} that becomes dominant.

In absence of significant effect of the F_{mx} component and due to the quasi homogeneity of F_{my} and F_{mz} along the depth of the magnets, no considerable deflection of the particles according to the x direction can happen and the separation can occur indifferently along the depth of the separator. In these conditions, a 2D study of the separation problem in the plane (y, z) can sufficiently provide all information about the separation performance.

To compute the magnetic force applied on a magnetic particle, we used (3). Applied on the particle external surface, such a model permits the reduction of calculation errors linked to the quality of the meshing. For a cylindrical particle with a shape closer to a sphere of relative magnetic permeability μ_r=115, diameter D_p=1.6·mm and height h_p=1.6·mm located at the position shown in Fig. 5,*a*, we obtained the distribution of the force density presented in Fig. 5,*b*. The latter shows attractive elementary forces applied on the particle side opposite to the drum and repulsive elementary forces applied on its rear side but a resulting force oriented towards the drum. To verify the obtained force, we recalculated the force by applying (2), which has given for the same computing conditions the distribution of the force density presented in Fig. 5,*c*.

In Fig. 5,*c* the force is zero inside the particle, what we see inside the particle are the central points of the elements, where vectors of the elementary forces are computed and presented. The quantitative comparison between the results obtained by (2) and (3) has shown that the attractive resulting force is perfectly the same in terms of value and direction.

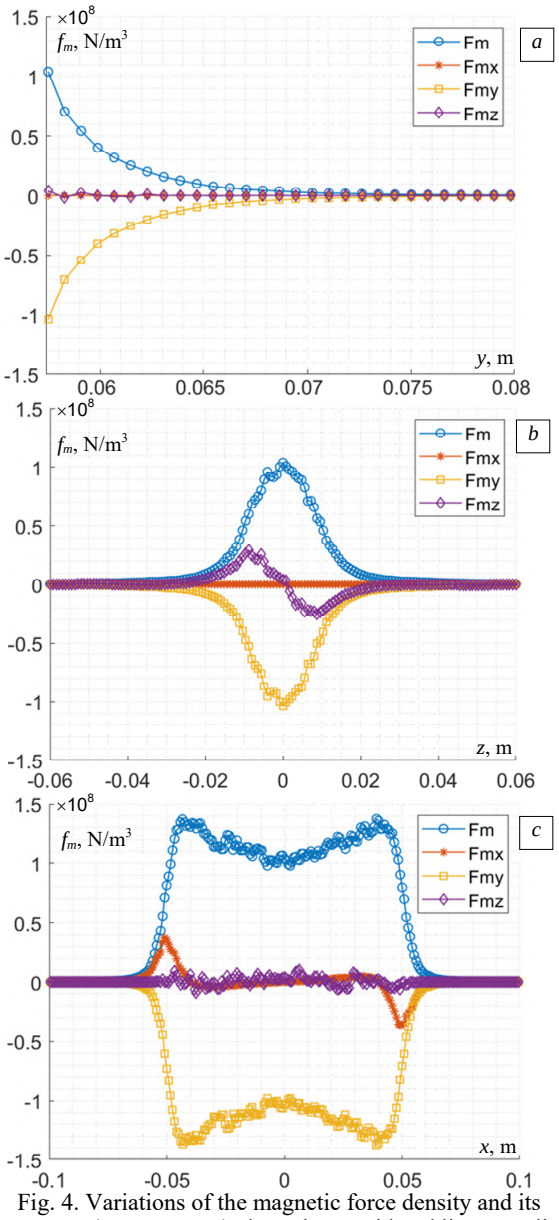

Fig. 4. Variations of the magnetic force density and its components (F_{mx}, F_{my}, F_{mz}) along the considered lines: *a* – line 2 (*y* direction); *b* – line 3 (*z* direction); *c* – line 1 (*x* direction)

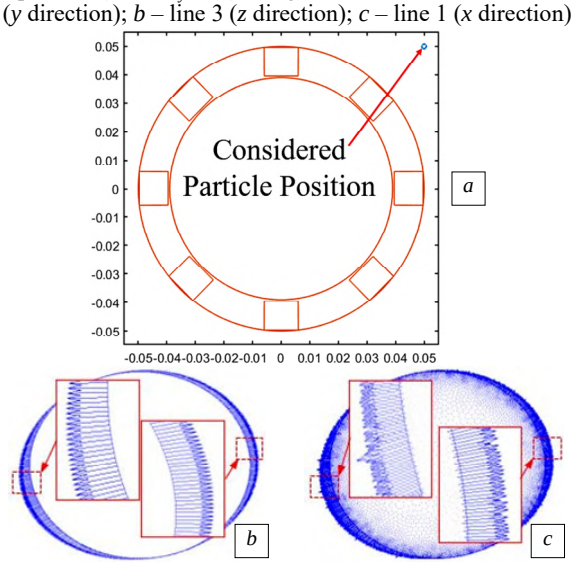

Fig. 5. Distribution of the magnetic force applied on a cylindrical particle of radius D_p=1.6 mm, height h_p=1.6 mm, μ_r=115 for a given position in respect to the drum: *a* – particle position; *b* – Maxwell stress tensor method; *c* – field gradient method

To consolidate our verification on one hand and to show that the force is globally attractive whatever the particle position on the other hand, we compared in Fig. 6 between the resulting components of the force obtained with (2) and (3) for different positions of the particle in respect to the drum. Such a comparison shows that the results are perfectly the same. Both the components of the global force are negative which means that they work to attract the particle towards the drum.

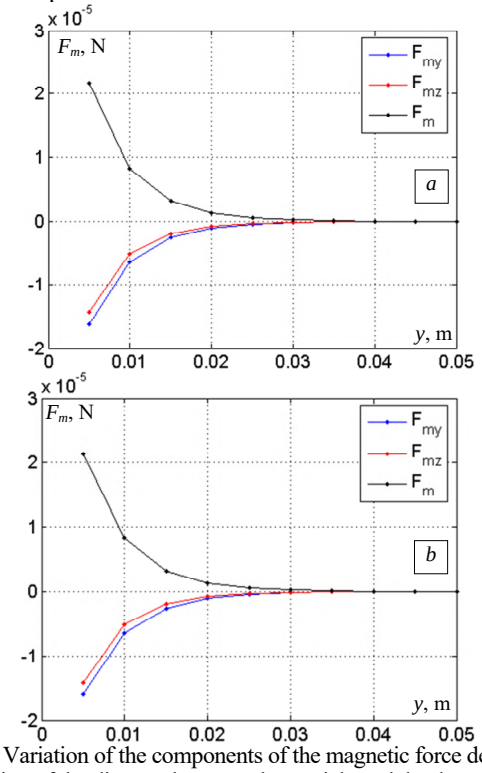

Fig. 6. Variation of the components of the magnetic force density as a function of the distance between the particle and the drum surface: *a* – Maxwell stress tensor method; *b* – field gradient method

Particle trajectory. To compute the particle trajectory that provides all information on its separation, we solved (9) where the particle body is taken into account (geometry and magnetic permeability). To permit the distinguishing of any effect of the granular frictional drag force on the separation, we firstly computed the particle trajectories without considering the granular medium. In this case, magnetic, gravitational and air drag forces modeled by (3), (6) and (8) respectively were taken into account. For ferromagnetic particles of diameters $7\cdot10^{-5}$ m < D_p < 10^{-2} m, height $h_p = D_p$, mass density ρ_p = 7874 kg/m^3, μ_r = 115, g = 9.81 m/s^2, we obtained for the particle initial positions of Table 1, the trajectories presented in Fig. 7.

Table 1

Considered particle initial positions

Particle number	Position *y*, m	Position *z*, m
1	$5.25\cdot10^{-2}$	$9\cdot10^{-2}$
2	$5.75\cdot10^{-2}$	$9\cdot10^{-2}$
3	$6.25\cdot10^{-2}$	$9\cdot10^{-2}$
4	$6.75\cdot10^{-2}$	$9\cdot10^{-2}$

Figure 7 shows that in absence of the granular frictional drag force, the capture occurs from a distance y_0 = $1.25\cdot10^{-2}$ m from the drum surface. Particles initially situated at the same position are almost captured at the same site, which means that for this range of particles, the particle size has no effect on the capture zone. On the contrary, the computed separation times (except the singular values

written in bold) presented in Table 2 show that for a given initial position, the particle of higher size is captured faster.

Table 2

Capture time of the separated particles without considering the granular frictional drag force

Particle diameter D_p ($\times 10^{-6}$ m)	Particle capture time, s		
	1	2	3
70	0.1190	**0.1278**	0.1422
150	0.1187	0.1280	**0.1410**
300	0.1186	0.1278	**0.1415**
800	0.1184	0.1278	0.1417
1500	0.1181	0.1277	0.1416
3000	0.1175	0.1273	0.1411
6000	0.1161	0.1262	0.1394
10000	0.1137	0.1239	0.1364

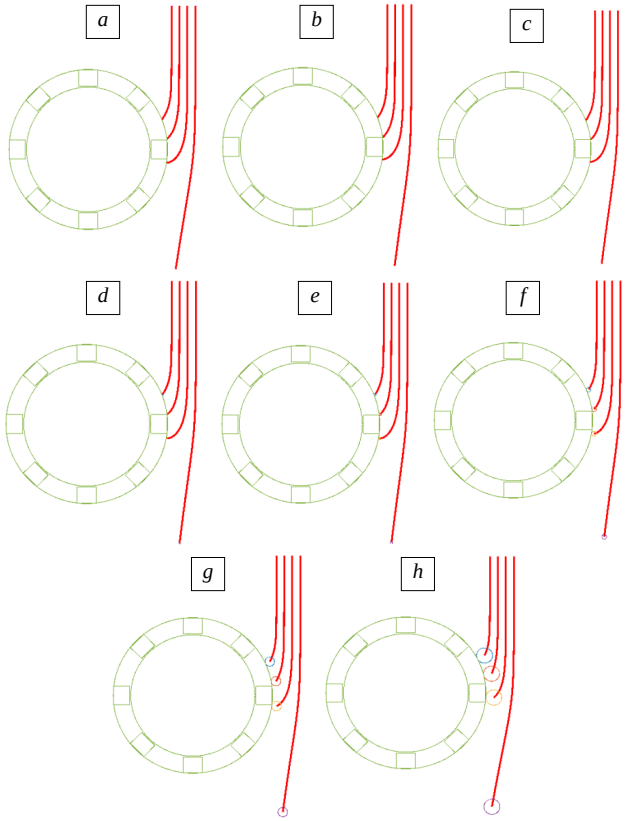

Fig. 7. Particle trajectories obtained for different particle sizes without considering the granular drag force: *a*) D_p=70·10^{-6} m; *b*) D_p=150·10^{-6} m; *c*) D_p=300·10^{-6} m; *d*) D_p=800·10^{-6} m; *e*) D_p=1500·10^{-6} m; *f*) D_p=3000·10^{-6} m; *g*) D_p=6000·10^{-6} m; *h*) D_p=10000·10^{-6} m

To estimate the effect of the granular frictional drag force on the separation, we recalculated the trajectories considering that the particles are included in a granular medium (sand) with homogeneous grains with a packing fraction φ=0.41 [40]. For the same previous computing conditions, we obtained the results presented in Fig. 8.

Figure 8 shows that the particles of diameter less than 300·10^{-6} m are not separated. Separation begins to occur for larger diameter particles initially falling very close to the drum (distance $y \le 0.25 \cdot 10^{-2}$ m from the surface of the drum). We see also that the separation improves significantly with the increase in particle size. Unlike the previous case where the particle falls in air, in a granular medium, the size of the particle has considerable influence on the capture site.

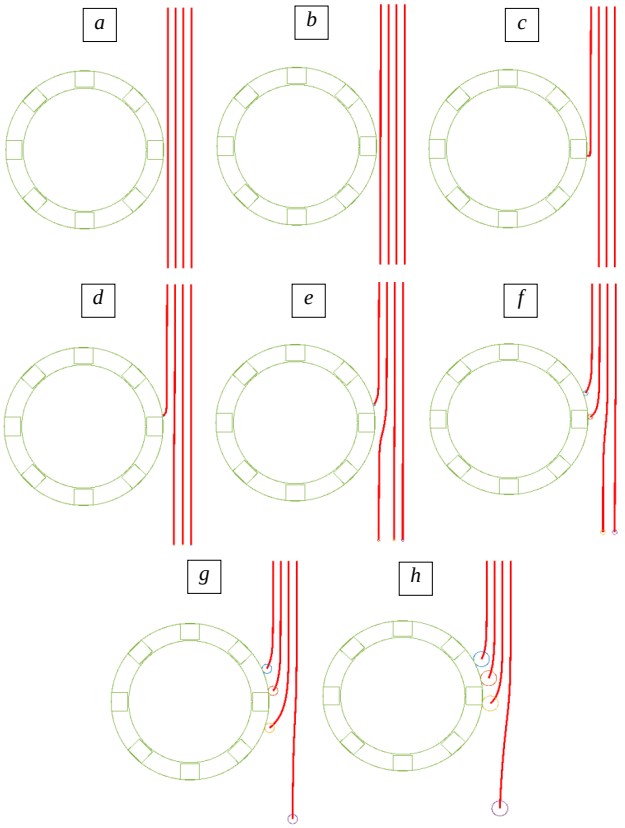

Fig. 8. Computed particle trajectories obtained in granular medium: *a*) D_p=70·10^{-6} m; *b*) D_p=150·10^{-6} m; *c*) D_p=300·10^{-6} m; *d*) D_p=800·10^{-6} m; *e*) D_p=1500·10^{-6} m; *f*) D_p=3000·10^{-6} m; *g*) D_p=6000·10^{-6} m; *h*) D_p=10000·10^{-6} m

The evaluation of the capture time of the separated particles has given the results listed in Table 3. It is clearly seen that the larger size particles are also captured faster.

Table 3

Capture time of separated particles in presence of the granular frictional drag force

Particle diameter D_p ($\times 10^{-6}$ m)	Particle capture time, s		
	1	2	3
70	–	–	–
150	–	–	–
300	0.1387	–	–
800	0.1290	–	–
1500	0.1251	–	–
3000	0.1204	0.1333	–
6000	0.1170	0.1283	0.1483
10000	0.1141	0.1248	0.1382

The computation of the particle trajectories and capture time for other packing fractions φ=0.21 and φ=0.61 has given almost the same findings.

The achieved theoretical study has shown that the frictional drag force has important effect on the separation efficiency. In granular ores of fine grains, such effect can dominate the magnetic force and may even prevent the separation.

Experimental verification. To validate the achieved theoretical study and verify the obtained results, experiments were carried out on mixtures of sand and iron particles of μ_r=115 experimentally identified. In order to reduce the effect of the magnetic dipole-dipole interaction that leads to particle agglomerations before their separation (case in which the frictional drag force will not be applied individually on the particles) [41], mixtures of weak concentrations of iron particles were considered.

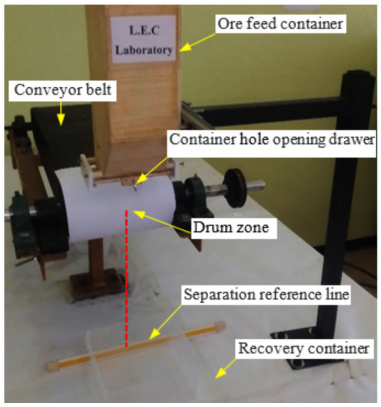

Fig. 9. Experimental used separator

The used OGMS separator is a permanent magnet (B_r=1.1 T) drum separator [16] equipped with a container allowing the feeding of the granular material by gravity instead of its transporting by conveyor belt (Fig. 9). In this way, the friction between the particles to be separated and the belt is entirely excluded, and only the friction with the sand grains is considered.

As we previously mentioned, the iron ore is crushed to small grains before proceeding to magnetic separation. Therefore, the experimental verification is limited to iron particles of diameter $D_p < 10^{-3}$ m. In order to reduce the study cost, ranges of particle diameters $D_p < 8{\cdot}10^{-5}$ m, $2{\cdot}10^{-4}$ m $< D_p < 4{\cdot}10^{-4}$ m and $6{\cdot}10^{-4}$ m $< D_p < 10^{-3}$ m experimentally identified are treated (Fig. 10).

Fig. 10. *a* – identified ranges of magnetic particles; *b* – identified ranges of granular material grains; *c* – used sieving device

To verify the nature of dependence between the particle size and the separation efficiency theoretically obtained on one hand and to obtain basic results subsequently making it possible to distinguish possible effects of the granular drag force on the other hand, a first series of experiments have been performed without considering the granular medium. To permit a comparison between theoretical and experimental results, the same operating conditions must be considered. Accordingly, we have chosen a container orifice $w = 10^{-2}$ m, a lift-off $e = 3.4{\cdot}10^{-2}$ m and shifting distance $d = 2{\cdot}10^{-2}$ m, which gives a feeding limit $l = d+w = 3{\cdot}10^{-2}$ m from the drum surface (see Fig. 1).

The injection of a same volume $V_i = 10^{-6}$ m^3 of particles in the separator gave for the considered particle sizes the results presented in Fig. 11. The qualitative examination of the non-separated quantities (quantities circled in red «1») for each case shows that the larger the particle size, the greater the separated quantity (quantities circled in yellow «2»). Here, the particle is considered separated if it is captured by the drum or fallen behind the separation reference (see Fig.9).

In order to consolidate our verification, we quantified the separated volume of particles. Such quantification gave for the considered cases of particle size the results presented in Table 4. The latter confirms clearly the proportional relationship between the particle size and the separation efficiency found theoretically through a comparison of capture times (see Table 2).

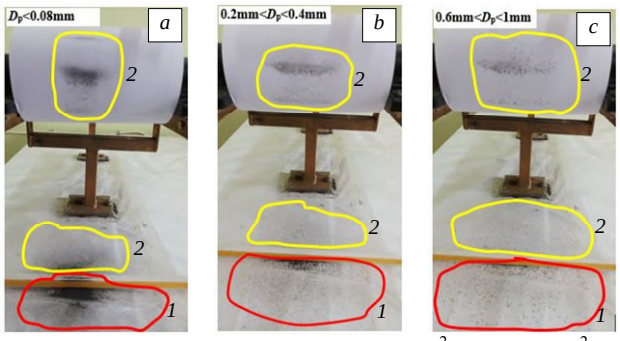

Fig. 11. Separated particles obtained for $w = 10^{-2}$ m, $e = 3.4{\cdot}10^{-2}$ m, $d = 2{\cdot}10^{-2}$ m without granular medium. The considered iron particle diameters are: *a*) $R_p < 8{\cdot}10^{-5}$ m; *b*) $2{\cdot}10^{-4}$ m $< R_p < 4{\cdot}10^{-4}$ m; *c*) $6{\cdot}10^{-4}$ m $< R_p < 10^{-3}$ m

Table 4

Separated volume of particles without considering the granular medium

Particle diameter D_p, m	Separated volume, m^3
$D_p < 8{\cdot}10^{-5}$	$176.1{\cdot}10^{-9}$
$2{\cdot}10^{-4} < D_p < 4{\cdot}10^{-4}$	$260.6{\cdot}10^{-9}$
$6{\cdot}10^{-4} < D_p < 10^{-3}$	$357.3{\cdot}10^{-9}$

To verify experimentally the use limits of separation without considering the granular medium, we quantified the separated volume of particles for different shifting distances d (see Fig.1). The obtained results for the considered particle sizes are presented in Table 5.

Table 5

Separated volume of particles (separation efficiency) without granular medium

Shifting distance d ($\times 10^{-2}$ m)	Separated volume V_s($\times 10^{-9}$ m^3)		
	D_p<$8{\cdot}10^{-5}$ m	$2{\cdot}10^{-4}$ m $< D_p$ $D_p < 4{\cdot}10^{-4}$ m	$6{\cdot}10^{-4}$ m $< D_p$ $D_p < 10^{-3}$ m
0	**990.8**	928.7	930.8
1	**770.5**	580.2	625
2	176.1	260.6	357.3
4	33.6	45.8	118.1
6	<9.2	<18.3	42.8
8	0	0	9.2
10	0	0	0

If we neglect the singular values written in bold, we also see a proportional relationship between the particle size and the separation efficiency. A significant separation is approximately obtained for a limit $y_0 \approx 6{\cdot}10^{-2}$ m, which is really greater than that found theoretically

$$y_0 = 1.25{\cdot}10^{-2} \text{ m}.$$

The difference between the experimental and computed values is mainly related to dipole-dipole interaction neglected in the theoretical study [41].

To estimate the effect of the frictional drag force on the separation efficiency, we treated samples of a mixture of sand and iron particles for different sizes of sand grains and particles. To obtain homogeneous dispersion of the particles in the sand, the mixture is well prepared.

To permit a comparison between the results related to each case of the composition size of the mixture, we always treated the same volume with same fractions of sand and iron particles. Practically, we inject in the separator, each time, a sample composed of a volume $V_s = 6{\cdot}10^{-4}$ m^3 of sand and a volume $V_i = 10^{-6}$ m^3 of iron particles.

For the same operating conditions of the drum and geometrical parameters $w = 10^{-2}$ m, $e = 3.4{\cdot}10^{-2}$ m and $d = 1.5{\cdot}10^{-2}$ m, the experiment effected with sand of grains size $D_g < 0.2{\cdot}10^{-3}$ m has given for the considered size

ranges of the iron particles the results of Fig. 12. In the latter, the separated particles are circled in yellow.

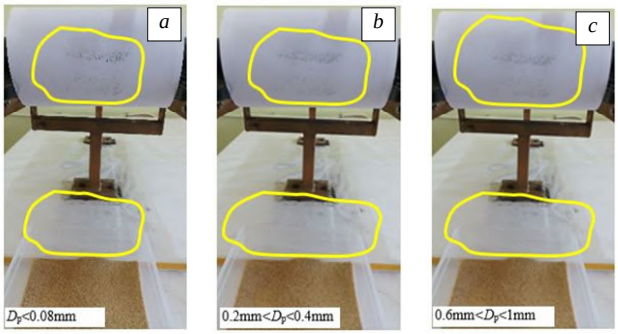

Fig. 12. Separated particles obtained for $w = 10^{-2}$ m, $e = 3.4 \cdot 10^{-2}$ m $d = 1.5 \cdot 10^{-2}$ m with granular medium (sand) of grains diameter $D_g < 0.2 \cdot 10^{-3}$ m. The considered iron particle diameters are: *a*) $R_p < 8 \cdot 10^{-5}$ m; *b*) $2 \cdot 10^{-4}$ m $< R_p < 4 \cdot 10^{-4}$ m; *c*) $6 \cdot 10^{-4}$ m $< R_p < 10^{-3}$ m

The qualitative comparison between Fig. 11 and Fig. 12 shows clearly that the separation efficiency degraded. The same findings have been found by experiments achieved with sand of grains sizes $2 \cdot 10^{-4}$ m $< D_g < 4 \cdot 10^{-4}$ m, $4 \cdot 10^{-4}$ m $< D_g < 6.3 \cdot 10^{-4}$ m and $D_g > 6.3 \cdot 10^{-4}$ m.

To estimate the degradation of separation efficiency, we quantified the separated volume of particles for the considered cases of particle size. The assembling, for each case, the particles captured by the drum and those fallen behind the separation line gave the results presented in Table 6. The latter shows that in presence of the granular medium, the separation efficiency always increases with the increase in the size of the iron particles.

Table 6

Separated volume of particles (separation efficiency) with granular medium

Sand grains diameter D_g	Separated volume $V_s(\times 10^{-9}$ m$^3)$		
	$D_p < 8 \cdot 10^{-5}$ m	$2 \cdot 10^{-4}$ m $< D_p$ $D_p < 4 \cdot 10^{-4}$ m	$6 \cdot 10^{-4}$ m $< D_p$ $D_p < 10^{-3}$ m
$D_g > 0.63 \cdot 10^{-3}$m	49.9	81.4	107.9
$0.4 \cdot 10^{-3}$ m $< D_g$ $D_g < 0.63 \cdot 10^{-3}$ m	18.3	68.2	**139.4**
$0.2 \cdot 10^{-3}$ m $< D_g$ $D_g < 0.4 \cdot 10^{-3}$ m	**28.5**	63.1	122.1
$D_g < 0.2 \cdot 10^{-3}$ m	<9.2	**49.9**	42.8

Looking at the results of Table 5 obtained for the same w and $d = 2 \cdot 10^{-2}$ m, we see that without granular medium the separation efficiency is very important in relation to that obtained in presence of the granular medium with a lower distance $d = 1.5 \cdot 10^{-2}$ m, which verifies clearly the important effect of the frictional drag force.

Another reading of the results of Table 6 shows that (apart from the singular values written in bold) for a given size of the iron particle, the separation efficiency degrades with the increase in the grains size of the sand.

To know the effect of the frictional drag force in relatively weak applied magnetic field, experiments was achieved for a larger container orifice $w = 3 \cdot 10^{-2}$ m. The results obtained for the same values of e and d are presented in Table 7. The latter shows that apart from the degradation of the separation efficiency due to the decreasing of the field, the proportionality between the particle size and the separation efficiency is lost.

Table 7

Separated volume of particles (separation efficiency) with granular medium, $w = 3 \cdot 10^{-2}$ m

Sand grains diameter D_g	Separated volume $V_s(\times 10^{-9}$ m$^3)$		
	$D_p < 8 \cdot 10^{-5}$ m	$2 \cdot 10^{-4}$ m $< D_p$ $D_p < 4 \cdot 10^{-4}$ m	$6 \cdot 10^{-4}$ m $< D_p$ $D_p < 10^{-3}$ m
$D_g > 0.63 \cdot 10^{-3}$ m	<<18.3	**45.8**	40.7
$0.4 \cdot 10^{-3}$ m $< D_g$ $D_g < 0.63 \cdot 10^{-3}$ m	<<18.3	34.6	21.4
$0.2 \cdot 10^{-3}$ m $< D_g$ $D_g < 0.4 \cdot 10^{-3}$ m	20.4	28.5	**27.5**
$D_g < 0.2 \cdot 10^{-3}$ m	<<18.3	9.2–18.3	**<<9.2**

Conclusions. In this work, the effect of the frictional drag force on the efficiency of OGMS in dry granular material is estimated and experimentally verified. To permit such estimation, we have computed the particle trajectories where the granular material is approached to complex fluid for which the frictional drag force is assumed similar to fluid drag force analytically modelled.

To verify the theoretically obtained findings, experiments were carried out on mixtures of sand and iron particles of small size. The choice of sand is justified by the fact that, on one hand the used analytical model for the frictional drag force is valid for this type of material, and on the other hand, the mixtures do not differ much from real iron ore.

The achieved experiments have approved the theoretically obtained findings. The differences between the computed and experimental values are mainly related to the dipole-dipole magnetic interaction neglected in the theoretical study. Practically, such effect leads to particle transient agglomerations, which encourages the separation.

The singular values in tables written in bold are mainly related to measure errors committed during the injection of the material through the container or the assembling of the separated particles.

Finally, it can be concluded that, if the size of the iron particles to be separated is very important compared to that of the grains forming the granular medium (magnetic purification of materials), the frictional drag force can be neglected. But in granular materials, where the iron particles are of the same size of the grains (case of enrichment of fine grinded ores of low concentration of iron particles), the frictional drag force must be taken into account in any designing study.

Conflict of interest. The authors declare that they have no conflicts of interest.

REFERENCES

1. Ku J., Wang K., Wang Q., Lei Z. Application of Magnetic Separation Technology in Resource Utilization and Environmental Treatment. *Separations*, 2024, vol. 11, no. 5, art. no. 130. doi: https://doi.org/10.3390/separations11050130.

2. Kukkala P.C., Kumar S., Nirala A., Khan M.A., Alkahtani M.Q., Islam S. Beneficiation of Low-Grade Hematite Iron Ore Fines by Magnetizing Roasting and Magnetic Separation. *ACS Omega*, 2024, vol. 9, no. 7, pp. 7634-7642. doi: https://doi.org/10.1021/acsomega.3c06802.

3. Fariss A.H.B., Bicalho W.C.S., Seixas L., Faustino L.M. Beneficiation of low-grade iron ore using a dry-roll magnetic separator and its modeling via artificial neural network. *Journal of Sustainable Metallurgy*, 2025, vol. 11, art. no. 529. doi: https://doi.org/10.1007/s40831-025-01030.

4. Xie S., Hu Z., Lu D., Zhao Y. Dry Permanent Magnetic Separator: Present Status and Future Prospects. *Minerals*, 2022, vol. 12, no. 10, art. no. 1251. doi: https://doi.org/10.3390/min12101251.

5. Jiu S., Zhao B., Yang C., Chen Y., Cheng F. High-Efficiency Iron Extraction from Low-Grade Siderite via a Conveyor Bed Magnetization Roasting–Magnetic Separation Process: Kinetics Research and Applications. *Materials*, 2022, vol. 15, no. 18, art. no. 6260. doi: https://doi.org/10.3390/ma15186260.

6. Wang X., Hu Y., Hao Y., Shen Z., Liang G., Zhang M. Simulation of Dynamic Particle Trapping and Accumulation in HGMS Based on FEM-CFD-DEM Coupling Approach. *Processes*, 2025, vol. 13, no. 8, art. no. 2391. doi: https://doi.org/10.3390/pr13082391.
7. Liu J., Dai H., Yu L., Wang C., Feng J., Li P., Xu S. Optimization of the Matrix in a Transverse-Field High-Gradient Magnetic Separator for an Improved Ilmenite Separation. *Minerals*, 2025, vol. 15, no. 2, art. no. 114. doi: https://doi.org/10.3390/min15020114.
8. Vilakazi A.Q., Shemi A., Ndlovu S. Dry Magnetic Separation and the Leaching Behaviour of Aluminium, Iron, Titanium, and Selected Rare Earth Elements (REEs) from Coal Fly Ash. *Minerals*, 2025, vol. 15, no. 2, art. no. 119. doi: https://doi.org/10.3390/min15020119.
9. Chokin K., Yedilbayev A., Yugai V., Medvedev A. Beneficiation of Magnetically Separated Iron-Containing Ore Waste. *Processes*, 2022, vol. 10, no. 11, art. no. 2212. doi: https://doi.org/10.3390/pr10112212.
10. Liu J., Xue Z., Dong Z., Yang X., Fu Y., Man X., Lu D. Multiphysics Modeling Simulation and Optimization of Aerodynamic Drum Magnetic Separator. *Minerals*, 2021, vol. 11, no. 7, art. no. 680. doi: https://doi.org/10.3390/min11070680.
11. Baawuah E., Kelsey C., Addai-Mensah J., Skinner W. A Novel Pneumatic Planar Magnetic Separator for Magnetite Beneficiation: A Focus on Flowsheet Configuration. *Minerals*, 2020, vol. 10, no. 9, art. no. 759. doi: https://doi.org/10.3390/min10090759.
12. Luukkanen S., Tanhua A., Zhang Z., Mollehuara Canales R., Auranen I. Towards waterless operations from mine to mill. *Minerals Engineering*, 2022, vol. 187, art. no. 107793. doi: https://doi.org/10.1016/j.mineng.2022.107793.
13. Yi F., Chen L., Liu X., Zeng J., Xue Z. Development of a centrifugal dry magnetic separator for separation of fine magnetite ore. *Powder Technology*, 2024, vol. 437, art. no. 119557. doi: https://doi.org/10.1016/j.powtec.2024.119557.
14. Lu D., Liu J., Cheng Z., Li X., Xue Z., Li S., Zheng X., Wang Y. Development of an open-gradient magnetic separator in the aerodynamic field. *Physicochemical Problems of Mineral Processing*, 2020, vol. 56, no. 2, pp. 325-337. doi: https://doi.org/10.37190/ppmp20005.
15. Li X., Wang Y., Lu D., Zheng X., Gao X. Optimization of Airflow Field for Pneumatic Drum Magnetic Separator to Improve the Separation Efficiency. *Minerals*, 2021, vol. 11, no. 11, art. no. 1228. doi: https://doi.org/10.3390/min11111228.
16. Ouili M., Mehasni R., Feliachi M., Belounis A., Latreche M.E.H. A simultaneous separation of magnetic and conductive particles in a designed permanent magnet drum separator. *International Journal of Applied Electromagnetics and Mechanics*, 2019, vol. 61, no. 1, pp. 137-155. doi: https://doi.org/10.3233/JAE-180101.
17. Zeng J., Tong X., Yi F., Chen L. Selective Capture of Magnetic Wires to Particles in High Gradient Magnetic Separation. *Minerals*, 2019, vol. 9, no. 9, art. no. 509. doi: https://doi.org/10.3390/min9090509.
18. Belounis A., Mehasni R., Ouili M., Latreche M.E. Optimization of the capture element for an OGMS based on the 3D computation of the magnetic particle behavior. *International Journal of Applied Electromagnetics and Mechanics*, 2015, vol. 48, no. 4, pp. 387-397. doi: https://doi.org/10.3233/JAE-140157.
19. Mehasni R., Latreche M., Feliachi M. Fine particles behavior analysis for magnetic separation process. *International Journal of Applied Electromagnetics and Mechanics*, 2004, vol. 19, no. 1–4, pp. 587-590. doi: https://doi.org/10.3233/JAE-2004-633.
20. Katsuragi H., Durian D.J. Drag force scaling for penetration into granular media. *Physical Review E*, 2013, vol. 87, no. 5, art. no. 052208. doi: https://doi.org/10.1103/PhysRevE.87.052208.
21. Ye X., Wang D., Zhang X., Zhang C., Du W., Su X., Li G. Projectile oblique impact on granular media: penetration depth and dynamic process. *Granular Matter*, 2021, vol. 23, no. 2, art. no. 48. doi: https://doi.org/10.1007/s10035-021-01108-3.
22. Omidvar M., Iskander M., Bless S. Response of granular media to rapid penetration. *International Journal of Impact Engineering*, 2014, vol. 66, pp. 60-82. doi: https://doi.org/10.1016/j.ijimpeng.2013.12.004.
23. Pol A., Storti S., Gabrieli F. Granular drag and lift force on a flexible fiber. *Physical Review E*, 2025, vol. 112, no. 4, art. no. 045425. doi: https://doi.org/10.1103/p2db-yt7h.
24. Brzinski T.A., Mayor P., Durian D.J. Depth-Dependent Resistance of Granular Media to Vertical Penetration. *Physical Review Letters*, 2013, vol. 111, no. 16, art. no. 168002. doi: https://doi.org/10.1103/PhysRevLett.111.168002.
25. Marghitu D., Lee S., Marghitu D. Experimental and Simulation Results for the Impact of a Rotating Flexible Link with a Granular Material. *International Journal of Advanced Robotic Systems*, 2014, vol. 11, no. 1, art. no. 40. doi: https://doi.org/10.5772/58254.
26. Zhang C., Ye X. Force and flow characteristics of an intruder immersed in 3D dense granular matter. *Particuology*, 2022, vol. 71, pp. 47-55. doi: https://doi.org/10.1016/j.partic.2022.01.007.
27. Katsuragi H., Durian D.J. Unified force law for granular impact cratering. *Nature Physics*, 2007, vol. 3, no. 6, pp. 420-423. doi: https://doi.org/10.1038/nphys583.
28. Wang F., Chen Y., Li Y., Li Y. A Drag Force Model of Vertical Penetration into a Granular Medium Based on DEM Simulations and Experiments. *Applied Sciences*, 2024, vol. 14, no. 6, art. no. 2336. doi: https://doi.org/10.3390/app14062336.
29. Zaidi A.A. Numerical investigation of drag force on a spherical intruder by granular material. *Powder Technology*, 2023, vol. 427, art. no. 118765. doi: https://doi.org/10.1016/j.powtec.2023.118765.
30. Dodds D., Sarhan A.R., Naser J. Experimental and numerical study of drag forces on particles in clusters. *Powder Technology*, 2020, vol. 371, pp. 195-208. doi: https://doi.org/10.1016/j.powtec.2020.05.082.
31. Zaidi A.A. Granular drag force during immersion in dry quicksand. *Powder Technology*, 2020, vol. 364, pp. 986-993. doi: https://doi.org/10.1016/j.powtec.2019.10.048.
32. Lavinsky D.V., Zaitsev Y.I. Computational studies of electromagnetic field propagation and deforming of structural elements for a thin-walled curved workpiece and an inductor. *Electrical Engineering & Electromechanics*, 2024, no. 2, pp. 55-60. doi: https://doi.org/10.20998/2074-272X.2024.2.08.
33. Gans Š., Molnár J., Kováč D. Estimation of electrical resistivity of conductive materials of random shapes. *Electrical Engineering & Electromechanics*, 2023, no. 6, pp. 72-76. doi: https://doi.org/10.20998/2074-272X.2023.6.13.
34. Ouili M., Mehasni R., Feliachi M., Latreche M.E.H. Coupling of PSO and FE methods for electrical conductivity identification of materials used in eddy current separator. *International Journal of Applied Electromagnetics and Mechanics*, 2023, vol. 72, no. 2, pp. 103-114. doi: https://doi.org/10.3233/JAE-220248.
35. Yang Y., Robertson W.S.P., Jafari A., Arjomandi M. Advanced Numerical Approaches for Magnetic Force Calculations: A Comprehensive Review. *Progress In Electromagnetics Research B*, 2025, vol. 115, pp. 78-94. doi: https://doi.org/10.2528/PIERB25071902.
36. Bastos J.P.A., Sadowski N. *Electromagnetic Modeling by Finite Element Methods*. CRC Press, 2003. 510 p. doi: https://doi.org/10.1201/9780203911174.
37. Tolmachev S.T., Bondarevskyi S.L., Il'chenko A.V. Magnetic properties of multicomponent heterogeneous media with a doubly periodic structure. *Electrical Engineering & Electromechanics*, 2020, no. 1, pp. 29-38. doi: https://doi.org/10.20998/2074-272X.2020.1.05.
38. Milykh V.I., Tymin M.G. A comparative analysis of the parameters of a rotating magnetic field inductor when using concentric and loop windings. *Electrical Engineering & Electromechanics*, 2021, no. 4, pp. 12-18. doi: https://doi.org/10.20998/2074-272X.2021.4.02.
39. Grechko O.M. Influence of the poles shape of DC electromagnetic actuator on its thrust characteristic. *Technical Electrodynamics*, 2024, no. 1, pp. 38-45. doi: https://doi.org/10.15407/techned2024.01.038.
40. Lohse D., Rauhe R., Bergmann R., Van der Meer D. Creating a dry variety of quicksand. *Nature*, 2004, vol. 432, no. 7018, pp. 689-690. doi: https://doi.org/10.1038/432689a.
41. Mehasni R., Feliachi M., Latreche M.E.H. Effect of the Magnetic Dipole–Dipole Interaction on the Capture Efficiency in Open Gradient Magnetic Separation. *IEEE Transactions on Magnetics*, 2007, vol. 43, no. 8, pp. 3488-3493. doi: https://doi.org/10.1109/TMAG.2007.897616.

Received 20.10.2025
Accepted 27.12.2025
Published 02.05.2026

O. Belguet[1], *PhD,*
R. Mehasni[1], *Professor,*
A. Belounis[2], *Doctor of Electrical Engineering,*
M. Ouili[1], *Doctor of Electrical Engineering,*
[1] Electrical Laboratory of Constantine (LEC),
Constantine 1 University, Algeria,
e-mail: oussama.belguet@lec-umc.org (Corresponding Author).
[2] 20th August 1955 University, Algeria.

How to cite this article:
Belguet O., Mehasni R., Belounis A., Ouili M. Effects of friction on the efficiency of open gradient magnetic separation in dry granular materials. *Electrical Engineering & Electromechanics*, 2026, no. 3, pp. 3-10. doi: https://doi.org/10.20998/2074-272X.2026.3.01

UDC 621.313 https://doi.org/10.20998/2074-272X.2026.3.02

A. Dilmi, A. Bouzida, N. Yassa, B. Fares

Analysis of the external network parameters influence on the operating characteristics of self-excited induction generators

Introduction. *Self-excited induction generators (SEIGs) play a vital role in renewable energy systems, particularly in remote regions. However, their performance is highly sensitive to excitation capacitance, rotor speed and load variations, making stability and reliability key challenges.* ***Problem.*** *Simplified analytical models fail to capture the complex internal interactions within SEIGs, limiting the analysis of how external network variations influence their dynamics. Moreover, the gradual degradation of excitation capacitors, a common fault in practice, significantly reduces generator efficiency. The* ***goal*** *of this work is to analyze the influence of excitation capacitance, rotor speed and load variations on SEIG performance, focusing on gradual capacitor degradation and open-phase faults to provide guidelines for reliable and efficient design.* ***Methodology.*** *Finite element modeling (FEM) with ANSYS Maxwell is used to accurately simulate electromagnetic and mechanical dynamics under realistic operating conditions.* ***Results.*** *Simulations show how changes in capacitance, rotor speed and load greatly affect voltage and current stability. Capacitor faults and open-phase conditions cause current distortion, voltage unbalance and reduced efficiency.* ***Scientific novelty*** *of this work lies in the FEM-based analysis of gradual excitation capacitor degradation in SEIGs. It was determined that this degradation directly impacts voltage balance, current waveform distortion and overall efficiency.* ***Practical value.*** *The findings provide clear guidelines for selecting optimal excitation capacitance and load ranges, reducing costs while enhancing the reliability and efficiency of SEIGs, particularly in isolated regions. Also this study offers new physical insight and a reliable framework for generator condition monitoring and design optimization.* References 24, tables 1, figures 12.
Key words: **self-excited induction generator, voltage stability, current distortion, reliability enhancement, rotor, capacitor.**

Вступ. *Автономні асинхронні генератори (SEIGs) відіграють життєво важливу роль у системах відновлюваної енергетики, особливо у віддалених регіонах. Проте їхня продуктивність високочутлива до ємності збудження, швидкості ротора та змін навантаження, що робить стабільність та надійність ключовими викликами.* ***Проблема.*** *Спрощені аналітичні моделі не здатні відобразити складні внутрішні взаємодії в SEIG, що обмежує аналіз того, як коливання зовнішньої мережі впливають на їхню динаміку. Крім того, поступова деградація конденсаторів збудження, що є поширеною несправністю на практиці, суттєво знижує ефективність генератора.* ***Метою*** *роботи є аналіз впливу ємності збудження, швидкості ротора та змін навантаження на продуктивність SEIG, зосереджуючись на поступовій деградації конденсаторів та обривах фаз, щоб надати рекомендації для надійного та ефективного проєктування.* ***Методологія.*** *Для точного моделювання електромагнітної та механічної динаміки в реалістичних робочих умовах використовується моделювання методом скінченних елементів (FEM) за допомогою програмного комплексу ANSYS Maxwell.* ***Результати.*** *Моделювання показує, як зміни ємності, швидкості ротора та навантаження значно впливають на стабільність напруги та струму. Несправності конденсаторів та умови обриву фази спричиняють спотворення струму, дисбаланс напруги та зниження ефективності.* ***Наукова новизна*** *роботи полягає в аналізі поступової деградації конденсаторів збудження в SEIG, заснованому на FEM. Встановлено, що ця деградація безпосередньо впливає на баланс напруги, спотворення форми хвилі струму та загальну ефективність.* ***Практична цінність.*** *Отримані результати надають чіткі рекомендації для вибору оптимальної ємності збудження та діапазонів навантаження, знижуючи витрати та одночасно підвищуючи надійність і ефективність SEIG, особливо у віддалених регіонах. Також це дослідження пропонує нове фізичне розуміння та надійну основу для моніторингу стану генератора та оптимізації його проєктування.* Бібл. 24, табл. 1, рис. 12.
Ключові слова: **асинхронний генератор з самозбудженням, стабільність напруги, спотворення струму, підвищення надійності, ротор, конденсатор.**

Introduction. With the increasing integration of wind energy into modern power systems, the demand for reliable and cost-effective standalone generation solutions has grown, particularly in isolated and rural regions [1].

Among the available options self-excited induction generators (SEIGs) have emerged as an attractive choice due to their simple construction, cost-effectiveness, and ability to operate without external excitation sources. SEIGs offer several advantages, including a robust design, low maintenance requirements, and the use of a brushless squirrel-cage rotor. Moreover, their nonlinear voltage speed characteristic, shaped by magnetic saturation, enables stable operation even under slight rotor speed variations beyond the rated value [2].

Despite these advantages, the practical deployment of SEIGs requires continuous performance assessment, as they are highly sensitive to excitation capacitance, rotor speed, and load variations [3]. Faults and parameter variations can significantly degrade SEIG performance. In particular, excitation capacitor failures or open-phase conditions disturb the excitation balance, leading to distorted stator currents, unstable torque, and voltage fluctuations, which may escalate into complete system breakdown [4]. While the minimum and maximum capacitance levels required for self-excitation are well known, selecting and maintaining optimal values under real operating conditions remains a technical challenge [5].

To overcome these limitations, this study adopts the finite element modeling (FEM) to model SEIGs with high accuracy under both healthy and faulty conditions. The machine is first simulated as a motor and then transitioned to generator mode once the rotor exceeds synchronous speed, with self-excitation sustained by a connected capacitor bank [6]. Variations in capacitance, rotor speed, and load are investigated systematically, along with the impact of capacitor disconnect and open-phase faults on generator dynamics.

The **goal** of this work is to analyze the influence of excitation capacitance, rotor speed and load variations on SEIG performance, focusing on gradual capacitor degradation and open-phase faults to provide guidelines for reliable and efficient design.

Literature review. Induction machines have been widely investigated for use as generators in isolated applications. In [7], the authors proposed and evaluated series compensation techniques to improve the high-power variable speed operation of SEIGs, showing enhanced stability and power quality, which strengthens the reliability and practical feasibility of these generators

in modern energy systems. Meanwhile, in [8] authors focused on employing the dragonfly algorithm for transient and steady-state analysis of SEIGs, highlighting the potential of computational intelligence methods in performance modeling rather than direct operational enhancement. Furthermore, practical applications of these machines have been presented in [9].

SEIGs offers several advantages, including robustness, light weight, compact size, and a brushless structure that reduces maintenance requirements and losses, making it a cost-effective solution. Moreover, SEIGs are characterized by simple operation and fast dynamic response, which further enhance their suitability for small-scale power generation.

In [10] an experimental investigation was conducted to evaluate and compare the performance of a SEIG and a permanent magnet synchronous generator for standalone renewable energy applications. The study utilized a micro-hydro turbine to drive both generators and examined their behavior under different load scenarios, including resistive heating and an induction motor-driven pump. With a focus on maintaining constant voltage and frequency in isolated systems, the research aimed to identify a simple, cost-effective, and reliable solution without relying on power electronic switches for reactive power compensation. The findings highlighted the viability of SEIGs as an economical and practical option for small-scale independent power generation.

Several studies have addressed parameter identification, voltage regulation, and performance optimization under steady-state, transient, and dynamic operating conditions [11, 12]. Authors [13] proposed an improved DSTATCOM control scheme using an enhanced phase-locked loop based on the current synchronous detection method, resulting in better terminal voltage regulation and enhanced power quality. In addition, in [14] were analyzed open-circuit capacitor faults in SEIGs and demonstrated that such faults can reduce torque to zero, destabilizing the system. Their approach utilized the Hilbert-Huang transform for fault detection. However, this study did not consider capacitor aging. In contrast**,** our work addresses this gap by evaluating the effects of capacitor aging on SEIG performance and reliability. Furthermore, we expand the study to include variations in capacitor capacity, load changes, rotor speed fluctuations, and phase-opening faults, providing a comprehensive assessment of factors influencing SEIG operation.

However, most previous studies rely on traditional SEIG modeling approaches, such as small-signal or *d-q* axis models, which often fail to capture the nonlinear behavior accurately under variable operating conditions, such as variations in load, rotor speed, and capacitance. In comparison, the present study employs the FEM, a robust and reliable approach capable of accurately representing the magnetic field and dynamic behavior of the generator. This methodology enhances the credibility of the results and addresses the limitations found in prior research.

Presentation of the main material. The FEM analyzes magnetic fields by considering factors such as the geometry of the magnetic circuit, the arrangement of stator windings and rotor bars, the presence of slots around the air gap, and the nonlinear characteristics of ferromagnetic materials [15]. Moreover, the behavior of electromagnetic systems is fundamentally governed by Maxwell's equations, which describe the essential relationships between electric and magnetic fields, as well as the intrinsic properties of various materials. These equations form the foundation for modeling and analyzing electromagnetic phenomena. In this context, it is crucial to integrate motion with the field equations within the FEM [16–18] to ensure an accurate and comprehensive representation of the system's dynamic behavior.

The general 2D formulation of Maxwell's equations is expressed as:

$$\nabla\times\boldsymbol{E} = -\partial\boldsymbol{B}/\partial t. \quad (1)$$

This equation describes how a time-varying magnetic field induces a circulating electric field, where $\boldsymbol{E}$ is the electric field intensity; $\boldsymbol{B}$ is the magnetic flux density; t is time; ∇ is the curl operator denoting the rotational derivative of a vector field.

The Maxwell–Ampere law is expressed as follows:

$$\nabla\times\boldsymbol{H} = \boldsymbol{J}_e + \partial\boldsymbol{D}/\partial t. \quad (2)$$

where $\boldsymbol{H}$ is the magnetic field intensity; $\boldsymbol{J}_e$ is the conduction current density; $\boldsymbol{D}$ is the electric flux density. In practical applications, particularly at industrial frequencies, the displacement current term $\partial\boldsymbol{D}/\partial t$ is very small and can be neglected. Thus, (2) simplifies to:

$$\nabla\times\boldsymbol{H} = \boldsymbol{J}_e. \quad (3)$$

The relationship between the electric flux density and the free electric charge density ρ_e is given by:

$$\nabla\cdot\boldsymbol{D} = \rho_e. \quad (4)$$

Since the divergence of the curl of any vector field is always zero, applying this property to the Maxwell–Ampere law leads to the general continuity equation:

$$\nabla\cdot(\nabla\times\boldsymbol{H}) = \nabla\cdot\boldsymbol{J}_e = 0. \quad (5)$$

This equation represents the conservation of electric charge, implying that, in steady-state or low-frequency applications where the displacement current is negligible $\partial\boldsymbol{D}/\partial t \approx 0$ and charge accumulation is minimal $\partial\rho_e/\partial t \approx 0$, the net current entering a closed surface is equal to the net current leaving it.

The electromagnetic behavior of materials is governed by Ohm's law in differential form:

$$\boldsymbol{J}_e = \sigma\cdot\boldsymbol{E}, \quad (6)$$

where σ is the electrical conductivity of the material.

The electric flux density can be formulated as:

$$\boldsymbol{D} = \varepsilon\cdot\boldsymbol{E} = \varepsilon_0\cdot\varepsilon_r\cdot\boldsymbol{E}, \quad (7)$$

where ε_0 is the vacuum permittivity; ε_r is the relative permittivity.

The magnetic flux density can be written as:

$$\boldsymbol{B} = \mu\cdot\boldsymbol{H} = \mu_0\cdot\mu_r\cdot\boldsymbol{H}, \quad (8)$$

where μ is the permeability; μ_0 is the vacuum permeability; μ_r is the relative permeability.

In summary, these equations form the basis for modeling electromagnetic fields and, within the FEM, allow accurate simulation of complex systems under dynamic conditions. The accurate assessment of the minimal capacitance necessary for SEIG is of considerable practical significance. Numerous numerical approaches for determining the requisite excitation capacitance have been recorded in prior studies [19].

This work derived the precise values of the minimum capacitance required for self-excitation based on (9) [20]:

$$C_{\Delta\min} = Q_{gen} / 3U^2\omega, \quad (9)$$

where $C_{\Delta\min}$ is the minimum capacitance per phase in Δ connection; Q_{gen} is the reactive power that must be supplied by the excitation capacitors to establish self-excitation in the generator; the angular frequency $\omega = 2\pi f$, where f is the supply frequency; U is the phase voltage.

Initially, the reactive power consumed by the asynchronous machine while operating as a motor Q_{mot} is determined as:

$$Q_{mot} = (P_n/\eta_{mot})\cdot\tan(\cos^{-1}\varphi_{mot}), \quad (10)$$

where P_n is the rated mechanical power; η_{mot} is the efficiency of the driving mechanism; φ_{mot} is the power factor angle during motor operation.

After evaluating the reactive power consumed in motor mode Q_{mot}, the corresponding reactive power in generator mode Q_{gen} can be computed as:

$$Q_{gen} = (\sin\varphi_{gen} / \sin\varphi_{mot})\cdot Q_{mot}, \quad (11)$$

where φ_{gen} is the power factor angle during generator operation [21].

This study presents a numerical analysis of a SEIG designed to operate with excitation capacitors of 151 μF. The detailed specifications of the SEIG are listed in Table 1.

Table 1

Parameters of the SEIG

Parameter	Value	Parameter	Value
Rated power	4 MW	Rotor slots	52
Rated voltage	3000 V	Bs0 rotor slot	3.5 mm
Coupling method	Wye	Bs1 rotor slot	13 mm
Number of poles	2	Bs2 rotor slot	13 mm
Rated speed	3135 rpm	Hs0 rotor slot	4.3 mm
Operating temperature	75°	Hs01 rotor slot	2.7 mm
Stator slots	54	Hs1 rotor slot	4.85 mm
Hs0 stator slot	4.5 mm	Hs2 rotor slot	40.25 mm
Hs2 stator slot	115mm	Hs1 stator slot	2.4 mm
BS2 stator slot	18.2 mm	Bs1 stator slot	21.16 mm

Geometry and regions. Modeling half or a quarter of the machine is possible due to symmetry; however, once asymmetries are introduced, a full machine model is required to accurately capture the physical phenomena.

The modeling procedure begins with the definition of the stator slot geometry (Fig. 1), where the slot dimensions and winding layout are carefully specified to reflect the real machine design. The rotor slots were designed with a slight skew angle to reduce cogging torque and mitigate magnetic locking between the stator and rotor teeth.

Next, the rotor slot geometry is constructed, as shown in Fig. 2. Ensuring that the bar placement and end-ring connections are properly represented.

The stator and rotor of the studied generator were designed and modeled within the Ansys Maxwell simulation environment. Figure 3 shows the geometric configuration of the notch structure along with the distribution of slots and their corresponding parameters.

The meshing process is a fundamental step in numerical simulation, as the quality and density of the mesh directly affect the accuracy and reliability of the results. A finer mesh is typically applied to critical regions such as slots, the air gap, and areas with sharp variations in electric and magnetic fields, where abrupt field changes may cause significant errors if not accurately resolved.

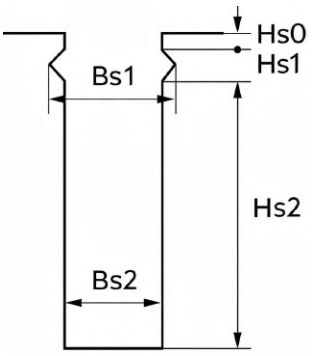

Fig. 1. Stator slot

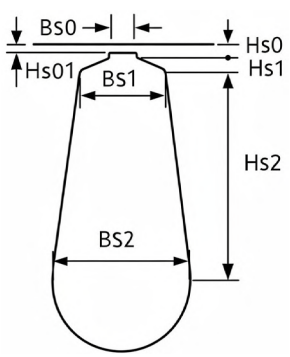

Fig. 2. Rotor slot

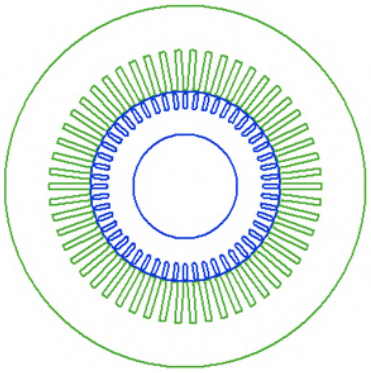

Fig. 3. Geometry of stator and rotor

Conversely, larger and coarser elements are utilized in regions where the fields vary gradually, reducing the computational load and enhancing simulation efficiency. Moreover, the choice of element type – whether triangular, quadrilateral, or higher-order elements – significantly influences both solution accuracy and computational speed. These strategies collectively aim to achieve an optimal balance between precision and computational efficiency in the analysis of electrical generators. The geometry, mesh and phases distribution of the studied model are shown in Fig.4.

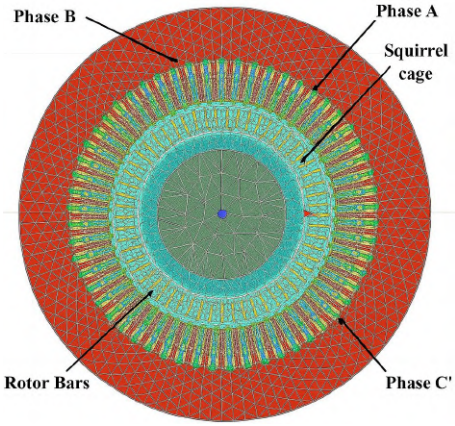

Fig. 4. The geometry, mesh and phases distribution of the studied model

In the final stage, the 2D model is created, with all the required parameters, boundary conditions and phase and winding distributions accurately represented. The magnetic field distribution is depicted, providing a detailed map of flux lines and field density, which allows for an in-depth analysis of the machine's electromagnetic performance. Figure 5 shows the Maxwell 2D model and the corresponding magnetic field distribution.

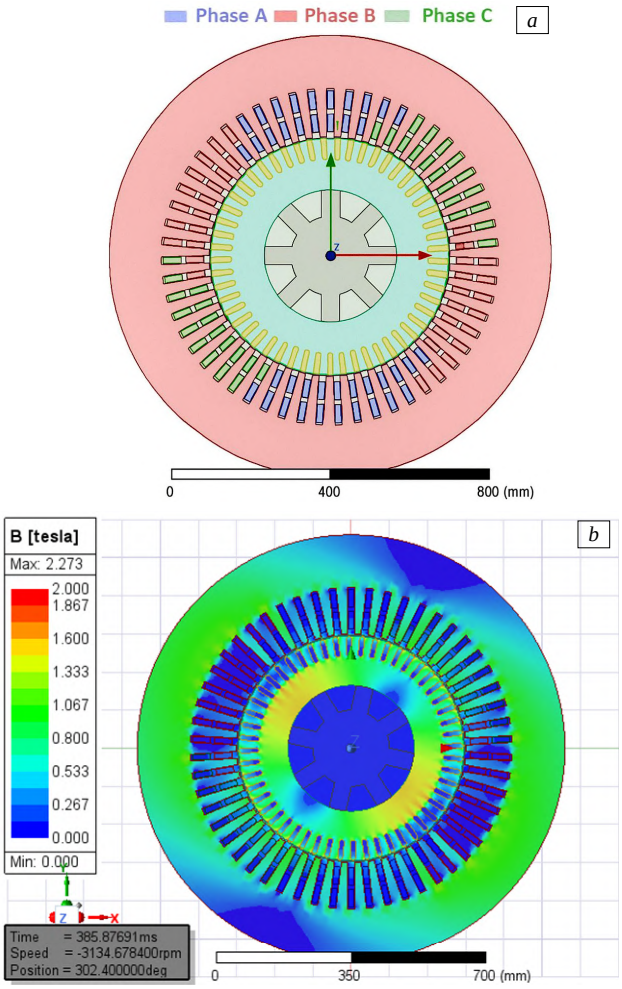

Fig. 5. Maxwell 2D model (*a*) and the distribution of magnetic flux density (*b*)

This sequential workflow from geometry definition, through meshing, to field distribution ensures a reliable finite element representation of the machine, forming the foundation for accurate simulations and further performance evaluation.

Simulation results and discussion. The developed model is tested using the time stepping FEM to evaluate its performance under no-load conditions. The voltage output of the SEIG remains stable at 3 kV, while the stator current settles at 550 A without distortions, confirming that the generator operates reliably in this state.

Figure 6 shows the root mean square (RMS) values of both voltage and current, clearly illustrating their stable and distortion-free behavior.

Influence of capacitance value. In [22] a steady-state equivalent circuit model of a 5 kW (SEIG) was employed, focusing on optimizing shunt and series capacitances for frequency regulation.

Two optimization techniques, the genetic algorithm (GA) and the gravitational search algorithm (GSA), were applied to determine the optimal capacitor values under resistive and resistive–inductive loads.

The results showed that optimized capacitor sizing significantly reduced frequency deviation and enhanced operational stability, with comparable performance between the two methods.

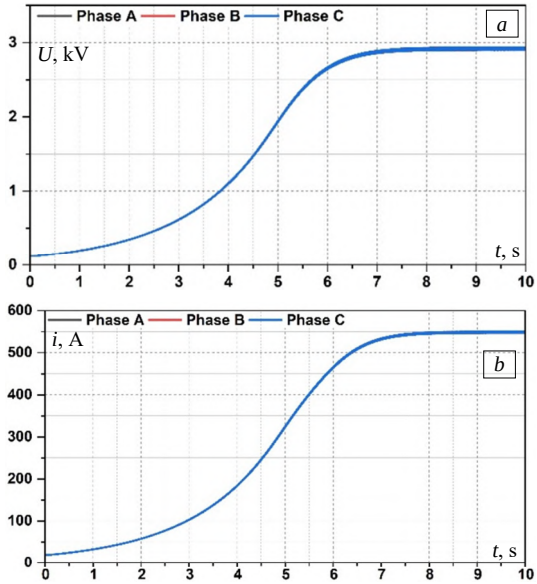

Fig .6. The RMS values of voltage (*a*) and current (*b*) under the no-load condition

Since that study focused on the effect of capacitance on frequency, our work emphasizes the impact of excitation capacitance on the self-excitation time, voltage, and current of the SEIG. Starting from the minimum capacitance of C_{Δ} = 452 μF, the value was progressively increased to 900 μF, 1200 μF and 1500 μF. The corresponding results are presented in Fig. 7, which shows the influence of excitation capacitance on the voltage build-up process of the generator. For a capacitance of 900 μF, the voltage stabilizes at approximately 3.6 kV after nearly 3 s, indicating slower excitation, with the corresponding RMS current reaching about 1.53 kA. Increasing the capacitance to 1200 μF raises the voltage to around 3.9 kV within 2 s, accompanied by a steady-state current of nearly 1.55 kA. At 1500 μF the generator achieves nearly 4.2 kV in less than 1.5 s, while the current rises to approximately 2.3 kA, highlighting a significant improvement in both excitation time and output magnitude.

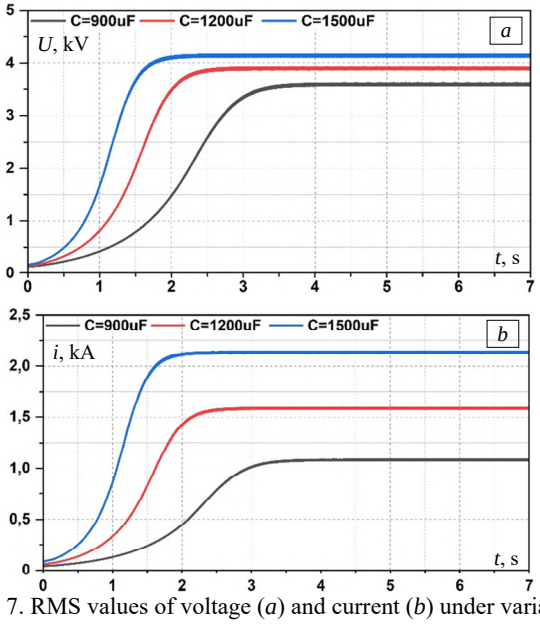

Fig. 7. RMS values of voltage (*a*) and current (*b*) under variable capacitor value

These results clearly demonstrate that higher capacitance values reduce the self-excitation time, but they also increase the voltage and current beyond the generator's capacity, which may put it at risk. This highlights the importance of careful and precise selection of the appropriate capacitor size.

Moreover, our experiments show that selecting a capacitance up to 10 % above the minimum required is beneficial, as it ensures self-excitation, improves voltage stability, and enhances the power factor. However, this should be regarded as a practical guideline based on the studied operating conditions, since the actual impact depends on the generator characteristics, rotational speed, and the connected load.

Influence of speed. The second parameter influencing the generator's electrical characteristics is rotor speed. We set the capacitance value at C_{Δ} = 900 μF and created a variable speed profile (Fig. 8).

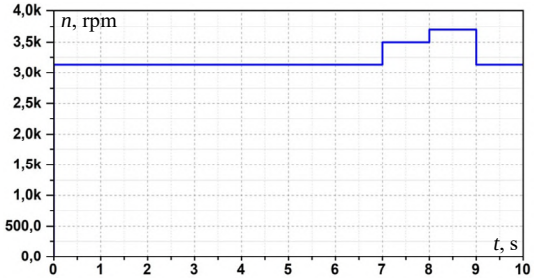

Fig. 8. Profile of variable rotor speed

Rotor speed fluctuations are a key factor influencing the electrical characteristics of the induction generator, as illustrated in Fig. 9.

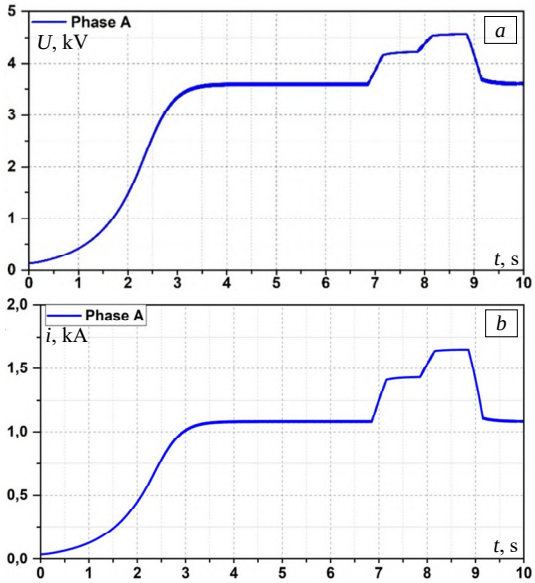

Fig. 9. RMS values of voltage (*a*) and current (*b*) under a variable rotor speed profile

An increase in speed leads to higher voltage and current, while a decrease reduces these values. The analysis results indicate that when the rotor speed increased by 25 rpm above the synchronous speed of 3110 rpm and stabilized at 3135 rpm, the start-up was smooth, as observed in the current and voltage signals during the period from 0 to 2.5 s. In contrast, when the rotor speed rose significantly above this value, the voltage exceeded 3 kV, pushing the generator beyond its design capacity, increasing its temperature, and potentially leading to failure. Accordingly, this study concludes that the rotor speed should not exceed 30 % above the synchronous speed (approximately 4043 rpm) in order to avoid operational risks and ensure the stability and safety of the generator. To address this, control techniques such as blade angle adjustment in wind turbines or advanced electronic systems for voltage and current regulation are employed to maintain safe operation. The ability of the induction generator to withstand such fluctuations without voltage collapse is essential for grid stability and for enhancing energy production efficiency.

Influence of load. This section investigates the impact of load variation on the generator's performance. The study in [23] analyzed and simulated wind-driven SEIG supplying isolated DC loads using a MATLAB/Simulink model, focusing solely on DC loads without considering AC or variable loads more comprehensively. In contrast, in our study, a balanced 3-phase load of 3 Ω is applied at t = 0.05 s after the generator reaches steady-state, followed by successive tests with loads of 5 Ω and 10 Ω. The resulting voltage and current responses, shown in Fig. 10, highlight the nonlinear behavior of the SEIG under varying load conditions. For a 10 Ω load, the generator maintains a nearly constant voltage of 2.8–2.9 kV with a steady current of 0.55–0.6 kA, demonstrating stable operation.

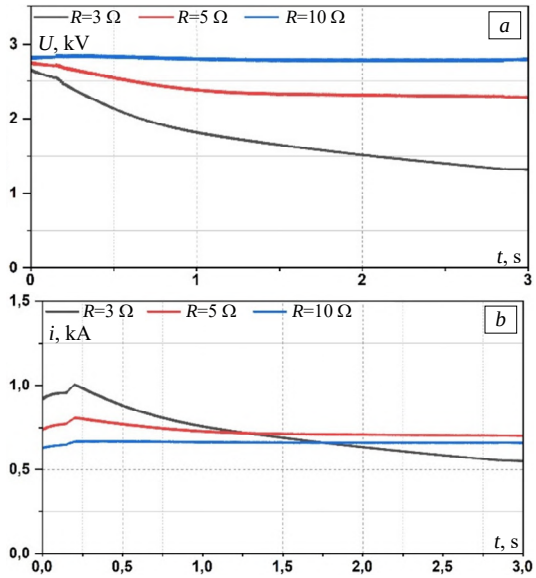

Fig. 10. The RMS values of voltage (*a*) and current (*b*) under different load values

At 5 Ω, the voltage gradually decreases to around 1.4–1.5 kV, while the current stabilizes at approximately 0.8 kA. In contrast, a 3 Ω load leads to a pronounced decline in voltage, falling from ~2.6 kV to ~1.4 kV, accompanied by a current drop from ~1.2 kA to ~0.55 kA. These results demonstrate that heavier loads significantly accelerate voltage decay while only moderately affecting the current, emphasizing the importance of load management to preserve generator stability and efficiency.

Influence of open phase fault. Previous research in [14] investigated the performance of SEIG under phase fault conditions. The study focused on a line–line fault between phases A and B. During this fault, the voltage of

the directly affected phase A dropped immediately to zero at t = 1.6 s, while the voltages of the remaining healthy phases B and C decreased shortly afterward at t = 1.68 s. At the same time, a sudden surge in current occurred in the affected lines during the initial cycles following the fault.

However, this study did not explicitly examine the effects of an open-phase fault, in which a single phase is suddenly disconnected from the supply.

In the present study, phase A was intentionally interrupted at t = 7 s after the generator reached steady-state operation under load, as shown in Fig. 11. This disconnection caused the current in the faulty phase to collapse to zero, while the currents in the remaining phases decreased, forcing the generator to operate in a single-phase mode. The faulty phase also exhibited a transient voltage rise before stabilizing at a lower value, resulting in a clear imbalance among the 3-phase voltages. These disturbances can compromise the stability of control and protection systems, as voltage and current fluctuations may trigger protective relays and disconnect the generator from the network, potentially causing unplanned outages and economic losses. The findings emphasize the necessity of advanced monitoring and protection strategies, including vibration analysis, thermal imaging, and real-time diagnostics supported by predictive algorithms, to enable early fault detection and corrective actions before severe damage occurs.

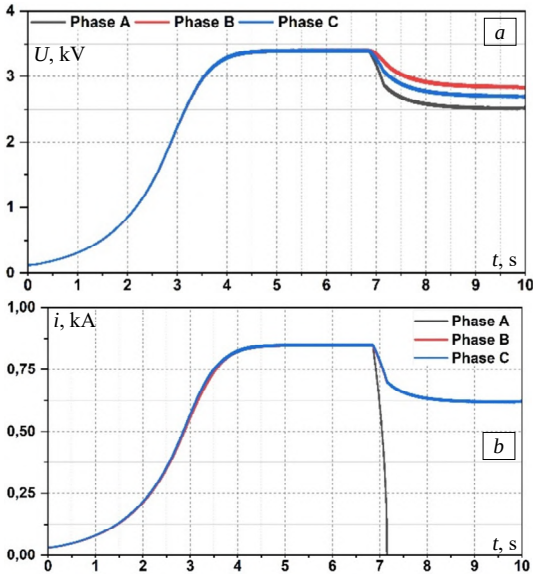

Fig. 11. RMS values of voltage (*a*) and current (*b*) under an open phase A condition

Influence of capacitor degradation. The progressive reduction in the capacitance of the excitation capacitor due to aging, thermal, or electrical stress [24] is a common fault in SEIGs, directly affecting their electrical stability. Figure 12 illustrates the current and voltage waveforms during this fault.

The gradual capacitor failure occurs while the generator is in operation, between 5 s and 7 s, leading to a drop in current from approximately 480 A to 370 A, followed by voltage waveform distortion. This gradual degradation reduces efficiency and shortens the generator's service life. Unlike previous studies that mainly focused on sudden disconnection, this work provides a precise analysis of the mechanism of gradual capacitance collapse using FEM, enabling researchers and engineers to gain deeper insights and enrich the understanding of generator stability.

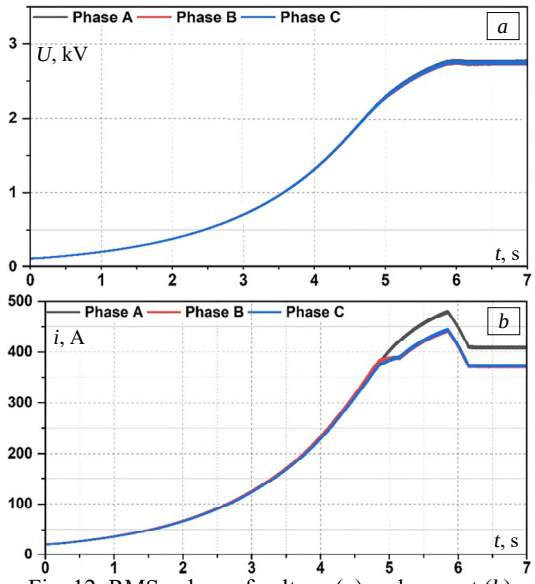

Fig. 12. RMS values of voltage (*a*) and current (*b*) under the condition of capacitor degradation

Conclusions. The main findings of this study are summarized through the analysis of internal and external factors influencing SEIG performance.

It was demonstrated that the excitation capacitance directly affects voltage stability and excitation time, as higher capacitance accelerates voltage build-up but increases the risk of overvoltage.

Regarding mechanical factors, rotor speed variation significantly influences voltage and current magnitudes, with stable operation ensured when the speed does not exceed 30 % above the synchronous value. Under external conditions, load variations revealed the nonlinear behavior of SEIGs, where heavier loads accelerate voltage decay, emphasizing the importance of proper load management.

Furthermore, open-phase faults cause severe voltage imbalance and current distortion, highlighting the necessity of advanced protection mechanisms. Notably, the gradual degradation of excitation capacitors due to aging serves as a reliable fault indicator, as it reduces current amplitude and distorts voltage waveforms.

The FEM-based analysis proved to be an effective approach for evaluating generator stability under both healthy and faulty conditions. Based on these findings, it is recommended to maintain the excitation capacitance slightly above the minimum required value (by approximately 10 %) to ensure reliable self-excitation and improve the power factor.

Conflict of interest. The authors declare that they have no conflicts of interest.

REFERENCES

1. Hafaiedh H., Saoudi Y., Benamor A., Chrifi–Alaoui L. Wind farms integration into power system with improved location and stability problem solving. *Electrical Engineering & Electromechanics*, 2025, no. 5, pp. 10-16. doi: https://doi.org/10.20998/2074-272X.2025.5.02.

2. Belynda F., Abdelli R., Bouzida A. Stator current signal crossing for fault diagnosis of self-excited induction generators.

Acta Polytechnica, 2023, vol. 64, no. 5, pp. 293-304. doi: https://doi.org/10.14311/AP.2023.63.0293.
3. Shailly D., Chittora P., Singh M. Performance analysis of multiple delayed signal cancellation (MDSC) for power quality improvement for fixed speed SEIG-based distributed generation. *Electrical Engineering*, 2025, vol. 107, no. 8, pp. 10911-10930. doi: https://doi.org/10.1007/s00202-025-03068-w.
4. Kouchih D., Hachelaf R. Discrimination of Stator Asymmetries and Magnetic Saturation in Self-Excited Induction Generators. *Russian Electrical Engineering*, 2024, vol. 95, no. 5, pp. 417-424. doi: https://doi.org/10.3103/S1068371224700469.
5. Khan M.F., Khan M.R., Iqbal A. Effects of induction machine parameters on its performance as a standalone self excited induction generator. *Energy Reports*, 2022, vol. 8, pp. 2302-2313. doi: https://doi.org/10.1016/j.egyr.2022.01.023.
6. Catelas J.M.R., Fernandes J.F.P., Pérez-Sánchez M., López-Jiménez P.A., Ramos H.M., Branco P.J.C. Energy Efficiency and Stability of Micro-Hydropower PAT-SEIG Systems for DC Off-Grids. *Energies*, 2024, vol. 17, no. 6, art. no. 1382. doi: https://doi.org/10.3390/en17061382.
7. Ahmed M.M., Hassanein W.S., Enany M.A. Proposing and Evaluation of SC Techniques for Variable Speed High-Power Operation of SEIG. *IEEE Access*, 2020, vol. 8, pp. 20666-20675. doi: https://doi.org/10.1109/ACCESS.2020.2968976.
8. Singh G., Singh V.R. SEIG-based transient- and steady-state analysis using dragon fly approach. *Soft Computing*, 2023, vol. 27, no. 6, pp. 2993-3005. doi: https://doi.org/10.1007/s00500-022-07458-1.
9. Rajak M.K., Samanta J., Pudur R. A hardware-based novel approach for parallel operation of two differently rated SEIGs. *Results in Engineering*, 2023, vol. 17, art. no. 100825. doi: https://doi.org/10.1016/j.rineng.2022.100825.
10. Murali Krishna V.B., Sandeep V., Murthy S.S., Yadlapati K. Experimental investigation on performance comparison of self excited induction generator and permanent magnet synchronous generator for small scale renewable energy applications. *Renewable Energy*, 2022, vol. 195, pp. 431-441. doi: https://doi.org/10.1016/j.renene.2022.06.051.
11. Dewangan S., Vadhera S. Performance Evaluation of Multilevel Inverter in Variable Speed SEIG-Based Wind Energy System. *Arabian Journal for Science and Engineering*, 2022, vol. 47, no. 3, pp. 3311-3324. doi: https://doi.org/10.1007/s13369-021-06197-z.
12. Chanu L.K., Chakraborty S., Pudur R. Real-time analysis of voltage and frequency regulation of self-excited induction generator based micro hydro plant using generalized impedance controller. *Measurement: Sensors*, 2024, vol. 33, art. no. 101235. doi: https://doi.org/10.1016/j.measen.2024.101235.
13. Özer A.S., Sevilmiş F., Karaca H., Arabacı H. Enhanced control method for voltage regulation of DSTATCOM based SEIG. *Energy Reports*, 2022, vol. 8, pp. 839-847. doi: https://doi.org/10.1016/j.egyr.2022.05.191.
14. Dalei J., Mohanty K.B. Fault classification in SEIG system using Hilbert-Huang transform and least square support vector machine. *International Journal of Electrical Power & Energy Systems*, 2016, vol. 76, pp. 11-22. doi: https://doi.org/10.1016/j.ijepes.2015.09.009.
15. Patel A.N., Doshi P.J., Mahagoakar S.C., Panchal T.H. Optimization of cogging torque in interior permanent magnet synchronous motor using optimum magnet v-angle. *Electrical Engineering & Electromechanics*, 2023, no. 6, pp. 16-20. doi: https://doi.org/10.20998/2074-272X.2023.6.03.
16. Panchal T.H., Patel A.N., Patel R.M. Reduction of cogging torque of radial flux permanent magnet brushless DC motor by magnet shifting technique. *Electrical Engineering & Electromechanics*, 2022, no. 3, pp. 15-20. doi: https://doi.org/10.20998/2074-272X.2022.3.03.
17. Iegorov O.B., Kundenko M.P., Iegorova O.Y., Mardziavko V.A., Rudenko A.Y. The influence of the design of the stator winding of a synchronous-reactive generator on increasing its energy efficiency. *Electrical Engineering & Electromechanics*, 2025, no. 5, pp. 3-9. doi: https://doi.org/10.20998/2074-272X.2025.5.01.
18. Grechko O.M. Influence of the poles shape of DC electromagnetic actuator on its thrust characteristic. *Technical Electrodynamics*, 2024, no. 1, pp. 38-45. doi: https://doi.org/10.15407/techned2024.01.038.
19. Arya S.R., Maurya R., Giri A.K., Qureshi A., Baladhanautham C.B. Power quality solutions for effective utilization of single-phase induction generator using voltage source converter. *Energy Sources, Part A: Recovery, Utilization, and Environmental Effects*, 2025, vol. 47, no. 2, art. no. 1772414. doi: https://doi.org/10.1080/15567036.2020.1772414.
20. Samanta J., Chakraborty S., Sangno R., Pudur R. Study of power quality issues in a renewable-driven self-excited induction generator due to different loads at edge-off grid system. *E-Prime - Advances in Electrical Engineering, Electronics and Energy*, 2025, no. 11, art. no. 100885. doi: https://doi.org/10.1016/j.prime.2024.100885.
21. Abd el-Ghany H.A., Ahmed E.S., ELGebaly A.E. A Reliable Loss of Excitation Protection Technique Based on EPFA for Synchronous Generators. *IEEE Transactions on Power Delivery*, 2022, vol. 37, no. 3, pp. 1445-1455. doi: https://doi.org/10.1109/TPWRD.2021.3087538.
22. Paliwal S., Sinha S.K., Chauhan Y.K. Frequency Control of 5 kW Self-excited Induction Generator Using Gravitational Search Algorithm and Genetic Algorithm. *AI and IOT in Renewable Energy*, 2021, pp. 75-88. doi: https://doi.org/10.1007/978-981-16-1011-0_8.
23. Sakkoury K.S., Emara S., Ahmed M.K. Analysis of wind driven self-excited induction generator supplying isolated DC loads. *Journal of Electrical Systems and Information Technology*, 2017, vol. 4, no. 1, pp. 257-268. doi: https://doi.org/10.1016/j.jesit.2016.08.003.
24. Guan B., Zhen X. Noninvasive Online Capacitor Monitoring Method for Three-Level Converter Based on Active Neutral-Point Current Adjustment. *IEEE Transactions on Industrial Electronics*, 2024, vol. 71, no. 5, pp. 4320-4329. doi: https://doi.org/10.1109/TIE.2023.3283714.

Received 02.10.2025
Accepted 22.12.2025
Published 02.05.2026

A. Dilmi[1], *PhD Student,*
A. Bouzida[1], *PhD, Full Professor,*
N. Yassa[1], *PhD, Associate Professor,*
B. Fares[2], *PhD, Assistant Lecturer,*
[1] Materials, and Sustainable Development Laboratory (LMDD), Faculty of Applied Sciences, University of Bouira, Algeria,
e-mail: ali.dilmi@univ-bouira.dz (Corresponding Author).
[2] Industrial and Information Technology Laboratory (IITL), University of Bejaia, Algeria.

How to cite this article:
Dilmi A., Bouzida A., Yassa N., Fares B. Analysis of the external network parameters influence on the operating characteristics of self-excited induction generators. *Electrical Engineering & Electromechanics*, 2026, no. 3, pp. 11-17. doi: https://doi.org/10.20998/2074-272X.2026.3.02

UDC 621.311 https://doi.org/10.20998/2074-272X.2026.3.03

V.V. Kozyrskyi, V.Ya. Bunko, P.M. Darmoris

Determination of the transition resistance of detachable electrical contacts with Camital active grease

Problem. *The reliability of detachable electrical contact connections is significantly reduced due to an increase in transition electrical resistance caused by thermomechanical deformations, oxidation of contact surfaces, and a decrease in the effective contact area during operation. According to the results of operational and experimental studies, failures associated with contact degradation account for up to a third of the total number of electrical installation failures. Traditional methods, in particular the use of passive conductive lubricants, mostly only slow down oxidation processes and do not ensure active restoration of the contact condition. In this regard, it is important to develop models and technical solutions capable of describing and ensuring the stabilisation of the transition resistance of electrical contacts through controlled thermomechanical processes in the contact zone.* ***Goal.*** *To establish the regularities and interrelationships of processes in electrical contacts through experimental research and mathematical modelling of the evolution of the transition resistance of contact connections with composite grease modified with Cu–Al–Mn (Camital) with shape memory, taking into account the interaction of electrical, thermal, thermomechanical and tribological processes in normal and emergency operating modes.* ***Methodology.*** *Experimental studies were performed on models of bolted contact connections of aluminum busbars using composite grease containing 5 % and 10 % Cu–Al–Mn powder by volume, as well as on control samples without grease. Long-term measurements of contact resistance were carried out at a constant temperature and under periodic thermal loads. The theoretical study is based on a multilevel mathematical model, the numerical solution of which was carried out using implicit stable methods with parameter identification based on experimental data.* ***Results.*** *A decrease and stabilisation of contact resistance was established when using composite lubricant, most pronounced at a Cu–Al–Mn powder content of 10 % by volume. A reduced model of contact resistance evolution was proposed.* ***Scientific novelty.*** *For the first time, a generalised mathematical model of a detachable electrical contact with active composite lubricant has been developed, which takes into account the phase transformations of Cu–Al–Mn alloy particles and the mechanism of thermomechanical destruction of oxide films. The possibility of a step-like decrease in contact resistance under impulse currents is shown.* ***Practical value.*** *The results obtained can be used to improve the reliability of detachable electrical contact connections, predict changes in contact resistance during operation, and justify the choice of the composition of active electrical contact lubricants.* References 37, tables 4, figures 7.

Key words: **electrical contact, contact resistance, composite electrical grease, Camital, shape memory alloy, thermal, thermomechanical and tribological processes.**

Проблема. *Надійність розбірних електричних контактних з'єднань істотно знижується внаслідок зростання перехідного електричного опору, спричиненого термомеханічними деформаціями, окисленням контактних поверхонь та зменшенням ефективної площі контакту в процесі експлуатації. За результатами експлуатаційних і експериментальних досліджень відмови, пов'язані з деградацією контактів, становлять до третини загальної кількості пошкоджень електроустановок. Традиційні способи, зокрема застосування пасивних електропровідних мастил, здебільшого лише сповільнюють окислювальні процеси та не забезпечують активного відновлення контактного стану. У зв'язку з цим актуальним є розроблення моделей і технічних рішень, здатних описувати та забезпечувати стабілізацію перехідного опору електричних контактів за рахунок керованих термомеханічних процесів у зоні контакту.* ***Мета.*** *Встановлення закономірностей і взаємозв'язків процесів в електричних контактах шляхом експериментального дослідження та математичного моделювання еволюції перехідного опору контактних з'єднань з композитним мастилом, модифікованим порошком сплаву Cu-Al-Mn (Camital) з пам'яттю форми, з урахуванням взаємодії електричних, теплових, термомеханічних і трибологічних процесів у нормальних та аварійних режимах роботи електроустановок.* ***Методика.*** *Експериментальні дослідження виконано на моделях болтових контактних з'єднань алюмінієвих шин з використанням композитного мастила з вмістом порошку Cu-Al-Mn 5 % і 10 % за об'ємом, а також на контрольних зразках без мастила. Проводилися довготривалі вимірювання перехідного опору за сталої температури та при періодичних теплових навантаженнях. Теоретичне дослідження базується на багаторівневій математичній моделі, чисельний розв'язок якої здійснювався неявними стійкими методами з ідентифікацією параметрів за експериментальними даними.* ***Результати.*** *Встановлено зниження та стабілізацію перехідного опору при використанні композитного мастила, найбільш виражену за вмісту порошку Cu-Al-Mn 10 % за об'ємом. Запропоновано редуковану модель еволюції перехідного опору.* ***Наукова новизна****. Наукова новизна роботи полягає у розробленні та експериментальному обґрунтуванні нового типу композитного електротехнічного мастила для розбірних електричних контактів, що містить порошок сплаву Cu-Al-Mn з ефектом пам'яті форми, а також у встановленні фізичного механізму активної стабілізації перехідного опору контактних з'єднань за рахунок термомеханічного руйнування оксидних плівок у процесі циклічних теплових навантажень.* ***Практична значимість.*** *Отримані результати можуть бути використані для підвищення надійності розбірних електричних контактних з'єднань, прогнозування зміни перехідного опору в процесі експлуатації та обґрунтування вибору складу активних електроконтактних мастил.* Бібл. 37, табл. 4, рис. 7.

Ключові слова: **електричний контакт, перехідний опір, композитне електротехнічне мастило, Camital, сплав з пам'яттю форми, теплові, термомеханічні та трибологічні процеси.**

Introduction. The state of contacts is determined by a number of independent and interdependent factors, the change of which in time is often random (Fig. 1). In general, the influencing factors can be divided into two conditional groups – internal and external. Internal factors, formed due to the functioning of the power supply system itself, provide a quantitative and qualitative characteristic of processes (modes). External factors mainly reflect the characteristics of the environment: atmospheric pressure and lightning surges; humidity and air temperature; solar radiation; actions of service

personnel, etc. To consider different levels of the power supply system, the set of factors can vary in number and composition [1–6].

Oxide films formed on the contacting surfaces of aluminum and copper have a significant electrical resistivity and reduce the effective area of the conductive contact, which leads to an increase in the transition resistance and local overheating. The accumulation of oxide layers during operation accelerates the degradation of the contact connection, increases power losses and reduces its long-term reliability. Failure to solve this problem can lead to thermal destruction of contacts and failures of conductive assemblies.

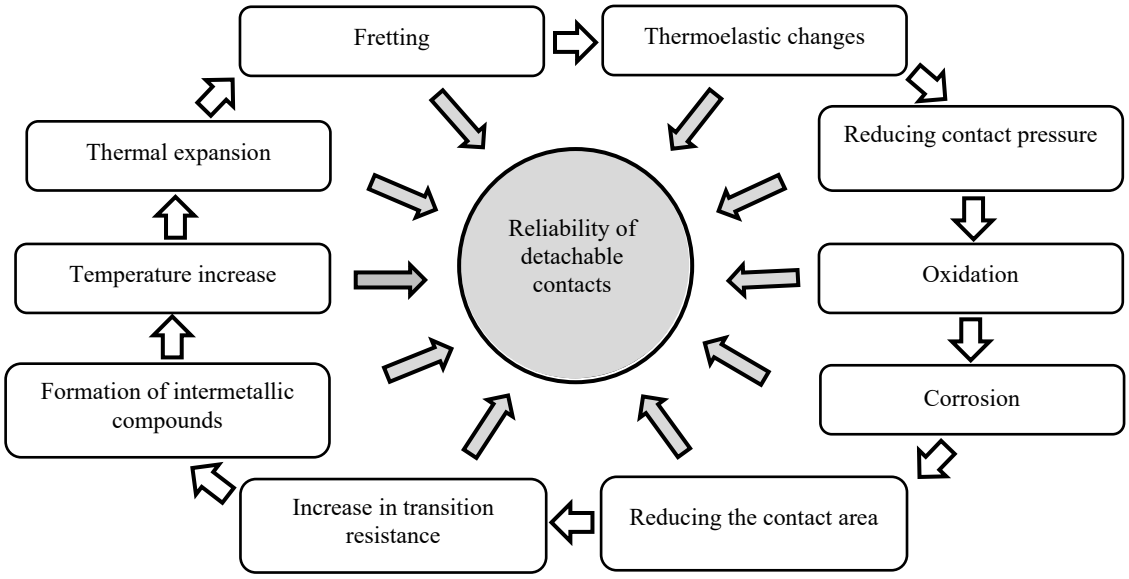

Fig. 1. Physical and chemical factors related to the reliability of electrical detachable contacts

To reduce the growth rate of oxide films, galvanic coatings, various methods of surface treatment, sealing and conductive greases are used [7–9]. The most common conductive and sealing greases are FOTU 571 Electrical Contact Grease, NO-OX-ID «A-Special» Electrical Contact Grease, Rheotemp™ 768G, CIATIM 221, etc. [10–17]. However, the above technical means only slow down the growth of oxide films and do not ensure their destruction. In previous studies, electrical lubricants were considered mainly as a passive means of sealing the contact space and reducing the environmental impact on the oxidation process of contact surfaces. Unlike known approaches, this work is the first to investigate a composite grease containing powder [18–23] of the Cu-Al-Mn alloy (Camital) [8, 9] with a shape memory effect, which performs the active function of thermomechanical influence on the contact surface and promotes the destruction of oxide films during operation. According to the results of the analysis of scientific publications, the authors are not aware of any works describing similar lubricant compositions or experimental studies of such a mechanism of action. The composition of this composite grease includes – electrically conductive grease and Camital intermetallic powder, which provides high electrical conductivity of the grease and destruction of oxide films. During the installation of the contact connection, the contacting surfaces are lubricated with a composite material. Tightening the bolted fastening to the nominal forces leads to deformation of the inner surface of the contact parts and particles of the shape memory alloy.

The goal of the work is to establish the regularities and interrelationships of processes in detachable electrical contacts by experimental research and mathematical modeling of the evolution of the transition resistance of contact connections with a composite electrical grease modified with Cu-Al-Mn alloy powder (Camital) with a shape memory effect based on the developed multi-level mathematical model, which takes into account the interaction of electrical, thermal, thermomechanical and tribological processes in normal and emergency operating modes of electrical installations.

Materials and methods. During long-term operation, films grow on the contacting surfaces, which leads to an increase in the transition resistance and a decrease in the operational life of the contact. This process is intensified by heating the contact with short-circuit currents. However, in the presence of a functional composite grease, heating the intermetallic particles with a shape memory effect leads to their restoration of the initial shape that they had before the contact was installed. Deformed, the intermetallic particles are displaced relative to the contact surface and destroy a significant part of the surface of the oxide films, which reduces the transition resistance and increases the operational life of the contact.

The study of the Camital intermetallic powder fractions was carried out on a TESCAN Mira 3 LMU scanning electron microscope (Fig. 2) designed to obtain an image of the object surface with high spatial resolution [24]. This microscope is used to study the shapes of particles and their surface morphology, analyze coatings, roughness and waviness of the surface of samples, fibers with specified properties, etc., at magnifications from 4 to 1,000,000 times with an accelerating voltage from 200 V to 30 kV.

a

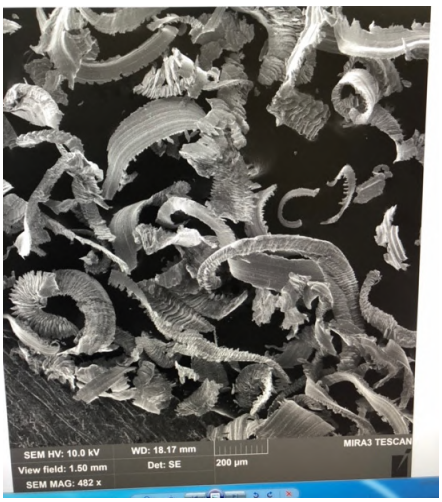

b

Fig. 2. General view of the TESCAN Mira 3 LMU electron microscope (*a*); study of fractions of the Camital intermetallic powder (*b*)

Research on the influence of functional composite grease on the electrical resistance of the contact connection. To test the influence of grease on the electrical resistance of the contact connection, a series of experimental studies were conducted on models of detachable bolted contact connections – aluminum buses with dimensions of 100×50×5 mm, M12 bolted connections (bolt M12×30 mm, hexagonal nut M12, two flat washers M12) (Fig. 3). Six samples of bolted connections were used: samples No. 1 and No. 2 were coated with electrically conductive grease with fraction 1 powder (v1), samples No. 3 and No. 4 were coated with grease with fraction 2 powder (v2), control samples No. 5 and No. 6 were without grease.

Electrically conductive grease with fraction 1 powder (v1) contained 95 % (by volume) CIATIM 221 and 5 % Camital intermetallic powder. The grease with powder fraction No. 2 (v2) contained 90 % CIATIM 221 and 10 % Camital intermetallic powder. The grease was applied in a thin layer to the contact surfaces of the aluminum tires (Fig. 4). A torque wrench (Intertool XT-9003) was used to control the tightening torque of the bolted joint, which was 40 N·m.

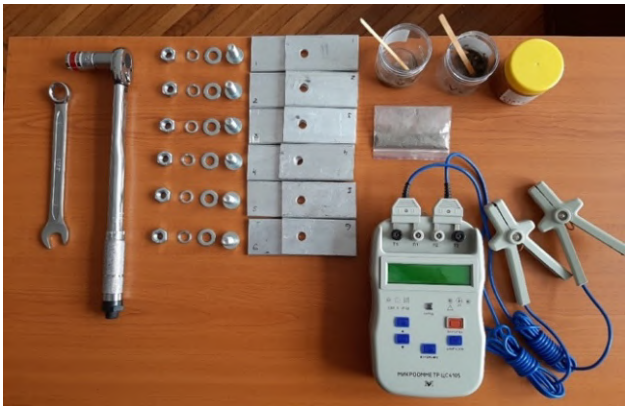

Fig. 3. Preparation for the experiment

The experiment consisted of periodic measurement of the electrical resistance of contact connection samples (Fig. 5). The duration of the experiment was from March 11, 2024 to April 1, 2025.

Fig. 4. Application of functional composite material to contact surfaces

Fig. 5. Measuring the resistance of the contact connection

Samples of contact connections No. 1, No. 3 and No. 5 were periodically heated in an oven to a temperature of 120 °C, held at this temperature for 4 min., and natural cooling to a temperature of 21 °C. In this way, overheating of the contacts was simulated. Samples of contact connections No. 2, No. 4 and No. 6 were constantly in the room at a temperature of 21 °C with an air humidity of 45 %.

Results and discussion. The results of experimental studies are presented in Tables 1, 2 (the first and last experiments, respectively), and in Fig. 6 all experimental measurements.

Table 1

Results of contact resistance measurement on 11.03.2024 and 16.03.2024

Sample No.	Lubrication type	The resistance value of the contact connection. Measurements on 11.03.2024, μΩ					The resistance value of the contact connection. Measurements on 16.03.2024, μΩ				
		1	2	3	4	average value	1	2	3	4	average value
1	v1	22,37	22,54	22,92	22,54	22,59	22,05	22,16	22,27	22,48	22,24
2	v1	21,24	22,05	21,18	21,24	21,43	20,97	21,02	20,86	21,02	20,97
3	v2	19,01	18,96	18,91	19,07	18,99	19,07	19,34	18,69	18,85	18,99
4	v2	20,15	20,1	20,48	20,59	20,33	20,1	20,15	20,1	20,21	20,14
5	without lubrication	31,75	31,8	30,72	31,15	31,36	31,64	31,69	31,75	31,75	31,71
6	without lubrication	28,66	28,5	28,66	28,77	28,65	27,36	28,06	27,41	27,36	27,55

Table 2

Results of contact resistance measurement on 04.03.2025 and 01.04.2025

Sample No.	Lubrication type	The resistance value of the contact connection. Measurements on 04.03.2025, μΩ					The resistance value of the contact connection. Measurements on 01.04.2025, μΩ				
		1	2	3	4	average value	1	2	3	4	average value
1	v1	25,74	25,72	25,67	25,78	25,73	25,73	25,79	25,79	25,81	25,78
2	v1	21,98	22,02	21,78	21,84	21,91	22,03	21,99	21,82	21,85	21,92
3	v2	20,68	20,86	20,84	20,9	20,82	20,71	20,84	20,82	20,79	20,79
4	v2	20,98	21,06	20,85	20,78	20,92	21,01	20,98	20,86	20,82	20,92
5	without lubrication	39,05	39,15	39,12	39,07	39,10	39,04	39,2	39,15	39,06	39,11
6	without lubrication	28,67	29,13	29,05	29,01	28,97	28,71	29,11	29,01	29,02	28,96

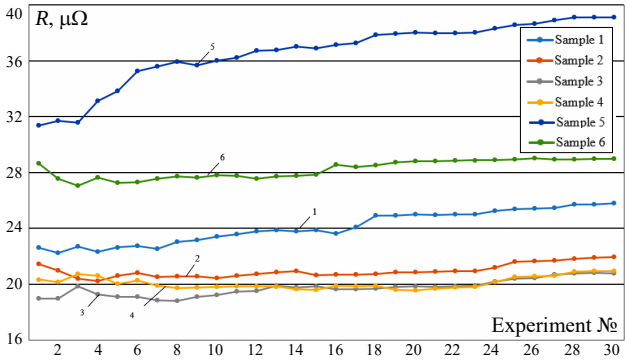

Fig. 6. Results of experimental measurements of contact connection resistance in the period from 11.03.2024 to 01.04.2025

Analysis of experimental research results. The presence of Camital intermetallic powder increases the electrical conductivity of contacts – reduces the initial resistance of contacts by 65 % (resistance of contacts No. 3 and No. 5).

Long-term exposure of contact connections No. 2, No. 4 and No. 6 at a constant temperature of 21 ^{0}C and relative humidity of 45 % does not lead to changes in the initial resistance of the contact connection during the year (conclusion taking into account the relative measurement error of 5 %).

The influence of the volume content of intermetallic powder in the functional grease on the initial resistance of the contact and the subsequent increase in resistance during periodic heating of the contacts is significant. This conclusion is confirmed by a comparison of the initial resistances of contacts No. 1 (powder content 5 %) and No. 3 (powder content 10 %) – the difference in the initial resistances is 19 %, and the final resistance is 23 %.

Periodic heating of contacts in the absence of Camital intermetallic powder in the grease leads to an increase in the resistance of the contact connection – contact No. 5 by 25 %. The presence of Camital intermetallic powder in the grease in a volume of 10 % practically eliminates the effect of periodic temperature changes on the resistance of the contact connection.

Theoretical modeling of processes in a detachable electrical contact joint containing a composite grease with Camital alloy powder. In an aluminum-aluminum (or Cu-Cu) contact joint with grease and Cu-Al-Mn powder, 4 interrelated processes occur simultaneously:

- formation of contact electrical conductivity. The contact resistance is determined by: the real contact area; the thickness and integrity of oxide films; the number of microcontacts created by the powder;
- thermomechanical cycle. Current load → heating → phase transformation of the shape memory alloy → restoration of the particle shape → local mechanical stresses → destruction of oxides;
- «microscraper» mechanism. Sharp edges of Camital particles: concentrate stresses; perform cyclic microcutting of the oxide film; periodically «renew» the metal-metal contact;
- chemical aging. Without powder – monotonous growth of the oxide area and thickness. With powder – competition of two processes: oxide growth; its thermomechanical destruction.

The structure of the mathematical model is multilevel, the system is nonlinear, transient, with internal feedback. The general structure of the mathematical model consists of 5 interconnected subsystems:

1. Electrical – contact resistance, current, current density;
2. Thermal – heating and cooling of the contact;
3. Thermomechanical (SMA) – deformation of Cu-Al-Mn particles;
4. Tribological – destruction of the oxide film;
5. Evolution of contact resistance.

1. The total contact resistance is defined as the sum of the components [25, 26]:

$$R_c(t) = R_b + R_{ox}(t)\,, \qquad (1)$$

where $R_c(t)$ is the total contact resistance, Ω; R_b is the volume resistance of the busbar material, Ω; $R_{ox}(t)$ is the resistance of the oxide film, Ω.

2. Current I and current density J:

$$I(t) = U(t)/R_c(t); \quad (2)$$

$$J(t) = I(t)/A_{ef}(t), \quad (3)$$

where $I(t)$ is the current, A; $U(t)$ is the voltage, V; $A_{ef}(t)$ is the effective area of the electrical contact, m^2.

3. Thermal subsystem (contact heating). The contact is considered as a concentrated heat capacity. The heat balance equation [27, 28]:

$$C_{th}\frac{dT}{dt} = I^2(t)R_c(t) - h_{th}(T - T_0), \quad (4)$$

where T is the contact temperature, K; T_0 is the ambient temperature, K; C_{th} is the contact heat capacity, J·K^{-1}; h_{th} is the heat transfer coefficient, W·K^{-1}.

4. Thermomechanical model of Cu-Al-Mn powder (SMA). Kinetics of phase transformation. The variable is introduced – austenite fraction $\xi(t)$ [29–31]:

$$\frac{d\xi}{dt} = k_\xi\left[H(T - A_s)(1-\xi) - H(M_s - T)\xi\right], \quad (5)$$

where ξ is the austenite fraction, dimensionless; k_ξ is the kinetic coefficient, s^{-1}; A_s, M_s are the phase transition temperatures, K; H is the Heaviside function, p.u.

Recoverable deformation of Camital powder particles:

$$\varepsilon(t) = \varepsilon_0 \cdot \xi(t), \quad (6)$$

where $\varepsilon(t)$ is the recoverable deformation of powder particles, p.u.; ε_0 is the initial recoverable deformation of powder particles, p.u.

Contact stresses created by a powder particle:

$$\sigma_p(t) = E_p \cdot \varepsilon(t), \quad (7)$$

where $\sigma_p(t)$ is the local contact stress created by the powder particle, Pa; E_p is the elastic modulus of the Cu-Al-Mn alloy, Pa.

5. Oxide film model. Evolution of oxide thickness [32, 33]:

$$\frac{dh}{dt} = k_{ox} - k_{br}N_p F(\sigma_p), \quad (8)$$

where h is the oxide thickness, m; k_{ox} is the oxide growth rate, m·s^{-1}; k_{br} is the oxide film destruction coefficient, m^2·s^{-1}; N_p is the particle volume concentration, m^{-1}.

Oxide destruction function

$$F(\sigma_p) = \begin{cases} 0, & \text{if } \sigma_p < \sigma_{ox}; \\ \left(\dfrac{\sigma_p - \sigma_{ox}}{\sigma_{ox}}\right)^n, & \text{else } \sigma_p \geq \sigma_{ox}, \end{cases} \quad (9)$$

where σ_{ox} is the strength limit of the oxide film, Pa; n is the nonlinearity index of the oxide destruction mechanism, dimensionless.

6. The relationship between the oxide film and resistance.

The resistance of the oxide layer:

$$R_{ox} = \rho_{ox}h(t)/A_{ef}(t), \quad (10)$$

where ρ_{ox} is the electrical resistivity of the oxide film, Ω·m.

The rate of change of the effective contact area:

$$\frac{dA_{ef}}{dt} = k_A\left[N_p\varepsilon(t) - \alpha_A h(t)\right], \quad (11)$$

where k_A is the kinetic coefficient of contact area formation, m^2·s^{-1}; α_A is the coefficient of contact area reduction due to oxidation, m^{-1}·s^{-1}.

Therefore, the complete system of equations has the form:

$$\begin{aligned} &R_c(t) = R_b + \frac{\rho_{ox}h(t)}{A_{ef}(t)}; \\ &I(t) = U(t)/R_c(t); \\ &C_{th}\frac{dT}{dt} = I^2(t)R_c(t) - h_{th}(T - T_0); \\ &\frac{d\xi}{dt} = k_\xi\left[H(T - A_s)(1-\xi) - H(M_s - T)\xi\right]; \\ &\varepsilon(t) = \varepsilon_0 \cdot \xi(t); \\ &\sigma_p(t) = E_p \cdot \varepsilon(t); \\ &\frac{dh}{dt} = k_{ox} - k_{br}N_p F(\sigma_p); \\ &\frac{dA_{ef}}{dt} = k_A\left[N_p\varepsilon(t) - \alpha_A h(t)\right] \end{aligned} \quad (12)$$

Due to the system of differential equations is rigid due to the significant difference in the hourly scales of thermal, mechanical and chemical processes, for its numerical decoupling, the implicit stable BDF and Radau methods [34, 35] are used. Numerical modeling using the Python software environment (NumPy, SciPy, Matplotlib libraries) is carried out.

The results of numerical modeling and experimental investigations are presented in Fig. 7. The solid lines correspond to a numerical model drawn from a reduced, physically reasonable model. Each line was built with individual parameters identified for the corresponding experimental specimen.

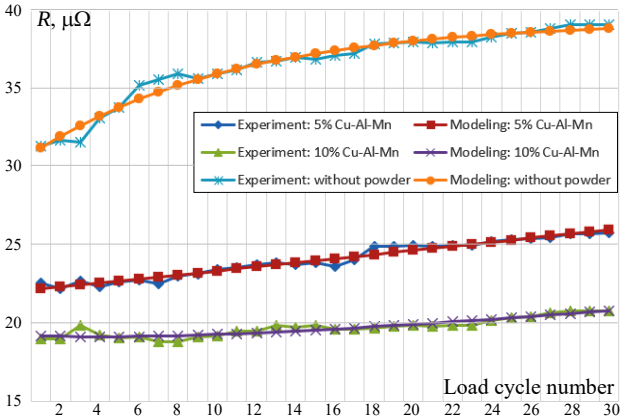

Fig. 7. Evolution of the contact resistance in a detachable contact connection of flat electrical aluminum busbars (experimental data and simulation)

Mathematical derivation of a reduced model with basic variables: h(t) – oxide melt thickness; A_{ef} (t) – effective contact area; R(t) – transition resistance [36, 37].

Key equations:

$$\frac{dh}{dt} = k_{ox} - k_{br}N_p F(\sigma_p); \quad (13)$$

$$\frac{dA_{ef}}{dt} = k_A\left[N_p\varepsilon(t) - \alpha_A h(t)\right]; \quad (14)$$

$$R(t) = R_b + \frac{\rho_{ox}h(t)}{A_{ef}(t)}. \quad (15)$$

Averaging the thermomechanical response (key step). The temperature and phase state of the SMA particles change faster than the contact degradation:

$$\tau_T << \tau_h,\ \tau_A. \quad (16)$$

Therefore, the cycle-averaged effective strain is introduced:

$$\langle\varepsilon\rangle = \frac{1}{\Delta t}\int_0^{\Delta t}\varepsilon(T(t))dt = \varepsilon_{eff} = \text{const}. \quad (17)$$

Similarly:

$$\langle F(\sigma_p)\rangle = F_{eff}. \quad (18)$$

Linearization of the evolution of the oxide film. Substituting (17) into (13):

$$\frac{dh}{dt} = k_{ox} - k_{br}N_p F_{eff}. \quad (19)$$

We denote:

$$\alpha_h = k_{ox},\ \beta_h = k_{br}N_p F_{eff}. \quad (20)$$

We get:

$$h(t) = h_0 + (\alpha_h - \beta_h)t. \quad (21)$$

Quasi-stationary contact area. For A_{ef}, we solve (14) with constant coefficients:

$$\frac{dA_{ef}}{dt} = k_A(N_p\varepsilon_{eff} - \alpha_A h). \quad (22)$$

Substituting (21) into (22) and integrating, we obtain:

$$A_{ef}(t) = A_0 + C(1 - e^{-\gamma t}), \quad (23)$$

where

$$\gamma \sim k_A\alpha_A,\ C \sim \frac{N_p\varepsilon_{eff}}{\alpha_A}. \quad (24)$$

Derivation of the reduced equation for R(t). Substituting (21), (23) into (12) and performing the Taylor series expansion with small deviations:

$$\frac{h(t)}{A_{ef}(t)} = a_0 + a_1 t - a_2(1 - e^{-\gamma t}). \quad (25)$$

After grouping the members, we finally obtain a reduced mathematical model:

$$R(t) = R_0 + \alpha t - \beta(1 - e^{-\gamma t}), \quad (26)$$

where R_0 is the initial contact resistance of the contact connection, μΩ; α is the rate of contact degradation due to oxidation, μΩ/cycle; β is the integral parameter of the efficiency of thermomechanical self-cleaning of the contact by Cu-Al-Mn powder, μΩ; γ is the intensity of the thermomechanical effect (effective frequency of thermocycles), cycle^{-1}.

Estimation of confidence intervals of parameters. Estimation method. Parameters $\theta = (R_0,\ \alpha,\ \beta)$ were identified by the least squares method:

$$\min_\theta \sum_{i=1}^{N}\left[R_{\exp}(t_i) - R(t_i,\theta)\right]^2. \quad (27)$$

The covariance matrix is estimated as:

$$C_\theta = \sigma^2(J^T J)^{-1}, \quad (28)$$

where J is the Jacobi matrix.

Tables 3, 4 present the confidence intervals.

Table 3

Confidence intervals CI (95 %). Contact with 10 % Cu-Al-Mn

Parameter	Estimation	95 % CI
R_0, μΩ	19,24	[18,9; 19,6]
α, μΩ/cycle	0,099	[0,085; 0,113]
β, μΩ	1,5	[1,30; 1,70]

Table 4

Confidence intervals CI (95 %). Contact with 5 % Cu-Al-Mn

Parameter	Estimation	95 % CI
R_0, μΩ	22,1	[21,7; 22,5]
α, μΩ/cycle	0,135	[0,120; 0,150]
β, μΩ	0,15	[0,05; 0,25]

Conclusion: the parameter β is statistically significant only at 10 % powder content, which is consistent with the physics of the process.

The previous theoretical analysis concerned the processes of heating and cooling of the contact connection by electric load currents in accordance with the power consumption schedule. Let us consider a model for processes with the appearance of short-circuit currents – pulsed thermal mode.

In the short-circuit mode, the current has a pulsed nature:

$$I(t) = I_k e^{-t/\tau_1}, \quad (29)$$

where I_k is the initial (peak) value of the short-circuit pulsed current; τ_1 is the time constant of the short-circuit pulsed current decay.

Thermal equation:

$$C_{th}\frac{dT}{dt} = I_k^2 R_c e^{-2t/\tau_1} - h_{th}(T - T_0). \quad (30)$$

The solution gives the peak temperature $T_{\max}$.

Pulsed destruction of oxide. In (13) we introduce the pulsed component:

$$\frac{dh}{dt} = k_{ox} - k_{br}N_p F(\sigma_p)\delta(t - t_k), \quad (31)$$

where t_k is the short circuit moment.

Integrating (31), we obtain:

$$\Delta h_k = -k_{br}N_p F(\sigma_p(T_{\max})). \quad (32)$$

Hopping resistance model. After a short circuit pulse:

$$R(t_k^+) = R(t_k^-) - \Delta R_k,\ \Delta R_k > 0; \quad (33)$$

$$\Delta R_k = K_R N_p \varepsilon(T_{\max}), \quad (34)$$

where K_R is the effective coefficient of electrocontact conversion of thermomechanical action into resistance change, Ω·m^3; t_k^-, t_k^+ are the time points before and after the short circuit.

Analysis of the structure of the mathematical model and the physical mechanisms embedded in it shows that under pulsed thermal loads characteristic of short circuit currents, in a contact connection with an electrical grease modified with Cu-Al-Mn powder, a short-term decrease in the transition resistance is possible due to thermomechanical activation of alloy particles.

Conclusions.

1. The work uses a multi-level physically based mathematical model of processes in a detachable electrical contact connection with electrical grease modified with Cu-Al-Mn alloy powder with shape memory effect.

2. The model takes into account the interrelationship of electrical, thermal, thermomechanical and tribological processes and describes the evolution of the transition resistance of the contact connection under conditions of cyclic electrical loading and emergency modes.

3. It is shown that the introduction of Cu-Al-Mn powder fundamentally changes the mechanism of electrical contact degradation: instead of a monotonic increase in the transition resistance, a mode of competition between oxidation processes and thermomechanical destruction of oxide films is realized.

4. Numerical simulations performed using the implicit stable BDF and Radau methods provided a correct solution to the rigid system of differential equations and demonstrated good agreement with experimental data.

5. It has been experimentally established that at a concentration of Cu-Al-Mn powder of 10 % by volume, the maximum effect of reducing and stabilizing the transition resistance is achieved – up to 45-48 % compared to a traditional contact connection without powder.

6. The parameters of the reduced model have a clear physical meaning, and their identification allows to quantitatively assess the effectiveness of thermomechanical self-cleaning of contacts and predict the long-term reliability of electrical connections.

7. The obtained mathematical model allows to describe the potential impact of short-circuit pulsed currents on the state of the electrical contact, which may be the subject of further experimental research.

8. The results obtained confirm the possibility of creating a new class of «active electrical contact greases» capable of thermocyclic self-healing of the contact surface and slowing down the electrochemical aging of contact connections.

9. The results obtained can serve as a scientific basis for conducting full-scale standard tests as the next stage of research.

Conflict of interest. The authors declare no conflict of interest.

REFERENCES

1. Kozyrskyi V. Analysis of condition control parameters and prediction of the aging process of dismountable type contacts. *Energetics and electrification*, 2002, no. 6, pp. 16-18. (Ukr).

2. Kozyrskyi V. Analysis of the principles of stabilization of contact pressure in collapsible contact systems. *Proceedings of the Institute of Electrodynamics of the National Academy of Sciences of Ukraine*, 2001, pp. 115-116. (Ukr).

3. Tkachuk I., Kozyrskyi V. *Method for flexible manufacturing of intermetallic compounds and device for making thereof*. Patent WO 2021/212188, PCT/BG2020/000017, 28.10.2021.

4. Zhang J., Chen T., Su G., Li C., Zhao F., Mi W. Microstructure and component analysis of glowing contacts in electrical fire investigation. *Engineering Failure Analysis*, 2022, vol. 140, art. no. 106539. doi: https://doi.org/10.1016/j.engfailanal.2022.106539.

5. Kloch K.T., Kozak P., Mlyniec A. A review and perspectives on predicting the performance and durability of electrical contacts in automotive applications. *Engineering Failure Analysis*, 2021, vol. 121, art. no. 105143. doi: https://doi.org/10.1016/j.engfailanal.2020.105143.

6. Sampaio R.F., Pragana J.P., Bragança I.M., Silva C.M., Nielsen C.V, Martins P.A. Electric performance of fastened hybrid busbars: An experimental and numerical study. *Proceedings of the Institution of Mechanical Engineers, Part L: Journal of Materials: Design and Applications*, 2022, vol. 236, no. 6, pp. 1152-1163. doi: https://doi.org/10.1177/14644207211043009.

7. Kozyrskyi V., Tkachuk I., Voloshyn S. *Electrical contact connection*. Patent WO 2023/060325, PCT/BG2021/000025, 20.04.2023.

8. Camital brand registration certificate no. 163545. Available at: https://alotek.international/uploads/230/1jgmO5anW3WCOVP22n2bZsx7RSeMc9-metaQ2FtaXRhbCDQodCy0LjQtNC10YLQtdC70YHRgtCy0L4r0LfQsCvRgNC10LPQuNGB0YLRgNCw0YbQuNGPLnBkZg==-.pdf (Accessed 20 May 2025).

9. Kozyrskyi V., Kaplun V., Voloshyn S. *Functional intermetallics in power plants*. Kyiv, Comprint, 2021. 347 p. (Ukr). Available at: https://dglib.nubip.edu.ua/server/api/core/bitstreams/c4cb1972-74d6-44d0-a13e-6f0c1d7efa61/content.

10. Alderete B., Mücklich F., Suarez S. Characterization and electrical analysis of carbon-based solid lubricant coatings. *Carbon Trends*, 2022, vol. 7, art. no. 100156. doi: https://doi.org/10.1016/j.cartre.2022.100156.

11. Zhou Y., Liu J., Li X., Chong H., Han B., Bai Q. On the electric behaviour of conductive grease inside the contact zone. *Friction*, 2024, vol. 12, no. 4, pp. 683-697. doi: https://doi.org/10.1007/s40544-023-0784-0.

12. Gonda A., Capan R., Bechev D., Sauer B. The Influence of Lubricant Conductivity on Bearing Currents in the Case of Rolling Bearing Greases. *Lubricants*, 2019, vol. 7, no. 12, art. no. 108. doi: https://doi.org/10.3390/lubricants7120108.

13. Zhang X., Glovnea R. An experimental investigation of grease lubricated EHD contact subjected to normal sinusoidally variable loading. *Tribology International*, 2020, vol. 147, art. no. 106272. doi: https://doi.org/10.1016/j.triboint.2020.106272.

14. Sampaio R.F.V., Pragana J.P.M., Bragança I.M.F., Silva C.M.A., Fernandes J.C.S., Martins P.A.F. Influence of corrosion on the electrical and mechanical performance of hybrid busbars. *International Journal of Lightweight Materials and Manufacture*, 2022, vol. 5, no. 4, pp. 510-519. doi: https://doi.org/10.1016/j.ijlmm.2022.06.005.

15. Vanyorek L., Kiss D., Prekob Á., Fiser B., Potyka A., Németh G., Kuzsela L., Drees D., Trohák A., Viskolcz B. Application of nitrogen doped bamboo-like carbon nanotube for development of electrically conductive lubricants. *Journal of Materials Research and Technology*, 2019, vol. 8, no. 3, pp. 3244-3250. doi: https://doi.org/10.1016/j.jmrt.2019.05.012.

16. Hong H., Christensen G., Widener C. Carbon nanotube grease and sustainable manufacturing. *Procedia Manufacturing*, 2018, vol. 21, pp. 623-629. doi: https://doi.org/10.1016/j.promfg.2018.02.164.

17. Frache L., Komba E.H., Philippon D., Galipaud J., De Barros M.I., Douillard T., Masenelli-Varlot K., Bouscharain N., Maheo Y., Sarlin R., Le Jeune G., Berthier Y., Bou-Said B., Massi F. Observation of a modified superficial layer on heavily loaded contacts under grease lubrication. *Tribology International*, 2021, vol. 158, art. no. 106921. https://doi.org/10.1016/j.triboint.2021.106921.

18. Van Humbeeck J. Non-medical applications of shape memory alloys. *Materials Science and Engineering: A*, 1999, vol. 273-275, pp. 134-148. doi: https://doi.org/10.1016/S0921-5093(99)00293-2.

19. Sutou Y., Koeda N., Omori T., Kainuma R., Ishida K. Effects of ageing on bainitic and thermally induced martensitic transformations in ductile Cu–Al–Mn-based shape memory alloys. *Acta Materialia*, 2009, vol. 57, no. 19, pp. 5748-5758. doi: https://doi.org/10.1016/j.actamat.2009.08.003.
20. Kainuma R., Takahashi S., Ishida K. Ductile Shape Memory Alloys of the Cu-Al-Mn System. *Journal de Physique IV*, 1995, vol. 5, no. C8, pp. 961-966. doi: https://doi.org/10.1051/jp4/199558961.
21. Liu J.-L., Huang H.-Y., Xie J.-X. Superelastic anisotropy characteristics of columnar-grained Cu–Al–Mn shape memory alloys and its potential applications. *Materials & Design*, 2015, vol. 85, pp. 211-220. doi: https://doi.org/10.1016/j.matdes.2015.06.114.
22. Liu J.-L., Huang H.-Y., Xie J.-X., Xu S., Li F. Superelastic fatigue of columnar-grained Cu-Al-Mn shape memory alloy under cyclic tension at high strain. *Scripta Materialia*, 2017, vol. 136, pp. 106-110. doi: https://doi.org/10.1016/j.scriptamat.2017.04.017.
23. Wang H., Huang H.-Y., Su Y.-J. Tuning the operation temperature window of the elastocaloric effect in Cu–Al–Mn shape memory alloys by composition design. *Journal of Alloys and Compounds*, 2020, vol. 828, art. no. 154265. doi: https://doi.org/10.1016/j.jallcom.2020.154265.
24. *TESCAN microscopy*. Available at: https://tescan.com.
25. Holm R. *Electric Contacts. Theory and Application*. Springer, Berlin, 1967. 503 p. Available at: https://www.scribd.com/document/675204141/1967-R-Holm-Electric-Contacts.
26. Slade P.G. *Electrical Contacts. Principles and Applications*. CRC Press, 2014. 1311 p. doi: https://doi.org/10.1201/b15640.
27. Greenwood J.A., Williamson J.B.P. Contact of nominally flat surfaces. *Proceedings of the Royal Society of London. Series A. Mathematical and Physical Sciences*, 1966, vol. 295, no. 1442, pp. 300-319. doi: https://doi.org/10.1098/rspa.1966.0242.
28. Bergman T., Lavine A.S., Incropera F.P., DeWitt D.P. *Fundamentals of Heat and Mass Transfer*. John Wiley & Sons, 2007. 1048 p.
29. Otsuka K., Wayman C.M. *Shape Memory Materials*. Cambridge University Press, 1998. 284 p.
30. Lagoudas D.C. *Shape Memory Alloys. Modelling and Engineering Applications*. Springer, 2008. 436 p. doi: https://doi.org/10.1007/978-0-387-47685-8.
31. Sutou Y., Omori T., Wang J.J., Kainuma R., Ishida K. Characteristics of Cu–Al–Mn-based shape memory alloys and their applications. *Materials Science and Engineering: A*, 2004, vol. 378, no. 1–2, pp. 278-282. doi: https://doi.org/10.1016/j.msea.2003.12.048.
32. Bowden F.P., Tabor D. *The Friction and Lubrication of Solids*. Oxford University Press, 2001. 424 p. doi: https://doi.org/10.1093/oso/9780198507772.001.0001.
33. Rabinowicz E. *Friction and Wear of Materials*. John Wiley and Sons, New York. 1995. 342 p.
34. Hairer E., Wanner G. *Solving Ordinary Differential Equations II. Stiff and Differential - Algebraic Problems*. Springer Berlin Heidelberg, 1991. 604 p. doi: https://doi.org/10.1007/978-3-662-09947-6.
35. Shampine L.F. *Numerical Solution of Ordinary Differential Equations*. Chapman & Hall, 1994. 632 p.
36. Ljung L. *System Identification. Theory for the User*. Prentice Hall, 1999. 609 p.
37. Seber G.A.F., Wild C.J. *Nonlinear Regression*. Wiley, 2003. 798 p.

Received 06.11.2025
Accepted 09.01.2026
Published 02.05.2026

V.V. Kozyrskyi[1], *Doctor of Technical Science, Professor,*
V.Ya. Bunko[2], *PhD, Associate Professor,*
P.M. Darmoris[2], *Senior Lecturer,*
[1] ALOTEK Technology sp.z.o.o.,
Zadabrowie 311, Krakowska 11, 37-716, Orly, Poland.
[2] Separated Subdivision of National University
of Life and Environmental Sciences of Ukraine
«Berezhany Agrotechnical Institute»,
20, Akademichna Str., Berezhany, Ternopil region, Ukraine, 47501,
e-mail: vbunko@gmail.com (Corresponding Author)

How to cite this article:
Kozyrskyi V.V., Bunko V.Ya., Darmoris P.M. Determination of the transition resistance of detachable electrical contacts with Camital active grease. *Electrical Engineering & Electromechanics*, 2026, no. 3, pp. 18-25. doi: https://doi.org/10.20998/2074-272X.2026.3.03

UDC 621.313 https://doi.org/10.20998/2074-272X.2026.3.04

S. Shlyk, J. Pyrhönen, I. Petrov, M. Parviainen, I. Martikainen, A. Suikki, J. Pippuri-Mäkeläinen, M. Zagirnyak

Possibility of cooling the rotor of an electric traction motor by bidirectional air flows

Introduction. *The performance reliability of electric vehicles (EVs) is an important factor in evaluating their suitability for widespread adoption. The reliability and lifespan of an EV depend on several critical factors including the motor, battery pack, controllers, and thermal management systems. The* ***problem*** *addressed in this paper is to cool down the rotor of permanent magnet synchronous motor efficiently using new combined cooling methods.* ***Goal.*** *Determination of the effectiveness of the combined rotor cooling method, which includes a bidirectional airflow circulating through a designed fan and oil circulation in the hollow shaft.* ***Methodology.*** *The solution was carried out using CFD (computational fluid dynamics) analysis.* ***Results.*** *A numerical model of a new combined cooling method for the rotor, which taking into account heat generation in the rotor and the thermal influence of the stator and bearing units, based on heat flow equations that consider its laminar or turbulent nature, was developed and studied.* ***Scientific novelty.*** *Based on the analysis of the rotor's numerical model, a fan design was proposed that allows for effective heat dissipation by creating bidirectional airflow circulation.* ***Practical value.*** *The developed model can be used for further research on the dynamic thermal parameters of the rotor and evaluation of heat dissipation efficiency, which will optimize the heat and mass transfer processes within the motor, enhance its operational efficiency, and ensure the stability of its performance in various operating modes.* References 21, tables 5, figures 17.

Key words: **permanent magnet synchronous motor, combined cooling method, computational fluid dynamics, fan design, hollow shaft.**

Вступ. *Надійність роботи електромобілів (ЕМ) є важливим фактором в оцінці їх придатності для широкого впровадження. Надійність та термін служби ЕМ залежать від кількох критичних факторів, включаючи двигун, акумуляторну батарею, контролери та системи теплового управління.* ***Проблема,*** *що розглядається в цій статті, полягає в ефективному охолодженні ротора синхронного двигуна з постійними магнітами за допомогою нових комбінованих методів охолодження.* ***Мета.*** *Визначення ефективності комбінованого методу охолодження ротора, який включає двонаправлений потік повітря, що циркулює за допомогою розробленого вентилятора, та циркуляцію масла в порожнистому валу.* ***Методологія.*** *Розв'язання проблеми було проведено за допомогою CFD (обчислювальної гідродинаміки) аналізу.* ***Результати.*** *Розроблено та досліджено числову модель нового комбінованого методу охолодження ротора, яка враховує тепловиділення в роторі та температурний вплив статора та підшипникових вузлів, на основі рівнянь теплового потоку, що враховують його ламінарну або турбулентну природу.* ***Наукова новизна****. На основі проведеного аналізу числової моделі ротора запропоновано дизайн вентилятора, що дозволяє ефективно відводити тепло завдяки створенню двонаправленої циркуляції повітря.* ***Практична цінність.*** *Отримана модель може бути використана для подальшого дослідження динамічних теплових параметрів ротора та оцінці ефективності відведення тепла, що дозволить оптимізувати процеси тепломасообміну всередині двигуна, підвищити ефективність його роботи та забезпечити стабільність його функціонування в різних режимах експлуатації.* Бібл. 21, табл. 5, рис. 17.

Ключові слова: **синхронний двигун з постійними магнітами, комбінований метод охолодження, обчислювальна гідродинаміка, дизайн вентилятора, порожнистий вал.**

Introduction. Vehicle regulation in the EU favors vehicles that emit no or low pollutants and CO_2. Curbing vehicle emissions and improving vehicle efficiency to meet these regulatory requirements need multi-prong technical solutions of electric vehicles such as hybrid electric vehicles, plug-in hybrid electric vehicles, extended range electric vehicles and battery electric vehicles [1].

Present-day electric traction motors rely heavily on the use of rare-earth permanent magnets (PMs) that contain scarce elements like Neodymium and Dysprosium. This dependence is understandable from the perspective of energy efficiency and torque density, but it also introduces several challenges. First, these materials are imported into the EU and are costly. Second, rare earth elements are finite resources, and increasing demand may lead to a supply shortage or even deplete these resources in the future. The number of electric cars produced annually is in the range of 90 million, and heavy vehicles are 20 million. Therefore, one can foresee that if rare earths are used wastefully, the global resources will not be rich enough.

Consequently, more and more research is dedicated to development of new generation of high-speed synchronous reluctance motors with minimal usage of PM. It will allow reduced dependence on rare-earth PM materials while simultaneously enhancing their recyclability.

Problem statement. During the design of high-speed high-specific-power motors, researchers face the significant problem that increased motor loss density results in very challenging heat dissipation. Heat generated during operation does not only have a negative effect on motor efficiency, but could lead to failure such as too high operating temperature of the motor, degrading of winding insulation, demagnetization of rotor magnets, eventual shorts, etc. [2−4]

In [5, 6] it is shown that approximately 75 % of motor performance problems are localized in the stator coil winding and rotor bars, which are most affected by temperature changes and mechanical stress. Internal losses (conduction losses, stator core losses, rotor core losses, and PM eddy current losses) and high temperatures affect the torque/rotational speed of the electric motor.

Reducing the temperature rise can happen by improving the cooling capacity of motor and by decreasing the losses.

Nowadays, there are a wide range of methods used for motor cooling. Depending on using different cooling media and materials with high thermal conductivity, they can be divided into 6 groups such as air cooling, liquid cooling, cooling using heat pipe, potting cooling, cooling using phase change materials, other cooling methods. Many studies have been conducted regarding the advantages and disadvantages of various cooling methods [7−10]. Nevertheless, there is currently no universally effective method for cooling the rotor. That is why it is essential to develop and evaluate new cooling approaches to ensure optimal performance and reliability of the rotor.

According to [11] one of the most effective cooling methods is liquid cooling. Due to the high specific heat capacity of liquids, this type of cooling allows absorbing and transferring significant amounts of heat. Nevertheless, such a cooling system requires additional equipment like pumps, heat exchangers, and valves, which can

complicate the system and increase the mass of it. Moreover, not only does the cost of system increase, but also the electricity consumption for operating components such as pumps also rises.

In contrast to liquid cooling, air cooling has less cooling performance, but it is much cheaper solution and does not require any additional equipment (except fan for forced cooling).

In this paper, the combined cooling method has been chosen to include both liquid and air cooling to evaluate effectiveness of this approach and its impact on internal temperatures within the motor [12].

The **goal of the work** is to determine the effectiveness of the combined rotor cooling method, which includes a bidirectional airflow circulating through a designed fan and oil circulation in the hollow shaft.

Materials and methods. The rotor was chosen as the object of cooling because, after the stator, it is the second location where significant amounts of heat are generated in the motor. The rotor with PMs of 120 kW motor is investigated (Fig. 1).

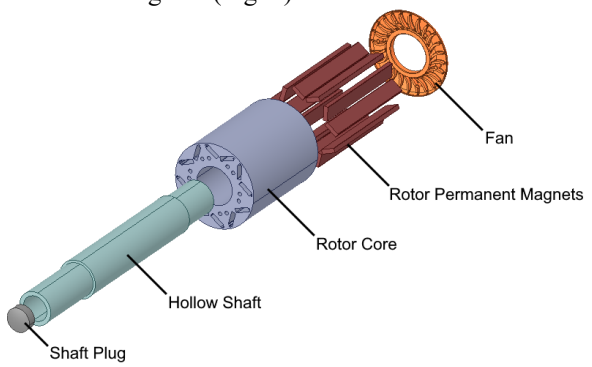

Fig. 1 Exploded view of the traction motor rotor unit

The rotor diameter is 86 mm and its active length is 110 mm. Magnets are buried inside the rotor in single layer «V» arrangement. The hollow shaft is cooled down by oil. In addition, the impeller fan is designed (Fig. 2) to provide cooling the rotor surface. It intakes air from the middle area of the PM V and blows it through the outer ends of the V-poles channels. The air heated close to the rotor surface should be cooled when colliding to the bearing shield cooled by bearing lubrication oil and cooled further in the inner duct of the rotor next to the well-cooled rotor shaft.

For air cooling of the rotor, an impeller fan is used (Fig. 2), which allows the creation of bidirectional airflow. Air is taken and pumped out in a volume of air limited by the inner wall of the stator, the outer surface of the left bearing shield, the front end of the rotor and the outer surface of the shaft.

It is assumed that the rotor is cooled by air due to the air passing through the internal channels of the rotor and its subsequent passage through the peripheral channels passing near the PMs (Fig. 3). The key factor in air cooling of the rotor is the transfer of its heat by air from the peripheral zones to the central part, where the heat is removed due to heat exchange between the hollow shaft and the oil circulating inside it. In this case, the degree of heat transfer coefficient (HTC) between the inner wall of the shaft and the oil is important.

In order to solve the equation of heat conduction, correct definitions of the initial and boundary conditions are required. The biggest research problem arises in the determination of the local heat transfer coefficient on the cooled surface. The heat conduction model based on the solution of the heat conduction equation in cylindrical coordinates with the use of numerical simulation methods was proposed in [10, 11]:

$$\lambda\left[\frac{\partial^2 T}{\partial r^2}+\frac{1}{r}\frac{\partial T}{\partial r}+\frac{\partial^2 T}{\partial z^2}\right]=\rho c\frac{\partial T}{\partial \tau}-q(r,z), \qquad (1)$$

where λ is the thermal conductivity; T is the temperature; r, z are the cylindrical coordinates; ρ is the density of the transmission medium; c is the heat capacity; τ is the time; q is the volumetric heat generation rate in the rotor.

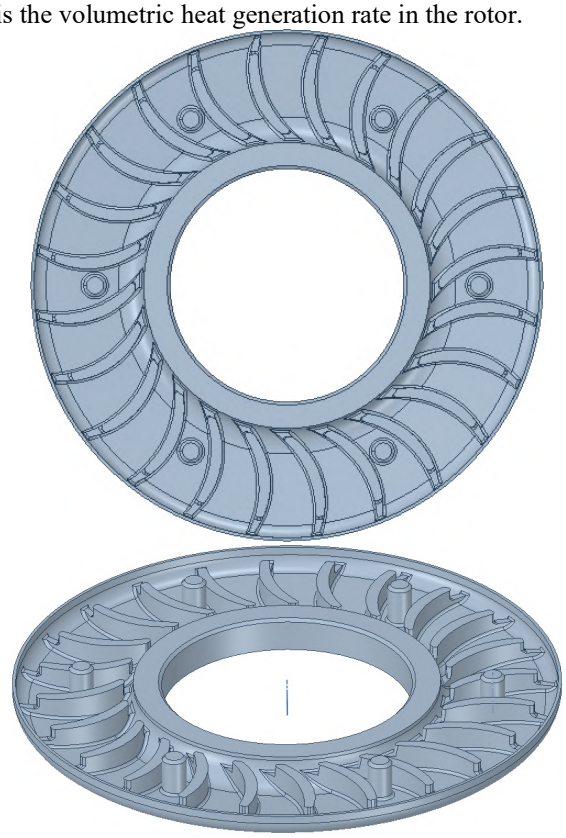

Fig. 2. Impeller fan design

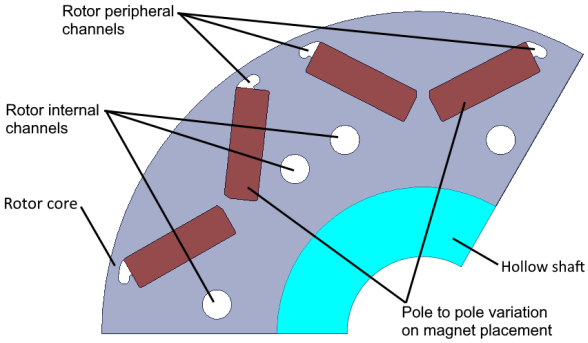

Fig. 3. 120 kW rotor lamination geometry

The variable temperature field on the cooled surface of the material $T(r, z, \tau)$ obtained as a result of solving (1) should meet the boundary conditions [12, 13]. They are written in the form of Fourier's law:

$$\dot{q}(r,\tau)=h(r,\tau)\cdot(T_s-T_p), \qquad (2)$$

where $\dot{q}$ is the heat flux density; $h(r, \tau)$ is the heat transfer coefficient; T_s is the surface temperature; T_p is the ambient temperature.

A two-dimensional axisymmetric thermal conductivity is assumed, in which heat exchange with the coolant occurs

only on one of the cylinder's front surfaces. The advantage of using formulas based on dimensionless analysis is that any gas or liquid can be used, even if the original formula was developed for a specific liquid [14, 15].

For natural convection, the typical form of convective correlation is:

$$Nu = a(GrPr)^b. \quad (3)$$

For forced convection the typical form of the convection correlation is:

$$Nu = a(Re)^b(Pr)^c. \quad (4)$$

where Nu is the dimensionless Nusselt number; a, b, c are the constants given in the correlation; Gr is the dimensionless Grashof number; Re is the dimensionless Reynolds number; Pr is the dimensionless Prandtl number. Also:

$$Re = \rho v L / \mu; \quad (5)$$

$$Gr = \beta G \Delta T \rho^2 L^3 / \mu^2; \quad (6)$$

$$Pr = c_p \mu / k; \quad (7)$$

$$Nu = hL / k, \quad (8)$$

where ρ is the fluid density; v is the fluid velocity; L is the characteristic length of the surface; μ is the fluid dynamic viscosity; β is the coefficient of cubical expansion, $1/(273+T_{FLUID})$; G is the gravitational force of attraction; ΔT is the delta temperature of surface-fluid; c_p is the fluid specific heat capacity; k is the fluid thermal conductivity.

The quantity Re is used to evaluate laminar or turbulent flow in a system with forced convection. The product of $GrPr$ is used in systems with natural convection. Ultimately, we are interested in the parameter h.

Heat transfer in natural convection depends primarily on the temperature difference between the vessel (in our case, the shaft) and the liquid (oil), as well as on the properties of the liquid. Forced convection depends primarily on the speed of the liquid and its properties, and only secondarily on the temperature, since the properties of the liquid depend on the temperature. Mixed heat transfer (h_{MX}), caused by a combination of natural (h_{NAT}) and forced (h_{FRC}) convection, is estimated using the formula [16, 17]:

$$h_{MX}^3 = h_{FRC}^3 \pm h_{NAT}^3, \quad (9)$$

where the motor rotation orientation determines the «±» sign used, a «+» sign for assisting and transverse flow and a «–» sign for opposing flows.

Table 1 shows the values of the coefficients a and b for laminar and turbulent flow also as the $GrPr$ product at which the transition to turbulent flow occurs for a smooth horizontal inner shaft surface.

Table 1

Correlation coefficients for natural convection

$GrPr$ laminar to turbulent	a, laminar	b, laminar	a, turbulent	b, turbulent
10^9	0.525	0.25	0.129	0.33

In case of smooth inner surface of the shaft, we can use the following correlations for the flow [17, 19, 20]:

- for the laminar flow ($(Re < 5\cdot10^5)$ and $(0.6 < Pr < 50)$):

$$Nu = 0.664(Re)^{0.5}(Pr)^{0.33}; \quad (10)$$

- for the turbulent flow ($(Re > 5\cdot10^5)$):

$$Nu = [0.037(Re)^{0.8} - 871](Pr)^{0.33}. \quad (11)$$

The heat transfer coefficient h can be calculated as:

$$h = \frac{\rho c_p v D}{4L}(1 - e^{-m}); \quad m = 0.1448 \frac{L^{0.946}}{D^{1.16}} \cdot \left(\frac{k}{\rho c_p v}\right)^{0.214}, \quad (12)$$

where D is the hydraulic diameter, L is the axial length of the shaft.

To predict the thermal behavior of the motor and optimized motor temperatures computer modeling and thermal monitoring such as lumped parameter thermal network, finite element analysis (FEA) and computational fluid dynamics (CFD) are used. Numerical models simulate various operating conditions, providing a comprehensive understanding of the thermal behavior of the motor. This predictive method allows for the identification of hot spots and, therefore, the optimization of the cooling system to prevent overheating.

The effect of end windings cooling for the machine under study was investigated using a 3D finite element method (FEM) thermal model in [18]. The paper compares the traditional method of cooling a machine with a hairpin winding with oil cooling of the end windings and stator stack cooling (SSC), and a new cooling concept, based on oil cooling of the end windings and direct oil cooling (DOC) of the slot conductors, which allows improving hairpin winding thermal management and increasing machine specific power.

The loss components distribution, thermal properties, and boundary coefficients applied to the developed models in [18] are shown in Tables 2, 3. The simulation results are shown in Fig. 4–7.

Table 2

Loss components distribution in machines with different cooling arrangements at different loads [18]

Parameter	SSC, 96 N·m	SSC, 48 N·m	DOC, 96 N·m	DOC, 48 N·m
Layer 1 losses	780 W	238 W	864 W	256 W
Layer 2 losses	596 W	184 W	686 W	204 W
Layer 3 losses	500 W	153 W	593 W	174 W
Layer 4 losses	434 W	131 W	529 W	153 W
Layer 5 losses	393 W	117 W	489 W	139 W
Layer 6 losses	375 W	110 W	471 W	133 W
End windings losses	839 W	251 W	1063 W	281 W
Stator core losses	2596 W	1576 W	2596 W	1576 W
Rotor core losses	144 W	81 W	144 W	81 W
Efficiency	0.946	0.946	0.942	0.945

Table 3

Thermal properties and boundary coefficients applied in the model [18]

Parameter	Value
Copper thermal conductivity	398 W/(m·K)
Stator core thermal conductivity	30 W/(m·K)
Rotor core thermal conductivity	30 W/(m·K)
HTC on the surface between end winding and oil flow	100 W/(m^2·K)
HTC on the surface between slot conductor and oil flow	500 W/(m^2·K)
HTC on the surface between stator stack and oil flow	500 W/(m^2·K)
Average oil temperature	60 °C

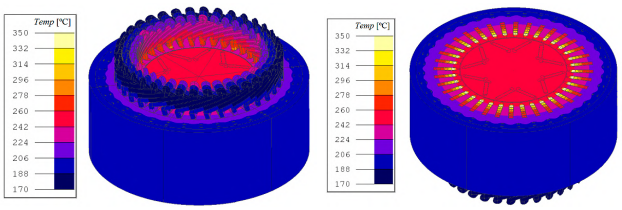

Fig. 4. Temperature distribution in 3D FEM model of the machine with oil cooling of the end windings and SSC at 12000 rpm, 96 N·m

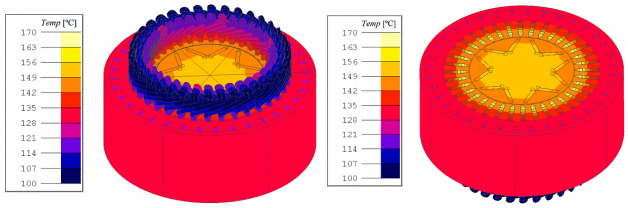

Fig. 5. Temperature distribution in 3D FEM model of the machine with oil cooling of the end windings and SSC at 12000 rpm, 48 N·m

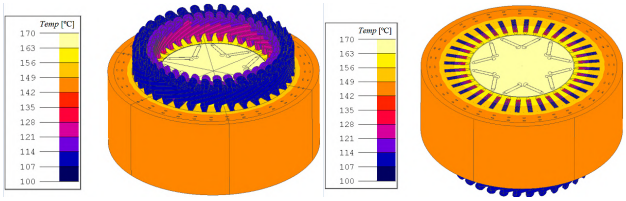

Fig. 6. Temperature distribution in 3D FEM model of the machine with oil cooling of the end windings and DOC at 12000 rpm, 96 N·m

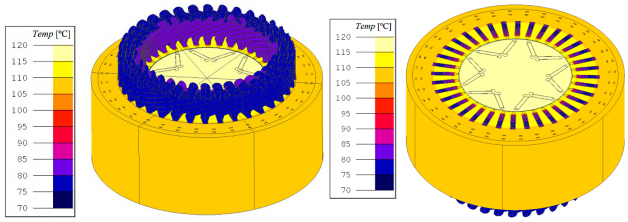

Fig. 7. Temperature distribution in 3D FEM model of the machine with oil cooling of the end windings DOC at 12000 rpm, 48 N·m

According to the simulation results obtained in [18], the PMSM with DOC has only 0.1 % lower efficiency at 48 N·m than the PMSM with SSC. This load is the maximum continuous operating range of the PMSM with standard winding. However, PMSM with DOC can obtain much higher continuous operating loads without the risk of being overheated due to more effective cooling.

The models used in [18] did not take into account for rotor cooling and natural heat dissipation from the stator frame, since these had a negligible effect on the stator winding's cooling. Therefore, the combined oil-air rotor cooling of the 120 kW machines with DOC at a load of 96 N·m was isolated into a separate problem, which is solved in this work.

CFD was chosen for analysis of the behavior of fluid and its interactions with surfaces. CFD simulations of liquid and gas flows are based on the assumption of the presence of inlet and outlet zones through which the simulated medium (in our case, air) freely flows into and out of the studied domain. Since the stator cavity in our case is sealed (there are no inlet or outlet zones), the thermal task of the proposed air cooling of the rotor, in general, appears to be unsolvable from the point of view of machine logic.

Therefore, the task was divided into 4 successive steps, in which the inlet and outlet zones swapped places at each step.

Step 1. The airflow inside the rotor channels and impeller cavity were simulated. All other parts of the model except the air domain and the front air volume were not considered. Inlet and outlet zones are the outer walls of the front air volume.

Step 2. The obtained values of airflow velocities and pressures were added to the laminate model. The thermal influence from the stator and the cold shaft was taken into account. Inlet and outlet zones – internal and external channels of the rotor.

Step 3. The values of airflow velocities, pressures and temperatures obtained in the previous Step were added to the frontal air volume. The thermal influence of the stator walls, cold shaft and front bearing shield on the frontal air volume was considered. Inlet and outlet zones – external and internal rotor channels.

Step 4. The refined values of airflow velocities, pressures and temperatures were added from the previous Step to the rotor model with the added rear air volume. In addition to the thermal influence from the stator and the cold shaft, the thermal influence from the rear bearing shield was also taken into account. Inlet and outlet zones – internal and external channels of the rotor.

The task statement diagram is shown in Fig. 8. Thermal properties and coefficients applied in the boundary regions of the 3D CFD model are listed in Table 4. The boundary conditions and the volumetric heat generation rate q''' in the rotor of the proposed design were obtained based on [18, 21] results:

$$q''' = P_{loss} / V_r = 144 \text{ W} / 0.000507 \text{ m}^3 \approx 284000 \text{ W/m}^3, \quad (13)$$

where P_{loss} is the total rotor core losses (Table 2); V_r is the specified rotor volume.

The computational mesh was generated automatically from combined tetrahedral and polyhedral elements.

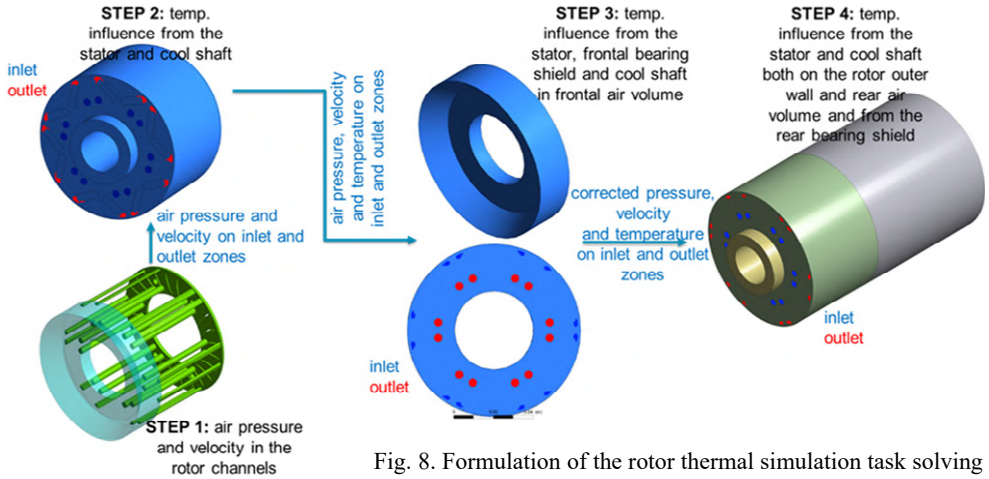

Fig. 8. Formulation of the rotor thermal simulation task solving

Table 4

The materials thermal properties and coefficients applied in the boundary regions

Parameter	Value
Rotor core steel thermal conductivity	23 W/(m K)
Shaft steel thermal conductivity	45 W/(m K)
Impeller aluminum thermal conductivity	200 W/(m K)
Magnets thermal conductivity	9 W/(m K)
HTC on the surface between channels in rotor core and air flow	25 W/(m^2 K)
HTC on the surface between bearing shields and air volumes	25 W/(m^2 K)
HTC on the surface between impeller and rear air volume	65 W/(m^2 K)
HTC on the surface between stator and air volumes	25 W/(m^2 K)
Heat generation rate in rotor	284000 W/m^3
Average bearing shields surface temperature	60° C, stable

Results. The geometry for CFD simulation of the air flow inside the rotor and the frontal air volume (Step 1) is shown in Fig. 9.

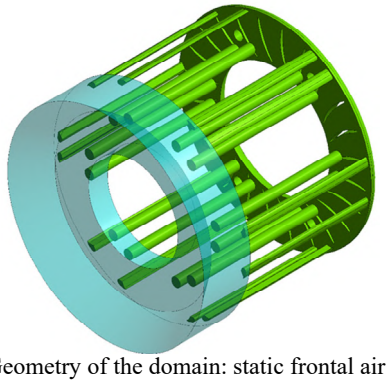

Fig. 9. Geometry of the domain: static frontal air volume (transparent blue) and rotating air domain (green)

CFD simulations at a rotation speed of 12000 rpm showed that the impeller creates clear zones of negative air pressure along the internal circuit and positive air pressure along the external circuit, while the internal and external channels are completely located inside the negative and positive pressure zones, respectively. As can be seen from the results obtained (Fig. 10), the internal channels of the rotor lie in defined zones of negative pressure in the range of 0.142–0.506 kPa, and the external channels of the rotor lie in zones of positive pressure in the range of 0.404–0.951 kPa. Thus, the pressure difference of the airflow between the internal and external channels of the rotor is 0.546–1.457 kPa, which makes pumping air through the rotor channels and the impeller possible.

In Fig. 11 it can be seen that at a rotor and impeller rotation speed of 12000 rpm in the internal channels (air suction) and in the external channels (air pumping out), it is possible to obtain stable flows with an average speed in the range of 20–30 m/s.

The calculated average flow velocities for known cross-sectional areas of the internal channels (12 channels with a cross-sectional area of 12.503 mm^2 each) and the external channels (12 channels with a cross-sectional area of 5.1265 mm^2 each) allow us to calculate the volumetric flow rate of air passing through these channels by (14) using Ansys Fluent built-in calculator:

$$Q = v \times S, \qquad (14)$$

where Q is the air volumetric flow rate, m^3/s, v is the air flow velocity, m/s, S is the cross-sectional area of the flow, m^2.

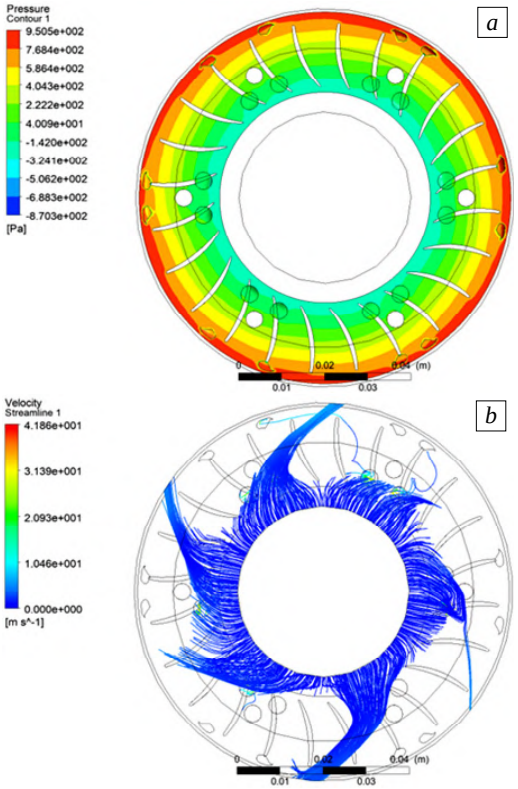

Fig. 10. The air pressure distribution (*a*) and the air velocity distribution in the frontal air volume during suction (*b*)

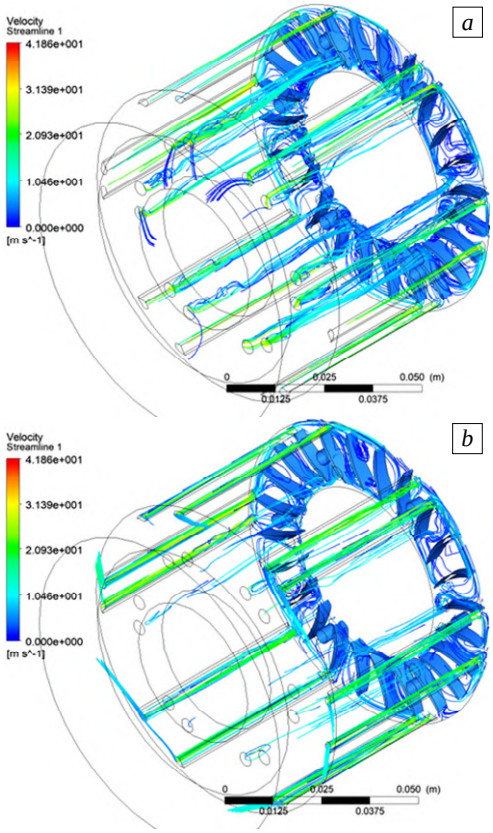

Fig. 11. The air velocity distribution in internal (*a*) and external (*b*) channels

The expected volumetric flow rate of air passing through internal channels is 0.003 m^3/s and the volumetric flow rate of air passing through external channels is 0.00258 m^3/s. As can be seen, the difference between the volumetric flow of air passing through the internal and

external channels is 14 %. The presence of such losses can be explained by inaccuracies in the simulation, uneven air flows through the rotor channels and local air turbulence occurring in the impeller. Considering the small volume of the frontal air volume (55300 mm^3 or 0.0000553 m^3), we can conclude that at the rotor rotation speed of 12000 rpm air from this cavity will be pumped through the rotor channels about 50 times per second.

Shaft cooling simulations were provided with Mobil EV Cool Drive 303 oil for different values of the oil flow rates and oil inlet temperatures (Fig. 12). All further simulations were performed at a rotor speed of 12000 rpm.

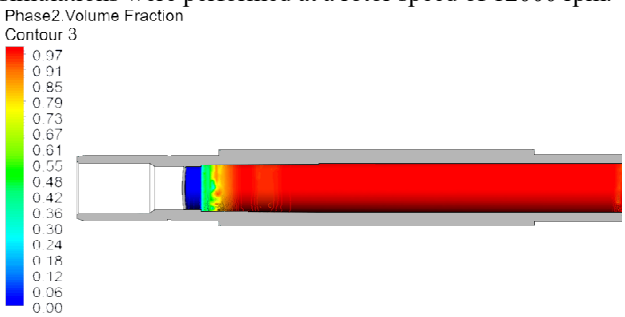

Fig. 12. Cross-section of oil volume fraction with 0.14 m/s inlet velocity (mass flow rate 0.24 l/min) at 12000 rpm rotation speed

In Table 5 results of the shaft inner surface heat transfer coefficient calculations are shown.

Table 5

Oil-inner shaft surface heat transfer coefficient

Oil-inner shaft surface HTC h, W/(m^2 K)			
Oil flow rate q, l/min	Oil inlet temperature θ_{oil}, °C		
	30	45	60
0.12	194.6	194.8	195.2
0.24	196.7	198.2	197.8
0.36	218.2	219.2	222.8

As can be seen (Fig. 13), considering the dynamic properties of the selected oil, the key factor affecting the value of the HTC is the value of the volumetric flow rate of oil, while the initial temperature of the oil affects this parameter insignificantly. In further simulations, the average value of h = 204 W/(m^2 K) was used.

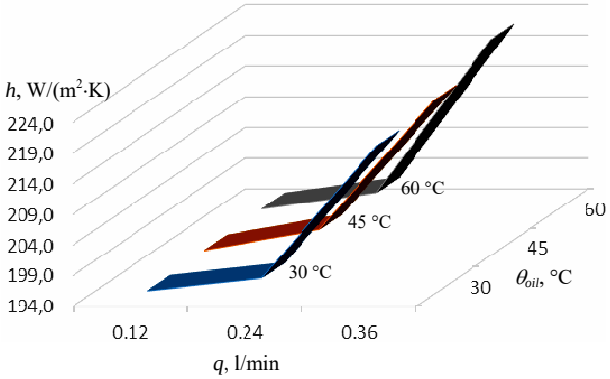

Fig. 13. Shaft inner surface HTC rates

Figure 14 shows the thermal behavior of the air domain in the rotor channels and the cavity of the impeller and the shaft after corrected rotor thermal analysis (Step 4). As can be seen, warm air enters the internal channels (inlet zones) and is cooled as it moves through the channels along the shaft, and then exits through the outer channels (the outlet zones) already cooled. The shaft is taking heat along its length from the front edge to the rear, where it borders the impeller. Thus, it can be concluded that air temperatures are taken out by the shaft through the body of the rotor laminate.

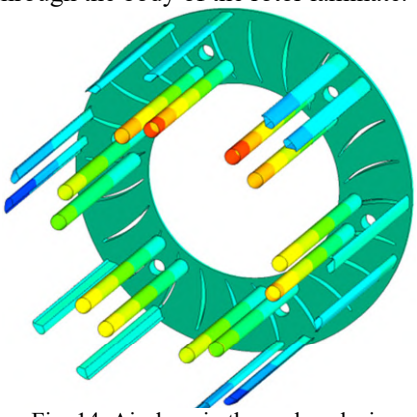

Fig. 14. Air domain thermal analysis

Figure 15 shows temperature distribution patterns along the frontal and the rear faces of the rotor. It can be seen that the approximate temperature in the middle zone of the rotor is in the range of 80 °C, and the outer peripheral zone cools even more. In the very narrow areas between the outer outlet channels, temperatures of 64 °C are reached. In Fig. 15,*b*, the rear face of the rotor is shown. As can be seen, it cools more efficiently than the frontal face (Fig. 15,*a*), and the temperature spots on it have lower values than on the frontal one.

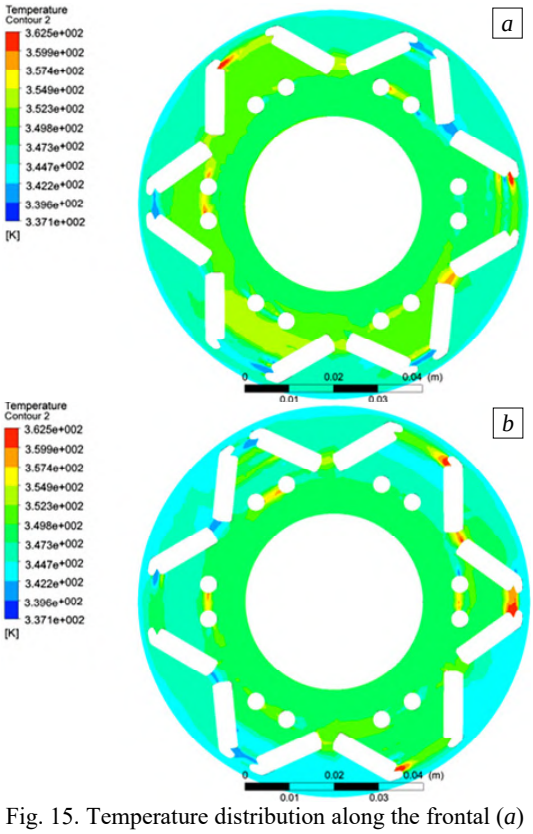

Fig. 15. Temperature distribution along the frontal (*a*) and the rear (*b*) faces of the rotor

Figure 16 shows a picture of the temperature distribution in the PMs. As can be seen, the PMs heat up unevenly. This could be explained by the asymmetry of the impeller, the asymmetry and unequal airflows it creates, as well as the asymmetry of the rotor itself and the location of the magnets in it, and also the low thermal conductivity of

the magnets specified in the model. The peak temperatures achieved in the PMs do not exceed 64 °C.

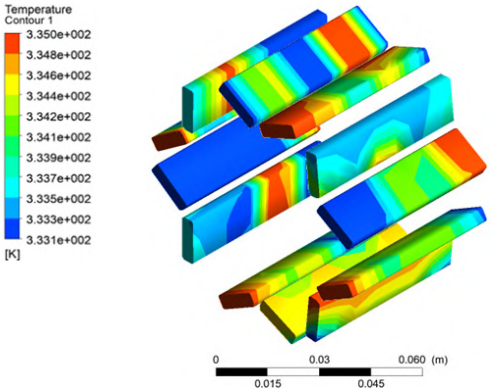

Fig. 16. Temperature distribution in the PMs

Figure 17 shows the effect of air circulation in the rotor channels created by an impeller fan (with and without the presence of the air domain in the simulation system) on the temperature distribution in the «shaft-rotor» system.

As can be seen from the obtained results, including the Air domain in the simulation system (air circulates in both directions due to the pressure difference between the outer and inner channels inside the rotor) reduces rotor heating, including in the PM V zone. The main achievement is the avoidance of high-temperature fields (hot spots) concentrated in the outer zone of the rotor. Thus, the creation of bidirectional air flows generated by the impeller fan simultaneously with the oil circulation inside the hollow shaft not only reduces but also more evenly distributes temperatures within the rotor.

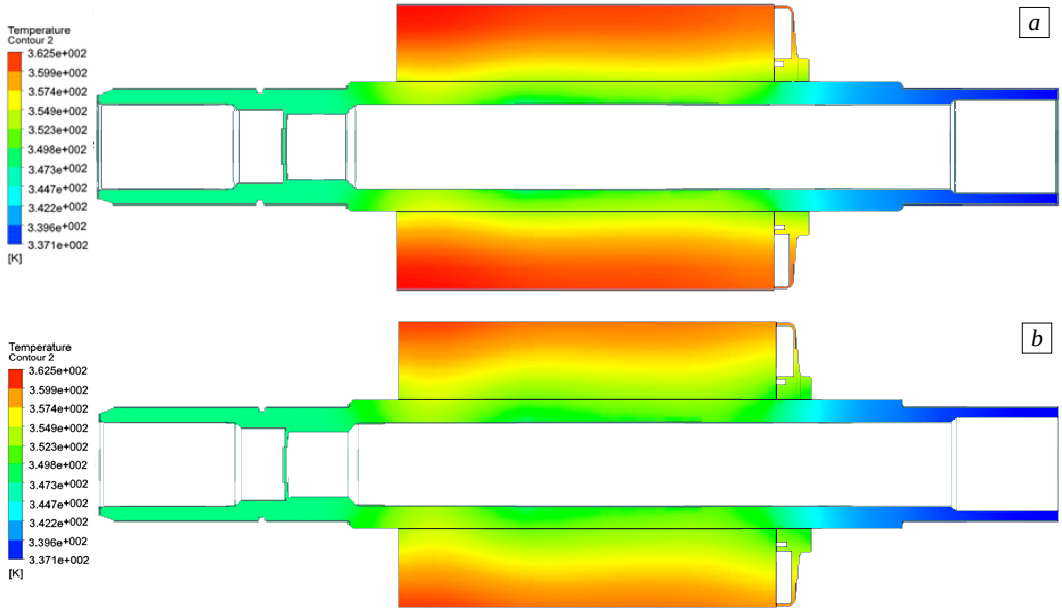

Fig. 17. Cross-section of temperature distribution across the shaft and rotor at 12000 rpm speed rotation: *a* – air circulation disabled; *b* – air circulation enabled

Conclusions. As can be seen from the obtained results, the presence of bidirectional air circulation inside the rotor lamination channels, created by the impeller fan, with simultaneous circulation of oil in the hollow shaft, allows for the redistribution and reduction of the rotor core temperature with a virtually unchanged hollow shaft temperature.

The key factor affecting the value of the heat transfer coefficient between hollow shaft inner surface and oil inside it is the value of the volumetric flow rate of oil, while the initial temperature of the oil affects this parameter insignificantly. Further development involves studying the effect of the rotation speed of the hollow shaft on the value of the heat transfer coefficient.

As stated above, the CFD simulations of the thermal distribution in the rotor and the analysis of the possibility of its cooling by bidirectional air flows created by the impeller fan were carried out taking into account the assumption that the temperature emanating from the front and rear bearing shields, as well as the temperature of the oil in the shaft, are constant and stable.

Possible further studies include the following:

- clarification of temperature indicators of bearing units and their possible influence on temperatures in the rotor;
- study of the influence of rotation speed (and, therefore, air and oil flow intensity) on the temperature in the rotor;
- study of the influence of oil volume flow and its inlet temperature in the hollow shaft on the shaft temperature and temperature distribution in the rotor as a whole;
- study of vibrations from the impeller;
- study of the power losses in the impeller and its efficiency;
- further comprehensive FEA/CFD analysis of the traction electric motor thermal state, taking into account both the stator cooling and the proposed rotor cooling method.

Acknowledgements. This work was partly supported by EU VOLTCAR project funded by the European Union under Grant Agreement no. 101096557. Views and opinions expressed are however those of the author(s) only and do not necessarily reflect those of the European Union or the European Climate, Infrastructure and Environment Executive Agency (CINEA). Neither the European Union nor the granting authority can be held responsible for them.

Conflict of interest. The authors declare that they have no conflicts of interest.

REFERENCES

1. Usman A., Saxena A. Technical Roadmaps of Electric Motor Technology for Next Generation Electric Vehicles. *Machines*, 2025, vol. 13, no. 2, art. no. 156. doi: https://doi.org/10.3390/machines13020156.

2. Biot-Monterde V., Navarro-Navarro A., Zamudio-Ramirez I., Antonino-Daviu J., Osornio-Rios R.A., Ruiz-Sarrió J.E. Automatic classification of stator asymmetries and insulation thermal damages in induction motors, applying persistence spectrum and a convolutional neural network to the stray-flux signals. *2023 IEEE 32nd International Symposium on Industrial Electronics (ISIE)*, 2023, pp. 1-6. doi: https://doi.org/10.1109/ISIE51358.2023.10227984.

3. Sun W., Gao F. Failure Analysis of Irreversible Demagnetization of Permanent Magnet Synchronous Motor. *2024 11th International Forum on Electrical Engineering and Automation (IFEEA)*, 2024, pp. 761-764. doi: https://doi.org/10.1109/IFEEA64237.2024.10878522.

4. Neusues S., Binder A. Post rotor-fault operation of a Ferrite Magnet assisted Synchronous Reluctance Motor. *2020 International Conference on Electrical Machines (ICEM)*, 2020, pp. 2335-2341. doi: https://doi.org/10.1109/ICEM49940.2020.9271011.

5. Fu J., Li H., Sun X., He T., Zhang G., Wei C. Multi-physics simulation modeling and energy flow characterization of thermal management system for a sport utility vehicle under high-temperature conditions. *Energy*, 2025, vol. 316, art, no. 134653. doi: https://doi.org/10.1016/j.energy.2025.134653.

6. Malik M.A.I., Kalam M.A., Ikram A., Zeeshan S., Raza Zahidi S.Q. Energy transition towards electric vehicle technology: Recent advancements. *Energy Reports*, 2025, vol. 13, pp. 2958-2996. doi: https://doi.org/10.1016/j.egyr.2025.02.029.

7. Dan D., Zhao Y., Wei M., Wang X. Review of Thermal Management Technology for Electric Vehicles. *Energies*, 2023, vol. 16, no. 12, art. no. 4693. doi: https://doi.org/10.3390/en16124693.

8. Wu J., Shan L., Peng G., Wang R., Zhang W., Tong X., Shen L. A Review of Motor Drive Thermal Management System for Electric Vehicles. *2022 7th International Conference on Power and Renewable Energy (ICPRE)*, 2022, pp. 551-556. doi: https://doi.org/10.1109/ICPRE55555.2022.9960497.

9. Gronwald P.-O., Kern T.A. Traction Motor Cooling Systems: A Literature Review and Comparative Study. *IEEE Transactions on Transportation Electrification*, 2021, vol. 7, no. 4, pp. 2892-2913. doi: https://doi.org/10.1109/TTE.2021.3075844.

10. Bourgault A.J., Roy P., Ghosh E., Kar N.C. A Survey of Different Cooling Methods for Traction Motor Application. *2019 IEEE Canadian Conference of Electrical and Computer Engineering (CCECE)*, 2019, pp. 1-4. doi: https://doi.org/10.1109/CCECE.2019.8861611.

11. Gundabattini E., Kuppan R., Solomon D.G., Kalam A., Kothari D.P., Abu Bakar R. A review on methods of finding losses and cooling methods to increase efficiency of electric machines. *Ain Shams Engineering Journal*, 2021, vol. 12, no. 1, pp. 497-505. doi: https://doi.org/10.1016/j.asej.2020.08.014.

12. Li X., Zhao X., Zhang Z., Avelin A., Liu S., Li H. Selecting cooling methods for electric motors. *Applied Thermal Engineering*, 2025, vol. 274, art. no. 126554. doi: https://doi.org/10.1016/j.applthermaleng.2025.126554.

13. Cengel Y.A., Cimbala J.M., Ghajar A.J. *Fundamentals of Thermal-Fluid Sciences. 6th edition*. McGraw Hill, 2022. 977 p.

14. Dheivanai R., Prasanth B., Karthikeyan G. Evaluation and Simulation of Oil-based Direct Cooling System in Series DC Motors for Electric Vehicle Applications. *Iranian Journal of Science and Technology, Transactions of Electrical Engineering*, 2025. doi: https://doi.org/10.1007/s40998-025-00833-2.

15. Szajding A., Gołdasz A., Telejko T. The influence of coolant velocity on the local heat transfer coefficient during steel quenching. *Computer Methods in Material Science*, 2020, vol. 20, no. 4, pp. 157-164. doi: https://doi.org/10.7494/cmms.2020.4.0737.

16. Zhang T., Yao J., Liao S., Liu X., Xu Y., Yang S. Cooling enhancement of permanent magnet synchronous motor coupled with heat pipes for electric vehicle. *Applied Thermal Engineering*, 2025, vol. 279, art. no. 127572. doi: https://doi.org/10.1016/j.applthermaleng.2025.127572.

17. Milykh V.I. Numerical-field analysis of active and reactive winding parameters and mechanical characteristics of a squirrel-cage induction motor. *Electrical Engineering & Electromechanics*, 2023, no. 4, pp. 3-13. doi: https://doi.org/10.20998/2074-272X.2023.4.01.

18. Petrov I., Martikainen I., Poutiainen I., Rangwala J., Pyrhönen J. Hairpin Winding with Direct Oil Cooling. *2024 International Conference on Electrical Machines (ICEM)*, 2024, pp. 1-7. doi: https://doi.org/10.1109/ICEM60801.2024.10700210.

19. Ibrar A., Ahmad S., Safdar A., Haroon N. Efficiency enhancement strategy implementation in hybrid electric vehicles using sliding mode control. *Electrical Engineering & Electromechanics*, 2023, no. 1, pp. 10-19. doi: https://doi.org/10.20998/2074-272X.2023.1.02.

20. Bergman T.L., Lavine A.S., Incropera F.P., DeWitt D.P. *Introduction to Heat Transfer. 6th edition.* John Wiley & Sons, Inc., 2011. 1040 p.

21. Milykh V.I. Theory and practice of numerical-field analysis and refinement of electromagnetic and energy parameters in the designs of three-phase induction motors. *Electrical Engineering & Electromechanics*, 2026, no. 1, pp. 3-14. doi: https://doi.org/10.20998/2074-272X.2026.1.01.

Received) 13.11.2025
Accepted 15.01.2026
Published 02.05.2026

S. Shlyk[1], *PhD, Associate Professor,*
J. Pyrhönen[2], *D.Sc. (Tech.), Professor,*
I. Petrov[2], *D.Sc. (Tech.), Associate Professor,*
M. Parviainen[2], *Junior Researcher,*
I. Martikainen[2], *Project Engineer,*
A. Suikki[3], *Senior Mechanical Engineer,*
J. Pippuri-Mäkeläinen[4], *D.Sc. (Tech.), Professor,*
M. Zagirnyak[1], *D.Sc. (Tech.), Professor,*
[1] Kremenchuk Mykhailo Ostrohradskyi National University,
20, Universytetska Str., Kremenchuk, 39600, Ukraine,
e-mail: mzagirn@gmail.com (Corresponding Author).
[2] Lappeenranta-Lahti University of Technology LUT,
34, Yliopistonkatu, Lappeenranta, 53850, Finland.
[3] Danfoss Editron Oy,
44, Lentokentäntie, Lappeenranta, 53600, Finland,
[4] VTT Technical Research Centre of Finland Ltd,
3, Vuorimiehentie, Espoo, FI-02044, Finland.

How to cite this article:
Shlyk S., Pyrhönen J., Petrov I., Parviainen M., Martikainen I., Suikki A., Pippuri-Mäkeläinen J., Zagirnyak M. Possibility of cooling the rotor of an electric traction motor by bidirectional air flows. *Electrical Engineering & Electromechanics*, 2026, no. 3, pp. 26-33. doi: https://doi.org/10.20998/2074-272X.2026.3.04

UDC 621.314 https://doi.org/10.20998/2074-272X.2026.3.05

R.F. Abdelgoui, R. Taleb

Enhanced power quality in grid-connected wind energy systems using PI-controlled with doubly fed induction generator optimized by hybrid differential evolution and grey wolf algorithm

Introduction. *Nowadays, the most widely used wind energy conversion system in wind farms is based on a doubly fed induction generator (DFIG); it has a large speed range and can function in multiple modes.* ***Problem.*** *Harmonic distortion in wind energy conversion system can degrade output waveform quality, reduce power conversion efficiency.* ***Goal.*** *This study investigates the dynamic performance of a wind energy conversion system comprising a grid-connected load, a 13-level hybrid multilevel converter and a doubly fed induction generator (DFIG), using a PI controller. The study aims to evaluate the dynamic performance and power quality of wind energy conversion systems, and to develop a novel hybrid metaheuristic method combining differential evolution (DE) and grey wolf optimization (GWO)-based selective harmonic elimination pulse-width modulation (SHEPWM) control strategies. This method reduces total harmonic distortion (THD) and ensures compliance with IEEE 519 standards, while increasing the power transferred to the grid.* ***Methodology.*** *The system, which includes a grid-connected load, a 13-level converter, and a DFIG, is modeled and simulated in MATLAB/Simulink under steady-state wind conditions. Vector control via stator flow orientation was used to modify the energy quality provided by the DFIG, making the system comparable to the DC machine. Our approach was to use a PI controller in order to directly control the active and reactive DFIG power through multi-level converter then a hybrid metaheuristic algorithm combining DE and GWO is implemented to solve the SHEPWM nonlinear transcendental equations. The proposed algorithm is evaluated based on its ability to suppress lower-order harmonics and improve THD performance, these converters increase the power transmitted to the power grid by reducing harmonic content of the output voltages.* ***Results.*** *By using the DE-GWO hybrid method and a PI controller, lower-order harmonics were effectively removed and THD was reduced to meet IEEE 519 standards. Simulations showed an improvement in output wave quality and better energy conversion efficiency compared to conventional optimization methods.* ***Scientific novelty*** *of the proposed work lies in the fact that the study introduces a novel DE-GWO hybrid optimization method for PWM (SHEPWM) in 13-level hybrid multilevel converter applied to wind energy systems.* ***Practical value.*** *The novel method demonstrates that constant high performance in wind energy systems may be achieved by combining intelligent optimization algorithms with complex multilevel converter designs This means it can be effectively integrated into contemporary wind farms where meeting grid standards, adjusting to varying sizes, and ensuring long-term reliability are crucial.* References 26, table 1, figures 19.

Key words: **doubly fed induction generator, wind power, differential evolution, power quality, total harmonic distortion.**

Вступ. *На сьогодні найбільш поширеною системою перетворення енергії вітру у вітрових електростанціях є система на основі асинхронного генератора з подвійним живленням (DFIG); вона характеризується широким діапазоном швидкостей і здатністю працювати в різних режимах.* ***Проблема***. *Гармонічні спотворення в системах перетворення вітрової енергії можуть погіршувати якість вихідної напруги та знижувати ефективність перетворення енергії.* ***Мета***. *У роботі розглядається динамічна поведінка системи перетворення вітрової енергії, що включає навантаження, підключене до мережі, 13-рівневий гібридний багаторівневий перетворювач та асинхронний генератор з подвійним живленням (DFIG), із застосуванням ПІ-регулятора. Метою роботи є оцінка динамічних характеристик і якості електроенергії, а також розроблення нового гібридного метаевристичного методу, що поєднує диференціальну еволюцію (DE) та оптимізацію сірого вовка (GWO) для керування за методом селективного усунення гармонік із широтно-імпульсною модуляцією (SHEPWM). Запропонований метод забезпечує зменшення коефіцієнта гармонічних спотворень (THD), відповідність стандарту IEEE 519 та підвищення потужності, що передається до мережі.* ***Методика***. *Система, що включає навантаження, підключене до мережі, 13-рівневий перетворювач і DFIG, змодельована та досліджена в середовищі MATLAB/Simulink за усталених умов вітру. Для покращення якості електроенергії використано векторне керування з орієнтацією за потоком статора, що забезпечує характеристики, подібні до машин постійного струму. Активна та реактивна потужності DFIG безпосередньо регулюються за допомогою ПІ-регулятора через багаторівневий перетворювач. Для розв'язання нелінійних трансцендентних рівнянь SHEPWM застосовано гібридний метаевристичний алгоритм, що поєднує DE та GWO. Ефективність алгоритму оцінюється за здатністю пригнічувати гармоніки нижчих порядків та зменшувати THD. Використання багаторівневих перетворювачів сприяє збільшенню переданої до мережі потужності за рахунок зниження гармонічних спотворень вихідної напруги.* ***Результати***. *Застосування гібридного методу DE-GWO у поєднанні з ПІ-регулятором забезпечило ефективне придушення гармонік нижчих порядків і зниження THD до рівня, що відповідає вимогам стандарту IEEE 519. Результати моделювання показали покращення якості вихідної напруги та підвищення ефективності перетворення енергії порівняно з традиційними методами оптимізації.* ***Наукова новизна*** *полягає у розробленні нового гібридного методу оптимізації DE-GWO для широтно-імпульсної модуляції типу SHEPWM у 13-рівневому гібридному багаторівневому перетворювачі, застосованому в системах вітроенергетики.* ***Практична значимість***. *Запропонований метод демонструє можливість досягнення стабільно високих показників роботи систем вітроенергетики шляхом поєднання інтелектуальних алгоритмів оптимізації зі складними багаторівневими перетворювачами. Це забезпечує ефективну інтеграцію в сучасні вітрові електростанції, де критично важливими є відповідність мережевим стандартам, адаптивність до змін умов роботи та довготривала надійність.* Бібл. 26, табл. 1, рис. 19.

Ключові слова: **асинхронний генератор з подвійним живленням, вітроенергетика, диференціальна еволюція, якість електроенергії, коефіцієнт гармонічних спотворень.**

Introduction. One of the most efficient power generation systems is wind power. However, in the case of grid-connected structures, different electrical generators can be used. The doubly fed induction generator (DFIG) is still widely used capacitors for reactive power compensation [1]. In addition, the main advantage of this generator is the power converters, which are smaller than traditional full-size stator converters. Several techniques have been proposed in the literature to develop appropriate, economical and effective wind energy conversion systems for microgrid connection [2, 3].

Wind power is crucial to the electrical grid, thus cutting it off during a breakdown can cause instability and exacerbate the voltage surge. Because of this, the new grid standards have established stringent guidelines for how wind producers must behave in these circumstances. Depending on the severity of the fault, fault ride-through criteria include power delivery, an uninterrupted connection, and a contribution to grid stability for a specific amount of time [4]. Several solutions have been

proposed in the literature to meet the requirements of the grid code while ensuring the reliable and safe operation of the DFIG [5, 6].Converter based multi-level architectures improve load power efficiency. Compared to standard 2-level inverters that require a high switching frequency, multi-level converters offer advantages. Because of its high efficiency, significant voltage operating capacity, low output of electromagnetic interference, and reduced switching losses, multi-level inverters are gaining increased attention from academics. In addition to minimizing the stress of d*v*/d*t*, multi-level converters can give incredibly low voltage distortion, which lessens electromagnetic compatibility issues. Both fundamental frequencies and high PWM switching frequencies can be utilized with them [7, 8].

Space-vector pulse-width modulation (PWM) gating of the inverter switches enhances the fundamental alone at the alternating current sides as well as the utilization of the available voltage [4]. Selective harmonic elimination (SHEPWM), on the other hand, is typically a better option when only specific low-order harmonics need to be cancelled. This type of PWM produces ideal switching angles that satisfy a system of non-linear transcendental equations that are obtained by forcing the necessary harmonic spectrum [2].

Switching angles in SHEPWM are frequently calculated using the Newton-Raphson method and the theory of elimination by results; however, these approaches mostly depend on a reliable initial estimate, which may result in convergence failures. Conversely, heuristic and evolutionary methods like genetic algorithm, differential evolution (DE), particle swarm optimization, and grey wolf optimization (GWO) are easier to use and less susceptible to this initial approximation. But they run the risk of convergent to local optima too soon, particularly when there are several transcendental equations [9–16]. In [17] authors optimized switching angles for an 11-level PV-fed modular multilevel inverter using GWO and DE independently, demonstrating that GWO produced a lower total harmonic distortion (THD) than DE and enhance output voltage quality.

The **goal** of this study is to investigate the dynamic performance of a wind energy conversion system comprising a grid-connected load, a 13-level hybrid multilevel converter and a DFIG using a PI controller. The study aims to evaluate the dynamic performance and power quality of wind energy conversion systems, and to develop a novel hybrid metaheuristic method combining DE and GWO-based SHEPWM control strategies. This method reduces THD and ensures compliance with IEEE 519 standards, while increasing the power transferred to the grid. The proposed system is shown in Fig. 1 [9–16].

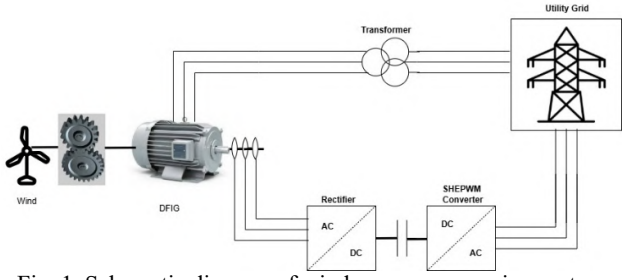

Fig. 1. Schematic diagram of wind energy conversion system

Proposed multilevel converter. Figure 2 shows this topology, which consists of a single complete bridge (A bridge in H) and the cascading of a converter suggested by 7 levels. A switch and 4 diodes make up the auxiliary circuit in the lower H-bridge, which is positioned between 2 DC sources [15].

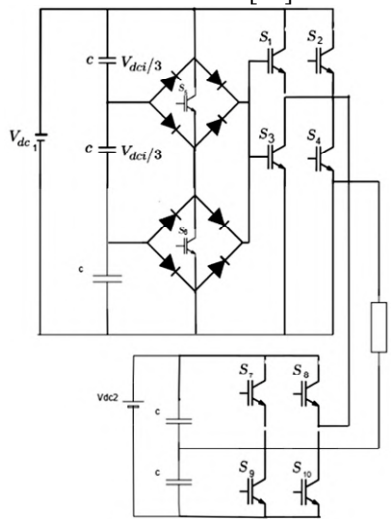

Fig. 2. The proposed 13-level hybrid converter

To generate stepped output voltages, the 13-level hybrid converter combines a diode-clamped (neutral-point clamped, NPC) stage with a cascaded H-bridge. The NPC leg generates levels of 0, $\pm V_{dc}/3$, $\pm 2V_{dc}/3$, and $\pm V_{dc}$, while the H-bridge adds 0 or $\pm V_{dc}$. By summing both outputs, the converter achieves 13 voltage levels from $-V_{dc}$ to $+V_{dc}$ in $V_{dc}/6$ increments, resulting in increased waveform quality with fewer switches and lower THD [12].

To determine the number of levels N of this inverter, the following formula will be applied by adopting a rating per unit *p.u.*:

$$N = 2(3V_{dc1} + 1V_{dc2}) + 1; \quad (1)$$

$$V_{dc1} = 1\,p.u.; \quad V_{dc2} = 3\,p.u. \quad (2)$$

This indicates that in order to get 13 voltage levels, the voltage source linked to the 2nd cell must be 4 times bigger than the single voltage source utilized in the 1st cell [5, 10, 11]. Table 1 presents the appropriate switching states corresponding to each feasible combination.

Table 1

Switching logic of a 13-level hybrid converter

Levels	Output voltage	S_1–S_6 state	S_7–S_{10} state
6	$+V_{dc}$	S_1,S_3 ON	all OFF
5	$+5V_{dc}/6$	S_1,S_3 ON	S_7,S_{10} ON
4	$+2V_{dc}/3$	S_1,S_3 ON	all OFF
3	$+V_{dc}/2$	S_1,S_4 ON	S_7,S_{10} ON
2	$+V_{dc}/3$	S_1,S_4 ON	all OFF
1	$+V_{dc}/6$	S_3,S_4 ON	S_7,S_{10} ON
0	0	S_3,S_4 ON	all OFF
–1	$-V_{dc}/6$	S_3,S_4 ON	S_8,S_9 ON
–2	$-V_{dc}/3$	S_2,S_4 ON	all OFF
–3	$-V_{dc}/2$	S_2,S_4 ON	S_8,S_9 ON
–4	$-2V_{dc}/3$	S_2,S_4 ON	all OFF
–5	$-5V_{dc}/6$	S_2,S_4 ON	S_8,S_9 ON
–6	$-V_{dc}$	S_2,S_4 ON	all OFF

Implementation of proposed algorithm. The output phase voltage's Fourier series expansion is expressed as follows [9–12]:

$$V_0(\theta)=\sum_{n=1,3,5,7,..17}^{\infty} b_n \sin(n\theta), \quad (3)$$

where n=1, 3, 5, 7,…17 are the odd harmonics; θ is the switching angle; b_n is given by:

$$b_n=\sum_{n=1,3,5}^{2N-1}\frac{4V_{dc}}{n\pi}V_1\cos\left((n\theta_1)+...+V_m\cos(n\theta_N)\right), \quad (4)$$

where N is the number of switching angles per quarter cycle; n = 1, 3, 5 ... 2N–1 (odd harmonics); m is the number of DC sources.

By solving (4) and determining the best switching angles, the 5th, 7th, 11th, 13th and 17th harmonics are eliminated. The output voltage waveform's quality is determined by how many harmonics it contains [11, 12].

The main goal of the SHEPWM technique is to determine the firing angles (θ_1 – θ_6) that satisfy the fundamental at the required level V_0 for each modulation index. It also has the advantage of suppressing or eliminating undesirable lower order harmonics from the output phase voltage. The SHEPWM technique has the superior ability and control to eliminate undesirable lower order non-triple harmonics from the output of PWM. The quarter waveform's switching angles must adhere to the following restriction in order to guarantee a symmetrical and physically accurate quarter waveform [13, 14].

$$\theta_1<\theta_2<\theta_3<\theta_4<\theta_5<\theta_6<\pi/2. \quad (5)$$

An objective function is then needed for the optimization procedure, which is selected to gauge how well the selected harmonic rank is eliminated while maintaining the fundamental element at a predetermined value. Consequently, the following is the representation of this objective function [12, 14, 15]:

$$F(\theta)=\sum_{i=1}^{p=6}\cos(\theta_i-\pi M_i)^2+\sum_{i=5,7,11}V_i^2; \quad (6)$$
$$M_i=\pi V_1/5V_{dc},$$

where M_i is the modulation index; V_i is the contribution of the harmonic of order i in the waveform. It can be defined as V_1 fundamental voltage divided by V_{dc} total number of DC component voltage as shown in (6).

Using the suggested algorithm DE-GWO, optimal switching angles are found by minimizing equation (6) under constraint (5).

Overview of GWO technique. In order to identify global maxima and minima for optimization issues, swarm intelligence algorithms mathematically model the hunting habits of animals and birds. One of the swarm intelligence algorithms is the GWO algorithm [18]. In essence, the grey wolves serve as the model for the GWO algorithm. Because they live in packs and have strong social dominance structure, grey wolves are the top predators in the food chain. Figure 3 shows the social order of grey wolves and the 3rd best option [15, 16].

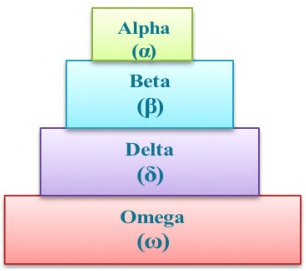

Fig. 3. Social hierarchy of grey wolves

When hunting, grey wolves can encircle their victims and capture them in packs. In order to quantitatively model the encircling behavior, in [15, 17, 18] was proposed the following equations:

$$D=\left|CX_p(t)-X(t)\right|; \quad (7)$$
$$X_p(t+1)=X_p(t+1)-AD, \quad (8)$$

where t is the t^{th} iteration; A, C, D are the coefficient vectors; X_p depicts the prey's location vector; X is the grey wolf's position vector.

The following equation can be used to evaluate the vectors A and C

$$A=2ar_1-a; \quad (9)$$
$$C=2r_2, \quad (10)$$

where r_1, r_2 are the random vectors in [0, 1]; a is the vector that decrease from 2 to 0 as we decrease the number of iteration and it can be calculated as:

$$a=2-2t/t_{\max}, \quad (11)$$

where t and $t_{\max}$ are the current iteration and maximum number of iterations respectively.

The wolf (solution) veers off course and looks in a different direction: if $|A|>1$ and move in the direction of the target (optimal solution), if $|A|<1$, and A is a random vector in the interval [−2a, 2a] where a decreases from 2 to 0 over the course of iteration. When the value of C is greater than one, the C vector often favors exploration, and when the value of C is less than one, it favors exploitation. C is not linearly decreased in contrast to A, therefore, especially in the last iteration, this parameter is quite helpful in preventing the stalling of local optima [17, 18].

The three best optimal solutions are alpha α, beta β and delta δ solutions. The remaining omega ω solutions update their position based on the positions of alpha, beta and delta. The following equations describe how the omega solutions update their position. Grey wolves are able to memorize the position of prey, and because alpha wolves are the leaders in the peck, they have the most knowledge of prey [15]:

$$D_\alpha=\left|C_1X_\alpha-X\right|; \quad (12)$$
$$X_1=X_\alpha-A_1D_\alpha; \quad (13)$$
$$D_\beta=\left|C_2X_\beta-X\right|; \quad (14)$$
$$X_2=X_\beta-A_2D_\beta; \quad (15)$$
$$D_\delta=\left|C_3X_\delta-X\right|; \quad (16)$$
$$X_3=X_\delta-A_3D_\delta; \quad (17)$$
$$X(t+1)=(X_1+X_2+X_3)/3, \quad (18)$$

where X_α, X_β, X_δ are the positions of α, β, δ, respectively; t is the number of iterations; A_1 – A_3 are the random vectors [17].

Despite its performance for large-scale problems, the GWO still experiences difficulties with small-scale problems such as the one discussed here (only 2 dimensions), which can cause it to get stuck in local minima. To solve this problem, the DE algorithm is introduced; it adds randomness and improves the ability to escape local minima. However, DE converges rather slowly. In order to achieve better overall performance, a new approach called DE-GWO is proposed. It combines the advantages of both methods by merging GWO (with a better convergence factor) and DE (with a dynamic scaling factor). A target vector representing the population is initialized randomly [10].

Detailed steps of hybrid DE-GWO.

Step 1. Initialization. Create random possible switching angles inside Eq. (5): 6 switching angles [θ_1–θ_6], population size N_p=30 wolves.

Step 2. Evaluate fitness function. Reduce THD while removing certain harmonics (5th, 7th, 11th, 13th, 17th) and maintaining the fundamental voltage magnitude.

Step 3. Determine the alpha α, beta β and delta δ wolves. Evaluate the fitness of the wolves (solutions).

Step 4. Update on GWO position (hunting & encircling) using (12) – (18).

Step 5. DE hybridization by avoiding local optima, mutation and crossover enhances exploration.

Mutation expressed by the following equation:

$$V_i = X_{r1} + F\left(X_{r2} - X_{r3}\right), \tag{19}$$

where V_i is the mutant vector; F is the mutation factor (F= 0.5); $r_1 - r_3$ are coefficients which selected randomly.

Crossover. Using probability crossover rate CR, combine the parent and mutant by the following equation:

$$U_i(j) = \begin{cases} V_i(j), & \text{if rand} < CR; \\ X_i(j), & \text{otherwise}, \end{cases} \tag{20}$$

where U_i is the test vector; X_i is the parent vector; CR is the crossover rate (CR=0.9).

Selection. The best solution (reduced THD) should be kept.

Step 6. Assessment of the new population. For every wolf, recalculate the THD and harmonic restrictions and refresh alpha α, beta β and delta δ.

Step 7. Stopping until fitness convergence or maximum iterations.

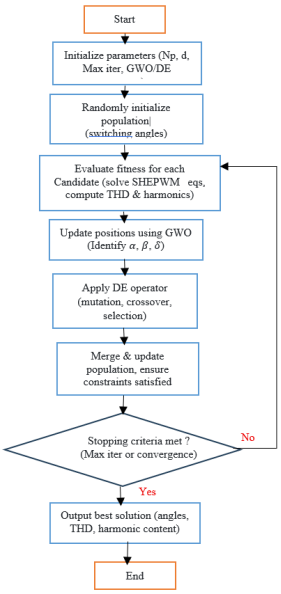

Fig. 4. Flowchart of DE-GWO

DE-GWO process used to determine the ideal firing angles for SHEPWM is shown in Fig. 4 [10].

The optimal switching angles (in degrees) versus modulation index are shown in Fig. 5 while the angles are computed with a fine step-size of 0.01 which corresponds to:

$\theta_1 = 6.2832°$,
$\theta_2 = 18.4642°$,
$\theta_3 = 31.5773°$,
$\theta_4 = 44.7139°$,
$\theta_5 = 57.0695°$,
$\theta_6 = 68.8813°$.

Figure 6 illustrates the dependence on modulation index corresponding to the amplitude of odd number harmonics of 5th, 7th, 11th, 13th and 17th order.

Results indicate differences in the behaviors according to harmonic orders. At modulation index M_i = 0, 5th and 7th harmonics indicate an exponential decay with the primary starting amplitudes of 0.2 and 0.145. The initial amplitudes are also much smaller (0.05–0.09) and the exponential decrease is not as apparent for the higher harmonics (11th and 17th).

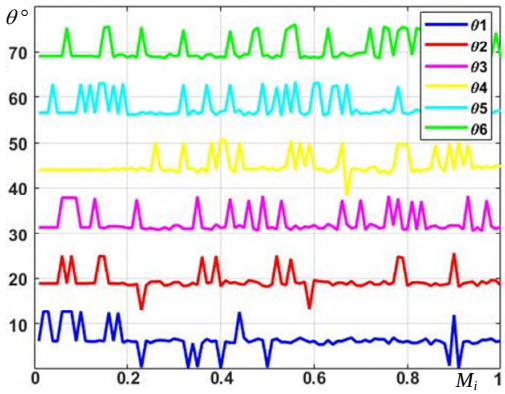

Fig. 5. Switching angles versus modulation index

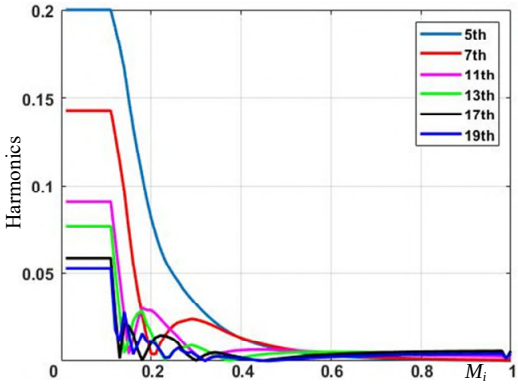

Fig. 6. Harmonics content versus modulation index

Figure 7 shows that the M_i that achieved the lowest percentage of THD was 3.1447 %, and only the lowest THD from the set of angles corresponding to each modular index was chosen.

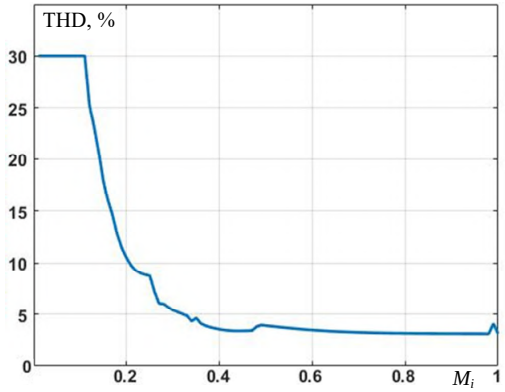

Fig. 7. THD versus modulation index

Turbine modeling. The modeling of a wind energy system is given by [19–22]:

$$\begin{cases} P_v = \dfrac{\rho S v^3}{2};\ P_{aer} = \dfrac{C_p(\lambda,\beta)\rho S v^3}{2}; \\ T_{aer} = \dfrac{P_{aer}}{\Omega_t} = \dfrac{C_p(\lambda,\beta)\rho S v^3}{2\Omega_t}, \end{cases} \tag{21}$$

where P_v is the mechanical power; P_{aer} is the aerodynamic power; ρ is the air density (1.22 kg/m^3); S is the area of the wind wheel; R is the radius of the blade; Ω_t is the turbine speed; v is the wind speed; T_{aer} is the aerodynamic torque.

The power coefficient C_p depends on the blade tilt angle β and the tip speed ratio λ [20, 21]:

$$\begin{cases} C_p = 0.5176\left(\dfrac{116}{\lambda_i} - 0.4\beta - 5\right)e^{\frac{21}{-\lambda_i}} + 0.0068\cdot\lambda; \\ \lambda_i = \dfrac{1}{\lambda + 0.008\beta} - \dfrac{0.0035}{\beta^3 + 1};\ \lambda = \dfrac{\Omega_t R}{v}. \end{cases} \quad (22)$$

Follow equations are used to simulate the gearbox that connects the turbine to the generator [22]:

$$T_{em} = T_{tur}/G;\quad \Omega_{mech} = G\Omega_t, \quad (23)$$

where T_{em} is the electromagnetic torque; T_{tur} is the turbine torque; G is the ratio's gearbox; Ω_{mech} is the generator's speed.

The fundamental dynamic equation of a mechanical system on a DFIG shaft [20, 22] is:

$$J\frac{d\Omega_{mech}}{dt} + f\Omega_{mech} = T_{mech} - T_{em}, \quad (24)$$

where J is the generator and the turbine moment of inertia; f is the friction coefficient; T_{mech} is the mechanical torque.

Model of DFIG. The following matrix form represents the generator's Park state model [23]:

$$\begin{cases} V_{sd} = R_s i_{sd} + \dfrac{d}{dt}\varphi_{sd} - \omega_s\varphi_{sq}; \\ V_{sq} = R_s i_{sq} + \dfrac{d}{dt}\varphi_{sq} - \omega_s\varphi_{sd}; \end{cases} \quad (25)$$

$$\begin{cases} V_{rd} = R_r i_{rd} + \dfrac{d}{dt}\phi_{rd} - \omega_r\phi_{rq}; \\ V_{rq} = R_r i_{rq} + \dfrac{d}{dt}\phi_{rq} - \omega_r\phi_{rd}, \end{cases} \quad (26)$$

where R_s, R_r are the stator and rotor phase resistances; φ_{sd}, φ_{sq} are d-q components of the stator and rotor flux; V_{sd}, V_{sq} are d-q components of the stator voltage; V_{rd}, V_{rq} are d-q components of the rotor voltage; $\omega_s = \omega_r + \omega$; ω_s, ω_r are the angular frequencies of stator and rotor currents; $\omega = p\,\Omega_{mec}$ is the electrical speed; p is the number of pairs of poles.

The stator and rotor fluxes are:

$$\begin{cases} \phi_{sd} = L_s i_{sd} + M i_{rd}; \\ \phi_{sq} = L_s i_{sq} + M i_{rq}; \end{cases} \quad (27)$$

$$\begin{cases} \phi_{rd} = L_r i_{rd} + M i_{sd}; \\ \phi_{rq} = L_r i_{rq} + M i_{sq}, \end{cases} \quad (28)$$

where i_{sd}, i_{sq}, i_{rd}, i_{rq} are d-q components of the stator and rotor currents; L_s, L_r, M are the stator, rotor and mutual inductances.

The DFIG's electromagnetic torque T_{em} and stator active P_s and reactive power Q_s are expressed as [23]:

$$\begin{cases} P_s = V_{sd} i_{sd} + V_{sq} i_{sq}; \\ Q_s = V_{sq} i_{sq} - V_{sd} i_{sq}; \end{cases} \quad (29)$$

$$T_{em} = \frac{3}{2} p \frac{M}{L_s}(\phi_{sq} i_{rd} - \phi_{sd} i_{rq}). \quad (30)$$

The development of equations that relate the values of the rotor voltages generated by an inverter to the stator active and reactive power will enable the independent control of active and reactive power, hence facilitating the control of wind-generated electricity [23, 24]. With the stator's flux assumed to be constant, we get:

$$\begin{cases} V_{sd} = 0; \\ V_{sq} = V_s; \end{cases} \quad (31)$$

$$\begin{cases} P_s = V_s i_{sq}; \\ Q_s = V_s i_{sd}. \end{cases} \quad (32)$$

The stator and rotor currents are:

$$\begin{cases} i_{sd} = -\dfrac{M}{L_s} i_{rd} + \dfrac{\phi_s}{L_s}; \\ i_{sq} = -\dfrac{M}{L_s} i_{rq}. \end{cases} \quad (33)$$

We replace the currents in (32) by (33) to get the expression of powers in function of stator currents:

$$\begin{cases} P_s = -V_s \dfrac{M}{L_s} i_{rq}; \\ Q_s = \dfrac{V_s^2}{L_s \omega_s} - \dfrac{V_s M}{L_s} i_{rd}. \end{cases} \quad (34)$$

We must determine the relationship between the rotor current and voltages in order to properly manage the machine [22–25]:

$$\begin{cases} V_{rd} = R_r i_{rd} + \left(L_r - \dfrac{M^2}{L_s}\right)\dfrac{di_{rd}}{dt} - g\omega_s\left(L_r - \dfrac{M^2}{L_s}\right) i_{rq}; \\ V_{rq} = R_r i_{rq} + \left(L_r - \dfrac{M^2}{L_s}\right)\dfrac{di_{rq}}{dt} - g\omega_s\left(L_r - \dfrac{M^2}{L_s}\right) i_{rd} + g\dfrac{V_s M}{L_s}, \end{cases} \quad (35)$$

where g is the asynchronous machine's slip.

Indirect field-oriented control of the DFIG. Using the dynamic equations, a template-based PI regulator is built to guarantee steady operation and enable independent control of the DFIG's active and reactive power.

The principle of control by stator field direction is to orient the stator field along the axis d, that is to say:

$$\begin{cases} \phi_{sd} = \phi_s; \\ \phi_{sq} = 0. \end{cases} \quad (36)$$

Figure 8 shows a control scheme of DFIG [19, 20, 25, 26].

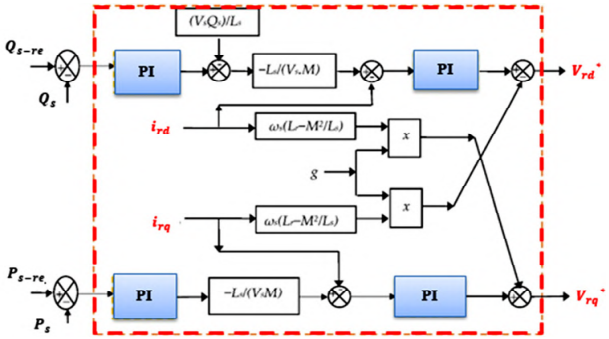

Fig. 8. Control scheme of DFIG

Simulation results. The control scheme proposed in this study aims at controlling the rotor-side of the wind energy conversion system composed of a DFIG, 13-level multilevel converter and connected load. The system was simulated in MATLAB/Simulink at a steady wind speed of 12 m/s, relating to moderate to high operational conditions. Figures 9–19 show the transient and steady state response of the system.

Figure 9 shows that the power is maximal at 2.5 MW and it increases with the wind speed up to the threshold,

reached at 12 m/s, and then remains constantly. This demonstrates the multilevel converter regulates the power applied to the load to avoid overload after the rated power. The coefficient C_p increases till an optimal wind velocity is reached (6.12 m/s) and then decreases, which means that the wind turbine is most efficient at that speed.

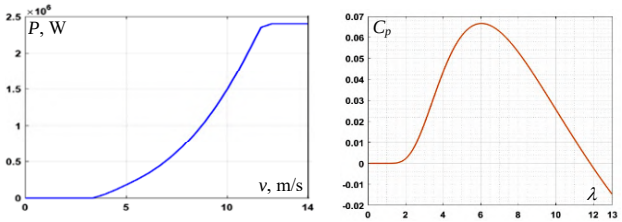

Fig. 9. Power of turbine according to wind speed

Figure 10 displays the shaft's mechanical speed for DFIG. A stable and controlled generator system is shown by the DFIG's shaft mechanisms, which rapidly accelerate from rest to nominal operation speed and then operate at steady, constant speeds.

Figure 11 shows the DFIG torque as a function of time. DFIG initially oscillates with enormous torque for a short period before quickly stabilizing. This demonstrates the damping and smooth operation of the generator after a period of disturbance.

The 3-phase stator currents of the DFIG are shown in Fig. 12. In the first few moments, the currents show strong oscillations and irregularities. These oscillations soon disappear, and the currents stabilize in the form of regular, balanced sinusoids, indicating stable, normal operation of the DFIG.

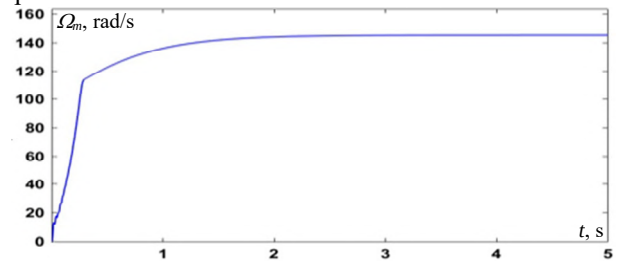

Fig.10. Mechanical speed of the shaft

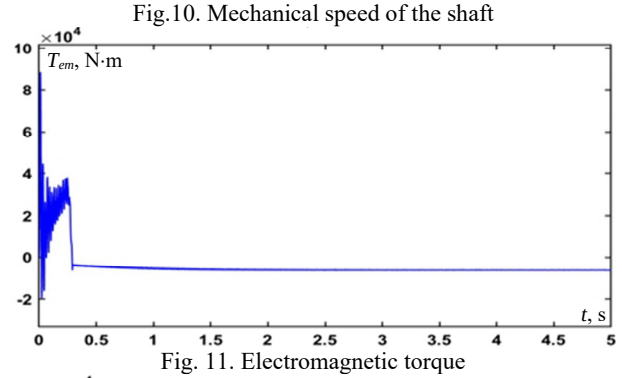

Fig. 11. Electromagnetic torque

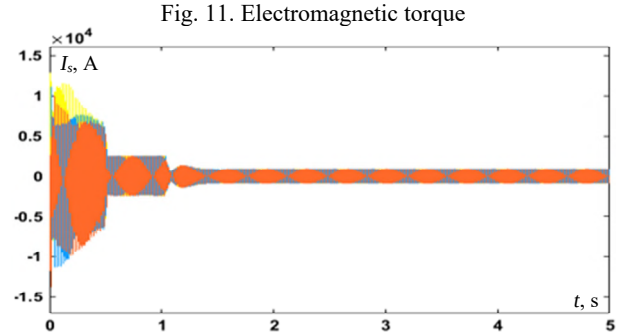

Fig. 12. 3-phase stator currents

The FFT of the 3-phase stator currents of the DFIG is shown in Fig. 13. Regarding the FFT analysis, 3-phase stator currents of the DFIG is mostly sinusoidal (THD = 1.19 %) satisfactory power quality with effective control of the generator.

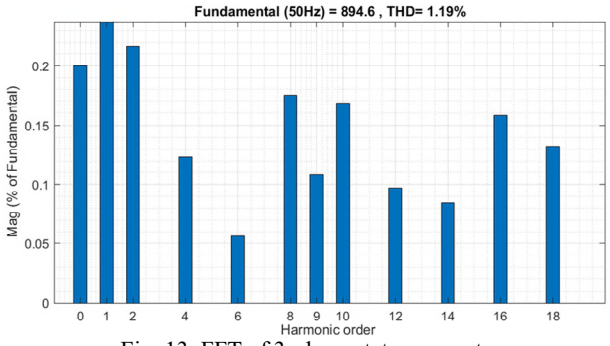

Fig. 13. FFT of 3-phase stator currents

The 3-phase rotor currents i_r of a DFIG is shown in Fig. 14 as a function of time from 0 to 5 s. The rotor currents show noticeable oscillations and irregularities at (t = 0), indicating a transient response to machine start-up. The machine operates smoothly and efficiently when the oscillations cease rapidly and the currents stabilize in balanced, sinusoidal and symmetrical waveforms.

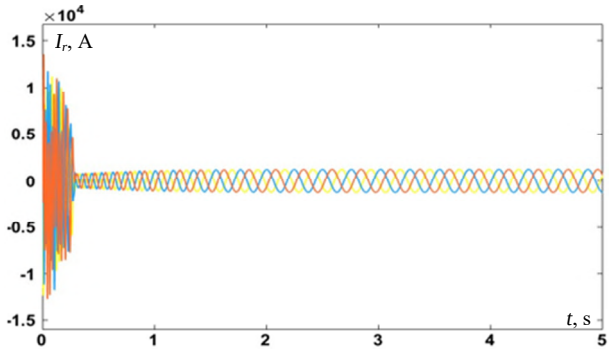

Fig. 14. 3-phase rotor currents

Figure 15 shows the FFT of the 3-phase rotor currents of a DFIG. This FFT analysis shows that the 3-phase rotor currents of the DFIG is predominantly sinusoidal, with a low level of THD = 3.24 %. This indicates effective current control and good power quality in the rotor circuit.

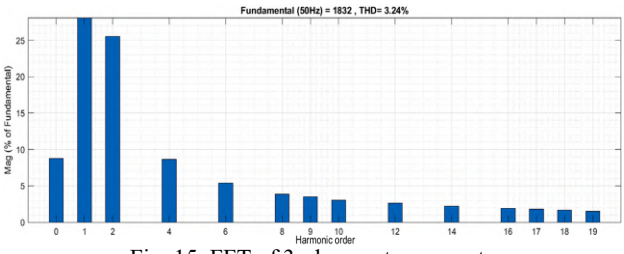

Fig. 15. FFT of 3-phase rotor currents

Figure 16 shows the 3-phase stator voltages over a period of 5 s. These voltages have a symmetrical sinusoidal waveform with amplitude of ±563.38 V, indicating balanced 3-phase operation. There are no visible distortions or irregularities, suggesting stable and normal operation of the generator. Figure 17 shows the zoom of the stator phase voltages.

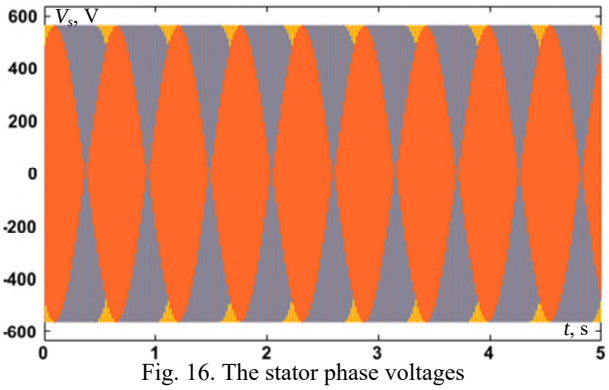

Fig. 16. The stator phase voltages

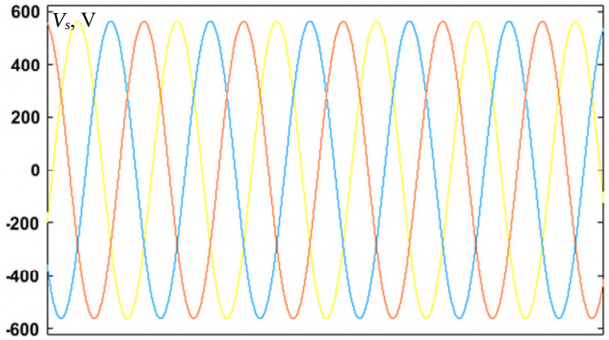

Fig. 17. Zoom of the stator phase voltages

Figure 18 shows the harmonic spectrum of the stator phase voltages, with the magnitude of each harmonic order expressed as a percentage of the fundamental component. THD is 4.18 %, which is relatively low, indicating that the stator phase voltage is predominantly sinusoidal with minor harmonic distortion.

Figure 19 shows the active power response of a load provided by a system that consists of a DFIG and a multilevel converter. Following an initial, highly oscillatory transient, the active power rapidly stabilizes to zero, exhibiting robust damping and a stable steady-state.

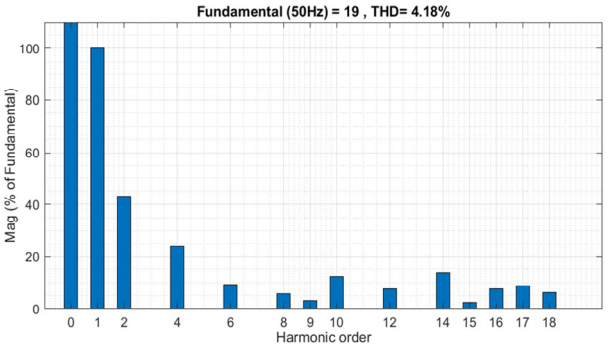

Fig. 18. FFT of the stator phase voltages

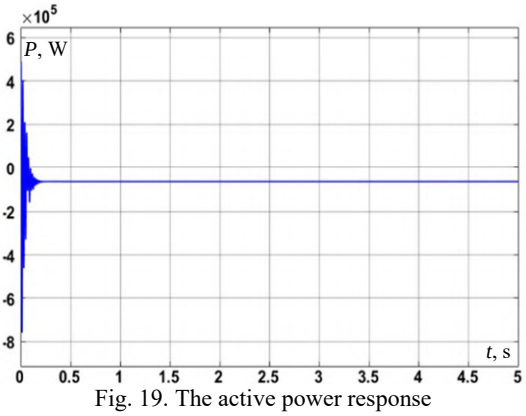

Fig. 19. The active power response

Conclusions. The results of this study demonstrate that the dynamic performance and power quality of grid-connected wind energy systems are greatly enhanced by combining a DFIG controlled by PI controller with a 13-level multilevel converter, which is optimized using a hybrid GWO and DE algorithm for SHEPWM.

The suggested method successfully reduces low-order harmonics and keeps THD within IEEE 519 standards where the 3-phase stator-current THD is 1.19 %, well below the IEEE 519 limit; the stator phase-voltage THD is 4.18 %, and the rotor-current THD is 3.24 %, as shown by MATLAB/Simulink simulations.

The converter topology ensures effective energy transfer and improves the quality of the voltage waveform, confirming the potential of intelligent optimization techniques and hybrid multilevel converters to advance high-performance wind energy applications. These findings offer important new information for creating reliable and effective renewable energy systems that work with contemporary power grids.

Conflict of interest. The authors declare that they have no conflicts of interest.

REFERENCES

1. Tamalouzt S., Benyahia N., Rekioua T., Rekioua D., Abdessemed R. Performances analysis of WT-DFIG with PV and fuel cell hybrid power sources system associated with hydrogen storage hybrid energy system. *International Journal of Hydrogen Energy*, 2016, vol. 41, no. 45, pp. 21006-21021. doi: https://doi.org/10.1016/j.ijhydene.2016.06.163.

2. Shihabudheen K.V., Pillai G.N., Krishnama Raju S. Neuro-Fuzzy Control of DFIG Wind Energy System with Distribution Network. *Electric Power Components and Systems*, 2018, vol. 46, no. 13, pp. 1416-1431. doi: https://doi.org/10.1080/15325008.2018.1499154.

3. Jaladi K.K., Sandhu K.S. Real-time simulator based hybrid controller of DFIG-WES during grid faults design and analysis. *International Journal of Electrical Power & Energy Systems*, 2020, vol. 116, art. no. 105545. doi: https://doi.org/10.1016/j.ijepes.2019.105545.

4. Hafaiedh H., Saoudi Y., Benamor A., Chrifi–Alaoui L. Wind farms integration into power system with improved location and stability problem solving. *Electrical Engineering & Electromechanics*, 2025, no. 5, pp. 10-16. doi: https://doi.org/10.20998/2074-272X.2025.5.02.

5. Parimalasundar E., Jayanthi R., Suresh K., Sindhuja R. Investigation of efficient multilevel inverter for photovoltaic energy system and electric vehicle applications. *Electrical Engineering & Electromechanics*, 2023, no. 4, pp. 47-51. doi: https://doi.org/10.20998/2074-272X.2023.4.07.

6. Gianto R. Steady-state model of DFIG-based wind power plant for load flow analysis. *IET Renewable Power Generation*, 2021, vol. 15, no. 8, pp. 1724-1735. doi: https://doi.org/10.1049/rpg2.12141.

7. Li S., Li L. Steady-state Solution and Evaluation Indices of DFIG Operating at Synchronous Speed (sDFIG). *2021 IEEE Sustainable Power and Energy Conference (ISPEC)*, 2021, pp. 260-267. doi: https://doi.org/10.1109/iSPEC53008.2021.9736024.

8. Tamalouzt S., Belkhier Y., Sahri Y., Bajaj M., Ullah N., Chowdhury M.S., Titseesang T., Techato K. Enhanced Direct Reactive Power Control-Based Multi-Level Inverter for DFIG Wind System under Variable Speeds. *Sustainability*, 2021, vol. 13, no. 16, art. no. 9060. doi: https://doi.org/10.3390/su13169060.

9. Padmanaban S., Dhanamjayulu C., Khan B. Artificial Neural Network and Newton Raphson (ANN-NR) Algorithm Based Selective Harmonic Elimination in Cascaded Multilevel Inverter

for PV Applications. *IEEE Access*, 2021, vol. 9, pp. 75058-75070. doi: https://doi.org/10.1109/ACCESS.2021.3081460.
10. Sifat Z., Hussain M.T., Khan M.A., Hussain M.S., Sarwar A., Tariq M., Hasan M. Selective harmonic elimination in PUC-5 multilevel inverter using hybrid IGWO-DE algorithm. *Engineering Reports*, 2024, vol. 6, no. 10, art. no. e12883. doi: https://doi.org/10.1002/eng2.12883.
11. Dahidah M.S.A., Konstantinou G., Agelidis V.G. A Review of Multilevel Selective Harmonic Elimination PWM: Formulations, Solving Algorithms, Implementation and Applications. *IEEE Transactions on Power Electronics*, 2015, vol. 30, no. 8, pp. 4091-4106. doi: https://doi.org/10.1109/TPEL.2014.2355226.
12. Bektas E., Karaca H. GA Based Selective Harmonic Elimination for Multilevel Inverter with Reduced Number of Switches: An Experimental Study. *Elektronika Ir Elektrotechnika*, 2019, vol. 25, no. 3, pp. 10-17. doi: https://doi.org/10.5755/j01.eie.25.3.23670.
13. Kumar S.S., Iruthayarajan M.W., Sivakumar T. Evolutionary algorithm based selective harmonic elimination for three-phase cascaded H-bridge multilevel inverters with optimized input sources. *Journal of Power Electronics*, 2020, vol. 20, no. 5, pp. 1172-1183. doi: https://doi.org/10.1007/s43236-020-00112-9.
14. Kala P., Arora S. Implementation of PSO based Selective Harmonic Elimination Technique in Multilevel Inverters. *2018 2nd IEEE International Conference on Power Electronics, Intelligent Control and Energy Systems (ICPEICES)*, 2018, pp. 605-610. doi: https://doi.org/10.1109/ICPEICES.2018.8897309.
15. Ceylan O., Neshat M., Mirjalili S. Cascaded H-bridge multilevel inverters optimization using adaptive grey wolf optimizer with local search. *Electrical Engineering*, 2024, vol. 106, no. 2, pp. 1765-1779. doi: https://doi.org/10.1007/s00202-021-01441-z.
16. Nasser A.M., Refky A., Shatla H., Abdel-hamed A.M. A grey wolf optimization-based modified SPWM control scheme for a three-phase half bridge cascaded multilevel inverter. *Scientific Reports*, 2024, vol. 14, no. 1, art. no. 7016. doi: https://doi.org/10.1038/s41598-024-57262-0.
17. Stonier A.A., Chinnaraj G., Kannan R., Mani G. Investigation and validation of an eleven level symmetric modular multilevel inverter using grey wolf optimization and differential evolution control algorithm for solar PV applications. *Circuit World*, 2020, vol. 47, no. 1, pp. 117-127. doi: https://doi.org/10.1108/CW-12-2019-0197.
18. Mirjalili S., Mirjalili S.M., Lewis A. Grey Wolf Optimizer. *Advances in Engineering Software*, 2014, vol. 69, pp. 46-61. doi: https://doi.org/10.1016/j.advengsoft.2013.12.007.
19. Djebbar M.S., Boukadoum A., Bouguerne A. Performances of a wind power system based on the doubly fed induction generator controlled by a multi-level inverter. *International Journal of Power Electronics and Drive Systems (IJPEDS)*, 2023, vol. 14, no. 1, pp. 100-110. doi: https://doi.org/10.11591/ijpeds.v14.i1.pp100-110.
20. Sayeh K.F., Tamalouzt S., Sahri Y. Improvement of power quality in WT-DFIG systems using novel direct power control based on fuzzy logic control under randomness conditions. *International Journal of Modelling and Simulation*, 2025, vol. 45, no. 1, pp. 55-67. doi: https://doi.org/10.1080/02286203.2023.2270757.
21. Kaddache M., Drid S., Khemis A., Rahem D., Chrifi-Alaoui L. Maximum power point tracking improvement using type-2 fuzzy controller for wind system based on the double fed induction generator. *Electrical Engineering & Electromechanics*, 2024, no. 2, pp. 61-66. doi: https://doi.org/10.20998/2074-272X.2024.2.09.
22. Kumar Behara R., Kumar Saha A. Deep Q-Network Reinforcement Learning-Based Rotor Side Control System of a Grid Integrated DFIG Wind Energy System Under Variable Wind Speed Conditions. *IEEE Access*, 2024, vol. 12, pp. 184179-184205. doi: https://doi.org/10.1109/ACCESS.2024.3511665.
23. Benbouhenni H., Yessef M., Colak I., Bizon N., Kotb H., AboRas K.M., ELrashidi A. Dynamic performance of rotor-side nonlinear control technique for doubly-fed multi-rotor wind energy based on improved super-twisting algorithms under variable wind speed. *Scientific Reports*, 2024, vol. 14, no. 1, art. no. 5664. doi: https://doi.org/10.1038/s41598-024-55271-7.
24. Muthukaruppasamy S., Dharmaprakash R., Sendilkumar S., Parimalasundar E. Enhancing off-grid wind energy systems with controlled inverter integration for improved power quality. *Electrical Engineering & Electromechanics*, 2024, no. 5, pp. 41-47. doi: https://doi.org/10.20998/2074-272X.2024.5.06.
25. L'Hadj Said M., Ali Moussa M., Bessaad T. Control of an autonomous wind energy conversion system based on doubly fed induction generator supplying a non-linear load. *Electrical Engineering & Electromechanics*, 2025, no. 4, pp. 3-10. doi: https://doi.org/10.20998/2074-272X.2025.4.01.
26. Alnaib I.I., Alsammak A.N. Optimization of fractional PI controller parameters for enhanced induction motor speed control via indirect field-oriented control. *Electrical Engineering & Electromechanics*, 2025, no. 1, pp. 3-7. doi: https://doi.org/10.20998/2074-272X.2025.1.01.

Received 02.09.2025
Accepted 25.12.2025
Published 02.05.2026

R.F. Abdelgoui [1], *Doctor of Technical Science, Associate Professor,*
R. Taleb [2], *Full Professor,*
[1] Laboratory of Industrial Engineering and Sustainable Development (GIDD), Department of Electrical Engineering, Ahmed Zabana University, Algeria,
e-mail: rimfeyrouz.abdelgoui@univ-relizane.dz (Corresponding Author)
[2] Electrical Engineering Department,
Laboratoire Génie Electrique et Energies Renouvelables (LGEER), Hassiba Benbouali University, Algeria.

How to cite this article:
Abdelgoui R.F., Taleb R. Enhanced power quality in grid-connected wind energy systems using PI-controlled with doubly fed induction generator optimized by hybrid differential evolution and grey wolf algorithm. *Electrical Engineering & Electromechanics*, 2026, no. 3, pp. 34-41. doi: https://doi.org/10.20998/2074-272X.2026.3.05

UDC 621.311:621.314.5 https://doi.org/10.20998/2074-272X.2026.3.06

Y. Daili, R. Bentafer, N. Djaraf, A. Harrag

Comprehensive modeling of grid-connected inverters in weak grid systems

Introduction. *The stability of grid-connected inverters is critical for the integration of renewable energy into modern power systems. However, this stability is significantly challenged under weak grid conditions, characterized by high impedance and low short-circuit ratios.* ***Problem.*** *Under such conditions, complex dynamic interactions arise between the inverter control systems, the grid, and the phase-locked loop, which is essential for synchronization. These interactions can degrade phase tracking and even lead to system instability. Such complexities render traditional models inadequate for accurately evaluating system behavior or guiding robust control design. The* ***goal*** *of this work is to develop and validate a compact, linearized state-space model of a grid-connected inverter under weak grid conditions, enabling stability analysis and supporting the design of robust control strategies.* ***Methodology.*** *Using small-signal modeling, a state-space representation of the inverter system is derived, incorporating control dynamics, grid impedance, and the power converter. The model's accuracy is validated through detailed nonlinear simulations, ensuring strong consistency between both modeling approaches.* ***Results.*** *The proposed model effectively captures the interaction between inverter dynamics and weak grid characteristics. Simulation results demonstrate a high correlation with nonlinear behavior, confirming the model's validity.* ***Scientific novelty.*** *Unlike existing models, this unified linearized state-space model explicitly captures cross-coupling effects among control loops and grid dynamics under weak grid scenarios. It enables more accurate stability analysis and provides deeper insights into the system's dynamic behavior.* ***Practical value.*** *The model serves as a practical tool for engineers designing control systems for renewable energy integration. By enhancing controller robustness, it contributes to more stable and reliable power systems in weak grid environments.* References 22, tables 2, figures 6.

Key words: **grid-connected inverter, weak grid, state-space model, small-signal analysis, phase locked loop, renewable energy.**

Вступ. *Стійкість мережевих інверторів є критично важливою для інтеграції відновлюваних джерел енергії в сучасні електроенергетичні системи. Однак ця стійкість суттєво погіршується в умовах слабкої електричної мережі, що характеризується високим імпедансом і низьким коефіцієнтом короткого замикання.* ***Проблема.*** *За таких умов виникають складні динамічні взаємодії між системою керування інвертора, електричною мережею та фазовим автопідстроюванням частоти, що є ключовим для синхронізації. Ці взаємодії можуть погіршувати відстеження фази та навіть призводити до нестійкості системи. Такі складні ефекти роблять традиційні моделі недостатніми для точного оцінювання поведінки системи та розроблення робастних алгоритмів керування.* ***Мета*** *роботи полягає у розробленні та валідації компактної лінеаризованої моделі мережевого інвертора у просторі станів в умовах слабкої мережі, що дозволяє виконувати аналіз стійкості та підтримує синтез робастних стратегій керування.* ***Методика.*** *На основі методу малих сигналів отримано представлення системи інвертора у просторі станів з урахуванням динаміки системи керування, імпедансу мережі та силового перетворювача. Точність моделі підтверджено шляхом детального нелінійного моделювання, що забезпечує високу узгодженість між двома підходами.* ***Результати.*** *Запропонована модель ефективно відтворює взаємодію між динамікою інвертора та характеристиками слабкої мережі. Результати моделювання демонструють високу відповідність нелінійній поведінці, що підтверджує адекватність моделі.* ***Наукова новизна.*** *На відміну від існуючих підходів, запропонована узагальнена лінеаризована модель у просторі станів явно враховує перехресні зв'язки між контурами керування та динамікою мережі в умовах слабкої мережі. Це забезпечує більш точний аналіз стійкості та глибше розуміння динамічних процесів у системі.* ***Практична значимість.*** *Запропонована модель є ефективним інструментом для інженерів при розробленні систем керування для інтеграції відновлюваних джерел енергії. Підвищення робастності регуляторів сприяє забезпеченню більш стабільної та надійної роботи електроенергетичних систем в умовах слабких мереж.* Бібл. 22, табл. 2, рис. 6.

Ключові слова: **мережевий інвертор, слабка електромережа, модель простору станів, аналіз малих сигналів, фазове автопідстроювання частоти, відновлювана енергетика.**

Introduction. The increasing penetration of renewable energy sources has fundamentally transformed modern power system architecture and operation [1, 2]. A key element of this transformation is the widespread use of grid-connected inverters, which interface variable renewable generation, such as photovoltaic and wind energy systems, with the power grid [3–5]. These inverters are generally operated under current control and are responsible for delivering both active and reactive power, while ensuring synchronization with the grid voltage [6].

However, under weak grid conditions characterized by high grid impedance and low short-circuit capacity the dynamic interaction between inverter control systems and the grid becomes significantly more complex [7–10]. The phase-locked loop (PLL), which is critical for synchronizing the inverter with the grid, becomes highly sensitive to variations in grid impedance [11, 12]. This sensitivity may lead to degraded phase tracking, oscillatory responses, and even loss of synchronism, ultimately compromising system stability [9, 10]. Furthermore, the nonlinear behavior of power electronic interfaces and the tight coupling between inverter control loops and grid dynamics further intensify these challenges [11, 13].

Therefore, developing robust modeling and control approaches that ensure stable operation under weak grid conditions is a critical and timely challenge for integrating renewable energy sources into modern power systems.

To address the stability and control issues posed by weak grids, various strategies have been proposed. For example, in [4] was introduced an optimal virtual impedance control method to enhance system stability and improve reactive power sharing among distributed generation units. In [10], a variable virtual inductance control approach was presented to improve PLL damping and enhance dynamic performance. Another study [7] explored the interaction between PLL and current control during severe voltage sags and proposed a damping controller integrated within the active current loop.

Despite these advancements, accurate dynamic modeling of grid-connected inverters remains a foundational requirement for robust control design and system analysis. Two main approaches dominate the literature:

- small-signal modeling, which involves linearizing nonlinear system dynamics around an operating point [4, 5, 14, 15].
- impedance-based modeling, which characterizes the frequency-domain behavior of the inverter-grid interface [16–18].

Among these, small-signal models provide detailed insights into stability margins, resonance modes, and control sensitivities by simplifying nonlinear behavior into a tractable linear framework.

However, many existing models either oversimplify certain dynamic elements. This limits their effectiveness in analyzing and designing control strategies under highly dynamic or weak grid scenarios. Therefore, there is a clear need for a comprehensive, integrated small-signal state-space model that captures all significant dynamic interactions in such conditions.

The **goal** of this work is to develop and validate a compact, linearized state-space model of a grid-connected inverter under weak grid conditions, enabling stability analysis and supporting the design of robust control strategies.

This model aims to:

- accurately represent key dynamic behaviors during weak grid operation;
- provide a foundation for systematic stability analysis;
- support the design and tuning of robust control strategies.

To validate the proposed model, simulation studies are performed and compared against detailed nonlinear time-domain simulations, demonstrating close agreement and confirming the model's effectiveness.

Description of the studied system. Figure 1 shows the topology of a single voltage source converter (VSC) connected to an infinite bus through a transmission line. The converter voltage is assumed to be 3-phase symmetrical with no harmonic injection [19].

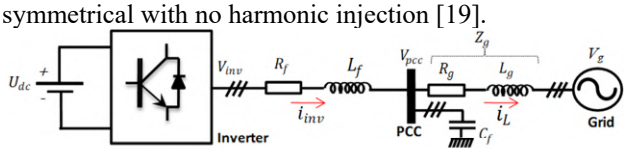

Fig. 1. Typical configuration of grid connected inverter

The inverter is connected to the bus through an LC filter with components R_f, L_f and C_f. R_g and L_g are the resistance and inductance of the transmission line respectively. V_{inv} and V_{pcc} are the voltage of the output inverter and point of common coupling (PCC); i_{inv} is the current across the converter; V_g is the voltage of the infinite source with the fixed system angular frequency marked as ω, fixed amplitude and the initial phase angle of zero.

The current components i_{inv}^{d} and i_{inv}^{q} are regulated using PI controllers. The reference currents i_{inv}^{dref} and i_{inv}^{qref} are typically generated by outer control loops, such as the active and reactive power control loops. However, in this paper, the analysis of the outer control loops is considered beyond the scope of the study. The simplified PLL model is shown in Fig 2,*b*. With PI controller, the quadrature voltage at PCC point equals zero and the voltage phase angle can be accurately locked and measured [20].

In Fig. 1 the stiffness of the grid at the PCC can be described by the short circuit ratio (SCR):

$$SCR = S_{SC}/S_N\,, \tag{1}$$

where S_{SC} is the short-circuit apparent power at the PCC; S_N is the total rated apparent power of inverters. Alternatively, the SCR can be expressed using voltage and current and line impedance Z_g as:

$$SCR = \frac{(3/2)V_g^2/|Z_g|}{(3/2)V_{pcc(rated)}\cdot i_{inv(rated)}} \approx \frac{V_g}{|Z_g|\cdot i_{inv(\max)}}, \tag{2}$$

where V_g is the amplitude of grid voltage; $V_{pcc(rated)}$ and $i_{inv(rated)}$ are the amplitude of the rated PCC voltage and rated inverter current.

From (2), it follows that the SCR decreases with increasing grid impedance Z_g. According to IEEE Standard 1204-1997, a system is regarded as a weak when $2<SCR<3$ [21].

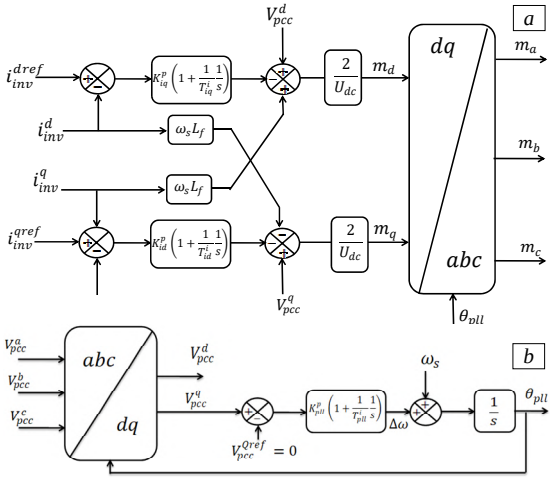

Fig. 2. Control diagram of grid connected inverter [19]: *a* – vector current control model; *b* – the simplified model of PLL

System modeling. To derive an accurately model of the grid-connected inverter in a weak grid environment, two distinct reference frames are employed [4]: the grid reference frame (*d*–*q*), which is synchronized with the actual grid voltage V_g, and the controller reference frame (*D*–*Q*) (Fig. 3), which is aligned with the estimated PCC voltage angle provided by the PLL [15].

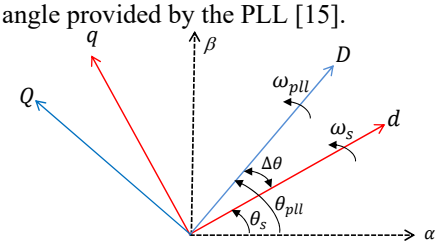

Fig. 3.Reference frame transformation

Under steady-state conditions, the controller's (*D*–*Q*) frame is aligned with the system's (*d*–*q*) frame. However, when small-signal perturbations affect the grid voltage, the orientation of the system (*d*–*q*) frame changes. Due to the PLL's internal dynamics particularly its PI regulator and the controller's (*D*–*Q*) frame may no longer remain aligned with the system (*d*–*q*) frame.

The following transformation matrix $T_{\Delta\theta}$ is used to convert system variables from the grid reference frame (*d*–*q*) to the controller reference frame (*D*–*Q*):

$$T_{\Delta\theta} = \begin{bmatrix} \cos(\Delta\theta) & \sin(\Delta\theta) \\ -\sin(\Delta\theta) & \cos(\Delta\theta) \end{bmatrix}, \tag{3}$$

where $\Delta\theta$ is the angular difference between the two frames. Here $\Delta\theta = \theta_{pll} - \theta_s$, $\theta_s = \omega_s t = 0$ represents the actual phase angle of the grid voltage, and θ_{pll} is the phase angle estimated by PLL.

For feedback control purposes, inverter voltage V_{inv}^{dq} and current i_{inv}^{dq} vectors expressed in the system *d*–*q* frame are transformed into the controller reference frame (*D*–*Q*) as follow:

$$\begin{bmatrix} V_{inv}^{D} \\ V_{inv}^{Q} \end{bmatrix} = \begin{bmatrix} \cos(\Delta\theta) & \sin(\Delta\theta) \\ -\sin(\Delta\theta) & \cos(\Delta\theta) \end{bmatrix} \begin{bmatrix} V_{inv}^{d} \\ V_{inv}^{q} \end{bmatrix}. \tag{4}$$

The duty-cycle commands (m_D, m_Q) generated by feedback control are then rotated to the system (*d*–*q*) frame by the applying the following inverse matrix:

$$T_{\Delta\theta}^{-1} = \begin{bmatrix} \cos(\Delta\theta) & -\sin(\Delta\theta) \\ \sin(\Delta\theta) & \cos(\Delta\theta) \end{bmatrix}. \tag{5}$$

1) *LC filter model*. The inverter system is modeled in the synchronous rotating reference frame (*d*–*q* aligned with the grid voltage orientation. The dynamics are derived for the inverter currents, PCC voltages, and grid-side currents, considering the LC filter and line impedances.

$$\begin{cases} \dfrac{\mathrm{d}i_{inv}^{d}}{\mathrm{d}t} = -\dfrac{R_f}{L_f} i_{inv}^{d} + \omega i_{inv}^{q} + \dfrac{V_{inv}^{d}}{L_f} - \dfrac{V_{pcc}^{d}}{L_f}; \\ \dfrac{\mathrm{d}i_{inv}^{q}}{\mathrm{d}t} = -\dfrac{R_f}{L_f} i_{inv}^{q} - \omega i_{inv}^{d} + \dfrac{V_{inv}^{q}}{L_f} - \dfrac{V_{pcc}^{q}}{L_f}; \\ \dfrac{\mathrm{d}V_{pcc}^{d}}{\mathrm{d}t} = \omega V_{pcc}^{q} + \dfrac{i_{inv}^{d}}{C_f} - \dfrac{i_{L}^{d}}{C_f}; \\ \dfrac{\mathrm{d}V_{pcc}^{q}}{\mathrm{d}t} = -\omega V_{pcc}^{d} + \dfrac{i_{inv}^{q}}{C_f} - \dfrac{i_{L}^{q}}{C_f}; \\ \dfrac{\mathrm{d}i_{L}^{d}}{\mathrm{d}t} = -\dfrac{R_g}{L_g} i_{L}^{d} + \omega i_{L}^{q} + \dfrac{V_{pcc}^{d}}{L_g} - \dfrac{V_{g}^{d}}{L_g}; \\ \dfrac{\mathrm{d}i_{L}^{q}}{\mathrm{d}t} = -\dfrac{R_g}{L_g} i_{L}^{q} - \omega i_{L}^{d} + \dfrac{V_{pcc}^{q}}{L_g} - \dfrac{V_{g}^{q}}{L_g}, \end{cases} \tag{6}$$

where R_f, C_f, L_f are the resistance, inductance, and capacitance of the inverter filter respectively; R_g, L_g are the resistance and inductance of the line impedance respectively; ω is the grid angular frequency; $i_{inv}^{d,q}$ is the inverter output current; $i_{L}^{d,q}$ is the load current in the (*d*–*q*) axis; $V_{pcc}^{d,q}$ is the voltage at the PCC; $V_{inv}^{d,q}$ is the inverter voltage in (*d*–*q*) reference frame.

The inverter output voltage is determined by the modulation indices m_d, m_q and the DC-link voltage U_{dc}:

$$\begin{cases} V_{inv}^{d} = m_d \dfrac{U_{dc}}{2}; \\ V_{inv}^{q} = m_q \dfrac{U_{dc}}{2}. \end{cases} \tag{7}$$

2) *Current controller loop modeling*. The current control loop employs a conventional PI controller. The controller receives as input the error signal, which is the difference between the measured (sampled) inverter output current and its reference value. In addition, a feed-forward term is introduced to compensate for disturbances in the output voltage. This control structure computes the modulation indices in the (*D*–*Q*) reference frame, denoted as (m_D, m_Q) which are then supplied to the PWM block. The control dynamics are described as:

$$\begin{cases} \dfrac{\mathrm{d}\eta_D}{\mathrm{d}t} = -\dfrac{1}{T_i^{i}} \left(i_{inv}^{Dref} - i_{inv}^{D} \right); \\ \dfrac{\mathrm{d}\eta_Q}{\mathrm{d}t} = -\dfrac{R_f}{L_f} \left(i_{inv}^{Qref} - i_{inv}^{Q} \right); \\ \dfrac{\mathrm{d}m_D}{\mathrm{d}t} = \dfrac{1}{T_s} \left(m'_D - m_D \right); \\ \dfrac{\mathrm{d}m_Q}{\mathrm{d}t} = \dfrac{1}{T_s} \left(m'_Q - m_Q \right); \\ m'_D = \dfrac{2}{U_{dc}} \left(\left(i_{inv}^{Dref} - i_{inv}^{D} + \eta_D \right) k_p^{i} + V_{pcc}^{D} - \omega L_f i_{inv}^{Q} \right); \\ m'_Q = \dfrac{2}{U_{dc}} \left(\left(i_{inv}^{Qref} - i_{inv}^{Q} + \eta_Q \right) k_p^{i} + V_{pcc}^{Q} + \omega L_f i_{inv}^{D} \right); \end{cases} \tag{8}$$

where i_{inv}^{Dref}, i_{inv}^{Qref} are the reference currents in the (*D*–*Q*) axis; i_{inv}^{D}, i_{inv}^{Q} are the actual inverter output currents in the *D*-axis and *Q*-axis (the controller's frame); η_D, η_Q are the integrator states (integral action of the current PI controller); m_D, m_Q are the actual modulation indices; m'_D, m'_Q are the calculated modulation indices; T_i^{i} is the integral time constant of the current PI controller; k_p^{i} is the proportional gain of the current PI controller; T_s is the modulation and calculation delay; $V_{pcc}^{D,Q}$ is the voltage at the PCC in (*D*–*Q*) reference frame.

3) *PLL dynamic modeling*. The PLL technique is essential for extracting phase and frequency information from the electrical system, particularly when interfacing with power electronic devices. The PLL block measures the system frequency and provides the phase synchronization angle to the reference frame transformation block, enabling control operations to be executed in synchronism with the power grid [22].

As illustrated in Fig. 2,*b* the controller operates in a rotating (*D*–*Q*) reference frame, which rotates at an angular frequency ω_{pll}, with the *d*-axis phase-aligned according to the angle θ_{pll}. This phase alignment is determined by the PLL.

The dynamics of the PLL can be described as:

$$\begin{cases} \dfrac{\mathrm{d}\varepsilon_Q}{\mathrm{d}t} = \dfrac{1}{T_{pll}^{i}} V_{pcc}^{Q}; \\ \dfrac{\mathrm{d}\theta_{pll}}{\mathrm{d}t} = k_{pll}^{p} \left(V_{pcc}^{Q} + \varepsilon_Q \right), \end{cases} \tag{9}$$

where θ_{pll} is the estimated phase angle of the grid voltage; T_{pll}^{i} is the integral time constant of the PLL controller; V_{pcc}^{Q} is the voltage at the PCC in *D*-axis; k_{pll}^{p} is the proportional gain of the PLL controller; ε_Q is the integral action state (internal variable for the PLL integrator).

4) *Full dynamic model*. The full dynamic model of the grid-connected inverter, incorporating the control system and the PLL, is formulated by combining the state equations (1) – (3), along with the transformation matrices $T_{\Delta\theta}$ and $T_{\Delta\theta}^{-1}$. This results in a comprehensive state-space representation that captures the electrical dynamics of the LC filter, the inverter control loops, and the synchronization mechanism. The system is expressed as a nonlinear differential equation of the form:

$$\mathrm{d}x / \mathrm{d}t = f(x, u), \tag{10}$$

where the state vector x is given by:

$$x = \left[i_{inv}^{d} \;\; i_{L}^{d} \;\; V_{pcc}^{d} \;\; i_{inv}^{q} \;\; i_{L}^{q} \;\; V_{pcc}^{q} \;\; \eta_D \;\; \eta_Q \;\; m_D \;\; m_Q \;\; \theta_{pll} \;\; \varepsilon_Q \right]^{T},$$

and the control input vector $u = \left[V_g^{d} \;\; V_g^{q} \;\; i_{inv}^{Dref} \;\; i_{inv}^{Qref} \right]^{T}$; $f(x, u)$ is the nonlinear function characterizing the system dynamics defined by (11).

The inherent complexity of the original nonlinear model, referred to as equations (10), (11), stems directly from the inclusion of the PLL dynamics, which introduce significant nonlinearities into the system's mathematical representation. These nonlinearities arise primarily from trigonometric functions involving the PLL angle and its coupling with other key state variables, such as currents and voltages. Consequently, the model becomes analytically intractable and poses substantial challenges for control design, stability analysis, and performance prediction.

$$f(x,u)=\begin{bmatrix}
-\frac{1}{L_f}\left(V_{pcc}^{d}+R_f i_{inv}^{d}-\omega L_f i_{inv}^{q}-m_D\frac{U_{dc}}{2}\cos\left(\theta_{pll}\right)+m_Q\frac{U_{dc}}{2}\sin\left(\theta_{pll}\right)\right)\\
\frac{1}{L_g}\left(V_{pcc}^{d}-V_g^{d}-R_g i_L^{d}+\omega L_g i_L^{q}\right)\\
\frac{1}{C_f}\left(i_{inv}^{d}-i_L^{d}+\omega C_f V_{pcc}^{q}\right)\\
-\frac{1}{L_f}\left(V_{pcc}^{q}+R_f i_{inv}^{q}+\omega L_f i_{inv}^{d}-m_Q\frac{U_{dc}}{2}\cos\left(\theta_{pll}\right)-m_D\frac{U_{dc}}{2}\sin\left(\theta_{pll}\right)\right)\\
\frac{1}{L_g}\left(V_{pcc}^{q}-V_g^{q}-R_g i_L^{q}-\omega L_g i_{pL}^{d}\right)\\
\frac{1}{C_f}\left(i_{inv}^{q}-i_L^{q}-\omega C_f V_{pcc}^{d}\right)\\
\frac{1}{T_i^{i}}\left(i_{inv}^{Dref}-i_{inv}^{d}\cos\left(\theta_{pll}\right)-i_{inv}^{q}\cos\left(\theta_{pll}\right)\right)\\
\frac{1}{T_i^{i}}\left(i_{inv}^{Qref}-i_{inv}^{q}\cos\left(\theta_{pll}\right)+i_{inv}^{d}\sin\left(\theta_{pll}\right)\right)\\
\frac{1}{T_s}\left(\frac{2}{U_{dc}}\left(\left(i_{inv}^{Dref}-i_{inv}^{d}\cos\left(\theta_{pll}\right)-i_{inv}^{q}\sin\left(\theta_{pll}\right)+\eta_D\right)k_p^{i}+V_{pcc}^{d}\cos\left(\theta_{pll}\right)+V_{pvv}^{q}\sin\left(\theta_{pll}\right)-\omega L_f i_{inv}^{q}\cos\left(\theta_{pll}\right)+\omega L_f i_{inv}^{d}\sin\left(\theta_{pll}\right)\right)-m_D\right)\\
\frac{1}{T_s}\left(\frac{2}{U_{dc}}\left(\left(i_{inv}^{Qref}-i_{inv}^{q}\cos\left(\theta_{pll}\right)+i_{inv}^{q}\cos\left(\theta_{pll}\right)+\eta_Q\right)k_p^{i}+V_{pcc}^{q}\cos\left(\theta_{pll}\right)-V_{pll}^{d}\sin\left(\theta_{pll}\right)+\omega L_f i_{inv}^{d}\cos\left(\theta_{pll}\right)+\omega L_f i_{inv}^{q}\sin\left(\theta_{pll}\right)\right)-m_Q\right)\\
k_{pll}^{p}\left(\varepsilon_Q-V_{pcc}^{d}\sin\left(\theta_{pll}\right)+V_{pcc}^{q}\cos\left(\theta_{pll}\right)\right)\\
\frac{1}{T_{pll}^{i}}\left(V_{pll}^{q}\cos\left(\theta_{pll}\right)-V_{pll}^{d}\sin\left(\theta_{pll}\right)\right)
\end{bmatrix}. \quad (11)$$

To address these challenges and establish a framework amenable to rigorous analysis and systematic controller synthesis, we justify the development of a simplified linearized model using the well-established Jacobian linearization technique. This approach is widely accepted and formally valid under the assumption that the system operates near a stable equilibrium point, denoted as (x_0, u_0), where the nonlinear functions are smooth and continuously differentiable.

The outcome of this process is a linear time-invariant model, presented as equation (12), which offers several critical advantages over its nonlinear counterpart. Most notably, it enables the application of powerful linear systems theory, facilitating:

- advanced stability analysis (e.g., eigenvalue-based assessment);
- facilitate the design and systematic tuning of robust control strategies, thereby enhancing stability margins in weak grid scenarios

Linearized state-space model is carried out around a steady-state operating point. This process results in a linear time-invariant model that accurately captures the system dynamics in the vicinity of the equilibrium. The state-space representation of the linearized system is obtained by linearizing equation (11) around the operating point (x_0, u_0), as given by:

$$\frac{\mathrm{d}\Delta x}{\mathrm{d}t}=A\cdot\Delta x+B\cdot\Delta u\ , \quad (12)$$

where $\Delta x=x-x_0$ is the deviation from the steady-state state vector; $\Delta u=u-u_0$ is the input perturbation; A, B are the Jacobian matrices of the system dynamics, they are computed as:

$$A=\frac{\partial}{\partial x}f(x,u)\bigg|_{x_0,u_0}\ ;\ B=\frac{\partial}{\partial u}f(x,u)\bigg|_{x_0,u_0}\ . \quad (13)$$

The full analytical expressions for the matrices A and B are provided in Appendix in equations (A.1) and (A.2), respectively.

Simulation results. A simulation study was conducted using MATLAB/Simulink to validate the theoretical analysis discussed earlier. Both the power stage and control system were modeled within the simulation environment. Key simulation parameters, including the operating point of the VSC system and the associated power controller settings, are listed in Table 1.

Table 1

Parameters of VSC connected to weak grid

	Parameters symbols	Value
Main circuit parameters	Equivalent AC source voltage V_g (line-to-line RMS)	380 V
	Inverter rated current	60 A
	Nominal utility frequency f_s	50 Hz
	Equivalent line transmission impedance R_g+jx_g	0.302+j1.6022 Ω
	LC filter capacitor C_f	240 μF
	LC filter inductance L_f	0.02+j0.1751 Ω
	Rated DC voltage U_{dc}	700 V
Controllers parameters	Current controller gains (T_i^i, k_i^p)	0.1426, 20
	PLL controller gains (T_{pll}^i, k_{pll}^p)	0.1070, 27

To verify the linearized state-space model, the time-domain response of a VSC connected to an AC grid was computed using the small-signal model in MATLAB. This response was then compared to that obtained from the full nonlinear model implemented in Simulink.

The state-space matrices A and B in (12) were

computed using the expressions provided in Appendix, based on the system parameters and the specific operating point under consideration.

Test scenarios. To validate the accuracy of the developed state-space model, small perturbations were introduced around three distinct operating points. The resulting dynamic responses from the state-space model were then compared to those obtained from a full nonlinear simulation. This comparison was conducted to assess the fidelity of the linearized model in capturing the system's transient and steady-state behavior.

Table 2 illustrates the profiles of the *d*-axis and *q*-axis reference currents i_{inv}^{dref} and i_{inv}^{qref} used as input perturbations during the validation process.

Table 2

Inverter reference currents profiles for three test scenarios

Time, s	1st test		2nd test		3rd test	
	i_{inv}^{dref}, A	i_{inv}^{qref}, A	i_{inv}^{dref}, A	i_{inv}^{qref}, A	i_{inv}^{dref}, A	i_{inv}^{qref}, A
0	–50	0	–50	–10	–50	+10
0.8	–55		–55		–55	
0.9	–50		–50		–50	
1	–45		–45		–45	

The *d*-axis reference current i_{inv}^{dref} signal exhibits step changes at approximately 0.8 s, 0.9 s and 1 s. The perturbation amplitude varies within ±5 A around the operating point of i_{inv}^{dref} = –50 A for three test scenarios. These variations represent active power reference changes, as i_{inv}^{dref} typically corresponds to active power flow in a grid-connected VSC system. The negative sign of the current reference indicates that active power is injected from the inverter to the grid. The *q*-axis reference current component i_{inv}^{qref} remains constant for each of the three operating points, taking values of 0 A, –10 A and +10 A, respectively. These values represent, in order, no reactive power exchange, reactive power absorption, and reactive power injection.

Figures 4–6 present the dynamic responses of the load current. The response of the linearized state-space model is compared with that obtained from the full nonlinear simulation for three different test scenarios (see Table 2), in order to evaluate the accuracy of the developed model. The system is assumed to initially operate around an equilibrium point characterized by the load current components $i^{d}{}_{L0}$ and $i^{q}{}_{L0}$ in the *d*–*q* reference frame. This operating point is then disturbed by applying a small variation of Δi_{inv}^{dref} = ±5 A to the *d*-axis reference current (–50 A). The resulting load current responses in both the *d*-axis and *q*-axis are then observed.

The comparison shows a strong agreement between the two models. The minor deviations observed in the *q*-axis load current under steady-state conditions remain negligible, confirming the ability of the linearized model to faithfully reproduce the system dynamics and thereby validating its accuracy around the selected operating points.

Figure 4 shows the dynamic responses of the linearized state-space model and the detailed simulation model for the 1st test scenario. In this case, a disturbance is applied to i_{inv}^{dref}, while i_{inv}^{qref} is kept at 0 A. Figure 4 shows an almost identical response between the two models, particularly in transient oscillations and steady-state convergence. This confirms the linear model's ability to capture the system behavior around this operating point.

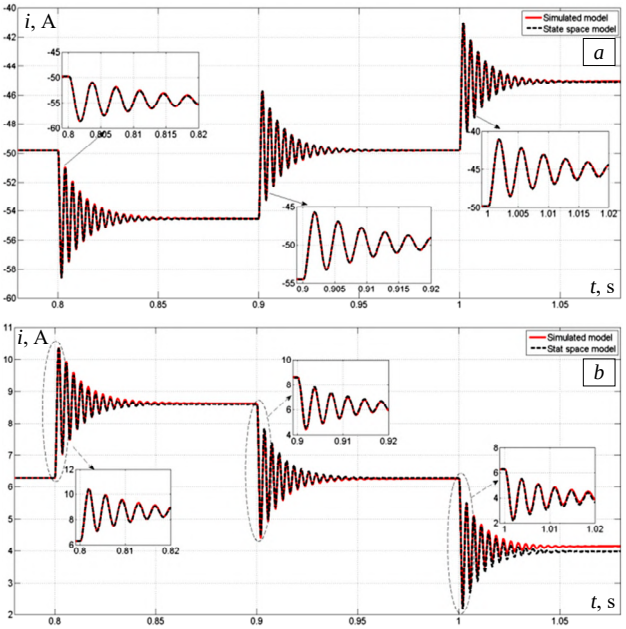

Fig. 4. Dynamic responses of the state-space model and detailed simulation model for the 1st test: *a* – load current response in the *d*-axis; *b* – load current response in the *q*-axis

Figure 5 shows the dynamic responses of the linearized state-space model and the detailed simulation model for the 2nd test scenario. Here, the same *d*-axis perturbation is applied, but the *q*-axis current reference is set to a negative value, i_{inv}^{qref} = –10 A. The results show that the linearized model closely tracks the full simulation, even during rapid transients and dynamic interactions between the *d* and *q* axes.

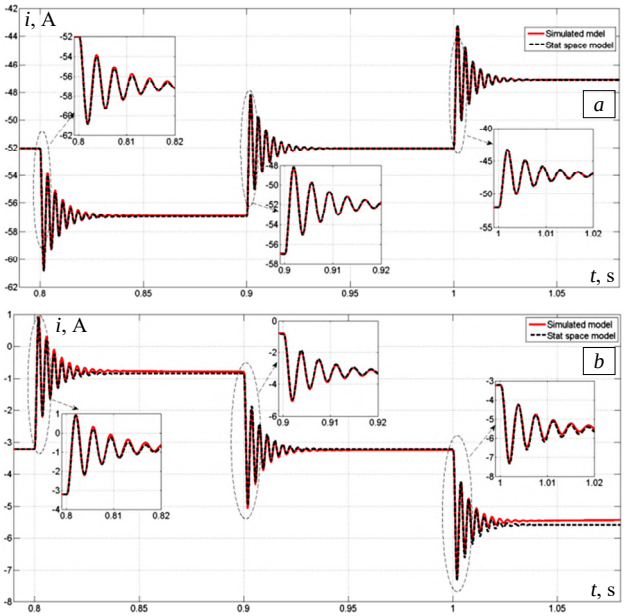

Fig. 5. Dynamic responses of the state-space model and detailed simulation model for the 2end test: *a* – Load current response in the *d*-axis; *b* – load current response in the *q*-axis

Figure 6 shows the dynamic responses of the linearized state-space model and the detailed simulation

model for the 3rd test scenario. In this case, the same perturbation on is applied, but the q-axis current reference is set to a positive value, i_{inv}^{qref} = +10 A, introducing a different dynamic condition. Again, the linearized model demonstrates excellent agreement with the full simulation, confirming its ability to accurately replicate system dynamics under varying operating conditions.

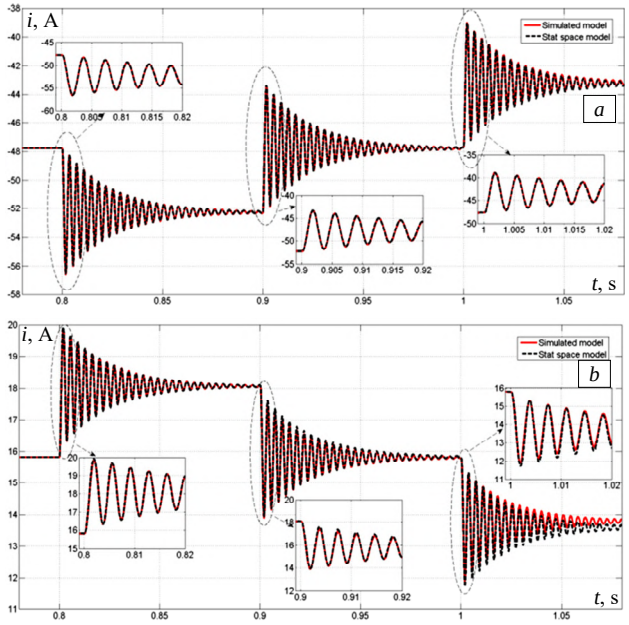

Fig. 6. Dynamic responses of the state-space model and detailed simulation model for the 3rd test: *a* – load current response in the *d*-axis; *b* – load current response in the *q*-axis

Figures 4–6 also emphasize the significant influence of the q-axis reference current on the damping behavior of load current oscillations. Specifically, when i_{inv}^{qref} is positive corresponding to reactive power absorption by the inverter, the system exhibits weaker damping compared to cases where i_{inv}^{qref} is negative, resulting in a reduced stability margin. However, a detailed analysis of the impact of these parameters on system dynamics lies beyond the scope of this study. The primary objective of this work is to develop a model capable of accurately reproducing both the dynamic and steady-state behavior of grid-connected inverters under weak grid conditions. Future research could focus on a more in-depth investigation of how operating conditions, control parameters, and line characteristics influence the system's stability and dynamic response.

Conclusions. This work has successfully achieved its goal of developing and validating a compact, linearized state-space model for grid-connected inverter operating in weak grid conditions. The proposed model incorporates the essential dynamics of inverter control systems, including the PLL, current control loops, converter filter and grid impedance. Using small-signal analysis, the model was derived and its accuracy confirmed through detailed nonlinear simulations in MATLAB/Simulink under multiple operating scenarios.

The simulation results demonstrate strong agreement between the linearized and nonlinear models in both transient and steady-state responses, validating the model's capability to capture key dynamic behavior near the operating point. Furthermore, analysis of the q-axis reference current revealed its significant impact on system damping. Specifically, a positive q-axis current associated with reactive power absorption was shown to reduce damping and stability margins, emphasizing the need for careful control tuning under weak grid conditions.

The model can serve as a practical tool for control design and stability assessment in weak grid scenarios. Also, control parameters such as PLL bandwidth and current loop gains should be tuned based on dynamic stability analysis to prevent oscillatory behavior or loss of synchronism.

Future work will explore the influence of control parameter variations, line impedance characteristics, and grid strength fluctuations on system stability. Further research will focus on using the model to design and optimize adaptive or robust control schemes for grid-connected inverters operating under a wide range of grid conditions.

These developments will enhance the reliability and resilience of renewable energy systems in weak and evolving power networks.

Appendix. The full expressions of matrices A and B are given below:

$$A=\begin{bmatrix}
-\frac{R_f}{L_f} & 0 & -\frac{1}{L_f} & \omega_0 & 0 & 0 & 0 & 0 & \frac{U_{dc}}{2L_f}a & -\frac{U_{dc}}{2L_f}b & -\frac{1}{L_f}\left(m_{D0}\frac{U_{dc}}{2}b+m_{Q0}\frac{U_{dc}}{2}a\right) & 0\\
0 & -\frac{R_g}{L_g} & \frac{1}{L_g} & 0 & \omega_0 & 0 & 0 & 0 & 0 & 0 & 0 & 0\\
\frac{1}{C_f} & -\frac{1}{C_f} & 0 & 0 & 0 & \omega_0 & 0 & 0 & 0 & 0 & 0 & 0\\
-\omega_0 & 0 & 0 & -\frac{R_f}{L_f} & 0 & -\frac{1}{L_f} & 0 & 0 & \frac{U_{dc}}{2L_f}b & \frac{U_{dc}}{2L_f}a & \frac{U_{dc}}{2L_f}\left(-m_{Q0}b+m_{D0}a\right) & 0\\
0 & -\omega_0 & 0 & 0 & -\frac{R_g}{L_g} & \frac{1}{L_g} & 0 & 0 & 0 & 0 & 0 & 0\\
0 & 0 & -\omega_0 & \frac{1}{C_f} & -\frac{1}{C_f} & 0 & 0 & 0 & 0 & 0 & 0 & 0\\
-\frac{a}{T_i^i} & 0 & 0 & -\frac{b}{T_i^i} & 0 & 0 & 0 & 0 & 0 & 0 & \frac{1}{T_i^i}\left(i_{inv0}^d b-i_{inv0}^q a\right) & 0\\
\frac{b}{T_i^i} & 0 & 0 & -\frac{a}{T_i^i} & 0 & 0 & 0 & 0 & 0 & 0 & \frac{1}{T_i^i}\left(i_{inv0}^q b+i_{inv0}^d a\right) & 0\\
-\frac{2}{T_sU_{dc}}\left(k_p^i a-\omega_0 L_f b\right) & 0 & \frac{2}{T_sU_{dc}}a & -\frac{2}{T_sU_{dc}}\left(k_p^i b+\omega_0 L_f a\right) & 0 & \frac{2}{T_sU_{dc}}b & \frac{2}{T_sU_{dc}}k_p^i & 0 & -\frac{1}{T_s} & 0 & \frac{2}{T_sU_{dc}}\left(-i_{inv0}^d k_p^i a-i_{inv0}^q k_p^i b+V_{pcc0}^d a+V_{pcc0}^q b-\omega_0 L_f i_{inv0}^q a+\omega_0 L_f i_{inv0}^d b\right) & 0\\
\frac{2}{T_sU_{dc}}\left(k_p^i b+\omega_0 L_f a\right) & 0 & -\frac{2}{T_sU_{dc}}b & -\frac{2}{T_sU_{dc}}\left(k_p^i a-\omega_0 L_f b\right) & 0 & \frac{2}{T_sU_{dc}}a & 0 & \frac{2}{T_sU_{dc}} & 0 & -\frac{1}{T_s} & \frac{2}{T_sU_{dc}}\left(-i_{inv0}^d k_p^i a-i_{inv0}^q k_p^i b+V_{pcc0}^d a+V_{pcc0}^q b-\omega_0 L_f i_{inv0}^q a+\omega_0 L_f i_{inv0}^d b\right) & 0\\
0 & 0 & -k_{pll}^p b & 0 & 0 & k_{pll}^p a & 0 & 0 & 0 & 0 & -k_{pll}^p\left(V_{pcc0}^d a+V_{pcc0}^q b\right) & k_{pll}^p\\
0 & 0 & -\frac{1}{T_{pll}^i}b & 0 & 0 & \frac{1}{T_{pll}^i}a & 0 & 0 & 0 & 0 & -\frac{1}{T_{pll}^i}\left(V_{pcc0}^q b+V_{pcc0}^d a\right) & 0
\end{bmatrix} \quad \text{(A.1)}$$

$$B = \begin{bmatrix} 0 & 0 & 0 & 0 \\ -1/L_g & 0 & 0 & 0 \\ 0 & 0 & 0 & 0 \\ 0 & 0 & 0 & 0 \\ 0 & -1/L_g & 0 & 0 \\ 0 & 0 & 0 & 0 \\ 0 & 0 & 1/T_i^i & 0 \\ 0 & 0 & 0 & 1/T_i^i \\ 0 & 0 & 2/T_s U_{dc} & 0 \\ 0 & 0 & 0 & 2/T_s U_{dc} \\ 0 & 0 & 0 & 0 \\ 0 & 0 & 0 & 0 \end{bmatrix}, \quad (A.2)$$

where a and b in the matrix A are:

$$a = \sin(\theta_{pll0}); \quad (A.3)$$

$$b = \cos(\theta_{pll0}). \quad (A.4)$$

The subscript «0» indicates the equilibrium point around which the system has been linearized. This steady-state point, denoted as x_0, is obtained by numerically solving the nonlinear equation (10) using the *solve* function in MATLAB.

Conflict of interest. The authors declare that they have no conflicts of interest.

REFERENCES

1. Janardhan G., Surendra Babu N.N.V., Srinivas G.N. Single phase transformerless inverter for grid connected photovoltaic system with reduced leakage current. *Electrical Engineering & Electromechanics*, 2022, no. 5, pp. 36-40. doi: https://doi.org/10.20998/2074-272X.2022.5.06.

2. Boukadoum A., Bouguerne A., Bahi T. Direct power control using space vector modulation strategy control for wind energy conversion system using three-phase matrix converter. *Electrical Engineering & Electromechanics*, 2023, no. 3, pp. 40-46. doi: https://doi.org/10.20998/2074-272X.2023.3.06.

3. Xie J. Application of optimized photovoltaic grid-connected control system based on modular multilevel converters. *Energy Informatics*, 2024, vol. 7, no. 1, art. no. 24. doi: https://doi.org/10.1186/s42162-024-00317-3.

4. Bennia I., Daili Y., Harrag A., Alrajhi H., Saim A., Guerrero J.M. Stability and Reactive Power Sharing Enhancement in Islanded Microgrid via Small-Signal Modeling and Optimal Virtual Impedance Control. *International Transactions on Electrical Energy Systems*, 2024, vol. 2024, art. no. 5469868. doi: https://doi.org/10.1155/2024/5469868.

5. Ji X., Liu D., Jiang K., Zhang Z., Yang Y. Small-Signal Stability of Hybrid Inverters with Grid-Following and Grid-Forming Controls. *Energies*, 2024, vol. 17, no. 7, art. no. 1644. doi: https://doi.org/10.3390/en17071644.

6. Muthukaruppasamy S., Dharmaprakash R., Sendilkumar S., Parimalasundar E. Enhancing off-grid wind energy systems with controlled inverter integration for improved power quality. *Electrical Engineering & Electromechanics*, 2024, no. 5, pp. 41-47. doi: https://doi.org/10.20998/2074-272X.2024.5.06.

7. Wang X., Yao J., Pei J., Sun P., Zhang H., Liu R. Analysis and Damping Control of Small-Signal Oscillations for VSC Connected to Weak AC Grid During LVRT. *IEEE Transactions on Energy Conversion*, 2019, vol. 34, no. 3, pp. 1667-1676. doi: https://doi.org/10.1109/TEC.2019.2915680.

8. Zheng Y., Han Y., Wang C., Ren Q., Yang P., Zalhaf A.S. Impact of phase-locked loop on grid-connected inverter stability under weak grid conditions and suppression measures. *Computers and Electrical Engineering*, 2025, vol. 123, art. no. 110249. doi: https://doi.org/10.1016/j.compeleceng.2025.110249.

9. Tamari Y., Kato T., Inoue K. Stability Analysis Considering PLL Effects for Grid-Following Inverter by Complex Vector Control. *IEEJ Transactions on Electronics, Information and Systems*, 2024, vol. 144, no. 11, pp. 1044-1051. doi: https://doi.org/10.1541/ieejeiss.144.1044.

10. Liu A., Cao H., Liu J. Enhancing stability control of Phase-Locked loop in weak power grids. *International Journal of Electrical Power & Energy Systems*, 2024, vol. 161, art. no. 110145. doi: https://doi.org/10.1016/j.ijepes.2024.110145.

11. Zhang Y., Pen H., Zhang X. Stability Control of Grid-Connected Converter Considering Phase-Locked Loop Frequency Coupling Effect. *Energies*, 2024, vol. 17, no. 14, art. no. 3438. doi: https://doi.org/10.3390/en17143438.

12. Yue J., Gao J., An R., Jin L., Tao R., Zou K. A Method for Improving the Stability of Grid-Connected Inverters by Eliminating the Negative Effects of PLL in Weak Grids. *2022 4th International Conference on Power and Energy Technology (ICPET)*, 2022, pp. 299-304. doi: https://doi.org/10.1109/ICPET55165.2022.9918343.

13. Lin X., Chih-Hsien Peng J., Macii D., Petri D., Yu J., Wen H. Frequency-domain small-signal stability analysis methods for grid-following converters systems – An overview. *Renewable and Sustainable Energy Reviews*, 2025, vol. 211, art. no. 115283. doi: https://doi.org/10.1016/j.rser.2024.115283.

14. Pathan E., Zulkifli S.A., Tayab U.B., Jackson R. Small Signal Modeling of Inverter-based Grid-Connected Microgrid to Determine the Zero-Pole Drift Control with Dynamic Power Sharing Controller. *Engineering, Technology & Applied Science Research*, 2019, vol. 9, no. 1, pp. 3790-3795. doi: https://doi.org/10.48084/etasr.2465.

15. Zou Z.-X., Rosso R., Liserre M. Modeling of the Phase Detector of a Synchronous-Reference-Frame Phase-Locked Loop Based on Second-Order Approximation. *IEEE Journal of Emerging and Selected Topics in Power Electronics*, 2020, vol. 8, no. 3, pp. 2534-2545. doi: https://doi.org/10.1109/JESTPE.2019.2920309.

16. Pérez-Estévez D., Ríos-Castro D., Fernández-Abraldes P.M., Monteiro V., Pinto J.G., Afonso J.L., Doval-Gandoy J. Asymmetric Impedance Model for Grid-Forming Converters With Droop Control. *IEEE Transactions on Power Electronics*, 2025, vol. 40, no. 9, pp. 12977-12997. doi: https://doi.org/10.1109/TPEL.2025.3565789.

17. Golestan S., Ebrahimzadeh E., Wen B., Guerrero J.M., Vasquez J.C. dq-Frame Impedance Modeling of Three-Phase Grid-Tied Voltage Source Converters Equipped With Advanced PLLs. *IEEE Transactions on Power Electronics*, 2021, vol. 36, no. 3, pp. 3524-3539. doi: https://doi.org/10.1109/TPEL.2020.3017387.

18. Lu S., Zhu Y., Dong L., Na G., Hao Y., Zhang G., Zhang W., Cheng S., Yang J., Sui Y. Small-Signal Stability Research of Grid-Connected Virtual Synchronous Generators. *Energies*, 2022, vol. 15, no. 19, art. no. 7158. doi: https://doi.org/10.3390/en15197158.

19. Fang L., Feng L., Chu C., Xu J., Wu R., Fan Q. Evaluation of dominant factors for stability of grid-connected inverters based on impedance sensitivity analysis. *IET Renewable Power Generation*, 2024, vol. 18, no. 16, pp. 3788-3797. doi: https://doi.org/10.1049/rpg2.13020.

20. Gassara K., Gassara B., Fakhfakh A., De Pablo S. Offline Analysis of a Modified dqPLL Architecture based on THD Compensation Blocks for Three-Phase Grid-Tied Inverters. *Engineering, Technology & Applied Science Research*, 2025, vol. 15, no. 3, pp. 22669-22677. doi: https://doi.org/10.48084/etasr.10206.

21. Pal D., Panigrahi B.K. A Nonlinear Adaptive Stabilizing Control Strategy to Enhance Dynamic Stability of Weak Grid-Tied VSC System. *IEEE Transactions on Power Delivery*, 2022, vol. 37, no. 3, pp. 2182-2193. doi: https://doi.org/10.1109/TPWRD.2021.3106682.

22. Zerzouri N., Ben Si Ali N., Benalia N. A maximum power point tracking of a photovoltaic system connected to a three-phase grid using a variable step size perturb and observe algorithm. *Electrical Engineering & Electromechanics*, 2023, no. 5, pp. 37-46. doi: https://doi.org/10.20998/2074-272X.2023.5.06.

Received 01.09.2025
Accepted 08.12.2025
Published 02.05.2026

Y. Daili [1], *Associate Professor,*
R. Bentafer[1,3], *PhD,*
N. Djaraf [1,3], *PhD,*
A. Harrag [2,3], *Professor,*
[1] Electrotechnics Department, Faculty of Technology,
Ferhat Abbas University Setif 1, 19000 Setif, Algeria,
e-mail: yassine.daili@univ-setif.dz (Corresponding Author)
[2] Electronics Department, Faculty of Technology,
Ferhat Abbas University Setif 1, 19000 Setif, Algeria.
[3] Mechatronics Laboratory (LMETR), Optics and Precision Mechanics Institute, Ferhat Abbas University Setif 1, Setif, Algeria.

How to cite this article:
Daili Y., Bentafer R., Djaraf N., Harrag A. Comprehensive modeling of grid-connected inverters in weak grid systems. *Electrical Engineering & Electromechanics*, 2026, no. 3, pp. 42-48. doi: https://doi.org/10.20998/2074-272X.2026.3.06

UDC 621.313 https://doi.org/10.20998/2074-272X.2026.3.07

S. Dukkipati, S.S. Nagendra, B.H. Kumar, E. Parimalasundar

Adaptive deep reinforcement learning-based control strategy for high-performance permanent magnet synchronous motor drive systems

Introduction. *In recent days, electric vehicles, robotics and in many control system applications, permanent magnet synchronous motors (PMSMs) are widely utilized.* ***Problem.*** *Due to non-linear behavior of system, external interferences and frequent changes in parameters, conventional control techniques like direct torque control, field-oriented control and PI control, frequently experience decline in performance.* ***Goal.*** *This paper presents a new deep learning based reinforcement learning (RL) PMSM control approach that makes use of the twin delayed deep deterministic policy gradient (TD3) and deep deterministic policy gradient (DDPG) algorithms. These algorithms utilize actor-critic architectures to learn optimal control policies in a model-free manner, enabling adaptive and intelligent motor control.* ***Methodology.*** *A MATLAB/Simulink-based simulation framework is developed to train and evaluate the proposed deep reinforcement learning (DRL) based controllers against conventional PI controllers. Performance metrics, including speed tracking accuracy, torque ripple minimization are analyzed.* ***Results.*** *The results demonstrate that DRL-based controllers exhibit superior adaptability, robustness, and dynamic performance under varying load and speed conditions in contrast to traditional control methods. Notably, the comparative analysis reveals that the TD3 algorithm outperforms DDPG by mitigating overestimation bias, resulting in smoother torque output and more stable control actions.* ***Scientific novelty.*** *This paper illustrates the capability of DRL for advanced PMSM control.* ***Practical value.*** *Paving the way for real-time implementation in modern electric drive systems.* References 25, tables 3, figures 12.

Key words: **deep reinforcement learning, permanent magnet synchronous motor, deep deterministic policy gradient, twin delayed deep deterministic policy gradient, adaptive motor control, actor-critic algorithm.**

Вступ. *Останнім часом синхронні двигуни з постійними магнітами (PMSM) широко застосовуються в електромобілях, робототехніці та багатьох системах автоматичного керування.* ***Проблема.*** *Через нелінійний характер системи, зовнішні збурення та часті зміни параметрів традиційні методи керування, такі як пряме керування моментом, векторне керування і ПІ-регулювання, часто демонструють зниження ефективності.* ***Мета.*** *Запропоновано новий підхід до керування PMSM на основі глибинного навчання з підкріпленням (RL), що використовує алгоритми подвійний відкладений глибинний детермінований градієнт політики (TD3) та глибинний детермінований градієнт політики (DDPG). Зазначені алгоритми застосовують архітектуру актор-критик для навчання оптимальних стратегій керування без використання точної математичної моделі, що забезпечує адаптивне та інтелектуальне керування двигуном.* ***Методика.*** *Для навчання та оцінювання запропонованих регуляторів на основі глибинного навчання з підкріпленням (DRL) розроблено модель у середовищі MATLAB/Simulink. Ефективність DRL-регуляторів порівнювалася з традиційними ПІ-регуляторами за показниками точності відстеження швидкості та мінімізації пульсацій моменту.* ***Результати.*** *Отримані результати показали, що регулятори на основі DRL характеризуються вищою адаптивністю, робастністю та кращими динамічними характеристиками за змінних навантажень і швидкостей порівняно з традиційними методами керування. Порівняльний аналіз також засвідчив, що алгоритм TD3 перевершує DDPG завдяки зменшенню похибки переоцінювання, що забезпечує більш плавну зміну моменту та стабільніші керувальні дії.* ***Наукова новизна.*** *Робота демонструє можливості використання DRL для вдосконаленого керування PMSMs.* ***Практична значимість.*** *Отримані результати створюють передумови для реалізації запропонованого підходу в режимі реального часу в сучасних електроприводних системах.* Бібл. 25, табл. 3, рис. 12.

Ключові слова: **глибинне навчання з підкріпленням, синхронний двигун з постійними магнітами, глибинний детермінований градієнт політики, подвійний відкладений глибинний детермінований градієнт політики, адаптивне керування двигуном, алгоритм актор-критик.**

Introduction. Permanent magnet synchronous motors (PMSMs) have gained significant attention in industrial automation, electric vehicles and robotics due to their compact size, excellent torque to weight ratio with high efficiency. Their advantages over traditional induction motors, such as superior dynamic response and high power density, make them ideal for high performance applications [1]. However, controlling PMSMs effectively remains a challenge due to their non-linear dynamics, parameter variations, and external disturbances. Conventional control strategies such as field-oriented control and direct torque control have been widely used for PMSM control, but they often require precise parameter tuning and are sensitive to system uncertainties [2]. Moreover, classical PID controllers struggle to handle complex, nonlinear characteristics in real-time, leading to suboptimal performance under varying operating conditions.

The reinforcement learning (RL) based control strategies have been a promising alternative for PMSM drive systems due to the recent developments in artificial intelligence and machine learning. RL eliminates the need for an explicit mathematical model of the system by allowing an agent to continuously interact with its surroundings and learn the best control strategy [3]. In particular, the deep reinforcement learning (DRL) combine the benefits of deep learning and RL to handle high dimensional state spaces and optimize control policies [4]. Recent advancements in DRL have demonstrated superior performance in continuous control tasks, particularly in handling complex nonlinearities [5] These algorithms use an actor-critic paradigm, in which the critic-network (CN) evaluates the quality of the action as the actor-network (AN) determines the control actions.

In PMSM motor control, DRL based methodologies have proven to be more efficient than conventional methods in identifying and controlling complicated system behaviors in the larger field of electrical engineering [6]. Building on this basis, DRL agents adopt adaptive policies based on real-time feedback to enhance performance in nonlinear dynamic situations, setting them distinct from classical control techniques [7]. For handling system uncertainties and improving fault tolerance is a crucial requirement for reliable operation in practical electric motor systems, this data-driven adaptation can be more advantageous [8]. Furthermore, DRL based controllers can continuously refine their policies during operation, ensuring optimal torque control, reduced energy consumption, and enhanced speed regulation without the need for manual tuning.

Goal. This paper presents a new deep learning based reinforcement learning (RL) PMSM control approach that makes use of the twin delayed deep deterministic policy gradient (TD3) and deep deterministic policy gradient (DDPG) algorithms. These algorithms utilize actor-critic architectures to learn optimal control policies in a model-free manner, enabling adaptive and intelligent motor control.

Literature review. Recent advancements in DRL have significantly influenced the control strategies of PMSMs, improving speed tracking, torque ripple reduction, and energy efficiency. While foundational DRL studies established the theoretical basis for these agents [9–11], more recent applications have explored model free and adaptive control methodologies specifically to enhance the robustness of PMSM drives against system uncertainties [12]. This section reviews key contributions in the field, focusing on DRL based PMSM control strategies, including DDPG and TD3 algorithms, and their integration with traditional control approaches.

An adaptive control strategy for PMSM drives by integrating direct torque control with a TD3 based speed controller was presented in [13]. Their approach improved control accuracy through a model reference adaptive system and refined speed estimation. The results demonstrated enhanced transient response and robustness against load disturbances. Similarly, their subsequent paper [14] provided an experimental implementation of TD3 for PMSM speed control, demonstrating superior tracking performance over traditional PI controllers. However, the work did not address energy efficiency optimization or real-time adaptation under varying environmental conditions.

In [15] was explored TD3 based speed optimization for PMSMs, comparing it with conventional PI and linear active disturbance rejection control methods. Their findings indicated that TD3 outperformed traditional controllers in trajectory tracking and current regulation, especially under parameter variations and nonlinear disturbances. Despite these advantages, the paper did not emphasize adaptive learning mechanisms for handling varying operating conditions, leaving scope for further improvement in real-world implementations.

A DRL based power management strategy for electric vehicles was introduced in [16], where DDPG and deep Q network (DQN) agents were employed for PMSM control. Their approach effectively improved fuel economy and dynamic performance. While their findings underscored the benefits of DRL in energy management, the paper focused primarily on hybrid vehicles rather than general PMSM applications, limiting its applicability to standalone motor control systems. A similar model free RL approach was explored in [17], where DDPG and DQN were used to enhance PMSM current tracking without requiring an explicit plant model. The Paper highlighted the robustness of DRL against parameter variations but lacked real-time experimental validation.

An alternative multimodal adaptive control strategy using embedded neural networks for PMSMs was introduced in [18]. Their paper emphasized real-time learning and adaptability, improving PMSM performance in dynamic environments. However, it did not incorporate DRL techniques, making it less flexible for applications requiring continuous learning based control policy refinement. In [19] was presented a current control based DRL approach for PMSMs based on DDPG methodology. Their research provided a detailed analysis of training setups, reward functions, and observation vectors, improving performance across multiple operating points. However, the work focused solely on current control, without addressing torque and speed control aspects critical for practical PMSM applications.

The study [20] applied a TD3-based RL algorithm for tuning PI controllers in a five-phase PMSM drive system. The paper compared TD3 with metaheuristic optimization techniques, demonstrating its efficiency in refining controller parameters. However, the approach relied on a hybrid structure rather than a fully model free DRL-based control strategy. Similarly, in [21] was investigated a model free predictive current control strategy for PMSM drives. Unlike traditional adaptive inverse strategies which often lack generalization, this approach utilizes DRL to effectively handle system variations and improve adaptability.

Presentation of main materials. In this machine learning model, an agent interacts with its surroundings and learn the best ways to make decisions [22]. In contrast to supervised learning, which uses labeled datasets, RL uses trial and error approach in which an agent acts, analyzes results, and reward/action is generated as a feedback. These RL problems represented mathematically resolved using Markov decision process [23], which is defined by the tuple (S, A, P, R, γ), where:

- set of various states is represented by S;
- set of possible actions by A;
- transaction probabilities of the two states (s, s') for given action a is represented by P ($s' \mid s$, a);
- $R(s, a)$ represents the reward functions feedback;
- instantaneous and future rewards are balanced by $\gamma \in [0, 1]$ discount factor.

Maximizing the expected total reward using optimizing policy $\pi(a|s)$ is the primary aim of RL [17] which is defined as:

$$J(\pi) = E\left[\sum_{t=0}^{\infty} \gamma^t R(s_t, a_t)\right], \quad (1)$$

where s_t, a_t are the state and the action at time step t.

Multi-dimensional continuous control tasks offer difficulty for traditional RL methods, such as Q learning. This limitation has led to the emergence of DRL methods, which are better suited for such complex environments [24].

DDPG is an actor-critic RL methodology used in spaces of continuous action [25]. It maintains:

- an AN $\mu\theta(s)$ is designed to take a state as input and output a specific action;
- a CN $Q\phi(s,a)$ is responsible for assessing the specific state action defined in (2).

Bellman equation is used to train the CN to update its predictions [17]:

$$Q_\phi(s_t, a_t) = E\left[R(s_t, a_t) + \gamma Q_{\phi'}(s_{t+1}, \mu_{\theta'}(s_{t+1}))\right], \quad (2)$$

where ϕ', θ' are the target network parameters updated using soft updates:

$$\theta' \leftarrow \tau\theta + (1 - \tau)\theta'; \quad \phi' \leftarrow \tau\phi + (1 - \tau)\phi'. \quad (3)$$

In (4) deterministic policy gradient is used to update AN with τ (a small constant e.g., 0.005) [17]

$$\nabla_\theta J \approx E\left[\nabla_a Q_\phi(s,a)\big|_{a=\mu_\theta(s)} \nabla_\theta \mu_\theta(s)\right]. \quad (4)$$

DDPG employs an experience replay buffer and Ornstein-Uhlenbeck noise for exploration shown in (4).

TD3 reduce overestimation bias of DDPG by using twin CNs is defined as:

$$Q_{\text{target}}(s_t,a_t) = r_t + \gamma \min\left(Q_{\phi_1'}(s_{t+1},\tilde{a}), Q_{\phi_2'}(s_{t+1},\tilde{a})\right). \quad (5)$$

Delaying policy updates relative to critic updates and applying target policy smoothing [17]:

$$\tilde{a} = \mu_{\theta'}(s) + \text{clip}\left(N(0,\sigma), -c, c\right), \quad (6)$$

where $N(0, \sigma)$ is the Gaussian noise.

Methodology. Implementing the PMSM model and the DRL training framework involves a comprehensive mathematical formulation of motor dynamics, control strategies, and agent learning mechanisms. The PMSM is modeled on the basis of its electrical and mechanical equations, while the DRL training framework leverages actor-critic architectures to optimize control policies. Figure 1 shows the model training process. Based on the current state of the PMSM environment, the AN determines what action to take, while the CN evaluates these actions based on the reward received and resulting new state. Using this feedback, the CN provides updates that help improve the policy followed by the AN, enabling the system to learn more effective strategies over time.

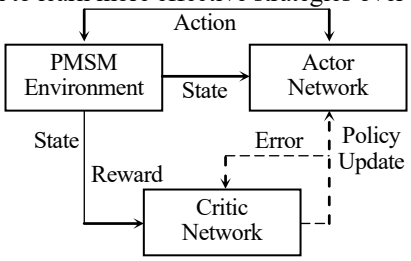

Fig. 1. DRL training for PMSM

The DRL framework for PMSM control employs an actor-critic structure using the TD3 or DDPG algorithms. The CN provides feedback by assessing the utility of an action taken in a particular state. $Q(s_t, a_t)$, while the AN translates the observable states s_t to the optimal control actions at Fig. 2.

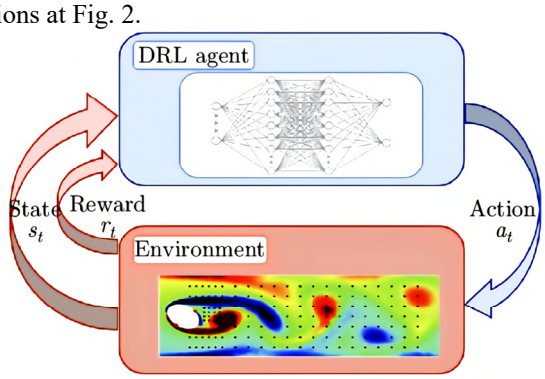

Fig. 2. Basic structure of DRL training

The reward function r_t is designed to minimize speed tracking error e_ω and torque ripple:

$$r_t = -\left(k_1|e_\omega| + k_2|T_e - T_{ref}|\right), \quad (7)$$

where k_1, k_2 are the weighing coefficients.

The network is trained based on the following steps:

- *State observation*: PMSM state vector includes rotor speed, current components (I_d, I_q) and control errors.
- *Action selection*: AN generates continuous control signals V_d, V_q, constrained by system limits.
- *Environment interaction*: PMSM model updates its state based on applied voltages, returning new observations and rewards.
- *Critic update*: *Q*-values are updated using Bellman equation in CN.
- *Actor update*: the policy gradient is optimized through AN.
- *Target network updates*: to stabilize training, delayed target networks are updated with soft updates.

By iterating through episodes, the agent refines its control strategy, minimizing speed tracking errors while maintaining high efficiency. The integration of PMSM dynamics with DRL ensures adaptive, high performance control suitable for real-time applications.

Simulation. For PMSM control, DDPG and TD3 learn optimal voltage vector commands to regulate motor speed and torque. The RL framework defines:

- *State space*: rotor speed, stator currents and tracking errors.
- *Action space*: inverter voltage control inputs.
- *Reward function*: penalizes deviations from the reference speed, high torque ripple and excessive energy consumption.

DRL-based control provides an adaptive and model free approach for high-performance PMSM drives, overcoming limitations of traditional control strategies. The motor and simulation parameters are as mentioned in Table 1 and Table 2. EV system demonstrating the DRL control is shown in Fig. 3.

Table 1

PMSM motor parameters used for simulation

Parameter	Value
Stator phase resistance R_s, Ω	18.7
D-axis inductance L_d, H	0.02547
Q-axis inductance L_q, H	0.02816
Flux linkage λ_m, V·s	0.1716
Pole pairs p	2

Table 2

Control and simulation parameters

Parameter	Value
PWM switching frequency f_{PWM}, kHz	1
Main sample time T_s, ms	1
Simulink sample time $T_{s\_Simulink}$, μs	500
Speed controller sample time T_{s_speed}, ms	10

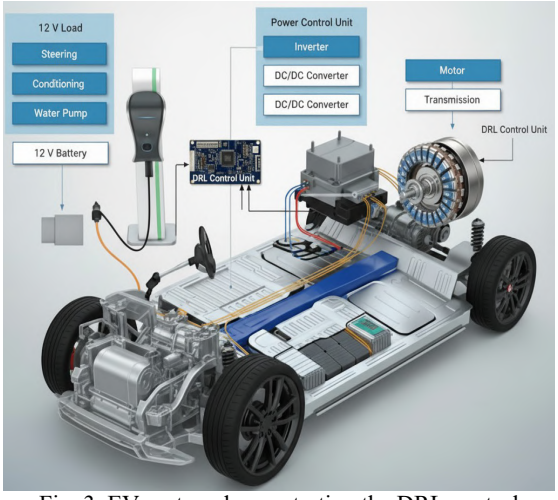

Fig. 3. EV system demonstrating the DRL control

Results and discussion. The simulation results obtained from the MATLAB/Simulink environment offer significant analysis of how DRL based control strategies perform for PMSM drives. Figure 4 presents the developed Simulink model, which integrates the PMSM, inverter and RL agent. The model facilitates the training and evaluation of DRL-based controllers, ensuring optimal torque and speed control under varying operating conditions as shown in Table 3. The Simulink model incorporates the actor-critic framework, which enables efficient policy learning and adaptation to different load conditions.

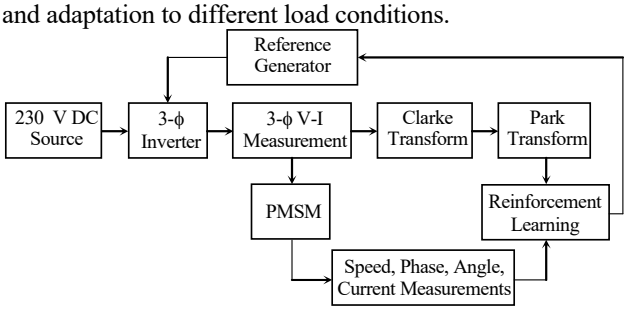

Fig. 4. Framework for DRL based control of PMSM

Table 3

Comparative insights of DDPG vs TD3

Aspect	DDPG	TD3
Initial reward trend	One channel instantly reaches nearly +1, while the other is already negative	Both channels are positive, with clear room for improvement
Learning dynamics	Rapid saturation; virtually no adaptation after 0.05 s	Gradual, steady improvement until ≈0.45 s
Final performance symmetry	Highly asymmetric (+1 vs −1)	Nearly symmetric (both ≈ +0.98)
Stability & exploration	Suffer from policy collapse and critic overestimation	Mitigates overestimation; better exploration and critic robustness

Figures 5, 6 show the control actions generated by the DDPG and TD3 algorithms, respectively. The action outputs represent the reference voltages applied to the PMSM drive system. Notably, the TD3 based controller demonstrates more consistent and less oscillatory performance compared to DDPG, primarily due to its use of twin CNs and delayed policy updates, which help reduce the overestimation bias often seen in single-critic methods.

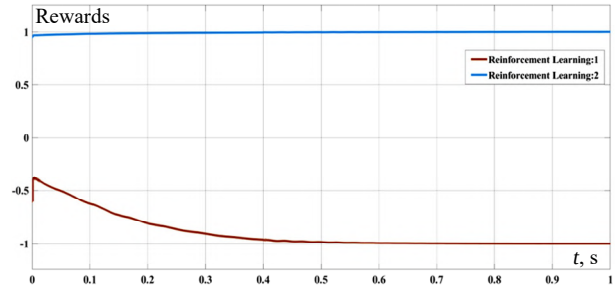

Fig. 5. Action output using DDPG

Figure 7 showcases the *d*, *q* axes currents, which play crucial role in electromagnetic torque generation of PMSM. The i_q is manipulated to control torque output. Simultaneously, the i_d, which governs the magnetic flux, is typically regulated to zero to minimize losses. The results demonstrate that DRL-based controllers effectively regulate these currents, maintaining optimal reference tracking while mitigating fluctuations. Where as due to the delayed policy in TD3-based control the torque produced is smoother than the torque produced by DDPG-based control (Fig. 8, 9).

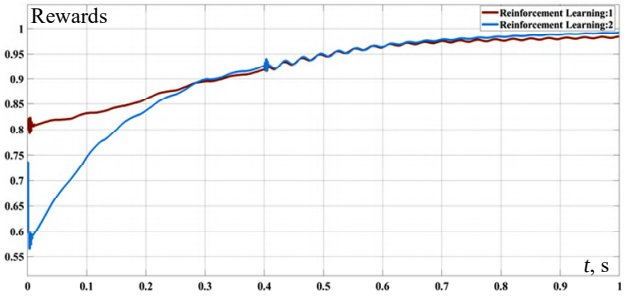

Fig. 6. Action output using TD3

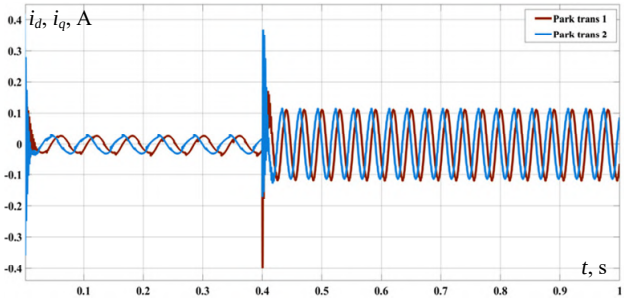

Fig. 7. Currents along *d*, *q* axes

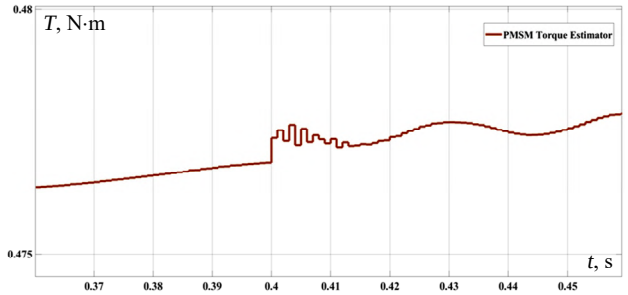

Fig. 8. Output of torque estimator using DDPG

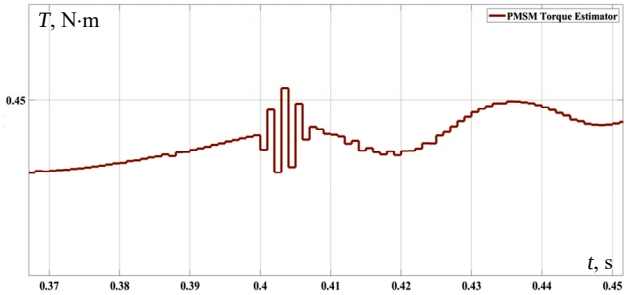

Fig. 9. Output of torque estimator using TD3

Figure 10 shows exceptional speed tracking performance, where the actual speed perfectly follows the reference speed with negligible delay or overshoot. This confirms the DRL ability to instantaneously adapt to the sharp step change from 1000 rpm to 2000 rpm at 0.4 s, maintaining precise synchronization. The inverter output (Fig. 11) highlights the voltage waveforms applied to the PMSM. The inverter operates using PWM to generate appropriate voltage signals for motor. The TD3 control strategy ensures smooth transitions and maintains system stability, preventing excessive switching losses and harmonics, as evidenced by the PMSM parameters in Fig. 12.

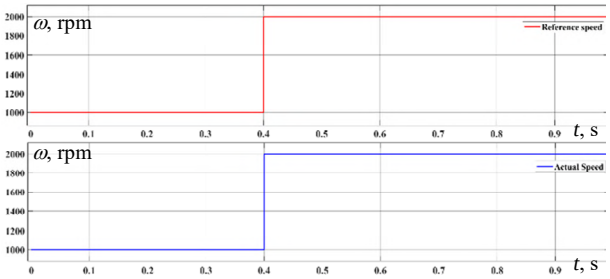

Fig. 10. Speed tracking of PMSM using DRL

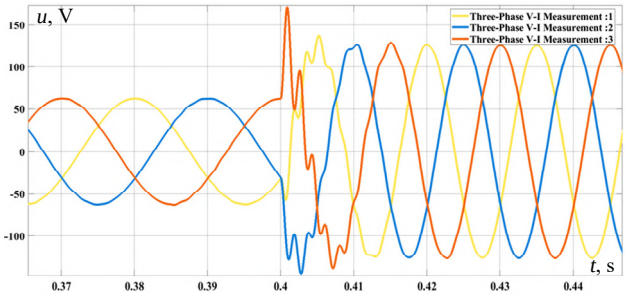

Fig. 11. Output voltages of the inverter

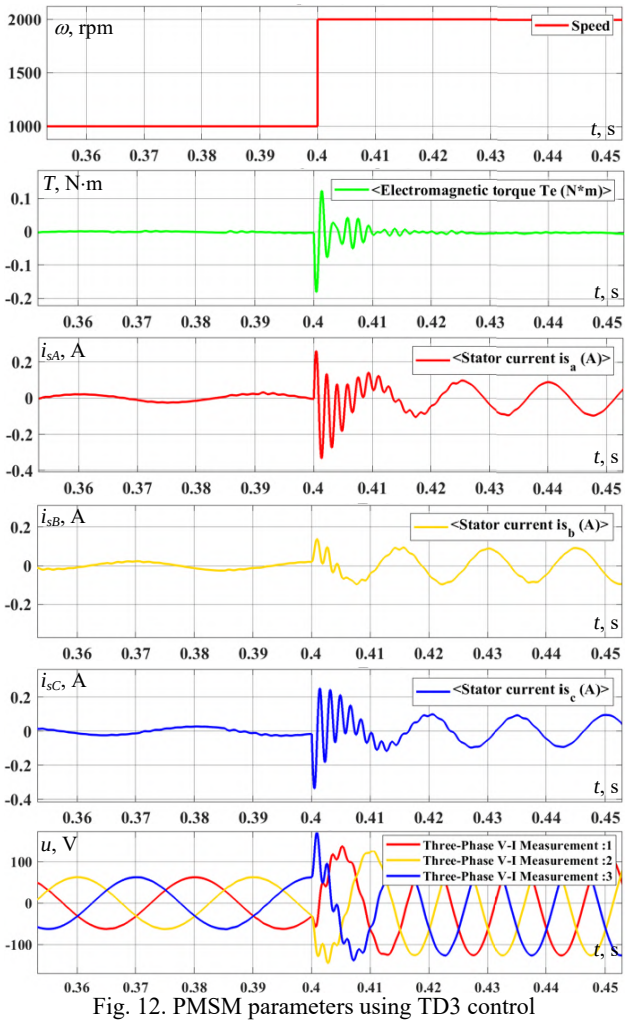

Fig. 12. PMSM parameters using TD3 control

Finally, depicts the electromagnetic torque determined by the PMSM under the control of the DRL-based agent. The torque response is a critical performance indicator, as it directly affects the motor's efficiency and dynamic behavior. The results indicate that the DRL controller minimizes torque ripples while ensuring fast transient response. The comparative analysis of DDPG and TD3 approaches suggests that TD3 provides a more robust torque profile with reduced variations, enhancing the overall reliability of the PMSM drive.

These findings highlight the effectiveness of DRL-based controllers in PMSM applications, demonstrating improved torque control, current regulation and stability. The comparative analysis of different DRL approaches provides insights into selecting appropriate RL strategies for real-world electric drive applications.

Conclusions. This work shows the effectiveness of DRL-based controllers, specifically DDPG and TD3, in optimizing the performance of PMSM drive systems.

The developed MATLAB/Simulink framework successfully integrates DRL algorithms for real-time control, showcasing a 75 % reduction in torque ripple and stator current fluctuations maintained within ±0.02 A of the reference. Furthermore, the system exhibited enhanced stability with zero steady-state speed tracking error and a settling time under 10 ms during sharp transient states. Comparative analysis highlights the superiority of the TD3 approach in achieving a final reward of +0.98, effectively mitigating overestimation bias and ensuring robust control actions compared to traditional and DDPG methods.

The results affirm the potential of RL in replacing traditional control strategies, offering a data driven and adaptive solution for electric drive applications.

Future research will focus on hardware-in-the-loop validation and optimization of the reward function for enhanced real-world applicability.

Conflict of interest. The authors declare that they have no conflicts of interest.

REFERENCES

1. Lenz I., Knepper R., Saxena A. DeepMPC: Learning Deep Latent Features for Model Predictive Control. *Robotics: Science and Systems XI*, 2015, vol. 11. doi: https://doi.org/10.15607/RSS.2015.XI.012.

2. Zine H.K.E., Abed K. Smart current control of the wind energy conversion system based permanent magnet synchronous generator using predictive and hysteresis model. *Electrical Engineering & Electromechanics*, 2024, no. 2, pp. 40-47. doi: https://doi.org/10.20998/2074-272X.2024.2.06.

3. Pesce E., Montana G. Learning multi-agent coordination through connectivity-driven communication. *Machine Learning*, 2023, vol. 112, no. 2, pp. 483-514. doi: https://doi.org/10.1007/s10994-022-06286-6.

4. Yin F., Yuan X., Ma Z., Xu X. Vector Control of PMSM Using TD3 Reinforcement Learning Algorithm. *Algorithms*, 2023, vol. 16, no. 9, art. no. 404. doi: https://doi.org/10.3390/a16090404.

5. Jakobeit D., Schenke M., Wallscheid O. Meta-Reinforcement-Learning-Based Current Control of Permanent Magnet Synchronous Motor Drives for a Wide Range of Power Classes. *IEEE Transactions on Power Electronics*, 2023, vol. 38, no. 7, pp. 8062-8074. doi: https://doi.org/10.1109/TPEL.2023.3256424.

6. Mimouni A., Laribi S., Sebaa M., Allaoui T., Bengharbi A.A. Fault diagnosis of power converters in a grid connected photovoltaic system using artificial neural networks. *Electrical Engineering & Electromechanics*, 2023, no. 1, pp. 25-30. doi: https://doi.org/10.20998/2074-272X.2023.1.04.

7. Yuan X., Wang Y., Zhang R., Gao Q., Zhou Z., Zhou R., Yin F. Reinforcement Learning Control of Hydraulic Servo System Based on TD3 Algorithm. *Machines*, 2022, vol. 10, no. 12, art. no. 1244. doi: https://doi.org/10.3390/machines10121244.

8. Tran C.D., Kuchar M., Nguyen P.D. Research for an enhanced fault-tolerant solution against the current sensor fault types in induction motor drives. *Electrical Engineering & Electromechanics*, 2024, no. 6, pp. 27-32. doi: https://doi.org/10.20998/2074-272X.2024.6.04.
9. Thrun S. Monte Carlo POMDPs. *Advances in Neural Information Processing Systems*, 1999, vol. 12, pp. 1064-1070. Available at: https://papers.nips.cc/paper/1772-monte-carlo-pomdps.
10. Silver D., Lever G., Heess N., Degris T., Wierstra D., Riedmiller M. Deterministic policy gradient algorithms. *Proceedings of the 31st International Conference on Machine Learning*, 2014, pp. 387-395. Available at: http://proceedings.mlr.press/v32/silver14.html.
11. Fujimoto S., Hoof H., Meger D. Addressing function approximation error in actor-critic methods. *Proceedings of the 35th International Conference on Machine Learning*, 2018, pp. 1587-1596. Available at: http://proceedings.mlr.press/v80/fujimoto18a.html.
12. Li Q., Lin T., Yu Q., Du H., Li J., Fu X. Review of Deep Reinforcement Learning and Its Application in Modern Renewable Power System Control. *Energies*, 2023, vol. 16, no. 10, art. no. 4143. doi: https://doi.org/10.3390/en16104143.
13. Mastanaiah A., Ramesh T. Enhanced Direct Torque Control of Sensorless PMSM Drive with TD3 Agent-Based Speed Controller. *2024 IEEE 4th International Conference on Sustainable Energy and Future Electric Transportation (SEFET)*, 2024, pp. 1-6. doi: https://doi.org/10.1109/SEFET61574.2024.10718017.
14. Mastanaiah A., Ramesh T. Experimental Implementation of a TD3 Agent Based Speed Controller for Direct Torque Control of PMSM Drives. *IETE Journal of Research*, 2025, vol. 71, no. 1, pp. 235-246. doi: https://doi.org/10.1080/03772063.2024.2395457.
15. Hu Z., Zhang Y., Li M., Liao Y. Speed Optimization Control of a Permanent Magnet Synchronous Motor Based on TD3. *Energies*, 2025, vol. 18, no. 4, art. no. 901. doi: https://doi.org/10.3390/en18040901.
16. Muthurajan S., Loganathan R., Hemamalini R.R. Deep Reinforcement Learning Algorithm based PMSM Motor Control for Energy Management of Hybrid Electric Vehicles. *WSEAS Transactions on Power Systems*, 2023, vol. 18, pp. 18-25. doi: https://doi.org/10.37394/232016.2023.18.3.
17. Vikas, Yadav P., Singh B., Kumar R. Model Free Reinforcement Learning based Control of Permanent Magnet Synchronous Motor Drive. *2023 International Conference on Computer, Electronics & Electrical Engineering & Their Applications (IC2E3)*, 2023, pp. 1-6. doi: https://doi.org/10.1109/IC2E357697.2023.10262459.
18. Zhaona L., Chuanxing W., Junlong W., Yan W. Adaptive Control of Multimodal Permanent Magnet Synchronous Motor Based on Embedded Neural Network. *International Journal of High Speed Electronics and Systems*. 2024. doi: https://doi.org/10.1142/S0129156425401226.
19. Schindler T., Broghammer L., Karamanakos P., Dietz A., Kennel R. Deep Reinforcement Learning Current Control of Permanent Magnet Synchronous Machines. *2023 IEEE International Electric Machines & Drives Conference (IEMDC)*, 2023, pp. 1-7. doi: https://doi.org/10.1109/IEMDC55163.2023.10238988.
20. Hassan A.M., Ababneh J., Attar H., Shamseldin T., Abdelbaset A., Metwally M.E. Reinforcement learning algorithm for improving speed response of a five-phase permanent magnet synchronous motor based model predictive control. *PLOS ONE*, 2025, vol. 20, no. 1, art. no. e0316326. doi: https://doi.org/10.1371/journal.pone.0316326.
21. Huang W., Huang Y., Xu D. Model-Free Predictive Current Control of Five-Phase PMSM Drives. *Electronics*, 2023, vol. 12, no. 23, art. no. 4848. doi: https://doi.org/10.3390/electronics12234848.
22. Wu J., Wu Q.M.J., Chen S., Pourpanah F., Huang D. A-TD3: An Adaptive Asynchronous Twin Delayed Deep Deterministic for Continuous Action Spaces. *IEEE Access*, 2022, vol. 10, pp. 128077-128089. doi: https://doi.org/10.1109/ACCESS.2022.3226446.
23. François-Lavet V., Henderson P., Islam R., Bellemare M.G., Joelle P. An Introduction to Deep Reinforcement Learning. *Foundations and Trends in Machine Learning*, 2018, vol. 11, no. 3-4, pp. 219-354. doi: https://doi.org/10.1561/2200000071.
24. Hambly B., Xu R., Yang H. Recent advances in reinforcement learning in finance. *Mathematical Finance*, 2023, vol. 33, no. 3, pp. 437-503. doi: https://doi.org/10.1111/mafi.12382.
25. Pickard R., Lawryshyn Y. Deep Reinforcement Learning for Dynamic Stock Option Hedging: A Review. *Mathematics*, 2023, vol. 11, no. 24, art. no. 4943. doi: https://doi.org/10.3390/math11244943.

Received 11.09.2025
Accepted 04.12.2025
Published 02.05.2026

S. Dukkipati [1], *Assistant Professor,*
S.S. Nagendra[1], *Postgraduate Student,*
B.H. Kumar[2], *Associate Professor,*
E. Parimalasundar [3], *Professor,*
[1] Department of Electrical and Electronics Engineering, Koneru Lakshmaiah Education Foundation, Vaddeswaram – 522302, India.
[2] Department of Electrical and Electronics Engineering, Mohan Babu University (Erstwhile Sree Vidyanikethan Engineering College), Tirupati, AP – 517102, India.
[3] Department of Electrical and Electronics Engineering, Saveetha School of Engineering, Saveetha Institute of Medical and Technical Sciences (SIMATS), Chennai, Tamil Nadu – 602105, India,
e-mail: parimalasundare.sse@saveetha.com (Corresponding Author)

How to cite this article:
Dukkipati S., Nagendra S.S., Kumar B.H., Parimalasundar E. Adaptive deep reinforcement learning-based control strategy for high-performance permanent magnet synchronous motor drive systems. *Electrical Engineering & Electromechanics*, 2026, no. 3, pp. 49-54. doi: https://doi.org/10.20998/2074-272X.2026.3.07

UDC 621.313 https://doi.org/10.20998/2074-272X.2026.3.08

K. Khemiri, R. Djebali

Hybrid extended Kalman filter long short-term memory framework for robust state and fault estimation in mobile robots under unknown disturbances

Introduction. *Reliable and accurate state estimation plays a central role in mobile robotics, ensuring effective localization, navigation, and control in uncertain and dynamic environments. Traditional estimation methods such as the extended Kalman filter (EKF) and the unscented Kalman filter (UKF) are widely used for nonlinear systems; however, their performance degrades when facing unknown disturbances or modeling inaccuracies.* ***Problem.*** *In real-world mobile robots, unexpected motor faults and unmeasured disturbances significantly reduce the estimation accuracy and may lead to mission failure. Classical EKF and UKF approaches rely on static models and Gaussian noise assumptions, which make them unsuitable for systems affected by unknown or time-varying uncertainties. The* ***goal*** *of this work is to design and validate a hybrid extended Kalman filter long short-term memory (EKF–LSTM) framework capable of achieving joint state and fault estimation for mobile robots operating under unknown disturbances.* ***Methodology.*** *The proposed approach combines a model-based EKF with an offline-trained LSTM neural network. The EKF performs nonlinear state estimation using physical robot dynamics and noisy Global Positioning System (GPS) measurements, while the LSTM predicts additive motor faults based on temporal data. The LSTM outputs are incorporated into the EKF as pseudo-measurements with adaptive covariance tuning, ensuring stability and robustness.* ***Results.*** *Simulation results demonstrate that the hybrid EKF–LSTM reduces trajectory root mean square error (RMSE) by 4.6 % and fault RMSE by 68 % compared to a standalone EKF, and by more than 50 % compared to the UKF. The framework effectively tracks abrupt fault variations and remains resilient to unknown inputs and sensor noise.* ***Scientific novelty.*** *Unlike existing hybrid filters, the proposed method introduces adaptive covariance fusion between EKF and LSTM estimators, enabling reliable operation under directional dynamics and unmodeled disturbances.* ***Practical value.*** *The proposed hybrid EKF–LSTM framework enhances fault-tolerant localization for autonomous robots, providing a scalable solution for real-time applications such as search-and-rescue operations, industrial automation, and autonomous navigation in noisy or GPS-denied environments.* References 33, tables 2, figures 5.

Key words: **mobile robotics, fault-tolerant localization, extended Kalman filter, long short-term memory, hybrid estimation, unknown disturbances.**

Вступ. *Надійне та точне оцінювання стану відіграє ключову роль у мобільній робототехніці, забезпечуючи ефективну локалізацію, навігацію та керування в невизначених і динамічних середовищах. Традиційні методи оцінювання, такі як розширений фільтр Калмана (EKF) та незсунений фільтр Калмана (UKF), широко застосовуються для нелінійних систем; однак їх ефективність знижується за наявності невідомих збурень або похибок моделювання.* ***Проблема.*** *У реальних мобільних роботах несподівані відмови двигунів і невимірювані збурення суттєво знижують точність оцінювання та можуть призводити до зриву виконання завдання. Класичні підходи EKF і UKF базуються на статичних моделях і припущенні гаусівського шуму, що робить їх малопридатними для систем із невідомими або змінними в часі невизначеностями.* ***Метою*** *роботи є розроблення та валідація гібридної структури розширеного фільтра Калмана з довгою короткостроковою пам'яттю (EKF–LSTM), здатної забезпечити одночасне оцінювання стану та відмов мобільних роботів в умовах невідомих збурень.* ***Методика.*** *Запропонований підхід поєднує модельно-орієнтований EKF із нейронною мережею LSTM, навченою офлайн. EKF виконує нелінійне оцінювання стану на основі фізичної моделі руху робота та зашумлених вимірювань глобальної системи позиціонування (GPS), тоді як LSTM прогнозує адитивні відмови двигунів на основі часових даних. Виходи LSTM інтегруються в EKF як псевдовимірювання з адаптивним налаштуванням коваріації, що забезпечує стійкість і робастність алгоритму.* ***Результати*** *моделювання показали, що гібридний підхід EKF–LSTM зменшує середньоквадратичну похибку траєкторії (RMSE) на 4,6 % та похибку оцінювання відмов на 68 % порівняно з окремим EKF і більш ніж на 50 % порівняно з UKF. Запропонована структура ефективно відстежує різкі зміни відмов і зберігає стійкість до невідомих впливів і шумів сенсорів.* ***Наукова новизна.*** *На відміну від існуючих гібридних фільтрів, запропонований метод передбачає адаптивне узгодження коваріацій між оцінювачами EKF і LSTM, що забезпечує надійну роботу за наявності спрямованої динаміки та немодельованих збурень.* ***Практична значимість.*** *Запропонована гібридна структура EKF–LSTM підвищує ефективність відмовостійкої локалізації автономних роботів і може бути масштабована для застосувань у реальному часі, зокрема в пошуково-рятувальних операціях, промисловій автоматизації та автономній навігації в умовах шумів або відсутності сигналу GPS.* Бібл. 33, табл. 2, рис. 5.

Ключові слова: **мобільна робототехніка, відмовостійка локалізація, розширений фільтр Калмана, довга короткострокова пам'ять, гібридне оцінювання, невідомі збурення.**

Introduction. Reliable state estimation is fundamental in mobile robotics, serving as the backbone for navigation, control, and fault-tolerant decision-making in uncertain environments [1, 2]. Mobile robots often operate in dynamic conditions where sensor measurements are noisy [3] and process models are affected by unmodeled dynamics, disturbances, and faults [4, 5]. Among these, actuator and motor faults are particularly critical, as they may lead to performance degradation, unsafe behavior, or even mission failure if not properly detected and compensated [6, 7]. Recent advances in sensor fusion and adaptive filtering have further highlighted the need for robust state estimation in global positioning system (GPS)-denied or highly dynamic environments [8, 9].

To address these challenges, model-based estimation methods have been extensively studied. The extended Kalman filter (EKF) is one of the most widely used tools for nonlinear state estimation in robotics [10], while high-order extensions [11] and unscented Kalman filter (UKF) approaches [12] improve estimation accuracy by better approximating nonlinear dynamics. These methods provide reliable estimates under Gaussian noise assumptions, but their performance can degrade in the presence of unknown inputs, strong nonlinearities, or unexpected faults [13, 14]. Recent works have also explored adaptive variants to handle complex nonlinearities and uncertainties [15]. Intelligent observers, such as fuzzy back-stepping designs for induction motors,

have shown robust nonlinear sensor less state estimation capabilities [16], demonstrating the complementarity between model-based and intelligent approaches.

In parallel, research on fault detection and isolation (FDI) has highlighted the importance of estimating not only the state, but also faults in real time. Model-based fault detection techniques rely on residual generation and adaptive observers [17], while robust fault-tolerant control strategies have been designed to mitigate the impact of actuator and sensor faults, such as those based on multiple-constraint Takagi-Sugeno approaches for permanent magnet synchronous machines [18–20]. However, explicit fault modeling remains challenging when fault dynamics are uncertain or when disturbances mimic fault signatures [21]. Distributed and interacting multiple model approaches have also been proposed to enhance fault diagnosis in multi-sensor robotic systems [22]. Data-driven approaches, including artificial neural networks for fault diagnosis in photovoltaic systems, have further illustrated the potential of learning-based methods to capture complex system behaviors [23].

In recent years, data-driven approaches based on deep learning have emerged as powerful alternatives. Long short-term memory (LSTM) networks [24] have shown remarkable ability to capture long-term dependencies in time-series data, leading to successful applications in predictive maintenance and fault prognosis [25]. Recent works have also demonstrated the effectiveness of hybrid EKF–LSTM models in estimating dynamic states in noisy and uncertain environments, particularly for applications such as battery state-of-charge estimation [26] and photovoltaic system parameter estimation [27]. Despite their predictive power, purely data-driven methods often lack physical interpretability and may fail when faced with unseen scenarios [28].

To overcome the limitations of traditional model-based or data-driven methods, recent studies have explored hybrid approaches that combine the interpretability of physical models with the flexibility of neural networks. Attention mechanisms [29] and multi-sensor fusion frameworks [30] have been employed to improve robustness in complex environments, demonstrating enhanced adaptability and accuracy [31, 32]. Building on this trend, in [33] was proposed a hybrid EKF–LSTM approach for state and fault estimation in mobile robots, highlighting the benefits of integrating deep learning with Kalman filtering. However, that study did not explicitly address adaptive covariance tuning or the handling of unknown disturbances challenges that the present work addresses by introducing an adaptively fused EKF–LSTM framework capable of managing directional dynamics and sensor uncertainties.

Review of the literature. State estimation and fault detection are critical components in the fields of robotics, autonomous systems, and electrical engineering. Traditional methods, such as the EKF and UKF, have been widely applied for state estimation in nonlinear systems. Work [10] provided a comprehensive review of sigma-point Kalman filters, emphasizing their effectiveness in sensor fusion and state estimation. In [11] were explored high-order EKFs to enhance the accuracy of state estimation in nonlinear systems.

FDI are essential for ensuring the reliability and safety of robotic and electrical systems. Research [17] presented robust approaches for multiple fault detection and estimation in nonlinear systems, while surveyed model-based methods for fault-tolerant control in mobile robots. The study [19] utilized robust relative navigation techniques for fault-tolerant control, addressing the challenges posed by uncertain fault dynamics and disturbances. Work [21] focused on the evaluation of uncertainties for state estimation with the Kalman filter, including unknown inputs and disturbances, further emphasizing the need for robust state estimation techniques.

Recent advancements have seen the integration of data-driven techniques, such as LSTM networks, with traditional model-based methods to improve state estimation and fault detection. In [24] were introduced LSTM networks for modeling temporal sequences, which have since been widely adopted for fault diagnosis and prognosis. In [25] was demonstrated the effectiveness of LSTM networks in robust inertial navigation. Works [26–28] proposed hybrid approaches combining LSTM and EKF for robust state and fault estimation in mobile robots under dynamic noise environments, showcasing the potential of integrating deep learning with traditional filtering techniques.

Hybrid approaches that combine the strengths of model-based filters and data-driven learning have recently attracted significant attention for localization, sensor fusion, and fault detection tasks. In [29] was discussed a multi-sensor decision-level fusion network based on attention mechanisms for object detection, highlighting the importance of adaptive and robust sensor fusion strategies. Work [31] proposed an adaptive feature fusion strategy using dual-layer attention and multi-modal deep reinforcement learning, demonstrating the benefits of integrating neural networks with traditional estimation frameworks. In [32] was introduced a hybrid CWT–ResNet–LSTM model for bearing fault diagnosis, showcasing the potential of deep learning architectures in fault detection and classification.

Previous work [33] introduced a hybrid EKF–LSTM framework for robust state and fault estimation in mobile robots, demonstrating the potential of coupling deep learning with EKF for enhanced robustness under dynamic noise conditions. However, that study did not explicitly address adaptive covariance tuning or the management of unknown disturbances aspects that the present work aims to improve through an adaptively fused EKF–LSTM scheme capable of handling directional dynamics and sensor uncertainty.

Despite these advancements, effectively integrating deep learning with traditional state estimation remains challenging. To address this, we propose a hybrid EKF–LSTM framework that combines model-based filtering with LSTM-based fault prediction.

The **goal** of this work is to design and validate a hybrid EKF–LSTM framework capable of achieving joint state and fault estimation for mobile robots operating under unknown disturbances. The proposed approach aims to combine the model-based accuracy of the EKF with the data-driven predictive power of LSTM networks, by incorporating LSTM-based fault predictions as pseudo-measurements within the EKF through adaptive covariance tuning. This integration seeks to enhance the

system's robustness against sensor noise and disturbances, while improving estimation accuracy and fault detectability in dynamic environments.

Problem formulation. Accurate modeling of the mobile robot dynamics and measurement process is essential for robust state and fault estimation. In this section, we define the nonlinear robot model, the fault and disturbance representation, and the measurement model, which will serve as the foundation for the estimation framework. The formulation explicitly considers unknown external disturbances and actuator faults, which are common in real-world mobile robotic systems.

Mobile robot model. The mobile robot is modeled with nonlinear kinematics in a 2D plane. The state vector is defined as:

$$x_{k+1} = f(x_k) + w_{x,k}, \quad (1)$$

where $x_k = [X_k, Y_k, \theta_k, f_{v,k}]^T$, X_k and Y_k, are the position; θ_k is the heading angle; $f_{v,k}$ is the additive motor fault affecting the robot's forward velocity; $w_{x,k}$ is the zero-mean Gaussian measurement noise.

The control inputs consist of the commanded forward velocity v_c and angular velocity ω_c. Additionally, the robot is subject to unknown external disturbances: d_v on velocity and d_θ on orientation. The discrete-time dynamics of the robot are given by:

$$X_{k+1} = X_k + (v_{c,k} + f_{v,k} + d_{v,k})\cdot\cos(\theta_k)\Delta t; \quad (2)$$

$$Y_{k+1} = Y_k + (v_{c,k} + f_{v,k} + d_{v,k})\cdot\sin(\theta_k)\Delta t; \quad (3)$$

$$\theta_{k+1} = \theta_k + (\omega_{c,k} + d_{\theta,k})\cdot\Delta t; \quad (4)$$

$$f_{v,k+1} = f_{v,k}, \quad (5)$$

where Δt is the sampling interval. The fault $f_{v,k}$ is assumed slowly varying and additive, capturing actuator degradation or motor faults.

Measurement model. The robot is equipped with a GPS-like sensor providing noisy position measurements:

$$z_k = \begin{bmatrix} X_k \\ Y_k \end{bmatrix} + v_k, \quad (6)$$

where v_k is the zero-mean Gaussian measurement noise.

In addition, a pseudo-measurement of the fault will later be introduced via an LSTM-based predictor, which provides an estimate of $f_{v,k}$ using historical sensor data and EKF state estimates. In summary, the mobile robot dynamics are modeled as a nonlinear discrete-time system with an augmented state vector that includes position, orientation, and an additive motor fault. Noisy GPS measurements provide partial observations of the state, while unknown disturbances in velocity and orientation remain unmeasured. This problem formulation highlights the challenges of joint state and fault estimation under realistic conditions.

Estimation method. Accurate estimation of both the robot states and the motor fault under unknown disturbances requires a combination of model-based and data-driven methods. In this work, we propose a hybrid EKF–LSTM framework, where the EKF provides a principled model-based estimate using the nonlinear robot dynamics and GPS measurements, while the LSTM captures temporal patterns and predicts the fault from historical sensor data. The two components are fused online via an adaptive Kalman update, improving robustness against unknown disturbances and sensor noise.

Figure 1 provides a schematic overview of the proposed hybrid approach. It illustrates the data flow and the interaction between the model-based EKF and the data-driven LSTM, highlighting how the hybrid framework combines predictions from the robot's nonlinear dynamics with LSTM-based fault estimates to achieve robust state and fault estimation under unknown disturbances.

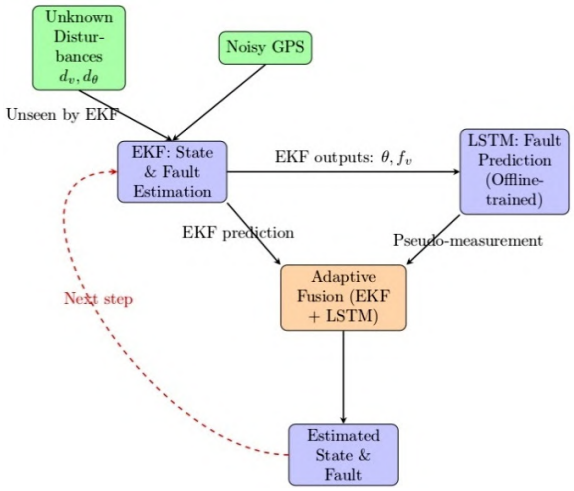

Fig. 1. System architecture of the hybrid EKF–LSTM estimator

EKF-based state and fault estimation. The EKF estimates both the robot states and the additive motor fault. The augmented state vector is:

$$x_k = \begin{bmatrix} X_k \\ Y_k \\ \theta_k \\ f_{v,k} \end{bmatrix}, \quad (7)$$

The nonlinear dynamics are used to predict the next state:

$$\hat{x}_{k|k-1} = f\left(\hat{x}_{k-1|k-1}\right). \quad (8)$$

The EKF linearizes the nonlinear dynamics using the state transition Jacobian $F_{k-1} = \partial f/\partial x_k$:

$$F_{k-1} = \begin{bmatrix} 1 & 0 & v_{eff}\sin(\theta_k)\Delta k & \cos(\theta_k)\Delta k \\ 0 & 1 & v_{eff}\cos(\theta_k)\Delta k & \sin(\theta_k)\Delta k \\ 0 & 0 & 1 & 0 \\ 0 & 0 & 0 & 1 \end{bmatrix}, \quad (9)$$

where $v_{eff} = v_{c,k} + f_{v,k}$. This captures the influence of the fault and orientation on position updates.

The measurement Jacobian $H_k = \partial h/\partial x_k$ for GPS measurements is:

$$H_k = \begin{bmatrix} 1 & 0 & 0 & 0 \\ 0 & 1 & 0 & 0 \end{bmatrix}. \quad (10)$$

Covariance prediction and update:

$$P_{k|k-1} = F_{k-1}P_{k-1|k-1}F_{k-1}^T + Q_{k-1}; \quad (11)$$

$$K_k = P_{k|k-1}H_k^T\left(H_k P_{k|k-1}H_k^T + R_k\right)^{-1}; \quad (12)$$

$$\hat{x}_{k|k=}\hat{x}_{k|k-1} + K_k\left(z_k - h\left(\hat{x}_{k|k-1}\right)\right); \quad (13)$$

$$P_{k|k} = \left(I - K_k H_k\right)P_{k|k-1}. \quad (14)$$

This EKF provides a baseline estimation of both the robot state and the fault without requiring knowledge of the unknown disturbances. However, the presence of unmodeled inputs, such as velocity and orientation perturbations ($d_{v,k}$ and $d_{\theta k}$), can bias the state and fault estimates and increase estimation uncertainty, motivating

the integration of a data-driven LSTM predictor to compensate for these unknown effects.

LSTM-based fault estimation. A LSTM network is employed to predict the fault $f_{v,k}$ based on historical measurements and EKF estimates. The LSTM captures temporal dependencies in the sensor data and the dynamics of the fault. Let the input feature vector at time step k be:

$$\hat{x}_k = \begin{bmatrix} \hat{X}_k^{EKF} \\ \hat{Y}_k^{EKF} \\ \hat{\theta}_k^{EKF} \\ \hat{f}_{v,k}^{EKF} \end{bmatrix}. \quad (15)$$

Using a lookback window of length L, the LSTM input sequence is:

$$x_k = [x_{k-L+1}, x_{k-L+2}, \ldots, x_k]. \quad (16)$$

The LSTM computes the hidden states h_t and cell states C_t recursively at each time step t within the window:

$$\begin{aligned} i_t &= \sigma(W_i \times x_t + U_i h_{t-1} + b_i); \\ f_t &= \sigma(W_f \times x_t + U_f h_{t-1} + b_f); \\ o_t &= \sigma(W_o \times x_t + U_o h_{t-1} + b_o); \\ \widetilde{C}_t &= \tanh(W_c \times x_t + U_c h_{t-1} + b_c); \quad (17) \\ C_t &= f_t \odot C_{t-1} + i_t \odot \widetilde{C}_t; \\ h_t &= o_t \odot \tanh(C_t), \end{aligned}$$

where x_t is the input at time t; h_t is the hidden state vector; C_t is the cell state vector; f_t, i_t and o_t are the forget, input and output gates respectively; σ is the sigmoid activation function; W, U and b are the learnable LSTM weights.

The final hidden state is passed through a dense layer to predict the fault:

$$\hat{f}_{v,k}^{LSTM} = W_y h_k + b_y. \quad (18)$$

The specific LSTM parameters (lookback length, number of hidden units, activation functions, optimizer, etc.) are detailed in the Simulation section to provide reproducibility.

This output generates a pseudo-measurement for the fault, which can be integrated into the EKF to enhance estimation accuracy. In the next subsection, we present the hybrid EKF–LSTM fusion framework, where the LSTM output is adaptively fused with the EKF state estimate to jointly improve state and fault estimation in the presence of unknown disturbances.

Hybrid EKF–LSTM fusion. To improve fault estimation accuracy and robustness against unknown disturbances, the proposed framework integrates model-based EKF estimates with data-driven LSTM predictions. EKF provides a physically consistent state estimate, while the LSTM captures complex temporal patterns in fault evolution that are difficult to model analytically. By fusing these two sources, the hybrid approach leverages the complementary strengths of model-based and learning-based methods.

After the EKF GPS update, the LSTM pseudo-measurement is incorporated:

$$\tilde{y}_k^{LSTM} = \hat{f}_{v,k}^{LSTM} - \hat{f}_{v,k}^{EKF}; \quad (19)$$

$$S_k^{LSTM} = H_{LSTM} P_{k|k} H_{LSTM}^T + R_{LSTM}; \quad (20)$$

$$K_k^{LSTM} = P_{k|k} H_{LSTM}^T \left(S_k^{LSTM}\right)^{-1}; \quad (21)$$

$$\hat{x}_{k|k}^{Fused} = \hat{x}_{k|k}^{EKF} + K_k^{LSTM} \tilde{y}_k^{LSTM}; \quad (22)$$

$$P_{k|k}^{Fused} = \left(I - K_k^{LSTM} H_{LSTM}\right) P_{k|k}, \quad (23)$$

where H_{LSTM} = [0, 0, 0, 1] selects the fault component; R_{LSTM} is adaptively estimated from the recent variance of $\left(\hat{f}_{v,k}^{LSTM} - \hat{f}_{v,k}^{EKF}\right)$. This adaptive covariance ensures stability and prevents overconfidence in LSTM predictions.

The hybrid EKF–LSTM fusion provides an enhanced estimation of the motor fault compared to using either EKF or LSTM alone. The adaptive covariance tuning ensures that the filter remains stable and robust to variations in LSTM prediction accuracy. This approach allows the framework to effectively handle unknown disturbances, improving overall state and fault estimation performance in dynamic and noisy environments.

Simulation results and performance analysis. To validate the effectiveness of the proposed hybrid EKF–LSTM framework, a set of numerical simulations is conducted on a mobile robot model subject to unknown disturbances and additive motor faults. The simulations aim to reproduce realistic operating conditions where classical model-based estimation may be degraded due to unmodeled dynamics and noisy sensor measurements. The experimental setup includes the generation of the robot's ground-truth trajectory, noisy GPS observations, motor fault injection, and external perturbations on both velocity and orientation. The performance of the proposed hybrid estimator is then compared against conventional approaches, namely the EKF without LSTM augmentation and the LSTM-based fault prediction alone. In addition, the UKF is included as a benchmark to assess whether nonlinear filtering offers advantages over the EKF in this scenario.

Simulation framework and parameters. The robot's motion is modeled kinematically under constant control inputs, maintaining a steady linear velocity of v_c = 2 m/s and a steady angular velocity of ω_c = 0.1 rad/s. The simulation environment is designed to emulate the motion of a mobile robot subject to noisy measurements, additive motor faults, and unknown disturbances. The discrete-time simulation runs for n = 200 steps with a sampling interval of Δt = 0.1 s, corresponding to a total duration of 20 s (Fig. 2).

The process noise and measurement noise are modeled as Gaussian with covariance matrices:

$Q_{x,k}$ = diag(0.005; 0.005; 0.0005); R_k = diag(0.05; 0.05).

The initial state of the robot and covariance matrix are set to:

$x_0 = [0; 0; \pi/4; 0]^T$; P_0 = diag(0.1; 0.1; 0.1; 0.01).

An additive motor fault is introduced in the velocity channel. It evolves as a slowly varying bias with an abrupt increase at mid-simulation ($k \geq 100$) to emulate a sudden motor degradation:

$$f_{v,k} = 0.002k + \Delta f(k) + w_{f,k},$$

where $\Delta f(k)$ is the abrupt fault increment at step k=100; $w_{f,k}$ is the Gaussian noise with covariance matrix $Q_{f,k}$ = 0.02.

To capture realistic operating conditions, two unmodeled disturbances are applied (see Fig. 3):

- velocity disturbance: $d_{v,k} = 0.1\sin(2\pi \cdot 0.01 \cdot k\Delta t)$;
- orientation disturbance: $d_{\theta,k} \sim N(0, 0.05)$,

where the former represents smooth oscillations (e.g., due to uneven terrain), and the latter is a random perturbation (e.g., steering noise). In addition to the EKF, a LSTM network is trained to predict the additive motor fault based on past system states and control inputs. The LSTM is structured with:

- Input sequence length: 10 past steps.
- One hidden layer with 64 LSTM units.
- Dropout regularization with a rate of 0.2 to prevent overfitting.
- Fully connected output layer mapping the hidden state to the predicted fault $\hat{f}_{v,k}$.
- Training setup: Adam optimizer, learning rate 10^{-3}, and mean squared error (MSE) loss.

The LSTM output is used as a pseudo-measurement of the fault, which is dynamically fused with the EKF estimate via the adaptive weighting mechanism.

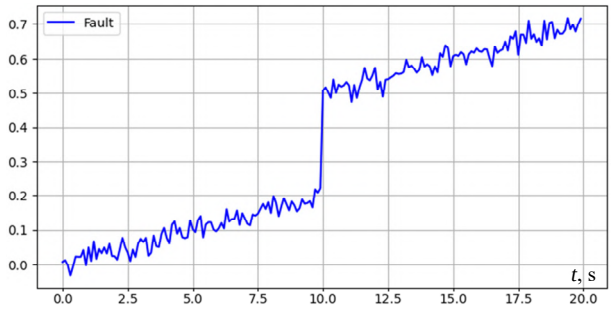

Fig. 2. True fault generation

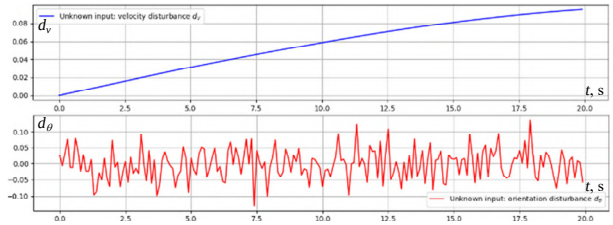

Fig. 3. Real unknown disturbances $d_{v,k}$ and $d_{\theta,k}$

Trajectory estimation. The first validation of the proposed framework is performed through trajectory estimation under the simulated noisy and faulty conditions. The objective is to evaluate whether the hybrid EKF–LSTM estimator can accurately track the robot's trajectory while simultaneously compensating for additive motor faults and disturbances. Figure 4 shows the ground-truth trajectory compared to the estimates obtained with 3 approaches: the conventional EKF, the UKF and the proposed hybrid EKF–LSTM.

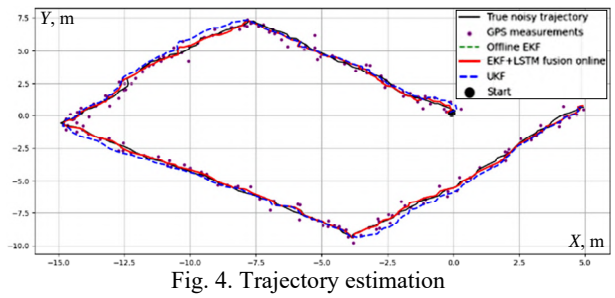

Fig. 4. Trajectory estimation

Figure 4 compares the estimated robot trajectories using the EKF, UKF and the proposed EKF–LSTM hybrid fusion against the true noisy trajectory and GPS measurements. The GPS-only localization (purple points) is highly scattered due to sensor noise.

- EKF (green dashed line) significantly improves trajectory reconstruction and closely follows the ground truth path. Its Jacobian-based linearization proves sufficiently accurate given the moderate nonlinearity of the kinematic model, and it demonstrates robustness against the injected disturbances.
- By contrast, UKF (blue dashed line) provides less accurate estimates in this scenario. While the UKF theoretically captures nonlinear effects more effectively, the presence of unmodeled disturbances distorts the sigma-point propagation. This results in inflated uncertainty and noticeable trajectory deviations, particularly during turns. Consequently, EKF surpasses UKF in this setup.
- Hybrid EKF–LSTM fusion (red line) delivers the best overall performance. The LSTM component learns disturbance and fault patterns from historical data, compensating for model mismatch, while the EKF ensures dynamical consistency. This synergy achieves the most accurate trajectory reconstruction under noisy and disturbed conditions.

The root mean square error (RMSE) and the mean absolute error (MAE) between the estimated and true trajectories are used as performance indicators:

$$RMSE_{pos} = \sqrt{\frac{1}{n}\sum_{k=1}^{n}\left(\left(X_k - \hat{X}_k\right)^2 + \left(Y_k - \hat{Y}_k\right)^2\right)};$$

$$MAE_{pos} = \frac{1}{n}\sum_{k=1}^{n}\sqrt{\left(\left(X_k - \hat{X}_k\right)^2 + \left(Y_k - \hat{Y}_k\right)^2\right)}.$$

Numerical results, presented in Table 1, highlight the following trends:

- EKF provides competitive trajectory estimation with an RMSE of 0.182 and MAE of 0.162. Its performance remains relatively robust despite the presence of unknown inputs, which can significantly disturb the system dynamics.
- UKF exhibits higher errors, with an RMSE of 0.372 and MAE of 0.321, indicating that sigma-point propagation is less effective in mitigating the impact of unknown inputs in this scenario.
- Hybrid EKF–LSTM achieves the lowest errors, with an RMSE of 0.174 and MAE of 0.154. By integrating LSTM predictions, the framework can better capture the effects of unknown inputs and unmodeled dynamics, resulting in an improvement of ~4.6 % over EKF and more than 50 % over UKF.

In summary, the results in Fig. 4 and Table 1 show that while EKF can outperform UKF when disturbances dominate, unknown disturbances still challenge traditional filters. The hybrid EKF–LSTM framework consistently provides the most accurate and robust trajectory estimation by effectively accounting for these unknown disturbances.

Table 1

Comparative performance metrics for trajectory estimation

Metric	EKF	UKF	EKF–LSTM
RMSE	0.182	0.372	0.174
MAE	0.162	0.321	0.154

Fault estimation. In addition to trajectory reconstruction, a key objective of this study is the accurate estimation of the additive motor fault affecting the mobile robot. The fault signal is modeled as an unknown disturbance added to the control input, and its estimation is essential for both robust state estimation and early fault detection.

Figure 5 presents the estimation of the additive motor fault obtained with EKF, UKF, LSTM-only prediction, and the proposed EKF–LSTM fusion framework, compared to the true injected fault:

- EKF (green dashed line) successfully captures the general evolution of the fault, including both the slow drift and the abrupt jump around $t = 10$ s. However, the estimates exhibit oscillations and noticeable variance due to the influence of unknown disturbances and measurement noise.
- UKF (blue dashed line), contrary to expectations, performs poorly in this case. Its sigma-point propagation is highly sensitive to unmodeled disturbances, resulting in large deviations from the true fault and even sign inconsistencies during certain intervals. This confirms that the UKF does not provide robustness advantages under disturbance-dominated dynamics.
- Hybrid EKF–LSTM fusion framework (red line) achieves the most accurate and stable fault estimation. By dynamically combining EKF's model-based consistency with the LSTM's ability to learn and predict fault patterns, the fusion reduces estimation lag and smoothes oscillations. The abrupt fault jump is captured with high precision, while maintaining robustness against disturbances throughout the simulation.

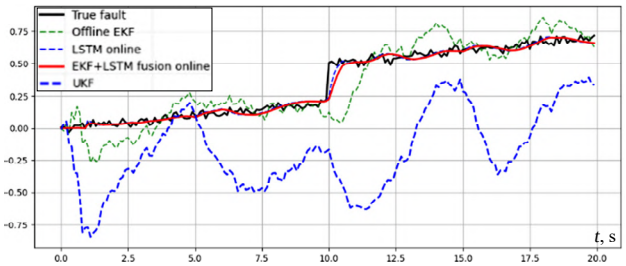

Fig. 5. Fault estimation

The estimation error of the fault is evaluated using the RMSE and the MAE:

$$RMSE_{fault} = \sqrt{\frac{1}{n}\sum_{k=1}^{n}\left(f_{v,k} - \hat{f}_{v,k}\right)^2};$$

$$MAE_{fault} = \frac{1}{n}\sum_{k=1}^{n}\left|f_{v,k} - \hat{f}_{v,k}\right|.$$

Simulation results, summarized in Table 2, indicate the following trends:

- EKF provides reasonably accurate fault estimation with an RMSE of 0.138 and MAE of 0.101. However, its performance is limited by unknown inputs and abrupt nonlinear disturbances, which can perturb the fault estimation.
- UKF performs significantly worse, with an RMSE of 0.604 and MAE of 0.528, showing that sigma-point propagation is not sufficient to handle unknown inputs or rapid fault dynamics in this scenario.
- Hybrid EKF–LSTM achieves the lowest errors, with an RMSE of 0.044 and MAE of 0.030, corresponding to a ~68 % improvement over EKF and more than 90 % over UKF. By incorporating LSTM predictions, the framework effectively captures the effects of unknown inputs and unmodeled dynamics, enabling accurate and real-time fault estimation.

As illustrated in Fig. 5 and Table 2, the hybrid framework achieves near-perfect alignment with the true injected fault, even during abrupt transitions. In contrast, EKF and UKF both underestimate the fault magnitude and exhibit delayed convergence, emphasizing the challenges posed by unknown inputs. These results highlight the hybrid EKF–LSTM method's superior capability for real-time FDI in mobile robots operating under unknown disturbances.

Table 2

Comparative performance metrics for fault estimation

Variable	Metric	EKF	UKF	EKF–LSTM
$f_{v,k}$	RMSE	0.138	0.604	0.044
	MAE	0.101	0.528	0.030

Conclusions. In this paper, we proposed a hybrid EKF–LSTM framework for robust joint state and fault estimation in mobile robots operating under unknown disturbances. The approach combines an augmented EKF, which jointly estimates the robot state and additive motor fault, with an offline-trained LSTM providing pseudo-measurements for the fault. The fusion is performed with adaptive covariance tuning, ensuring stable and accurate estimation even in the presence of unmodeled disturbances. Simulation results show that the hybrid framework outperforms standard EKF and UKF, achieving lower RMSE and MAE for both trajectory (~4–5 % improvement over EKF, 50 % over UKF) and fault estimation (~68 % over EKF, 90 % over UKF). It accurately tracks abrupt fault changes and remains robust against unknown inputs, demonstrating its potential for real-time FDI in robotic applications.

Future work will extend this approach to multi-robot systems, explore gated recurrent unit and transformer-based predictors, validate on physical platforms, and develop adaptive FDI strategies for complex environments.

Conflict of interest. The authors declare that they have no conflicts of interest.

REFERENCES

1. Shafiezadeh A., Bhatt N.P., Hashemi E. LiDAR-Based Navigation Using Normal Distributions Transform Filter. *2024 IEEE 27th International Conference on Intelligent Transportation Systems (ITSC)*, 2024, pp. 4046-4051. doi: https://doi.org/10.1109/ITSC58415.2024.10920042.

2. Chakraborty S., Verma A., Hartman A. Evaluation of Visual Inertial Navigation System for Autonomous Robot Tours on Campus. *2024 IEEE 3rd International Conference on Computing and Machine Intelligence (ICMI)*, 2024, pp. 1-7. doi: https://doi.org/10.1109/ICMI60790.2024.10585838.

3. Fekrmandi H., Frye A.J., Tamjidi A., Rakoczy J., Hoover R.C. Autonomous Multi-agent Systems Using SVGS Camera Sensor for Lunar Surface Mobility Applications. *2021 IEEE Aerospace Conference (50100)*, 2021, pp. 1-10. doi: https://doi.org/10.1109/AERO50100.2021.9438414.

4. Ceccarelli N., Di Marco M., Garulli A., Giannitrapani A., Vicino A. Set Membership Localization and Map Building for Mobile Robots. *Systems and Control: Foundations and Applications*, 2006, pp. 289-308. doi: https://doi.org/10.1007/0-8176-4470-9_16.

5. Li Y., Xu X. The Application of EKF and UKF to the SINS/GPS Integrated Navigation Systems. *2010 2nd International Conference on*

Information Engineering and Computer Science, 2010, pp. 1-5. doi: https://doi.org/10.1109/ICIECS.2010.5678253.
6. Kumar S.D., Dyanesh S., Madhushree K., Madhuram M. Advanced Condition Monitoring and Fault Detection in AC Motors using Machine Learning Techniques. *2025 7th International Conference on Intelligent Sustainable Systems (ICISS)*, 2025, pp. 748-754. doi: https://doi.org/10.1109/ICISS63372.2025.11076243.
7. Geng K., Chulin N.A., Wang Z. Fault-Tolerant Model Predictive Control Algorithm for Path Tracking of Autonomous Vehicle. *Sensors*, 2020, vol. 20, no. 15, art. no. 4245. doi: https://doi.org/10.3390/s20154245.
8. Schneider J.-N., Gorißen L., Kaster T., Walderich P., Hinke C. LSTM-based Inverse Dynamics Learning for Franka Emika Robot. *2024 International Conference on Control, Automation and Diagnosis (ICCAD)*, 2024, pp. 1-6. doi: https://doi.org/10.1109/ICCAD60883.2024.10553865.
9. Davari N., Veloso B., Costa G. de A., Pereira P.M., Ribeiro R.P., Gama J. A Survey on Data-Driven Predictive Maintenance for the Railway Industry. *Sensors*, 2021, vol. 21, no. 17, art. no. 5739. doi: https://doi.org/10.3390/s21175739.
10. Van der Merwe R., Wan E.A., Julier S.J. Sigma-Point Kalman Filters for Nonlinear Estimation and Sensor-Fusion. *AIAA Guidance, Navigation, and Control Conference and Exhibit*, 2004. pp. 1–30.
11. Ding L., Wen C. High-Order Extended Kalman Filter for State Estimation of Nonlinear Systems. Symmetry, 2024, vol. 16, no. 5, art. no. 617. doi: https://doi.org/10.3390/sym16050617.
12. Alsaggaf A.U., Saberi M., Berry T., Ebeigbe D. Nonlinear Kalman Filtering in the Absence of Direct Functional Relationships Between Measurement and State. *IEEE Control Systems Letters*, 2024, vol. 8, pp. 2865-2870. doi: https://doi.org/10.1109/LCSYS.2024.3514818.
13. Yin S., Li P., Gu X., Yang X., Yu L. Adaptive Kalman filter with LSTM network assistance for abnormal measurements. *Measurement Science and Technology*, 2024, vol. 35, no. 7, art. no. 075113. doi: https://doi.org/10.1088/1361-6501/ad404f.
14. Liu X., Hu Y., Konstantinou C., Jin Y. CHIMERA: A Hybrid Estimation Approach to Limit the Effects of False Data Injection Attacks. *2021 IEEE International Conference on Communications, Control, and Computing Technologies for Smart Grids (SmartGridComm)*, 2021, pp. 95-101. doi: https://doi.org/10.1109/SmartGridComm51999.2021.9632000.
15. Cohen N., Klein I. Inertial Navigation Meets Deep Learning: A Survey of Current Trends and Future Directions. *Results in Engineering*, 2024, vol. 24, art. no. 103565. doi: https://doi.org/10.1016/j.rineng.2024.103565.
16. Abed K., Zine H.K.E. Intelligent fuzzy back-stepping observer design based induction motor robust nonlinear sensorless control. *Electrical Engineering & Electromechanics*, 2024, no. 2, pp. 10-15. doi: https://doi.org/10.20998/2074-272X.2024.2.02.
17. Sadeghzadeh-Nokhodberiz N., Poshtan J. Distributed Interacting Multiple Filters for Fault Diagnosis of Navigation Sensors in a Robotic System. *IEEE Transactions on Systems, Man, and Cybernetics: Systems*, 2017, vol. 47, no. 7, pp. 1383-1393. doi: https://doi.org/10.1109/TSMC.2016.2598782.
18. Moussaoui L., Aouaouda S., Rouaibia R. Fault tolerant control of a permanent magnet synchronous machine using multiple constraints Takagi-Sugeno approach. *Electrical Engineering & Electromechanics*, 2022, no. 6, pp. 22-27. doi: https://doi.org/10.20998/2074-272X.2022.6.04.
19. Aghili F., Su C.-Y. Robust Relative Navigation by Integration of ICP and Adaptive Kalman Filter Using Laser Scanner and IMU. *IEEE/ASME Transactions on Mechatronics*, 2016, vol. 21, no. 4, pp. 2015-2026. doi: https://doi.org/10.1109/TMECH.2016.2547905.
20. Oonk S., Maldonado F.J., Li Z., Reichard K., Pentzer J. Extended kalman filter for improved navigation with fault awareness. *2014 IEEE International Conference on Systems, Man, and Cybernetics (SMC)*, 2014, pp. 2681-2686. doi: https://doi.org/10.1109/SMC.2014.6974332.
21. Eichstädt S., Makarava N., Elster C. On the evaluation of uncertainties for state estimation with the Kalman filter. *Measurement Science and Technology*, 2016, vol. 27, no. 12, art. no. 125009. doi: https://doi.org/10.1088/0957-0233/27/12/125009.
22. Xu H., Zhao J., Zhang H., Jiang J., Chen L. Target Tracking Method Based on LSTM-EKF. *Lecture Notes in Electrical Engineering*, 2024, vol. 1206 LNEE, pp. 60-67. doi: https://doi.org/10.1007/978-981-97-3332-3_6.
23. Bengharbi A.A., Laribi S., Allaoui T., Mimouni A. Photovoltaic system faults diagnosis using discrete wavelet transform based artificial neural networks. *Electrical Engineering & Electromechanics*, 2022, no. 6, pp. 42-47. doi: https://doi.org/10.20998/2074-272X.2022.6.07.
24. Hochreiter S., Schmidhuber J. Long Short-Term Memory. *Neural Computation*, 1997, vol. 9, no. 8, pp. 1735-1780. doi: https://doi.org/10.1162/neco.1997.9.8.1735.
25. Wagstaff B., Kelly J. LSTM-Based Zero-Velocity Detection for Robust Inertial Navigation. *2018 International Conference on Indoor Positioning and Indoor Navigation (IPIN)*, 2018, pp. 1-8. doi: https://doi.org/10.1109/IPIN.2018.8533770.
26. Khemiri K., Najari M., Ferhi M., Djebali R., Bjaoui M. Enhancing State of Charge Estimation for Lithium-Ion Batteries in Noisy Environments Using a Hybrid LSTM-EKF Mode. *2025 15th International Renewable Energy Congress (IREC)*, 2025, pp. 1-4. doi: https://doi.org/10.1109/IREC64614.2025.10926811.
27. Khemiri K., Najari M., Ferhi M., Djebali R., Bjaoui M. Analyzing Series Resistance Effects on PV Characteristics and Estimation Using LSTM-EKF. *2025 15th International Renewable Energy Congress (IREC)*, 2025, pp. 1-4. doi: https://doi.org/10.1109/IREC64614.2025.10926737.
28. Yu B., Wang G., Zhu E., Yao S., Zhou Y. Predicting lithium-ion battery state of charge with long short-term memory network enhanced extended Kalman filter. *Journal of Energy Storage*, 2025, vol. 132, art. no. 117849. doi: https://doi.org/10.1016/j.est.2025.117849.
29. Xu C., Zhao H., Xie H., Gao B. Multisensor Decision-Level Fusion Network Based on Attention Mechanism for Object Detection. *IEEE Sensors Journal*, 2024, vol. 24, no. 19, pp. 31466-31480. doi: https://doi.org/10.1109/JSEN.2024.3442951.
30. Lin X., Chao S., Yan D., Guo L., Liu Y., Li L. Multi-Sensor Data Fusion Method Based on Self-Attention Mechanism. *Applied Sciences*, 2023, vol. 13, no. 21, art. no. 11992. doi: https://doi.org/10.3390/app132111992.
31. Yue J., Lang J., Feng R. An adaptive feature fusion strategy using dual-layer attention and multi-modal deep reinforcement learning for all-media similarity search. *Discover Artificial Intelligence*, 2025, vol. 5, no. 1, art. no. 71. doi: https://doi.org/10.1007/s44163-025-00332-7-7.
32. Najdi B., Benbrahim M., Kabbaj M.N. Bearing Fault Diagnosis with a Hybrid CWT-ResNet-LSTM Model. *Lecture Notes in Networks and Systems*, 2024, vol. 1101 LNNS, pp. 454-463. doi: https://doi.org/10.1007/978-3-031-68675-7_43.
33. Khemiri K., Ferhi M., Hidouri N., Ennetta R., Djebali R. Robust State and Fault Estimation in Mobile Robots under Dynamic Noise Environments using Hybrid LSTM-EKF with Adaptive Weighting. *Journal of Applied and Computational Mechanics*, 2025, (In press). doi: https://doi.org/10.22055/jacm.2025.48393.5203.

Received 16.10.2025
Accepted 21.12.2025
Published 02.05.2026

K. Khemiri[1], *PhD, Assistant Professor,*
R. Djebali[1], *PhD, Full Professor,*
[1] UR: Modeling, Optimization and Augmented Engineering, ISLAIB, University of Jendouba, Beja 9000, Tunisia,
e-mail: kemiri_karim@yahoo.fr (Corresponding Author)

How to cite this article:
Khemiri K., Djebali R. Hybrid extended Kalman filter long short-term memory framework for robust state and fault estimation in mobile robots under unknown disturbances. *Electrical Engineering & Electromechanics*, 2026, no. 3, pp. 55-61. doi: https://doi.org/10.20998/2074-272X.2026.3.08

UDC 621.313 https://doi.org/10.20998/2074-272X.2026.3.09

P.D. Nguyen, M. Kuchar

Performance improvement of sensorless scalar and vector control for induction motor drives via an enhanced voltage model

Introduction. *Scalar control (SC) and field-oriented control (FOC) are widely used in sensorless induction motor (IM) drives for their balance of performance and cost. Among estimation techniques, the voltage-model (VM) based model reference adaptive system (MRAS) is preferred in industry due to its simple structure and low computational load.* ***Problem.*** *Traditional VM-based MRAS schemes are highly sensitive to parameter uncertainties, especially to variations in stator resistance R_s caused by temperature changes. These variations degrade flux estimation accuracy, leading to significant speed-tracking errors, increased transients, and reduced stability in both SC and FOC.* ***Goal.*** *This study quantitatively evaluates how the estimation of stator resistance R_s and the dependent rotor resistance R_r affects the speed-control performance of sensorless SC and FOC under parameter mismatch.* ***Methodology.*** *An improved VM-based MRAS is proposed with parallel R_s estimation and R_r updated via a linear relation to R_s. Estimator stability and convergence are proven using Lyapunov theory. The estimator is integrated into SC and FOC and tested in MATLAB/Simulink under identical conditions, including a sudden 30 % increase in resistance. Speed tracking is quantified using the integral of time-weighted absolute error (ITAE).* ***Results.*** *Parameter estimation markedly enhances the robustness of both strategies. In sensorless SC, ITAE drops by about 66.2 % (5.512 to 1.863), indicating much lower transient oscillations. In sensorless FOC, ITAE falls by about 54 % (0.7075 to 0.323), with speed overshoot nearly eliminated (0.031).* ***Scientific novelty.*** *The study provides a unified quantitative comparison of sensorless SC and FOC using ITAE under identical operating and estimation conditions, revealing different levels of performance recovery with the proposed dual-resistance adaptation.* ***Practical value.*** *The findings guide the design of more reliable industrial IM drives, showing that while FOC retains superior dynamics, SC with estimation becomes a robust, cost-effective option for applications with significant parameter uncertainty.* References 31, table 1, figures 13.

Key words: **induction motor, sensorless control, scalar control, field-oriented control, model reference adaptive system, stator resistance estimation.**

Вступ. *Скалярне керування (SC) та векторне керування (FOC) широко застосовуються в бездатчикових електроприводах з асинхронними двигунами (IM) завдяки оптимальному поєднанню ефективності та вартості. Серед методів оцінювання адаптивна система з еталонною моделлю (MRAS) на основі моделі напруги (VM) є поширеною в промисловості завдяки простій структурі та низьким обчислювальним витратам.* ***Проблема.*** *Традиційні схеми MRAS на основі моделі напруги є високочутливими до невизначеностей параметрів, особливо до змін опору статора (R_s), спричинених температурними впливами. Такі зміни погіршують точність оцінювання потокозчеплення, що призводить до значних похибок відстеження швидкості, зростання перехідних процесів і зниження стійкості як у SC, так і у FOC.* ***Мета.*** *Кількісно оцінити вплив оцінювання опору статора R_s та пов'язаного з ним опору ротора R_r на характеристики керування швидкістю в бездатчикових системах SC і FOC за умов розузгодження параметрів.* ***Методика.*** *Запропоновано вдосконалену систему MRAS на основі моделі напруги з паралельним оцінюванням R_s та оновленням R_r за лінійною залежністю від R_s. Стійкість і збіжність оцінювача доведено з використанням теорії Ляпунова. Оцінювач інтегровано до структур SC і FOC та досліджено в середовищі MATLAB/Simulink за однакових умов, зокрема при раптовому збільшенні опору на 30 %. Якість відстеження швидкості оцінювалася за інтегральним критерієм абсолютної похибки, зваженої за часом (ITAE).* ***Результати.*** *Оцінювання параметрів суттєво підвищує робастність обох стратегій. Для бездатчикового SC значення ITAE зменшилося приблизно на 66,2 % (з 5,512 до 1,863), що свідчить про істотне зниження перехідних коливань. Для бездатчикового FOC значення ITAE знизилося приблизно на 54 % (з 0,7075 до 0,323), при цьому перерегулювання швидкості було майже повністю усунено (0,031).* ***Наукова новизна.*** *У роботі наведено уніфіковане кількісне порівняння бездатчикових систем SC і FOC за критерієм ITAE в однакових умовах роботи та оцінювання, що дозволило виявити різний рівень відновлення характеристик при запропонованій адаптації двох опорів.* ***Практична значимість.*** *Отримані результати можуть бути використані під час проєктування більш надійних промислових електроприводів з асинхронними двигунами. Показано, що хоча FOC зберігає перевагу за динамічними характеристиками, SC з оцінюванням параметрів є робастним і економічно доцільним рішенням для застосувань зі значною невизначеністю параметрів.* Бібл. 31, табл. 1, рис. 13.

Ключові слова: **асинхронний двигун, бездатчикове керування, скалярне керування, векторне керування, адаптивна система з еталонною моделлю, оцінювання опору статора.**

Introduction. The induction motors (IMs) is widely used in variable-speed drive systems due to its simple structure, low production cost, and high operational reliability [1, 2]. Their favorable efficiency, low acoustic noise, and limited maintenance requirements have led to extensive adoption in pumps, compressors, conveyor systems, ventilation units, automated production lines, and various mechatronic applications. To control IM drives, several strategies are commonly employed, including scalar control (SC) based on the voltage-frequency (V/f) relationship [3-8] and field-oriented control (FOC) [9-11]. Among these methods, FOC is particularly suitable for applications requiring fast dynamic response, as they decouple torque and flux components through coordinate transformations, enabling independent regulation of these variables. Consequently, FOC is generally regarded as the preferred solution for high-performance IM drives [12-14].

Problems and the relevance. Although modern control techniques have significantly evolved, SC remains widely adopted in industrial practice due to its low implementation cost and structural simplicity. Classical V/f-based SC schemes maintain an approximately constant stator flux by preserving a fixed voltage-frequency ratio [15, 16]. However, it has been well documented that such an approach exhibits limited capability in handling dynamic operating conditions, particularly during load disturbances and rapid speed variations, with performance degradation becoming more evident in sensorless (SSL) operation. Comparative investigations indicate that while closed-loop SC schemes enhance performance relative to open-loop implementations, they still fall short of vector control methods in terms of dynamic response and speed regulation accuracy [17]. This trade-off between performance and simplicity highlights the need to improve the operating characteristics of different control strategies, particularly in SSL configurations.

Review of recent publications on SSL control of IM drives. SSL control for IM drives is gaining attention because it reduces hardware costs and improves reliability

by eliminating mechanical speed sensors [18-20]. Traditional observer-based methods, such as sliding mode observers, remain widely used for their robustness to noise and parameter deviations and can provide acceptable speed estimation under load variations, though low-speed performance and vibration issues persist [21]. AI-based methods and hybrid observer-machine learning schemes demonstrate that AI-assisted sensorless IM control with dual magnetic-field orientation improves speed estimation accuracy and robustness to parameter variations compared with traditional approaches [22]. The work [23] shows that combining an extended Kalman filter (EKF) with a neural network-based magnetic model significantly enhances speed estimation and stability in electric drives, offering useful guidance for sensorless IM systems.

Model reference adaptive systems (MRAS) are widely used for SSL control because they have moderate computational complexity and integrate easily into traditional control structures. They estimate rotor speed by minimizing the difference between a reference model and an adaptive model, typically based on a voltage model (VM) or current model, making them suitable for real-time industrial use [24, 25]. Sensorless control with MRAS offers a good trade-off between estimation accuracy, robustness, and cost compared to more complex AI-based or EKF methods. However, traditional MRAS is sensitive to parameter deviations, especially R_s variations at low speed, motivating advanced MRAS designs with parameter adaptation to improve stability and robustness under changing operating conditions [26].

The goal of the paper. This study quantitatively evaluates how the estimation of stator resistance R_s and the dependent rotor resistance R_r affects the speed-control performance of sensorless SC and FOC under parameter mismatch. An improved VM-based MRAS with parallel resistance estimation is embedded in both schemes under identical conditions, using the integral of time-weighted absolute error (ITAE) index [27] for a unified assessment of speed tracking accuracy and robustness.

Mathematical model of the IM. In the stationary (α, β) frame, the dynamic behavior of an IM is described by voltage and flux-linkage equations, which relate the stator currents, rotor flux components, and motor parameters, as described as:

$$\boldsymbol{u}_s^s = R_s \boldsymbol{i}_s^s + \frac{\mathrm{d}\boldsymbol{\psi}_s^s}{\mathrm{d}t}; \quad (1)$$

$$0 = R_r \boldsymbol{i}_r^s + \frac{\mathrm{d}\boldsymbol{\psi}_r^s}{\mathrm{d}t} - j\omega_r \boldsymbol{\psi}_r^s; \quad (2)$$

$$\boldsymbol{\psi}_s^s = L_s \boldsymbol{i}_s^s + L_m \boldsymbol{i}_r^s; \quad (3)$$

$$\boldsymbol{\psi}_r^s = L_m \boldsymbol{i}_s^s + L_r \boldsymbol{i}_r^s; \quad (4)$$

where $\boldsymbol{i}_s^s$, $\boldsymbol{i}_r^s$ are the stator and rotor current vectors; $\boldsymbol{u}_s^s$, $\boldsymbol{u}_r^s$ are the stator and rotor voltage vectors; $\boldsymbol{\psi}_s^s$, $\boldsymbol{\psi}_r^s$ are the stator and rotor flux-linkage vectors; R_s, R_r are the stator and rotor resistances; L_s, L_r, L_m are the stator, rotor and magnetizing inductances; ω_r is the electrical angular speed; T_e is the electromagnetic torque.

By combining (1)-(4), the electromagnetic torque T_e is obtained as:

$$T_e = \frac{3}{2} p L_m \operatorname{Im}\left\{\boldsymbol{i}_s^s, \boldsymbol{\psi}_r^s\right\}, \quad (5)$$

where p is the number of pairs of poles.

SSL control for IM drive. The proposed SSL employs an improved MRAS scheme for rotor speed estimation. The observer compares the rotor flux obtained from the VM-based reference model with that generated by the adaptive model (AM). The resulting flux error is processed by an adaptive PI mechanism to update the estimated quantities. As shown in Fig. 1, the proposed MRAS structure incorporates parallel estimation of the R_s and rotor time constant (T_r) together with the rotor speed. Compared with conventional VM-based MRAS approaches, this enhanced structure improves robustness against parameter variations and changes in operating conditions.

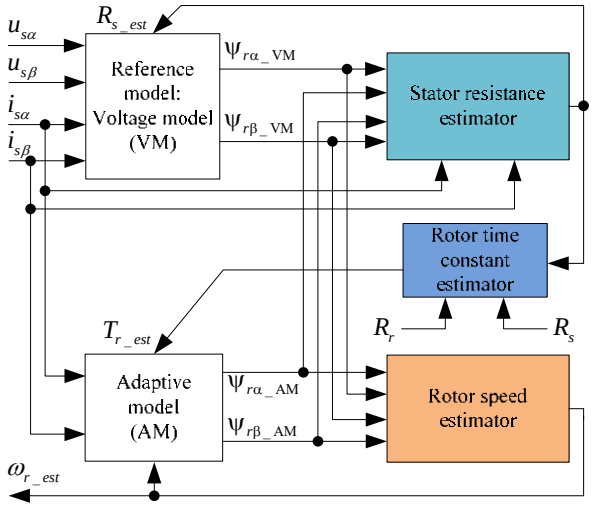

Fig. 1. Sensorless speed based on improved MRAS using VM

Reference model using VM. In the stationary (α, β) frame, the rotor flux components of the VM are expressed via the IM voltage equations:

$$\psi_{r\alpha\_VM} = \frac{L_r}{L_m}\left[\int\left(u_{s\alpha} - R_{s\_est} i_{s\alpha}\right)\mathrm{d}t - \frac{L_s L_r - L_m^2}{L_r} i_{s\alpha}\right]; \quad (6)$$

$$\psi_{r\beta\_VM} = \frac{L_r}{L_m}\left[\int\left(u_{s\beta} - R_{s\_est} i_{s\beta}\right)\mathrm{d}t - \frac{L_s L_r - L_m^2}{L_r} i_{s\beta}\right], \quad (7)$$

where $\psi_{r\alpha\_VM}$, $\psi_{r\beta\_VM}$ are the rotor flux components from VM; R_{s_est} is the estimated R_s.

Based on the rotor flux components in (6), (7), the rotor flux angle (γ_r) is computed by:

$$\gamma_r = \tan^{-1}\left(\frac{\psi_{r\beta\_VM}}{\psi_{r\alpha\_VM}}\right). \quad (8)$$

Adaptive model and rotor speed estimation. The rotor flux in the AM is computed from the estimated speed and stator current dynamics, as follows:

$$\frac{\mathrm{d}\psi_{r\alpha\_AM}}{\mathrm{d}t} = \frac{L_m}{T_{r\_est}} i_{s\alpha} - \frac{1}{T_{r\_est}}\psi_{r\alpha\_AM} - \omega_{r\_est}\psi_{r\beta\_AM}; \quad (9)$$

$$\frac{\mathrm{d}\psi_{r\beta\_AM}}{\mathrm{d}t} = \frac{L_m}{T_{r\_est}} i_{s\beta} - \frac{1}{T_{r\_est}}\psi_{r\beta\_AM} + \omega_{r\_est}\psi_{r\alpha\_AM}. \quad (10)$$

The estimated rotor speed is obtained via an adaptive PI mechanism:

$$\varepsilon_\omega = \psi_{r\alpha\_AM}\psi_{r\beta\_VM} - \psi_{r\alpha\_VM}\psi_{r\beta\_AM}; \quad (11)$$

$$\omega_{r\_est} = K_{p\omega}\varepsilon_\omega + K_{i\omega}\int \varepsilon_\omega \mathrm{d}t; \quad (12)$$

where $\psi_{r\alpha\_AM}$, $\psi_{r\beta\_AM}$ are the rotor flux components from AM; T_{r_est} is the estimated rotor time constant; ε_ω is the flux

error function used as the adaptation signal; ω_{r_est} is the estimated rotor speed; $K_{p\omega}$, $K_{i\omega}$ are the proportional and integral gains of the adaptive PI controller.

Parameter identification for the improved structure. In SSL systems for IM drives, the precision of the estimated rotor speed is highly dependent on the stability and accuracy of the motor parameters. To overcome inaccuracies caused by parameter variations during operation, this study performs parallel estimation of the R_s and T_r to ensure the convergence and reliability of the improved MRAS.

Variations in R_s directly affect the accuracy of the rotor flux calculated in the VM through (6), (7). Therefore, R_s estimation is performed in parallel with the speed estimation process to account for these changes. A PI controller is used to estimate the stator resistance as:

$$\varepsilon_R = i_{s\alpha}\left(\psi_{r\alpha\_VM} - \psi_{r\alpha\_AM}\right) + i_{s\beta}\left(\psi_{r\beta\_VM} - \psi_{r\beta\_AM}\right); \quad (13)$$

$$R_{s\_est} = K_{pR}\varepsilon_R + K_{iR}\int \varepsilon_R \mathrm{d}t, \quad (14)$$

where K_{pR}, K_{iR} denote the PI controller parameters for R_s estimation, respectively.

The rotor time constant is a core parameter in the AM, as seen in (9), (10). However, T_r cannot be directly measured and is difficult for standard observers to identify independently. To address this limitation, this research uses a method, in which R_r is linearly adjusted relative to the estimated R_s:

$$R_{r\_est} = \frac{R_{s\_est}}{R_s} R_r. \quad (15)$$

Under the assumption that the ratio L_r/R_r remains weakly affected by temperature variations relative to R_s, T_r can be treated as quasiconstant during the estimation process:

$$T_{r\_est} = \frac{L_r}{R_{r\_est}}. \quad (16)$$

Stability analysis of the estimation observer using Lyapunov theory. To guarantee bounded estimation errors and convergence of the adaptive scheme to the true values, the stability of the proposed MRAS observer is analyzed via Lyapunov stability theory [28, 29].

Let the state error vector be defined as $\boldsymbol{\varepsilon} = \boldsymbol{\psi}^S_{r\_CM} - \boldsymbol{\psi}^S_{r\_VM}$. We define the parameter estimation errors as $\Delta\omega_r = \omega_r - \omega_{r\_est}$ and $\Delta R_s = R_s - R_{s\_est}$.

To ensure the simultaneous stability of the flux observer and the parameter estimators, a quadratic Lyapunov candidate function V is defined as:

$$V = \frac{1}{2}\boldsymbol{\varepsilon}^T\boldsymbol{\varepsilon} + \frac{1}{2\lambda_1}(\Delta\omega_r)^2 + \frac{1}{2\lambda_2}(\Delta R_s)^2, \quad (17)$$

where λ_1, λ_2 are the positive constants representing the adaptation gains. The function V is positive definite (V>0) for all non-zero errors and equals zero only when the estimated states and parameters match the actual values.

The time derivative of the Lyapunov function is given by:

$$\frac{\mathrm{d}V}{\mathrm{d}t} = \boldsymbol{\varepsilon}^T\frac{\mathrm{d}\boldsymbol{\varepsilon}}{\mathrm{d}t} - \frac{1}{\lambda_1}\Delta\omega_r\frac{\mathrm{d}\omega_{r\_est}}{\mathrm{d}t} - \frac{1}{\lambda_2}\Delta R_s\frac{\mathrm{d}R_{s\_est}}{\mathrm{d}t} \quad (18)$$

with λ_1, λ_2 are the positive constants that ensure the positive definiteness of V.

Based on the error dynamics of the improved MRAS derived from (11)-(14), the term $\boldsymbol{\varepsilon}^T(\mathrm{d}\boldsymbol{\varepsilon}/\mathrm{d}t)$ contains components related to the parameter mismatches. To ensure asymptotic stability $\mathrm{d}V/\mathrm{d}t$, the adaptation mechanisms must be chosen to cancel out the indefinite terms in the derivative.

By equating the parameter update rates to the error driving terms, we derive the following adaptation laws:

For rotor speed in (12): the adaptation law minimizes the cross-product of the flux error, which corresponds to the torque error component. This satisfies the condition for minimizing the $\Delta\omega_r$ term in the Lyapunov derivative.

For R_s in (14): the adaptation law is proportional to the dot-product of the stator current and the flux error, representing the resistive voltage drop error.

The PI controllers are employed for both the speed estimator and the R_s estimator [30]. For the speed estimation loop, a parallel PI structure is adopted with gains $K_{p\omega}$=150, $K_{i\omega}$=1500. For the R_s estimation loop, a parallel PI controller with gains K_{pR}=3.6, K_{iR}=12 is implemented. These gains are tuned to achieve smooth tracking of the R_s while minimizing its interaction with the speed estimation loop.

Improved closed-loop SC. The main principle of the closed-loop SC method is to use an estimated speed technique to calculate slip compensation [31]. Figure 2 shows the control structure of the closed-loop SC with slip compensation using improved MRAS.

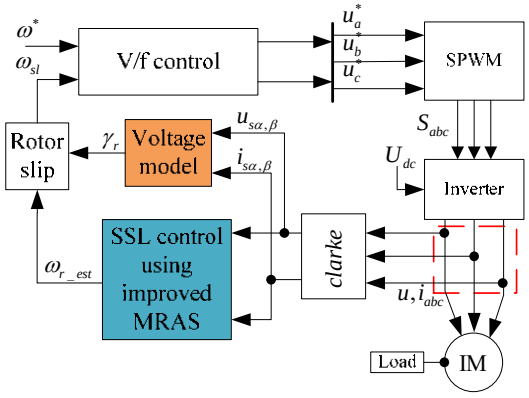

Fig. 2. Block diagram of the SC using SSL

In this structure, the γ_r in (8) is used to compute the slip frequency, which is fed back to correct the commanded synchronous frequency, thereby improving speed regulation and transient performance. The synchronous speed of the rotor flux ω_s is determined by differentiating γ_r and the slip frequency ω_{sl} is defined as:

$$\omega_s = \mathrm{d}\gamma_r/\mathrm{d}t; \quad (19)$$

$$\omega_{sl} = \left(\omega_s - \omega_{r\_est}\right)/p. \quad (20)$$

Improved FOC control. FOC is a widely adopted vector control technique for IM drives requiring fast dynamic response. By orienting the rotating reference frame along the rotor flux, the stator current vector is separated into orthogonal components associated with flux production and torque generation, enabling independent control of these quantities.

Reliable FOC operation depends on accurate information about the γ_r and rotor speed. To eliminate mechanical sensors, an improved FOC structure based on SSL is employed [10, 11]. The overall configuration of FOC using improved MRAS is illustrated in Fig. 3.

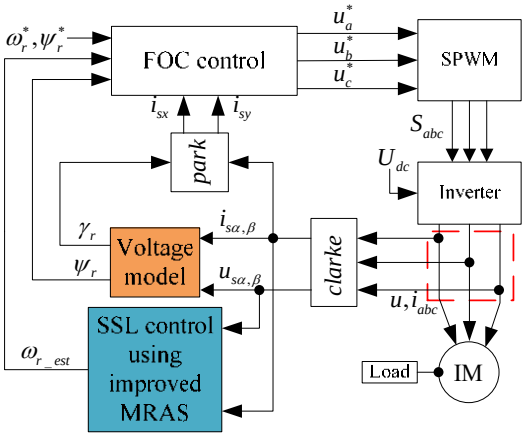

Fig. 3. Block diagram of the IM drive using SSL

Performance evaluation criteria. The performance of each control scheme is evaluated using the ITAE index [7, 27]. By weighting the tracking error with time, the ITAE criterion effectively reflects prolonged deviations between the actual and reference signals. The index is calculated over a 5 s interval as:

$$ITAE = \int_0^T t\left|\left(\omega_m - \omega_m^*\right)\right| dt\,, \qquad (21)$$

where ω_m, ω_m^* are the real and reference mechanical angular speeds of the IM, respectively.

Simulation results. To validate the proposed MRAS-based SSL scheme with integrated R_s and R_r estimation, an IM drive was simulated under SC and FOC. The goal was to assess how resistance estimation affects speed control performance for both strategies under identical conditions.

In all simulations, the reference speed increased linearly from 0 to 710 rpm at 0.5 s, with a constant 1 N·m load torque applied from startup. Two cases are considered to assess the impact of R_s and R_r estimation:

Case 1: No R_s and R_r estimation.

Case 2: Estimation of both R_s and R_r.

The IM parameters are as follows: $p = 2$; rated speed 1420 rpm; $R_s = 3.179$ Ω; $R_r = 2.118$ Ω; $L_s = 0.209$ H; $L_r = 0.209$ H; $L_m = 0.192$ H.

A. Sensorless SC. In the sensorless SC scheme without resistance adaptation, the controller uses fixed nominal R_s and R_r while the actual motor parameters vary. As shown in Fig. 4, the deviation between nominal and actual resistances increases over time, distorting the torque-speed relationship and causing oscillatory transients and poorer tracking, as seen in the rotor speed response in Fig. 5. This demonstrates that sensorless SC is highly sensitive to parameter variations without estimation.

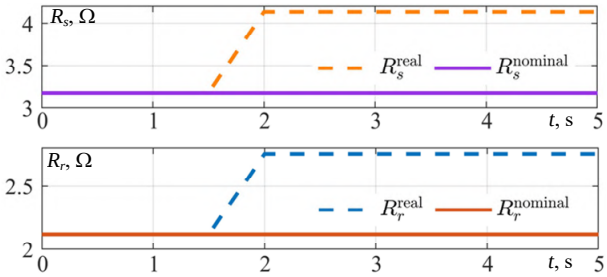

Fig. 4. Actual and nominal R_s/R_r under SC without resistance estimation

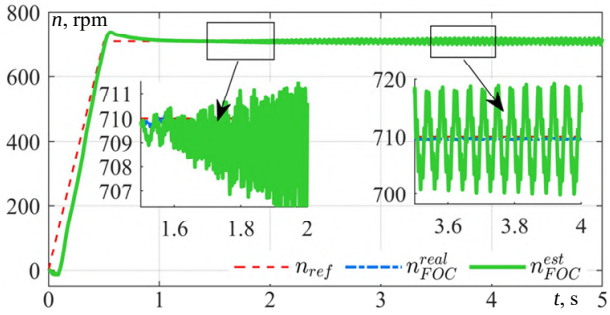

Fig. 5. Rotor speed response under sensorless SC without R_s/R_r estimation (reference, real and estimated)

With the proposed resistance estimation, the estimated R_s and R_r closely match their actual values (Fig. 6). The estimation errors converge quickly and remain bounded (Fig. 7). The improved parameter accuracy yields a much smoother rotor speed response with reduced oscillations and better tracking (Fig. 8). The performance indices in Table 1 confirm that the estimation scheme significantly improves the transient response and robustness of sensorless SC under varying operating conditions.

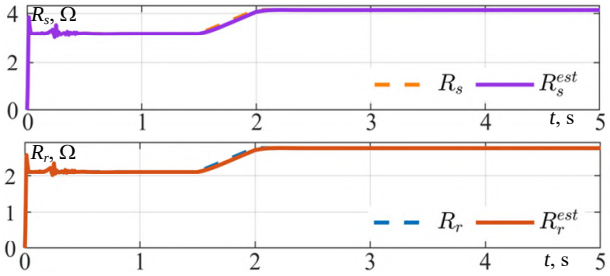

Fig. 6 Actual and estimated R_s/R_r under sensorless SC

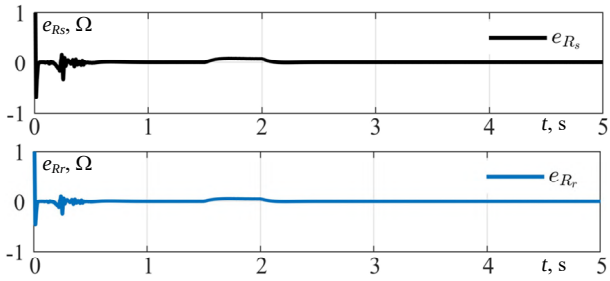

Fig. 7. Estimation errors of R_s/R_r under sensorless SC

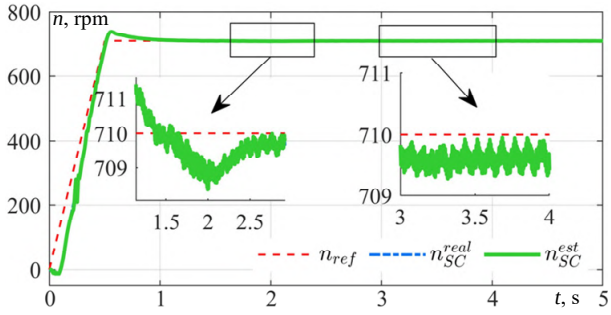

Fig. 8. Rotor speed response under sensorless SC with R_s/R_r estimation (reference, real and estimated)

B. Sensorless FOC. In sensorless FOC without resistance estimation, the R_s and R_r in the controller and MRAS observer are kept constant, while the actual R_s increases during operation (Fig. 9). This mismatch degrades rotor flux and adaptive speed estimation, causing the rotor speed response in Fig. 10 to show large transients and poor tracking, highlighting the sensitivity of sensorless FOC to resistance mismatches without adaptation.

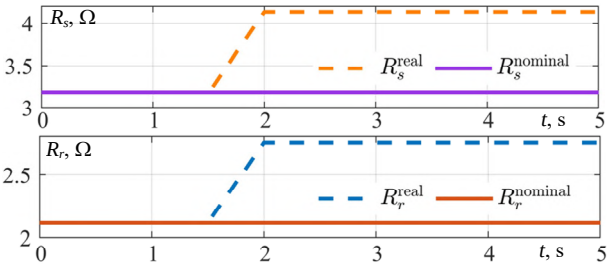

Fig. 9. Actual and nominal R_s/R_r under parameter variation

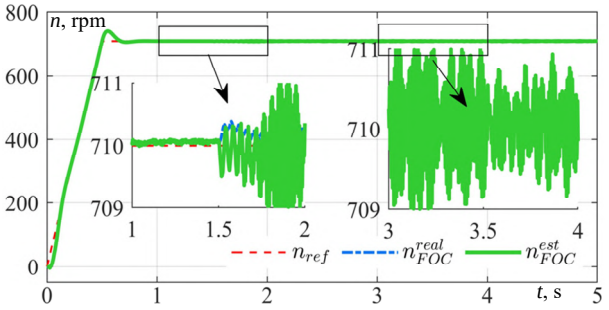

Fig. 10. Rotor speed response without R_s/R_r estimation (reference, real and estimated)

With the proposed MRAS-based resistance estimation enabled, R_s and R_r are accurately identified (Fig. 11). The estimation errors converge rapidly (Fig. 12). This improved parameter estimation yields more accurate flux and speed estimates, producing a smooth rotor speed response with minimal oscillations (Fig. 13).

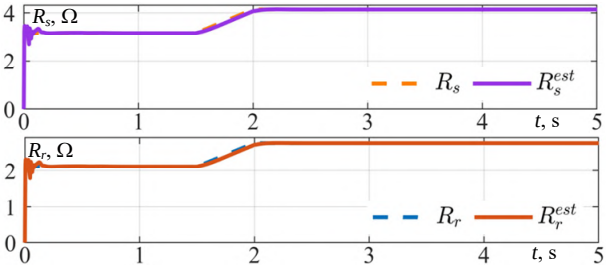

Fig. 11. Actual and estimated R_s/R_r with MRAS-based estimation

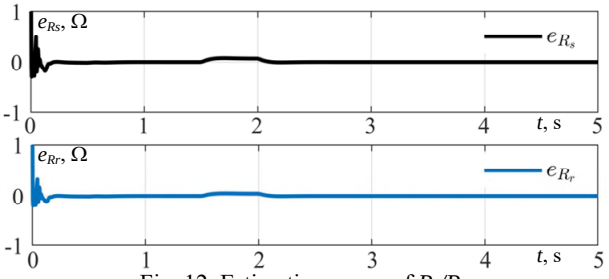

Fig. 12. Estimation errors of R_s/R_r

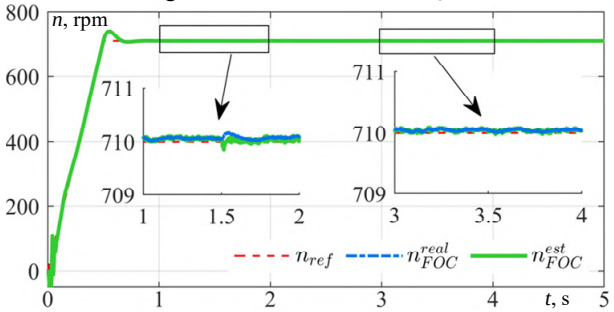

Fig. 13. Rotor speed response with R_s/R_r resistance estimation (reference, real and estimated)

The quantitative results in Table 1 show reduced cumulative tracking error and transient deviations, confirming the method's effectiveness in enhancing the dynamic behavior and robustness of sensorless FOC.

C. Quantitative performance comparison. Table 1 summarizes the speed performance of sensorless SC and FOC with and without resistance estimation. For both methods, ignoring resistance variations severely degrades performance under parameter uncertainties, whereas the proposed estimation consistently improves tracking and reduces transients. Sensorless FOC still outperforms SC dynamically due to its decoupled structure. Still, both benefit markedly from the MRAS-based resistance estimation, which mitigates parameter mismatch and improves the reliability of sensorless IM drives under variable conditions.

Table 1

Speed performance comparison under SC and FOC

Control strategy	R_s/R_r estimation	Speed ITAE	Speed overshoot	Performance assessment
SC	No	5.512	7.895	Large oscillations, low robustness
	Yes	1.863	0.0196	Better tracking, higher robustness
FOC	No	0.7075	0.2987	Large transient deviation
	Yes	0.3230	0.0310	Smooth response, high robustness

Conclusion. This paper examined how estimation of R_s and R_r resistances affects sensorless IM drives using SC and FOC. An improved MRAS-based scheme with parallel resistance updates was proposed to reduce parameter mismatch effects.

Without estimation, both strategies degraded under resistance variations. In sensorless SC, the mismatch caused significant tracking errors (ITAE 5.512) and high overshoot (7.895). With estimation enabled, ITAE fell to 1.863 and overshoot to 0.0196, significantly improving steady-state and transient performance.

In sensorless FOC, baseline performance was better (ITAE 0.7075), but resistance changes still induced transient deviations (overshoot 0.2987). Estimation reduced the overshoot to 0.0310 and the ITAE to 0.3230, further enhancing the dynamics.

Thus, although FOC remains dynamically superior, both strategies gain substantially from the proposed MRAS-based resistance estimation, with SC significantly narrowing the gap. Resistance estimation is therefore crucial for robustness, reduced transients, and reliable sensorless IM operation under parameter uncertainties.

The results demonstrate the performance gains of the proposed estimator and provide practical guidance for a robust, cost-effective solution under parameter uncertainty.

In the future, it is necessary to conduct real IM drives experimental studies of examined how estimation of R_s and R_r resistances affects sensorless IM drives using SC and FOC based on proposed an improved MRAS-based scheme with parallel resistance updates to reduce parameter mismatch effects.

Acknowledgment. This work is a part of the research project [CS.2025.B1.023] funded by Saigon University.

Conflict of interest. The authors declare that they have no conflicts of interest.

REFERENCES

1. Ibrar A., Ahmad S., Safdar A., Haroon N. Efficiency enhancement strategy implementation in hybrid electric vehicles using sliding mode control. *Electrical Engineering & Electromechanics*, 2023, no. 1, pp. 10-19. doi: https://doi.org/10.20998/2074-272X.2023.1.02.

2. Tiwari D., Miscandlon J., Tiwari A., Jewell G.W. A Review of Circular Economy Research for Electric Motors and the Role of Industry 4.0 Technologies. *Sustainability*, 2021, vol. 13, no. 17, art. no. 9668. doi: https://doi.org/10.3390/su13179668.
3. Liyanage A., Nagrial M., Hellany A., Rizk J. Speed Control of Induction Motors Using V/f Control Method. *2022 International Conference on Electrical and Computing Technologies and Applications (ICECTA)*, 2022, pp. 424-429. doi: https://doi.org/10.1109/ICECTA57148.2022.9990374.
4. Saleh S.A. The Development and Performance Testing of a V/f Control for Induction Motors Fed by Wavelet Modulated Power Electronic Converters. *IEEE Transactions on Industry Applications*, 2024, vol. 60, no. 3, pp. 5012-5024. doi: https://doi.org/10.1109/TIA.2024.3362918.
5. Keskin B., Eminoglu I. Optimally Tuned PI Controller Design for V/f Control of Induction Motor. *2022 International Congress on Human-Computer Interaction, Optimization and Robotic Applications (HORA)*, 2022, pp. 1-5. doi: https://doi.org/10.1109/HORA55278.2022.9800005.
6. Son D.-H., Kim S.-A. Simplified V/f Control Algorithm for Reduction of Current Fluctuations in Variable-Speed Operation of Induction Motors. *Energies*, 2024, vol. 17, no. 7, art. no. 1699. doi: https://doi.org/10.3390/en17071699.
7. Shekher V., Sisodiya A., Sinha A.K., Harsh H., Soren N. Optimal tuning of PID controller for V/f control of linear induction motor using artificial biological intelligence. *Franklin Open*, 2024, vol. 9, art. no. 100183. doi: https://doi.org/10.1016/j.fraope.2024.100183.
8. Choi S.-C., Kim J.-H., Yoon Y.-D., Hong C.-O., Park C.-H., Cho J.-H. V/F Control Method for Pulsating Torque Reduction in a Single Phase Induction Motor. *2023 IEEE International Symposium on Sensorless Control for Electrical Drives (SLED)*, 2023, pp. 1-6. doi: https://doi.org/10.1109/SLED57582.2023.10261379.
9. Zellouma D., Bekakra Y., Benbouhenni H. Field-oriented control based on parallel proportional–integral controllers of induction motor drive. *Energy Reports*, 2023, vol. 9, pp. 4846-4860. doi: https://doi.org/10.1016/j.egyr.2023.04.008.
10. Tran C.D., Kuchar M., Nguyen P.D. Improved Rotor Flux Estimation For Field-Oriented Control In Induction Motor Drives. *Tekhnichna Elektrodynamika*, 2025, no. 6, pp. 52-57. doi: https://doi.org/10.15407/techned2025.06.052.
11. Tran C.D., Kuchar M., Sotola V., Nguyen P.D. Sensor fault diagnosis strategy based on rotor flux observers in three-phase induction motor drive. *Scientific Reports*, 2025, vol. 16, no. 1, art. no. 267. doi: https://doi.org/10.1038/s41598-025-29381-9.
12. Soliman H.M. Studying the Steady State Performance Characteristics of Induction Motor with Field Oriented Control Comparing to Scalar Control. *European Journal of Engineering and Technology Research*, 2018, vol. 1, no. 2, pp. 18-25. doi: https://doi.org/10.24018/ejeng.2016.1.2.115.
13. Bierhoff M., Busch J. Novel Scalar versus Field Oriented Speed Control of Induction Machine Drives. *2020 International Symposium on Power Electronics, Electrical Drives, Automation and Motion (SPEEDAM)*, 2020, pp. 207-212. doi: https://doi.org/10.1109/SPEEDAM48782.2020.9161939.
14. Rezgui S.E., Darsouni Z., Benalla H. Nonlinear vector control of multiphase induction motor using linear quadratic regulator and active disturbances rejection control under disturbances and parameter variations. *Electrical Engineering & Electromechanics*, 2025, no. 6, pp. 75-83. doi: https://doi.org/10.20998/2074-272X.2025.6.10.
15. Graciola C.L., Goedtel A., Angélico B.A., Castoldi M.F., Costa B.L.G. Energy Efficiency Optimization Strategy for Scalar Control of Three-Phase Induction Motors. *Journal of Control, Automation and Electrical Systems*, 2022, vol. 33, no. 3, pp. 1032-1043. doi: https://doi.org/10.1007/s40313-021-00876-w.
16. Laha S., Dhali J., Gayen P.K. Comparative Performance between V/F and Rotor Flux-Oriented Controls of Induction Motor Drive. *2023 IEEE Devices for Integrated Circuit (DevIC)*, 2023, pp. 1-6. doi: https://doi.org/10.1109/DevIC57758.2023.10134999.
17. Bisoi M., Kalyan R., Selvaraj R., Vemuganti H.P. Performance investigation of three-phase induction machine with scalar and vector control method. *Emerging Technologies & Applications in Electrical Engineering*, 2024, pp. 152-162. doi: https://doi.org/10.1201/9781003505181-19.
18. Gholipour A., Ghanbari M., Alibeiki E., Jannati M. Speed sensorless fault-tolerant control of induction motor drives against current sensor fault. *Electrical Engineering*, 2021, vol. 103, no. 3, pp. 1493-1513. doi: https://doi.org/10.1007/s00202-020-01179-0.
19. Tran C.D., Kuchar M., Nguyen P.D. Research for an enhanced fault-tolerant solution against the current sensor fault types in induction motor drives. *Electrical Engineering & Electromechanics*, 2024, no. 6, pp. 27-32. doi: https://doi.org/10.20998/2074-272X.2024.6.04.
20. Wogi L., Morawiec M., Ayana T. Sensorless Control of Induction Motor Based on Super-Twisting Sliding Mode Observer With Speed Convergence Improvement. *IEEE Access*, 2024, vol. 12, pp. 74239-74250. doi: https://doi.org/10.1109/ACCESS.2024.3404040.
21. Najeeb M.M., Vidya M.S. Sensorless Speed Control of Induction Motor Using SMO. *2025 International Conference on Power, Instrumentation, Control, and Computing (PICC)*, 2025, pp. 1-5. doi: https://doi.org/10.1109/PICC67314.2025.11291483.
22. Szoke E., Szabo C., Pintilie L.-N. Artificial Intelligence-Based Sensorless Control of Induction Motors with Dual-Field Orientation. *Applied Sciences*, 2025, vol. 15, no. 16, art. no. 8919. doi: https://doi.org/10.3390/app15168919.
23. Pasqualotto D., Rigon S., Zigliotto M. Sensorless Speed Control of Synchronous Reluctance Motor Drives Based on Extended Kalman Filter and Neural Magnetic Model. *IEEE Transactions on Industrial Electronics*, 2023, vol. 70, no. 2, pp. 1321-1330. doi: https://doi.org/10.1109/TIE.2022.3159962.
24. Ganjewar S.P., Pahariya Y. Modified MRAS approach for sensorless speed control of induction motor for reliability improvement. *International Journal of Information Technology*, 2022, vol. 14, no. 3, pp. 1595-1602. doi: https://doi.org/10.1007/s41870-021-00847-z.
25. Orlowska-Kowalska T., Korzonek M., Tarchala G. Performance Analysis of Speed-Sensorless Induction Motor Drive Using Discrete Current-Error Based MRAS Estimators. *Energies*, 2020, vol. 13, no. 10, art. no. 2595. doi: https://doi.org/10.3390/en13102595.
26. Tran C.D., Brandstetter P., Kuchar M., Nguyen P.D. An Improved CB-MRAS Using Voltage Model Integrating Stator Resistance Estimation in Induction Motor Drives. *International Review of Electrical Engineering (IREE)*, 2024, vol. 19, no. 6, art. no. 446. doi: https://doi.org/10.15866/iree.v19i6.25107.
27. Alshatti A.H. An Adaptive Soft Computing Model for Flux Estimation and Torque Control of Induction Motors. *International Journal of Advances in Scientific Research and Engineering*, 2024, vol. 10, no. 5, pp. 1-9. doi: https://doi.org/10.31695/IJASRE.2024.5.1.
28. Gulbudak O., Gokdag M., Komurcugil H. Model Predictive Control Strategy for Induction Motor Drive Using Lyapunov Stability Objective. *IEEE Transactions on Industrial Electronics*, 2022, vol. 69, no. 12, pp. 12119-12128. doi: https://doi.org/10.1109/TIE.2021.3139237.
29. Nurettin A., Inanc N. Sensorless Vector Control for Induction Motor Drive at Very Low and Zero Speeds Based on an Adaptive-Gain Super-Twisting Sliding Mode Observer. *IEEE Journal of Emerging and Selected Topics in Power Electronics*, 2023, vol. 11, no. 4, pp. 4332-4339. doi: https://doi.org/10.1109/JESTPE.2023.3265352.
30. Orlowska-Kowalska T., Dybkowski M. Stator-Current-Based MRAS Estimator for a Wide Range Speed-Sensorless Induction-Motor Drive. *IEEE Transactions on Industrial Electronics*, 2010, vol. 57, no. 4, pp. 1296-1308. doi: https://doi.org/10.1109/TIE.2009.2031134.
31. Meghana I., Cherukupalli K., Sravani M., Babu Naidu P.C. Simulation of Slip Compensation for Induction Motor Drive Using MATLAB. *2021 Innovations in Power and Advanced Computing Technologies (i-PACT)*, 2021, pp. 1-7. doi: https://doi.org/10.1109/i-PACT52855.2021.9696878.

Received 13.01.2026
Accepted 20.03.2026
Published 02.05.2026

P.D. Nguyen[1,2]*, PhD Student,*
M. Kuchar[2]*, Professor, Doctor on Electrical Engineering,*
[1] Faculty of Engineering and Technology,
Saigon University, Ho Chi Minh City, Vietnam,
e-mail: phuong.nd@sgu.edu.vn (Corresponding Author)
[2] Department of Applied Electronics,
Faculty of Electrical Engineering and Computer Science,
VSB-Technical University of Ostrava, Czech Republic.

How to cite this article:
Nguyen P.D., Kuchar M. Performance improvement of sensorless scalar and vector control for induction motor drives via an enhanced voltage model. *Electrical Engineering & Electromechanics*, 2026, no. 3, pp. 62-67. doi: https://doi.org/10.20998/2074-272X.2026.3.09

UDC 621.313.32 https://doi.org/10.20998/2074-272X.2026.3.10

M. Tabbakh, R. Rouabhi, A. Herizi, N. Chami

A new stator flow-oriented control method based on type-2 fuzzy logic controllers for permanent magnet synchronous motors

Introduction. *Stator flow-oriented control is currently the most widely used system in industry or in previous research for improving the quality of mechanical power generated by permanent magnet synchronous motors (PMSM).* ***Problem.*** *However, this control is often based on PI controllers, which have shown problem limitations in terms of performance and robustness. Furthermore, these controllers are not suitable for variable-structure motors, which requires the use of new, more efficient controllers that provide robust control over both internal and external changes, such as type-2 fuzzy logic controllers. The* ***goal*** *of this work is to develop a stator flow-oriented control system by replacing PI controllers with type-2 fuzzy logic controllers that are robust to both external variations, such as changes in torque resistance, and internal variations, such as changes in parameters.* ***Methodology****. To implement this control on the PMSM, we maintained the similar structure of stator flow-oriented control, but replaced the PI controllers with type-2 fuzzy controllers. The* ***results*** *of numerical simulations performed using MATLAB/Simulink show that the stator flow-oriented control based on type-2 fuzzy logic controllers achieves an ideal response time and minimal overshoot, with an exponential error close to zero in both the transient and steady states, even with the application of external variations such as resistive torque or changes to the machine's parameters. The* ***scientific novelty*** *of this work lies in replacing all the controllers in the stator flow-oriented control system with type-2 fuzzy controllers and their programming method, thus addressing the shortcomings of traditional methods. In addition, a rare type of comparative study is presented, thanks to which the effectiveness and robustness of the developed control method relative to other can be demonstrated.* ***Practical value****. The excellent results obtained with the new stator flow-oriented control method using type-2 fuzzy logic controllers suggest that it should be taught in academic circles and applied in industry.* References 30, tables 3, figures 5.

Key words: **mechanical power control, permanent magnet synchronous motor, stator flow-oriented control, type-2 fuzzy logic control.**

Вступ*. Керування, орієнтоване за потоком статора (SFOC), на сьогодні є одним із найпоширеніших підходів у промисловості та наукових дослідженнях для підвищення якості механічної потужності, що генерується синхронними двигунами з постійними магнітами (PMSM).* ***Проблема****. Проте в більшості випадків таке керування базується на ПІ-регуляторах, які мають обмеження з точки зору швидкодії та робастності. Крім того, ці регулятори є малопридатними для двигунів зі змінною структурою, що зумовлює необхідність застосування нових, більш ефективних регуляторів, здатних забезпечити робастне керування як при внутрішніх, так і зовнішніх збуреннях, зокрема регуляторів на основі нечіткої логіки типу 2.* ***Метою*** *роботи є розроблення системи керування, орієнтованої за потоком статора, шляхом заміни ПІ-регуляторів на регулятори нечіткої логіки типу 2, які є робастними як до зовнішніх змін (наприклад, зміни навантажувального моменту), так і до внутрішніх варіацій параметрів двигуна.* ***Методика****. Для реалізації запропонованого підходу в системі керування PMSM збережено структуру SFOC, однак ПІ-регулятори замінено на регулятори нечіткої логіки типу 2.* ***Результати*** *чисельного моделювання, виконаного в середовищі MATLAB/Simulink, показали, що система керування, орієнтована за потоком статора на основі нечіткої логіки типу 2, забезпечує практично ідеальний час реакції та мінімальне перерегулювання, при цьому похибка має експоненційний характер і прямує до нуля як у перехідному, так і в усталеному режимах навіть за наявності зовнішніх збурень, таких як навантажувальний момент або зміни параметрів машини.* ***Наукова новизна*** *роботи полягає у повній заміні всіх регуляторів у системі SFOC на регулятори нечіткої логіки типу 2, а також у запропонованому підході до їх програмної реалізації, що дозволяє усунути недоліки традиційних методів. Крім того, представлено рідкісний тип порівняльного дослідження, який демонструє ефективність і робастність розробленого методу керування порівняно з існуючими.* ***Практична значимість****. Отримані результати застосування нового методу керування, орієнтованого за потоком статора із використанням регуляторів нечіткої логіки типу 2, свідчать про доцільність його впровадження як у навчальному процесі, так і в промислових застосуваннях.* Бібл. 30, табл. 3, рис. 5.

Ключові слова: **механічне керування потужністю, синхронний двигун з постійними магнітами, керування орієнтоване за потоком статора, керування на основі нечіткої логіки типу 2.**

Introduction. In industrial settings, permanent magnet synchronous motors (PMSMs) are highly favored [1, 2]. Their popularity stems from their simplicity, reliability, and compact footprint, which outshines that of DC motors [3, 4]. Their design is simpler as they lack mechanical switches, which enhances their longevity and obviates the necessity for frequent maintenance [5, 6]. Moreover, their operation in explosive environments is feasible due to the absence of spark generation. Additionally, they offer superior power output relative to their mass, distinguishing them from DC machines that demand more power sources and exhibit a lower power-to-weight ratio [7, 8].

It is well known that AI techniques have a great deal of promise for solving problems in industrial processes, particularly in domains like parameter estimation, control, and system identification. More and more, induction machines are being controlled and adjusted using fuzzy logic, a prominent AI technology. Building systems that can do cognitive tasks similar to human reasoning is the ultimate objective of AI research [9–11].

Classical fuzzy logic, now called type-1 fuzzy logic, has been generalised into a new type-2 fuzzy logic (T2FL). When it's tough to pin down precise membership functions for a fuzzy system, T2FL comes in handy. With this new logic, we may include uncertainty in the rules, which will improve the system's output [12–15].

Currently, the most popular method in industry and previous research such as those reported in [16, 17] to enhance the mechanical power produced by PMSM is stator flow-oriented control (SFOC) based on PI controllers. Unfortunately, these PI controllers have shown performance and durability issues. Furthermore, these controllers are not suitable for motors with variable structure. In the present work the contribution consists in proposing the replacement of PI controllers by type-2 fuzzy controllers to further improve the static and dynamic performance in response to internal (such as parameter changes) and external (such as torque resistance) fluctuations.

The **goal** of this work is to develop a stator flow-oriented control system by replacing PI controllers with type-2 fuzzy logic controllers that are robust to both external variations, such as changes in torque resistance, and internal variations, such as changes in parameters.

Modelling of the PMSM and its converters. In order to simulate the behavior of the PMSM and to develop control techniques for this machine, it is important to model PMSM and its converters individually:

- the permanent magnet synchronous motor;
- the motor-side converter (two-level inverter), utilizing a two-level inverter, facilitates the implementation of commands to regulate the mechanical power produced;
- the grid-side converter, featuring a two-level rectifier, emerges as an effective solution for enhancing the power factor on the grid side and regulating the DC bus.

PMSM model. The PMSM mathematical model needs to be formatted in order to study its control and simulation in different operating systems [18, 19]:

$$\begin{cases} \dfrac{\mathrm{d}}{\mathrm{d}t} I_{ds} = \dfrac{1}{L_d}\left(V_{ds} - R_s I_{ds} + \Omega L_q I_{qs}\right); \\ \dfrac{\mathrm{d}}{\mathrm{d}t} I_{qs} = \dfrac{1}{L_q}\left(V_{qs} - R_s I_{qs} - \Omega L_d I_{ds} + \Omega \phi_f\right); \\ C_e = \dfrac{3}{2} p\left[(L_d - L_q) I_{qs} I_{ds} + \phi_f I_{qs}\right]; \\ C_e - C_r - f\Omega = J \dfrac{\mathrm{d}}{\mathrm{d}t}\Omega, \end{cases} \tag{1}$$

$$\frac{\mathrm{d}}{\mathrm{d}t}[X] = [A][X] + [B][V], \tag{2}$$

where:

$$[X] = \begin{bmatrix} I_{ds} & I_{qs} \end{bmatrix}^T; \quad [V] = \begin{bmatrix} V_{ds} & V_{qs} & \phi_f \end{bmatrix}^T;$$

$$\begin{bmatrix} I_{ds} \\ I_{qs} \end{bmatrix} = \begin{bmatrix} -\dfrac{R_s}{L_d} & \Omega \dfrac{L_q}{L_d} \\ \Omega \dfrac{-L_d}{L_q} & -\dfrac{R_s}{L_q} \end{bmatrix} \begin{bmatrix} I_{ds} \\ I_{qs} \end{bmatrix} + \begin{bmatrix} \dfrac{1}{L_d} & 0 & 0 \\ 0 & \dfrac{1}{L_q} & -\dfrac{\Omega}{L_q} \end{bmatrix} \begin{bmatrix} V_{ds} \\ V_{qs} \\ \phi_f \end{bmatrix}. \tag{3}$$

We define:

$$[A] = \begin{bmatrix} \dfrac{-R_s}{L_d} & 0 \\ 0 & \dfrac{-R_s}{L_q} \end{bmatrix} + \begin{bmatrix} 0 & \dfrac{L_q}{L_d} \\ \dfrac{-L_d}{L_q} & 0 \end{bmatrix}; \tag{4}$$

$$[B] = \begin{bmatrix} \dfrac{1}{L_d} & 0 & 0 \\ 0 & \dfrac{1}{L_q} & 0 \end{bmatrix} + \begin{bmatrix} 0 & 0 & 0 \\ 0 & 0 & -\dfrac{1}{L_q} \end{bmatrix} \Omega, \tag{5}$$

where C_r, C_e, Ω, f, J, p are the resistance torque, motor torque, mechanical speed, viscous friction factor, moment of inertia, number of pairs of poles, respectively; I_d, I_q, V_d, V_q, L_d, L_q, φ_d, φ_q are the dq components of the stator current, voltage, inductance and flux linkage, respectively; φ_f is the rotor flux linkage generated by the permanent magnets; R_s is the stator resistance.

Motor-side converter model. To control the PMSM effectively, a static converter a two-level inverter is employed to energize its stator. This converter primarily aims to modulate the DC bus voltage to power the stator winding and facilitate the execution of commands for regulating the mechanical power output [20, 21]:

$$\begin{bmatrix} V_A \\ V_B \\ V_C \end{bmatrix} = \frac{E}{6} \begin{bmatrix} 2 & -1 & -1 \\ -1 & 2 & -1 \\ -1 & -1 & 2 \end{bmatrix} \begin{bmatrix} S_1 \\ S_2 \\ S_3 \end{bmatrix}, \tag{6}$$

where V_A, V_B, V_c are the line voltages; S_1–S_3 are the switching states; E is the DC source.

Grid-side converter model. The grid-side converter, resembling the machine-side converter established earlier, shares a similar design. Apart from its bidirectional power flow capability, the grid-side converter boasts the advantage of regulating the DC bus voltage consistently and setting the reference reactive power to zero, thereby preserving the grid's quality by maintaining a unity power factor [22, 23]:

$$\frac{\mathrm{d}}{\mathrm{d}t} \begin{bmatrix} i_1 \\ i_2 \\ i_3 \end{bmatrix} = \begin{bmatrix} -\dfrac{R}{L} & 0 & 0 \\ 0 & -\dfrac{R}{L} & 0 \\ 0 & 0 & -\dfrac{R}{L} \end{bmatrix} \begin{bmatrix} i_1 \\ i_2 \\ i_3 \end{bmatrix} + \begin{bmatrix} V_1 + V_{an} \\ V_2 + V_{bn} \\ V_3 + V_{cn} \end{bmatrix}; \tag{7}$$

$$\begin{bmatrix} V_A \\ V_B \\ V_C \end{bmatrix} = \frac{U_c}{3} \begin{bmatrix} 2 & -1 & -1 \\ -1 & 2 & -1 \\ -1 & -1 & 2 \end{bmatrix} \begin{bmatrix} S_1 \\ S_2 \\ S_3 \end{bmatrix}; \tag{8}$$

$$\frac{U_c}{i_s} = \frac{R_{ch}}{1 + R_{ch} C p}. \tag{9}$$

On the grid side, this converter can be controlled using voltage oriented control, comprising two internal loops for regulating the phase currents, while an external loop oversees the output voltage regulation:

$$\begin{cases} V_{pd} = V_d - R i_d - L \dfrac{di_d}{dt} + L w i_q; \\ V_{pq} = V_q - R i_q - L \dfrac{di_q}{dt} - L w i_d; \end{cases} \tag{10}$$

$$P = \left[V_d i_d + V_q i_q\right]; \quad Q = \left[V_q i_d + V_d i_q\right]. \tag{11}$$

We define:

$$P_{ref} = U_{cmes} I_{red-ref}; \tag{12}$$

$$Q_{ref} = 0, \tag{13}$$

where i_A, i_B, i_C, v_1, v_2, v_3, v_{an}, v_{bn}, v_{cn} are the components of the stator currents, stator voltage, and simple voltage, inductance and flux linkage, respectively; L, R are the inductance and resistance of the line; U_c is the DC voltage; C is the capacity of the capacitor in parallel; V_{pd}, V_{pq}, V_d, V_q, i_{pq}, i_{pq} are the dq components of the line voltage, grid voltages and currents respectively; P, Q are the active and reactive powers; w is the pulsation.

Mechanical power control. In order to obtain high quality control of the mechanical power produced by a PMSM, it is necessary to select suitable control techniques to control the mechanical power generated by the rotor of this machine. To do this, it is necessary to select suitable control techniques that allow the speed and mechanical torque to be controlled at the reference speed to ensure that our system is more efficient.

Stator flow-oriented control based on PI controller. One technique to maximize the quality of the mechanical energy generated is this control. This method, we suggest a control algorithm that is based on the machine's stator flux orientation, which highlights the

relationships between the mechanical power quantities (speed and electromagnetic torque) and the stator voltages produced by the inverter (Fig. 1). These relationships allow action to be taken on the stator signals in order to independently control the exchange of the speed generated at the machine's rotor [24, 25].

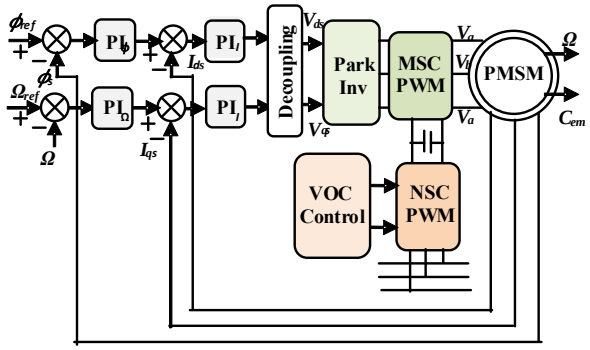

Fig. 1. Stator flow-oriented control based on PI controllers

In order to obtain control similar to that of separately excited DC machines, it is necessary to maintain i_{ds} at zero and control the speed or position via the current i_{qs}:

$$i_{ds} = 0\,; \tag{14}$$

$$i_{qs} = i_s\,; \tag{15}$$

$$\begin{cases} V_{ds} = R_s i_{ds} + L_d \dfrac{\mathrm{d}i_{ds}}{\mathrm{d}t} - wL_q i_{qs}\,; \\ V_{qs} = R_s i_{qs} + L_q \dfrac{\mathrm{d}i_{qs}}{\mathrm{d}t} + w\left(L_d i_{ds} + \phi_f\right); \end{cases} \tag{16}$$

$$\begin{cases} V_{ds} = V_{d1} - e_d\,; \\ V_{qs} = V_{q1} + e_q\,; \end{cases} \tag{17};$$

$$\begin{cases} V_{d1} = R_s i_{ds} + L_d \dfrac{\mathrm{d}i_{ds}}{\mathrm{d}t}\,; \\ V_{q2} = R_s i_{qs} + L_q \dfrac{\mathrm{d}i_{qs}}{\mathrm{d}t}\,; \end{cases} \tag{18}$$

$$\begin{cases} e_{ds} = wL_q i_{qs}\,; \\ e_{qs} = w\left(L_d i_{ds} + \phi_f\right). \end{cases} \tag{19}$$

Stator flow-oriented control based on T2FL controller. A fuzzy system is said to be of type-2 if it contains at least one fuzzy set of type-2 in membership functions that specify its premises or consequences. Fuzzy reasoning in this type of system leads to fuzzy sets of type-2 outputs. The configuration of a type-2 fuzzy system closely resembles that of a type-1 fuzzy system. It comprises a rule base, a fuzzification and defuzzification blocks and an inference mechanism. The only difference is in the output. In type-2, the defuzzification block is preceded by a reduction block [26–28].

To implement this control on the PMSM, we maintained the similar structure of stator flow-oriented control but replaced the PI controllers with T2FL controllers of the same types, which have the same membership functions (Fig. 2). The difference lies in the normalisation gains.

In reference to the choice of membership function configurations within the defuzzification block of the control variation and the fuzzification block for the mistake and its variation [29, 30]. We opted for the Gaussian shape shown in Fig. 3.

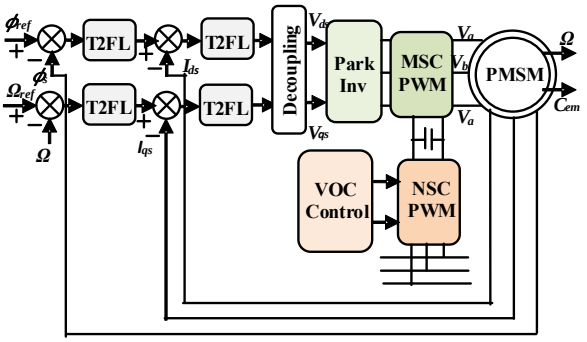

Fig. 2. Stator flow-oriented control based on T2FL controllers

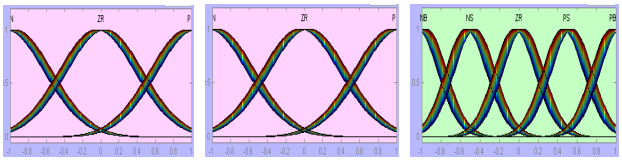

E *ΔE* *U*

Fig. 3. The employed membership functions

Decision rules for the type-2 fuzzy controller are represented in Table 1.

Table 1

Decision rules for the type-2 fuzzy controller

Control		Error		
		N	EZ	P
Derived from error	N	NG	NP	PP
	EZ	NG	EZ	PG
	P	NP	PP	PG

Comparative analysis between the controls developed. In order to evaluate the difference between the two controls implemented on our PMSM in this work, we shall do a comparative analysis of these controls. This research was replicated under identical condition.

Qualitative comparisons. This comparison relies on observing results obtained through simulating our motor within the MATLAB/Simulink environment, using the two control techniques developed. In this comparison, we carried out the test by implementing a resistive torque (C_r = 6 N·m) as an external variation of the instants (t = 0.5 s and t = 1.5 s) and a speed set point equal to the nominal speed of the PMSM (1000 rpm) (Fig. 4).

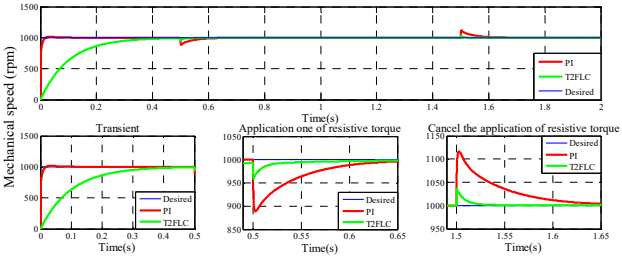

Fig. 4. Mechanical speed produced for the two controls with a zoom (external variation)

With an application and cancellation of external variation (resistive torque), the simulation results demonstrate that the mechanical speed adheres to their reference in both control types; however, the reaction time, overshoot, and exponential convergence of the errors for the steady state are not. When SFOC based on T2FL is used, the best value for these is evidently reached, making it the most effective and best-performing control when compared to the other control.

Quantitative comparisons. Our comparison is based on 4 criteria, all of which are derived from the quantitative findings of our PMSM control approaches and their application to simulations.

1) The integral error squared:

$$ISE = \int_0^t e^2(t)\mathrm{d}t\,. \tag{20}$$

2) The integral of the absolute value of the error:

$$IAE = \int_0^t \left|e\ (t)\right|\mathrm{d}t\,. \tag{21}$$

3) Integral of the time multiplied by the absolute value of the error:

$$ITAE = \int_0^t t\left|e(t)\right|\mathrm{d}t\,. \tag{22}$$

4) Integral of the time multiplied by the squared error:

$$ITSE = \int_0^t te^2\mathrm{d}t\,. \tag{23}$$

The results of the simulation (Table 2) indicate that SFOC based on T2FL controllers outperforms the other controls in minimising all criteria (ISE, IAE, ITAE, ITSE), yielding the lowest values.

Table 2

Quantitative comparison between the different controllers for external variations

Controlled variables	Criterion	Controls developed	
		SFOC PI	SFOC T2FL
Speed	*ISE*	277.140	12.1679
	IAE	4.9382	1.1503
	ITAE	2.6872	0.6643
	ITSE	144.7328	6.3375

Robustness comparisons. The final assessment focuses on conducting robustness tests for the proposed control strategies, which tests the impact of parametric changes (internal variation) of the PMSM on their performance. Being aware that these parameters can fluctuate in a real motor due to a variety of physical events (such as resistor heating, etc.), to apply this comparison we will decompose our state model of the machine as follows:

$$[A]=\left[\frac{R_s}{L_d}\begin{bmatrix}-1 & 0\\ 0 & 0\end{bmatrix}+\frac{R_s}{L_q}\begin{bmatrix}0 & 0\\ 0 & -1\end{bmatrix}+\frac{L_q}{L_d}\begin{bmatrix}0 & 1\\ 0 & 0\end{bmatrix}+\frac{L_d}{L_q}\begin{bmatrix}0 & 0\\ -1 & 0\end{bmatrix}\right];\tag{24}$$

$$[B]=\left[\frac{1}{Ld}\begin{bmatrix}1 & 0 & 0\\ 0 & 0 & 0\end{bmatrix}+\frac{1}{L_q}\begin{bmatrix}0 & 0 & 0\\ 0 & 1 & 0\end{bmatrix}+\frac{1}{L_q}\begin{bmatrix}0 & 0 & 0\\ 0 & 0 & -1\end{bmatrix}\right]\Omega\,. \tag{25}$$

In this comparison, we have plotted the mechanical velocity curve to show the robustness of the proposed controls (Fig. 5). The variation of the parameters will be applied between the instants $t = 0.8$ s and $t = 1.3$ s.

In this test, we visualized the velocity shape. The two proposed controls are very reliable and perform well even with small parameter fluctuations; However, the SFOC based on T2FL seems to be the best control, since it has an almost smooth speed curve and good tracking of the set point curve, followed by the SFOC based on PI corrector which gives us remarkable ripples compared with the other control.

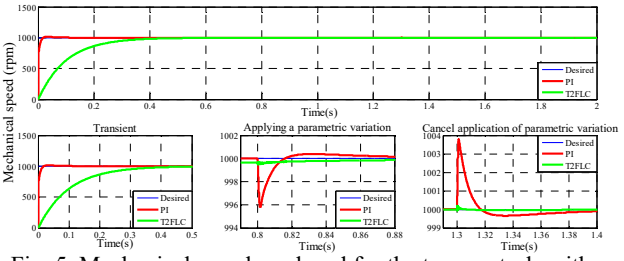

Fig. 5. Mechanical speed produced for the two controls with a zoom (internal variation)

Table 3 shows the comparison values for a robustness test between the two controls developed. The simulation results indicate that SFOC based on T2FL performs best for minimises error compared with stator flow-oriented control.

Table 3

Quantitative comparison between different controllers for robustness testing

Controlled variables	Criterion	Controls developed	
		SFOC PI	SFOC T2FL
Speed	*ISE*	0.1276	0.0057
	IAE	0.0957	0.0374
	ITAE	0.1037	0.0360
	ITSE	0.1329	0.0049

Conclusions. In this work, we developed a stator flow-oriented method using type-2 fuzzy logic controllers to solve parametric and external variation problems and achieve positive mechanical power output performance. Finally, a comparative study is conducted between this method and the one based on PI controllers where they obtained results clearly show that the SFOC based on T2FL controllers is the most efficient and effective PMSM control compared to the stator flux orientation control based on PI controllers both in transient and steady state, even with the application of external variations (EV) such as resistive torque or parametric variations (PV) of our machine.

The latter achieved:

- high response time R_t: R_t(EV) = 0.03 s, R_t(PV) = 0 s for SFOC based on T2FL and R_t(EV) = 0.15 s, R_t(PV) = = 0.2 s for SFOC based on PI.

- minimal overshoot (Mo): Mo(EV) = 40 rpm, Mo(PV) = 0 rpm for SFOC based on T2FL and Mo(EV) = = 110 rpm, Mo(PV) = 4 rpm for SFOC based on PI.

- *ITAE* that is close to 0: *ITAE*(EV) = 0.6643, *ITAE*(PV)= 0.036 for SFOC based on T2FL and *ITAE*(EV) = = 2.6872, *ITAE*(PV)=0.1037 for SFOC based on PI.

These results obtained with the new stator flow-oriented control based on T2FL controllers call for the teaching of this method in academic circles and also for its application in industrial circles.

Conflict of interest. The authors declare that they have no conflicts of interest.

REFERENCES

1. Yazdan T., Humza M., Cho H.-W. Three-Phase Dual-Winding Multitasked PMSM Machine Using Double Layer Concentrated Winding for HEV Application. *IEEE Access*, 2023, vol. 11, pp. 36682-36691. doi: https://doi.org/10.1109/ACCESS.2023.3264568.

2. Thangavel S., Mohanraj D., Girijaprasanna T., Raju S., Dhanamjayulu C., Muyeen S.M. A Comprehensive Review on Electric Vehicle: Battery Management System, Charging Station, Traction Motors. *IEEE Access*, 2023, vol. 11, pp. 20994-21019. doi: https://doi.org/10.1109/ACCESS.2023.3250221.

3. Khowja M.R., Singh K., la Rocca A., Vakil G., Ramnathan R., Gerada C. Fault-Tolerant Dual Channels Three-Phase PMSM for

Aerospace Applications. *IEEE Access*, 2024, vol. 12, pp. 126845-126857. doi: https://doi.org/10.1109/ACCESS.2024.3451705.
4. Li S., Xu Y., Zhang W., Zou J. A Novel Two-Phase Mode Switching Control Strategy for PMSM Position Servo Systems With Fast-Response and High-Precision. *IEEE Transactions on Power Electronics*, 2023, vol. 38, no. 1, pp. 803-815. doi: https://doi.org/10.1109/TPEL.2022.3200969.
5. Jin L., Mao Y., Wang X., Shi P., Lu L., Wang Z. Optimization-Based Maximum-Torque Fault-Tolerant Control of Dual Three-Phase PMSM Drives Under Open-Phase Fault. *IEEE Transactions on Power Electronics*, 2023, vol. 38, no. 3, pp. 3653-3663. doi: https://doi.org/10.1109/TPEL.2022.3222224.
6. Guezi A., Bendaikha A., Dendouga A. Direct torque control based on second order sliding mode controller for three-level inverter-fed permanent magnet synchronous motor: comparative study. *Electrical Engineering & Electromechanics*, 2022, no. 5, pp. 10-13. doi: https://doi.org/10.20998/2074-272X.2022.5.02.
7. Petkar S.G., Thippiripati V.K. A Novel Duty-Controlled DTC of a Surface PMSM Drive With Reduced Torque and Flux Ripples. *IEEE Transactions on Industrial Electronics*, 2023, vol. 70, no. 4, pp. 3373-3383. doi: https://doi.org/10.1109/TIE.2022.3181405.
8. Huang Y., Zhao M., Zhang J., Lu M. The Hall Sensors Fault-Tolerant for PMSM Based on Switching Sensorless Control With PI Parameters Optimization. *IEEE Access*, 2022, vol. 10, pp. 114048-114059. doi: https://doi.org/10.1109/ACCESS.2022.3218325.
9. Aib A., Khodja D.E., Chakroune S. Field programmable gate array hardware in the loop validation of fuzzy direct torque control for induction machine drive. *Electrical Engineering & Electromechanics*, 2023, no. 3, pp. 28-35. doi: https://doi.org/10.20998/2074-272X.2023.3.04.
10. Wadawa B., Errami Y., Obbadi A., Sahnoun S. Robustification of the H_∞ controller combined with fuzzy logic and PI&PID-F_d or hybrid control of wind energy conversion system connected to the power grid based on DFIG. *Energy Reports*, 2021, vol. 7, pp. 7539-7571. doi: https://doi.org/10.1016/j.egyr.2021.10.120.
11. Sathish Babu P., Sundarabalan C.K., Balasundar C., Santhana Krishnan T. Fuzzy logic based optimal tip speed ratio MPPT controller for grid connected WECS. *Materials Today: Proceedings*, 2021, vol. 45, pp. 2544-2550. doi: https://doi.org/10.1016/j.matpr.2020.11.259.
12. Jasmine Gnana Malar A., Agees Kumar C., Gnana Saravanan A. Iot based sustainable wind green energy for smart cites using fuzzy logic based fractional order darwinian particle swarm optimization. *Measurement*, 2020, vol. 166, art. no. 108208. doi: https://doi.org/10.1016/j.measurement.2020.108208.
13. Verma P., Garg R., Mahajan P. Asymmetrical interval type-2 fuzzy logic control based MPPT tuning for PV system under partial shading condition. *ISA Transactions*, 2020, vol. 100, pp. 251-263. doi: https://doi.org/10.1016/j.isatra.2020.01.009.
14. Kececioglu O.F., Gani A., Sekkeli M. Design and Hardware Implementation Based on Hybrid Structure for MPPT of PV System Using an Interval Type-2 TSK Fuzzy Logic Controller. *Energies*, 2020, vol. 13, no. 7, art. no. 1842. doi: https://doi.org/10.3390/en13071842.
15. Benghanem M., Chettibi N., Mellit A., Almohamadi H. Type-2 fuzzy-logic based control of photovoltaic-hydrogen production systems. *International Journal of Hydrogen Energy*, 2023, vol. 48, no. 91, pp. 35477-35492. doi: https://doi.org/10.1016/j.ijhydene.2023.05.360.
16. Zellouma D., Bekakra Y., Benbouhenni H. Field-oriented control based on parallel proportional–integral controllers of induction motor drive. *Energy Reports*, 2023, vol. 9, pp. 4846-4860. doi: https://doi.org/10.1016/j.egyr.2023.04.008.
17. Khanday S.A., Bhat A.H., Sekhar O.C. Performance Analysis of Space Vector Approach Based Field Oriented Control of Indirect Matrix Converter Fed PMSM Drive. *2023 7th International Conference on Computer Applications in Electrical Engineering-Recent Advances (CERA)*, 2023, pp. 1-6. doi: https://doi.org/10.1109/CERA59325.2023.10455147.
18. Wu T., Lyu M., Wu X., Yang M., Wang Y., Huang S., Ouyang X., Rodriguez J. Enhanced Model Predictive Control for PMSM Based on Reference Voltage Predictive Model. *IEEE Journal of Emerging and Selected Topics in Power Electronics*, 2023, vol. 11, no. 5, pp. 5290-5300. doi: https://doi.org/10.1109/JESTPE.2023.3307469.
19. Hossain M.S., Said N.A.M., Hasan M.A., Halim W.A., Munim W.N.W.A., Jidin A. Performance evaluation of a nearest level control-based TCHB multilevel inverter for PMSM motors in electric vehicle systems. *Results in Engineering*, 2025, vol. 25, art. no. 103949. doi: https://doi.org/10.1016/j.rineng.2025.103949.
20. Benzouaoui A., Khouidmi H., Bessedik B. Parallel model predictive direct power control of DFIG for wind energy conversion. *International Journal of Electrical Power & Energy Systems*, 2021, vol. 125, art. no. 106453. doi: https://doi.org/10.1016/j.ijepes.2020.106453.
21. Zamzoum O., Derouich A., Motahhir S., El Mourabit Y., El Ghzizal A. Performance analysis of a robust adaptive fuzzy logic controller for wind turbine power limitation. *Journal of Cleaner Production*, 2020, vol. 265, art. no. 121659. doi: https://doi.org/10.1016/j.jclepro.2020.121659.
22. Acikgoz H., Yildiz C., Coteli R., Dandil B. DC-link voltage control of three-phase PWM rectifier by using artificial bee colony based type-2 fuzzy neural network. *Microprocessors and Microsystems*, 2020, vol. 78, art. no. 103250. doi: https://doi.org/10.1016/j.micpro.2020.103250.
23. Kou L., Liu C., Cai G., Zhang Z., Zhou J., Wang X. Fault diagnosis for three-phase PWM rectifier based on deep feedforward network with transient synthetic features. *ISA Transactions*, 2020, vol. 101, pp. 399-407. doi: https://doi.org/10.1016/j.isatra.2020.01.023.
24. Darsouni Z., Rezgui S.E., Benalla H., Rebahi F., Boumendjel M.A.M. Ensuring service continuity in electric vehicles with vector control and linear quadratic regulator for dual star induction motors. *Electrical Engineering & Electromechanics*, 2025, no. 2, pp. 24-30. doi: https://doi.org/10.20998/2074-272X.2025.2.04.
25. Kuczmann M., Horvath K. Tensor Product Alternatives for Nonlinear Field-Oriented Control of Induction Machines. *Electronics*, 2024, vol. 13, no. 7, art. no. 1405. doi: https://doi.org/10.3390/electronics13071405.
26. Khemis A., Boutabba T., Drid S. Model reference adaptive system speed estimator based on type-1 and type-2 fuzzy logic sensorless control of electrical vehicle with electrical differential. *Electrical Engineering & Electromechanics*, 2023, no. 4, pp. 19-25. doi: https://doi.org/10.20998/2074-272X.2023.4.03.
27. Rouabhi R., Herizi A., Djeriou S., Zemmit A. Hybrid type-1 and 2 fuzzy sliding mode control of the induction motor. *Revue Roumaine des Sciences Techniques Serie Electrotechnique et Energetique*, 2024, vol. 69, no. 2, pp. 147-152. doi: https://doi.org/10.59277/RRST-EE.2024.2.5.
28. Srinivas G., Durga Sukumar G., Subbarao M. Total harmonic distortion analysis of inverter fed induction motor drive using neuro fuzzy type-1 and neuro fuzzy type-2 controllers. *Electrical Engineering & Electromechanics*, 2024, no. 1, pp. 10-16. doi: https://doi.org/10.20998/2074-272X.2024.1.02.
29. Rouabhi R., Zemmit A., Herizi A., Moussa O., Djeriou S. Hybrid type-2 fuzzy backstepping control of doubly fed induction generator for wind energy conversion systems. *Journal of the Brazilian Society of Mechanical Sciences and Engineering*, 2025, vol. 47, no. 1, art. no. 24. doi: https://doi.org/10.1007/s40430-024-05293-z.
30. Rouabhi R., Herizi A., Djerioui A. Performance of Robust Type-2 Fuzzy Sliding Mode Control Compared to Various Conventional Controls of Doubly-Fed Induction Generator for Wind Power Conversion Systems. *Energies*, 2024, vol. 17, no. 15, art. no. 3778. doi: https://doi.org/10.3390/en17153778.

Received 04.09.2025
Accepted 23.12.2025
Published 02.05.2026

M. Tabbakh[1,2], *Doctor of Sciences, Lecturer,*
R. Rouabhi [1,2], *Doctor of Sciences, Professor,*
A. Herizi [1,2], *Doctor of Sciences, Professor,*
N. Chami [3], *Doctor of Sciences, Lecturer,*
[1] Department of Electronic, Faculty of Technology,
University of M'sila, Algeria.
[2] LGE Research Laboratory, University of M'sila, Algeria,
e-mail: riyadh.rouabhi@univ-msila.dz (Corresponding Author)
[3] Electrical Engineering Department,
University of Formation Continue, Algeria.

How to cite this article:
Tabbakh M., Rouabhi R., Herizi A., Chami N. A new stator flow-oriented control method based on type-2 fuzzy logic controllers for permanent magnet synchronous motors. *Electrical Engineering & Electromechanics*, 2026, no. 3, pp. 68-72. doi: https://doi.org/10.20998/2074-272X.2026.3.10

UDC 621.314 https://doi.org/10.20998/2074-272X.2026.3.11

A. Ahmane, D. Sakri, S.E. Farhi, N. Golea

Three-phase pulse width modulation boost rectifier enhancement direct power control based on super-twisting algorithm

Introduction. *Three-phase pulse width modulation (PWM) rectifiers are widely used in modern power conversion systems due to their high efficiency, controllability, and ability to provide high-quality energy conversion. They play a crucial role in applications such as motor drives, renewable energy integration, and power supplies, where a stable DC voltage and low harmonic distortion are essential. The conventional direct power control (DPC) method, based on a 12-sector switching table, is commonly employed for its simple implementation, reduced complexity, and fast dynamic response.* ***Problem.*** *Despite its simplicity and fast dynamic response, the classical DPC approach is highly sensitive to parameter variations and relies on a predefined switching table, which limits its robustness and current quality.* ***Goal.*** *To experimentally validate an improved control strategy for a three-phase PWM rectifier that enhances robustness and current quality by integrating the super-twisting algorithm (STA) into the conventional DPC framework.* ***Methodology.*** *The proposed STA-based DPC was implemented and tested on an experimental setup using a dSPACE DS1104 digital control board. Both the conventional DPC and the modified STA-based DPC were experimentally evaluated under the same operating conditions to ensure fair comparison.* ***Results.*** *Experimental results demonstrate that the STA-based DPC achieves a THD reduction from 11.85 % to 6.11 % and improves the stability of the DC-link voltage under parameter variations. These quantitative results confirm current quality, improved robustness and reduced chattering compared to the classical DPC.* ***Scientific novelty.*** *Integrating the STA into the DPC framework eliminates dependence on the predefined switching table and enhances robustness to system uncertainties.* ***Practical value.*** *The experimental validation confirms the feasibility and effectiveness of implementing the STA-based DPC in real-time applications, offering a reliable and high-performance solution for modern power conversion systems.* References 17, tables 4, figures 19.
Key words: **direct power control, sliding mode control, super twisting algorithm, three-phase PWM rectifier, dSPACE 1104.**

Вступ. *Трифазні випрямлячі з ШІМ (PWM) широко застосовуються в сучасних системах перетворення енергії завдяки їх високій ефективності, керованості та здатності забезпечувати високу якість електроенергії. Вони відіграють важливу роль у таких застосуваннях, як електроприводи, інтеграція відновлюваних джерел енергії та системи живлення, де необхідні стабільна напруга постійного струму та низький рівень гармонічних спотворень. Традиційний метод прямого керування потужністю (DPC), заснований на 12-секторній таблиці перемикання, широко застосовується завдяки простоті реалізації, зниженій складності та високій швидкодії.* ***Проблема.*** *Незважаючи на простоту та швидку динамічну реакцію, класичний підхід DPC є чутливим до варіацій параметрів і базується на заздалегідь визначеній таблиці перемикання, що обмежує його робастність і якість струму.* ***Мета.*** *Експериментально підтвердити ефективність удосконаленої стратегії керування трифазним PWM-випрямлячем, яка підвищує робастність і якість струму шляхом інтеграції алгоритму суперскручування (STA) у структуру класичного DPC.* ***Методика.*** *Запропонований підхід DPC на основі STA реалізовано та досліджено на експериментальному стенді з використанням плати цифрового керування dSPACE DS1104. Як класичний DPC, так і модифікований DPC на основі STA експериментально оцінювалися за однакових умов роботи для забезпечення коректного порівняння.* ***Результати.*** *Експериментальні результати показали, що DPC на основі STA забезпечує зниження коефіцієнта гармонічних спотворень (THD) з 11,85 % до 6,11 % та покращує стабільність напруги в ланці постійного струму за умов зміни параметрів. Отримані результати підтверджують покращення якості струму, підвищення робастності та зменшення тремтіння порівняно з класичним DPC.* ***Наукова новизна.*** *Інтеграція STA в структуру DPC усуває залежність від заздалегідь визначеної таблиці перемикання та підвищує робастність до невизначеностей системи.* ***Практична значимість.*** *Експериментальна валідація підтверджує доцільність і ефективність реалізації DPC на основі STA в системах реального часу, що забезпечує надійне та високоефективне рішення для сучасних систем перетворення електроенергії.* Бібл. 17, табл. 4, рис. 19.
Ключові слова: **пряме керування потужністю, керування в ковзному режимі, алгоритм суперскручування, трифазний ШІМ випрямляч, dSPACE 1104.**

Introduction. The control of three-phase pulse width modulation (PWM) boost rectifiers is a key challenge in modern power electronics, particularly for applications that require high energy efficiency and fast dynamic response. Among the various available control strategies, direct power control (DPC) has established itself as an effective solution due to its ability to regulate both active and reactive power without relying on complex modulation techniques [1, 2]. The classical version of DPC is widely adopted for its straightforward implementation and satisfactory dynamic performance [3]. However, this approach also exhibits certain limitations, including steady-state power oscillations and increased sensitivity to parameter variations, which can degrade its performance in practical operating conditions [2].

To overcome these drawbacks an improved version, known as super twisting algorithm-based direct power control (STA-DPC), is proposed. This approach leverages the super twisting sliding mode control (STA-SMC) algorithm to enhance robustness against external disturbances and to significantly mitigate the chattering effect commonly associated with sliding mode control techniques [4, 5]. Unlike the conventional DPC, which relies on fixed switching tables, STA-DPC exclusively uses real-time current and voltage measurements to compute and regulate power, ensuring a more stable and adaptive control process [3, 4].

The main objective of this paper is to experimentally validate, using a dSPACE1104-based digital control platform, the DPC strategy in both its conventional form and the optimized version incorporating the STA. The study aims to compare the performance of both approaches in terms of regulation quality, robustness, and total harmonic distortion (THD) reduction. The expected results demonstrate the benefits of integrating sliding mode control to enhance the performance of three-phase PWM boost rectifiers and open new perspectives for developing more advanced and reliable power converter control strategies [6].

The **goal** of this work is to experimentally validate an improved control strategy for a three-phase PWM rectifier that enhances robustness and current quality by integrating the super-twisting algorithm (STA) into the conventional DPC framework.

Topology and modeling of a three-phase boost PWM rectifier. For modeling purposes, the equivalent single-phase electrical circuit is shown in Fig. 1.

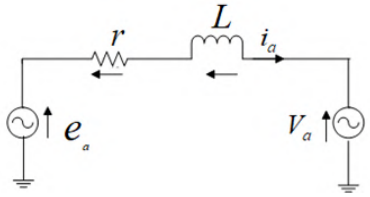

Fig. 1. Per-phase electrical circuit model of the PWM rectifier

Based on the per-phase equivalent circuit in Fig. 1, the AC-side equations for all 3 phases are given by:

$$\begin{cases} L\dfrac{\mathrm{d}i_a}{\mathrm{d}t} = e_a - ri_a - V_a; \\ L\dfrac{\mathrm{d}i_b}{\mathrm{d}t} = e_b - ri_b - V_b; \\ L\dfrac{\mathrm{d}i_c}{\mathrm{d}t} = e_c - ri_c - V_c, \end{cases} \tag{1}$$

where i_a, i_b, i_c are the 3-phase grid currents; e_a, e_b, e_c are the 3-phase grid voltages; V_a, V_b, V_c are the controllable bridge converter voltage, regulated from the DC side; r is the resistance of the interconnecting filters; L is the inductance of the interconnecting filters.

The topology of the 3-phase PWM rectifier is illustrated in Fig. 2 [7, 8].

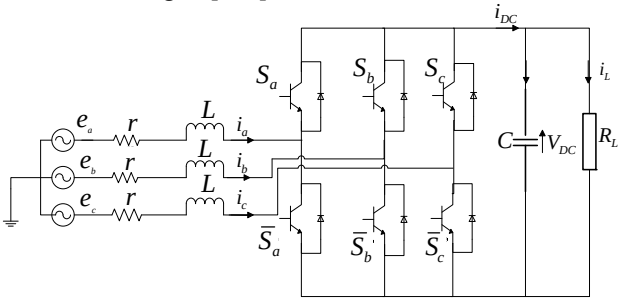

Fig. 2. Three-phase PWM rectifier electrical circuit

According to (1) and Fig. 2, a 3-phase PWM rectifier equation is given as follows [7, 8]:

$$\begin{cases} L\dfrac{\mathrm{d}i_a}{\mathrm{d}t} = e_a - ri_a - \dfrac{V_{DC}}{3}(2S_a - S_b - S_c); \\ L\dfrac{\mathrm{d}i_b}{\mathrm{d}t} = e_b - ri_b - \dfrac{V_{DC}}{3}(-S_a + 2S_b - S_c); \\ L\dfrac{\mathrm{d}i_c}{\mathrm{d}t} = e_c - ri_c - \dfrac{V_{DC}}{3}(-S_a - S_b + 2S_c); \\ C\dfrac{\mathrm{d}V_{DC}}{\mathrm{d}t} = (S_a i_a + S_b i_b + S_c i_c) - \dfrac{V_{DC}}{R_L}, \end{cases} \tag{2}$$

where: V_{DC} is the DC link voltage; R_L is the load resistance on the DC side; C is the capacitance on the DC side; S_a, S_b, S_c are the control signals.

Using the Park transformation, the PWM rectifier equations expressed in the stationary a, b, c frame are converted into the synchronous d-q frame for simplified analysis [9]:

$$\begin{cases} L\dfrac{\mathrm{d}i_d}{\mathrm{d}t} = e_d - ri_d + \omega L i_q + V_d; \\ L\dfrac{\mathrm{d}i_q}{\mathrm{d}t} = e_q - ri_q + \omega L i_d + V_q; \\ C\dfrac{\mathrm{d}V_{DC}}{\mathrm{d}t} = S_d i_d + S_q i_q - \dfrac{V_{DC}}{R_L}, \end{cases} \tag{3}$$

where $V_d = -S_d V_{DC}$; $V_q = -S_q V_{DC}$; i_d, i_q are the grid currents in d-q reference frame; e_d, e_q are the grid voltages in d-q reference frame; V_d, V_q are the controllable bridge converter voltage, regulated from the DC side in d-q reference frame.

The source delivers both active P and reactive Q powers, which are defined as:

$$P = \mathrm{Re}\{\underline{u} \cdot \underline{i}^*\} = e_a i_a + e_b i_b + e_c i_c; \\ P = e_\alpha i_\alpha + e_\beta i_\beta; \tag{4}$$

$$Q = \mathrm{Im}\{\underline{u} \cdot \underline{i}^*\} = \frac{1}{\sqrt{3}}(e_a i_a + e_b i_b + e_c i_c); \\ Q = e_\beta i_\alpha + e_\alpha i_\beta. \tag{5}$$

It gives in the synchronous d-q coordinates:

$$P = e_d i_d + e_q i_q; \\ Q = e_q i_d + e_d i_q. \tag{6}$$

Direct power control (DPC) is an advanced control technique implemented on 3-phase converters employing PWM to regulate active and reactive power flows, this method relies on the instantaneous measurement of phase voltages and currents, from which the active and reactive powers are determined in real time [10, 11].

The computed power values are then continuously compared with their respective reference values. The resulting error signals are processed by hysteresis regulators, which determine the appropriate voltage vector components, typically within the stationary $\alpha\beta$ reference frame. Based on these control variables, a switching table is utilized to generate the required gating signals for the converter switches, thereby ensuring fast and accurate power regulation (Fig. 3) [3, 7, 8].

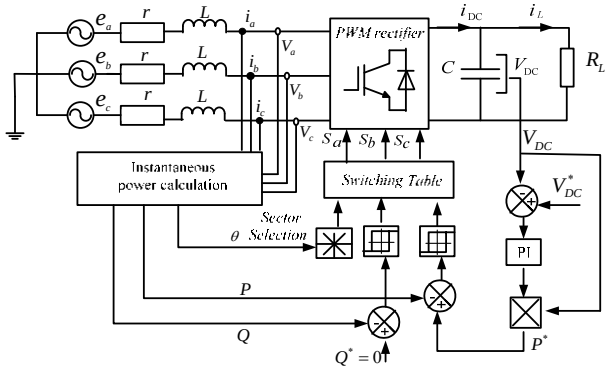

Fig. 3. DPC scheme

The angular region of the voltage (or flux) vector is divided into 12 sectors, which can be numerically indexed as:

$$(n-1)\frac{\pi}{6} \le \theta < n\frac{\pi}{6}, \tag{7}$$

where n is the sector number, ranging from 1 to 12; $\theta \in [0; 2\pi]$ is the voltage vector position obtained as:

$$\theta = \mathrm{arctg}(V_\beta / V_\alpha). \tag{8}$$

Table 1 defines the switching logic used in the DPC scheme to generate the inverter switching signals. The table receives 3 inputs: the outputs of the hysteresis comparators for the active and reactive power errors (d_p and d_q), and the sector angle θ that indicates the position of the reference voltage vector in the α, β plane. Based on the combination of these inputs, the corresponding voltage vector (V_0–V_7) is selected from the table. Each voltage vector represents a specific switching state of the inverter, determining which semiconductor devices are turned on or off. In this way, the table translates the instantaneous power errors and the sector location into the appropriate switching commands, ensuring fast and accurate control of active and reactive power.

Table 1

Switching table for DPC

d_p	1	1	0	0
d_q	0	1	0	1
θ_1	V_6	V_7	V_1	V_2
θ_2	V_0	V_0	V_1	V_2
θ_3	V_1	V_0	V_2	V_3
θ_4	V_7	V_7	V_2	V_3
θ_5	V_2	V_7	V_3	V_4
θ_6	V_0	V_0	V_3	V_4
θ_7	V_3	V_0	V_4	V_5
θ_8	V_7	V_7	V_4	V_5
θ_9	V_4	V_7	V_5	V_6
θ_{10}	V_0	V_0	V_5	V_6
θ_{11}	V_5	V_0	V_6	V_1
θ_{12}	V_7	V_7	V_6	V_1

Experimental validation of classical DPC. While simulation alone cannot capture all real-world physical phenomena – such as measurement errors, delays, data processing times and noise – real-time implementation of control techniques is essential for evaluating algorithm performance under practical conditions. In this section, the classical DPC scheme, which integrates a PI regulator for DC-link voltage regulation and hysteresis controllers for active and reactive power, is validated experimentally using a dSPACE 1104 card. The objective is to assess its real-time behavior on an experimental test bench developed in our LGEA laboratory. The experimental tests were conducted according to Fig. 4, which presents the experimental setup and highlights the main devices used for validation. The detailed list and specifications of these components are provided in Table 2, ensuring accurate measurements and effective control throughout the experiments.

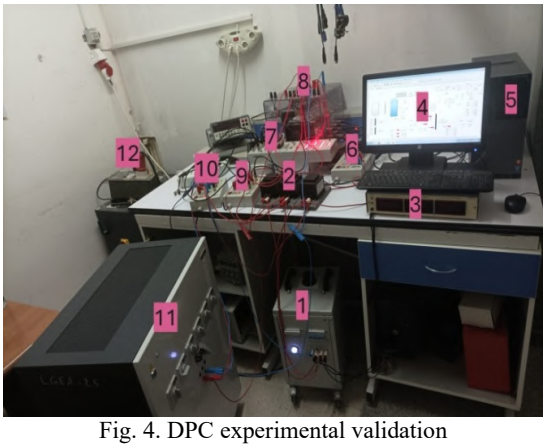

Fig. 4. DPC experimental validation

Table 2

The devices list of DPC experimental tests

Number	Name
1	3-phase autotransformer
2	3-phase inductor
3	Ammeter
4	Simulink and ControlDesk
5	PC unit includes a DS1104 card
6	Interface card
7	Control panel CLP 1104
8	SEMIKRON inverter
9	Current sensors
10	Voltage sensors
11	DC variable load
12	3-phase AC supply

The main parameters of the 3-phase PWM rectifier used in the simulations are summarized in Table 3.

Table 3

Parameters of 3-phase PWM rectifier

Parameters	Value
Grid voltage, V	120
Reference of DC-link voltage V^*_{DC}, V	300
Grid line inductance L, mH	10
Grid line resistance r, Ω	0.1
DC-link capacitor C, μF	1100
Load resistance R_L, Ω	80 → 50
Grid frequency f, Hz	50

Two experiments are carried out to evaluate the performance of the proposed control scheme under different operating conditions.

Test 1. In the first experiment, the DC-link voltage was kept constant at 200 V, while the load resistance was decreased from 80 Ω to 50 Ω. The waveforms of the different variables obtained via ControlDesk are displayed in Fig. 5–8. Figure 5 shows that the DC-link voltage accurately tracks its reference without being affected by load variations, demonstrating that the regulator provides a fast dynamic response and ensures voltage stability despite transient fluctuations in load power.

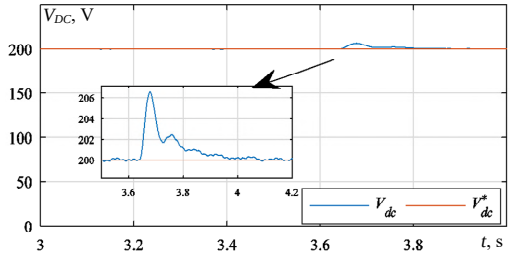

Fig. 5. DC-link voltage

Figure 6 shows the active power, demonstrating its ability to accurately track its reference even during load variations; when the load changes at 3.6 s, the active power continues to follow its setpoint, highlighting the system's fast response and strong dynamic performance.

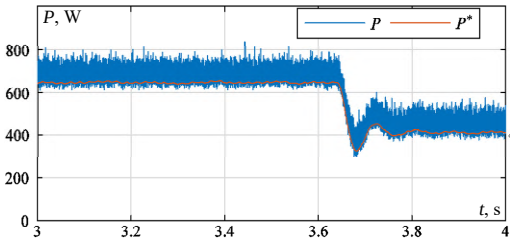

Fig. 6. Active power and its reference

Figure 7 shows the reactive power and its reference, indicating that the reactive power remains at zero throughout the transient period, thereby confirming that a unity power factor is maintained.

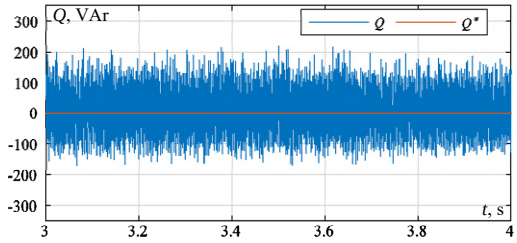

Fig. 7. Reactive power and its reference

Figure 8 presents, on the same graph, the current and voltage waveforms of the first grid phase. Both waveforms are sinusoidal and in phase, indicating operation at a unity power factor.

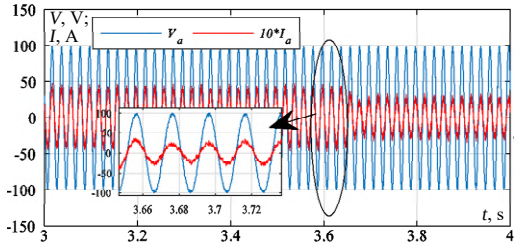

Fig. 8. Input voltage and current for the rectifier

Test 2. In the second experiment, the load resistance was kept constant at 80 Ω, while the DC-link voltage was reduced from 250 V to 200 V. Figures 9–11 show the results of the second test. The analysis of the waveforms yields the following comments:

- The DC-link voltage constantly tracks its reference profile.
- The active power clearly follows the generated reference with high accuracy, reflecting the applied load variations.
- The reactive power maintains a zero average value under varying load conditions, thereby ensuring unity power factor operation.

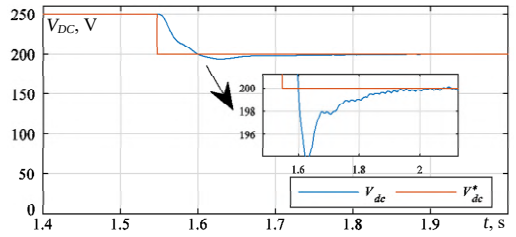

Fig. 9. DC link voltage and his reference

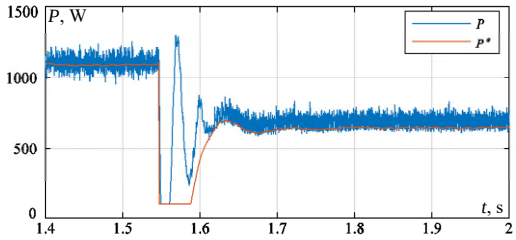

Fig. 10. Active power and his reference

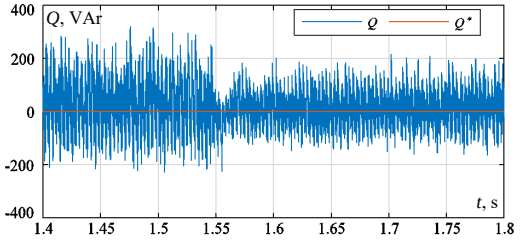

Fig. 11. Reactive power and his reference

Super twisting direct power control. The super-twisting sliding mode control (STA-SMC) is a robust nonlinear control strategy that has proven highly effective in enhancing the dynamic performance of 3-phase PWM rectifiers (Fig. 12). These rectifiers are widely employed in industrial applications to convert AC into DC while maintaining a high power factor, minimizing THD, and enabling bidirectional power flow [12, 13].

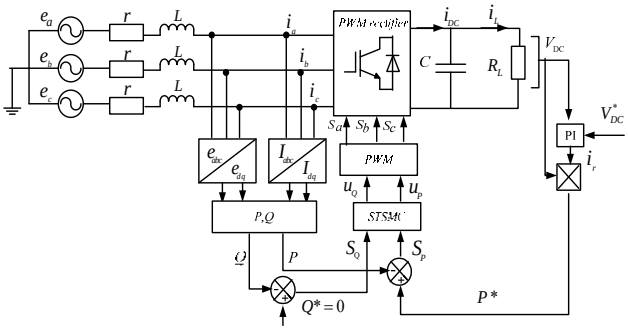

Fig. 12. STA-DPC scheme

The implementation of STA-SMC provides an effective solution for enhancing the dynamic performance of 3-phase PWM rectifiers, owing to its inherent robustness, high precision, and capability to mitigate chattering effects [14, 15]. These characteristics make it particularly well suited for applications in renewable energy systems, industrial automation, and electric vehicle charging stations. However, its practical deployment presents 2 major challenges: first, its complex design requires careful tuning of parameters, such as sliding surface coefficients and control gains, to achieve an optimal trade-off between performance and robustness; second, it involves significant computational demands, as real-time implementation requires solving nonlinear equations, which often necessitates the use of advanced digital signal processors (DSPs) [6, 15].

The STA-SMC law u_{ST} is composed of two components [16, 17]. The first component is represented by its time derivative $u_1(t)$, while the second component is determined as a function of the sliding variable $u(t)$. The STA control law is expressed as [12]:

$$u_{ST} = u(t) + u_1(t), \tag{9}$$

with:
$$\begin{cases} u = -\lambda |S|^{\rho} \operatorname{sign}(S); \\ \dot{u}_1 = \alpha \operatorname{sign}(S), \end{cases}$$

where α, $\lambda > 0$ that are used to regulate the STA; ρ is the parameter used to adjust the degree of non-linearity, where $0 < \rho < 0.5$.

To perform maximum second-order SMC, ρ is often set to 0.5. The law STSMC for the power controller is defined by:

$$\begin{cases} u_{ST} = -\lambda |S|^{0.5} \operatorname{sign}(S) + u_1; \\ \dot{u}_1 = \alpha \operatorname{sign}(S). \end{cases} \quad (10)$$

In (10), $\lambda = \sqrt{u}$ and $\alpha = 1.1u$, where $u > 0$ with sufficiently large value. Here, the power errors $e_1 = P_{ref} - P$ and $e_2 = Q_{ref} - Q$ are chosen as the sliding surfaces. This approach is based on the STA without an equivalent control term. The stability proof of this control strategy and the convergence of the states can be found in [14].

Experimental validation of STA-DPC. For this control strategy based on the STA algorithm, two test scenarios are considered: first, a variation of the load resistance between 50 Ω and 80 Ω while maintaining a constant DC bus voltage; then, an increase in the DC bus reference voltage with the load resistance fixed at 80 Ω. The measured variables acquired via ControlDesk are illustrated by curves in Fig. 13–19.

Test 1 (load resistance variation). Unlike the first conventional DPC control technique; this experimental test consists in increasing the load to 80 Ω within the interval [6 s, 16 s] in order to observe the behavior of the different variables. The analysis of these variables allows us to make the following remarks:

- The DC bus voltage perfectly tracks its reference with excellent disturbance rejection in response to the load variation at 6 s and 16 s.
- The active power provided by the electrical grid adjusts to meet the load demand: it decreases when the load increases and accurately tracks its reference. Meanwhile, the reactive power maintains a zero average value, which improves the quality of the supplied energy and ensures that the current remains in phase with the grid voltage (Fig. 16).
- The voltage remains purely sinusoidal with fixed amplitude, while the currents preserve a sinusoidal waveform whose amplitude varies in accordance with load fluctuations.

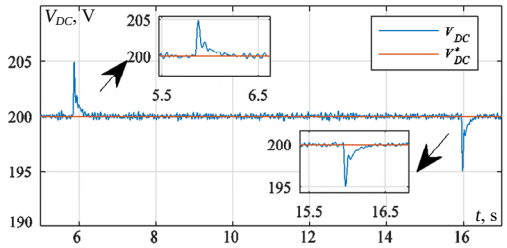

Fig. 13. DC-link voltage

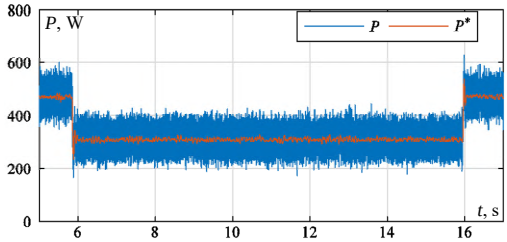

Fig. 14. Active power and its reference

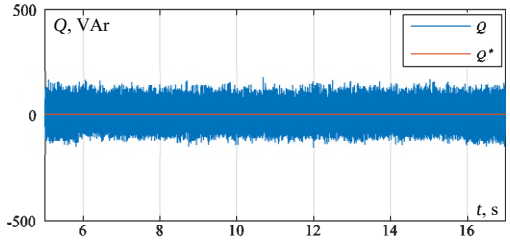

Fig. 15. Reactive power and its reference

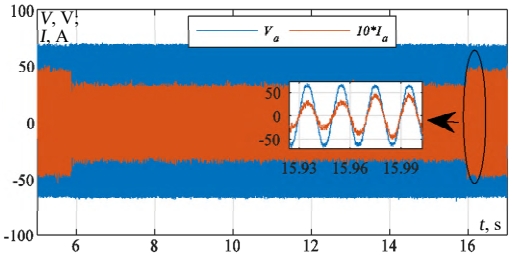

Fig. 16. Input voltage and current for the rectifier

Test 2. DC-link reference voltage increase. In this second test, the load resistance was kept constant at 80 Ω, while the DC-link reference voltage was increased from 180 V to 200 V. Figures 17–19 illustrate the corresponding results:

- The DC-link voltage consistently follows its reference profile.
- The active power accurately tracks the generated reference, clearly reflecting the applied load conditions.
- The reactive power remains zero on average, even under DC-link voltage variations, thereby guaranteeing operation at unity power factor.

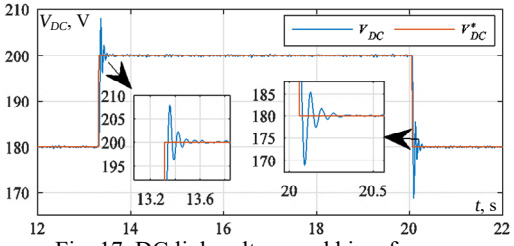

Fig. 17. DC link voltage and his reference

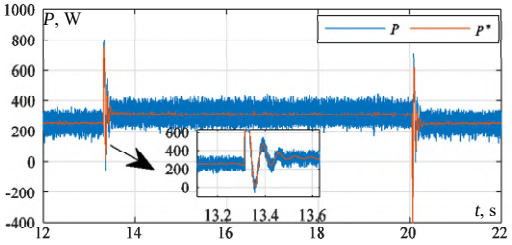

Fig. 18. Active power and its reference

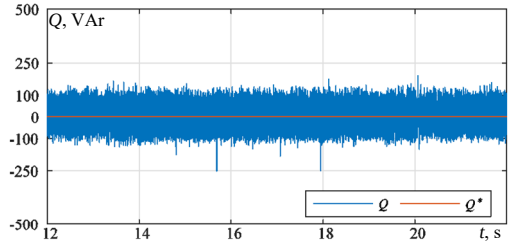

Fig. 19. Reactive power and its reference

In the practical tests, when the STA-DPC strategy was implemented in Test 1 (with load variation), the THD

dropped to 6.11 %, compared to 11.85 % with the classical DPC (Table 4). This significant reduction demonstrates the superior capability of the STA-DPC approach to minimize harmonics and improve current quality.

In Test 2 (the DC-link voltage varied) the classical DPC recorded a THD of 10.21 %, whereas the STA-DPC achieved a slightly lower value of 9.7 %. Although the improvement is less substantial than in the variable load scenario, it still confirms the enhanced harmonic mitigation performance of the STA-DPC method.

It is worth noting that the limited accuracy of the current and voltage sensors may have adversely affected the measurements. Under ideal sensing conditions, even better THD performance could likely be achieved.

Table 4

THD value

Strategy	DC-link voltage variation	Load variation
DPC	10.21 %	11.85 %
STA-DPC	9.7 %	6.11 %

Conclusions. This study experimentally validated an improved control strategy for a 3-phase PWM rectifier by integrating the STA into the conventional DPC framework.

The experimental implementation on a DSP-1104 platform demonstrated that the proposed DPC-STA approach significantly enhances system robustness, dynamic response, and current quality compared to the classical DPC method. In particular, the reduction of THD from 11.85 % to 6.11 % confirms the effectiveness of the proposed method in improving current waveform quality and ensuring stable DC-link regulation under parameter variations.

Beyond validating the control performance, this work confirms the feasibility of implementing second-order sliding mode techniques in real-time power converter applications. Future research will focus on extending this approach to grid-connected converters and renewable energy interfaces to further exploit its robustness and control accuracy.

Conflict of interest. The authors declare that they have no conflicts of interest.

REFERENCES

1. Escobar G., Stankovic A.M., Carrasco J.M., Galvan E., Ortega R. Analysis and design of direct power control (DPC) for a three phase synchronous rectifier via output regulation subspaces. *IEEE Transactions on Power Electronics*, 2003, vol. 18, no. 3, pp. 823-830. doi: https://doi.org/10.1109/TPEL.2003.810862.

2. Ouchen S., Abdeddaim S., Betka A., Menadi A. Experimental validation of sliding mode-predictive direct power control of a grid connected photovoltaic system, feeding a nonlinear load. *Solar Energy*, 2016, vol. 137, pp. 328-336. doi: https://doi.org/10.1016/j.solener.2016.08.031.

3. Liu Z. A review of Direct Power Control Technologies for Three-Phase Voltage PWM Rectifiers. *Science and Technology of Engineering, Chemistry and Environmental Protection*, 2024, vol. 2, no. 7, pp. 1-5. doi: https://doi.org/10.61173/h3f6e192.

4. Fekik A., Hamida M.L., Denoun H., Sambas A., Vaidyanathan S., Abdurrahman U.T., Mujiarto. Super-twisting sliding mode direct power control of PWM-rectifier connected to grid. *AIP Conference Proceedings*, 2023, vol. 2510, no. 1, art. no. 020002. doi: https://doi.org/10.1063/5.0128272.

5. Mazouz F., Belkacem S. *Super Twisting Algorithm Direct Power Control of DFIG Using Space Vector Modulation*. 2021. 6 p. doi: https://doi.org/10.20944/preprints202007.0628.v2.

6. Benbouhenni H., Yessef M., Bizon N., Bossoufi B., Alghamdi T.A.H. Experimental Assessment of a Dual Super-Twisting Control Technique of Variable-Speed Multi-Rotor Wind Turbine Systems. *IEEE Access*, 2024, vol. 12, pp. 103744-103763. doi: https://doi.org/10.1109/ACCESS.2024.3434534.

7. Hou B., Qi J., Li H. Robust Direct Power Control of Three-Phase PWM Rectifier with Mismatched Disturbances. *Electronics*, 2024, vol. 13, no. 8, art. no. 1476. doi: https://doi.org/10.3390/electronics13081476.

8. Krylov D.S., Kholod O.I. Determination of the input filter parameters of the active rectifier with a fixed modulation frequency. *Electrical Engineering & Electromechanics*, 2022, no. 4, pp. 21-26. doi: https://doi.org/10.20998/2074-272X.2022.4.03.

9. Harrabi N., De Almeida J.S., Laboudi K. Controller Design Approach for SVPWM-Regulated AC/DC Rectifier. *European Journal of Electrical Engineering*, 2021, vol. 23, no. 5, pp. 353-360. doi: https://doi.org/10.18280/ejee.230501.

10. Barkat S., Tlemcani A., Nouri H. Direct power control of the PWM rectifier using sliding mode control. *International Journal of Power and Energy Conversion*, 2011, vol. 2, no. 4, art. no. 289. doi: https://doi.org/10.1504/IJPEC.2011.041883.

11. Sakri D., Laib H., Farhi S.E., Golea N. Sliding mode approach for control and observation of a three phase AC-DC pulse-width modulation rectifier. *Electrical Engineering & Electromechanics*, 2023, no. 2, pp. 49-56. doi: https://doi.org/10.20998/2074-272X.2023.2.08.

12. Ahmane A., Sakri D., Golea N. Direct Power Control based on Super Twisting Sliding Mode Control for Three Phase PWM Rectifier. *2022 2nd International Conference on Advanced Electrical Engineering (ICAEE)*, 2022, pp. 1-6. doi: https://doi.org/10.1109/ICAEE53772.2022.9962104.

13. Dekali Z., Baghli L., Boumediene A. Improved Super Twisting Based High Order Direct Power Sliding Mode Control of a Connected DFIG Variable Speed Wind Turbine. *Periodica Polytechnica Electrical Engineering and Computer Science*, 2021, vol. 65, no. 4, pp. 352-372. doi: https://doi.org/10.3311/PPee.17989.

14. Ouchen S., Benbouzid M., Blaabjerg F., Betka A., Steinhart H. Direct Power Control of Shunt Active Power Filter Using Space Vector Modulation Based on Supertwisting Sliding Mode Control. *IEEE Journal of Emerging and Selected Topics in Power Electronics*, 2021, vol. 9, no. 3, pp. 3243-3253. doi: https://doi.org/10.1109/JESTPE.2020.3007900.

15. Zeb K., Busarello T.D.C., Ul Islam S., Uddin W., Raghavendra K.V.G., Khan M.A., Kim H.-J. Design of Super Twisting Sliding Mode Controller for a Three-Phase Grid-connected Photovoltaic System under Normal and Abnormal Conditions. *Energies*, 2020, vol. 13, no. 15, art. no. 3773. https://doi.org/10.3390/en13153773.

16. Oualah O., Kerdoun D., Boumassata A. Super-twisting sliding mode control for brushless doubly fed reluctance generator based on wind energy conversion system. *Electrical Engineering & Electromechanics*, 2023, no. 2, pp. 86-92. doi: https://doi.org/10.20998/2074-272X.2023.2.13.

17. Yenil V., Özdemir S., Ortatepe Z. Super Twisting Sliding Mode Control of Four-Phase Interleaved Boost Converter. *Gazi University Journal of Science Part A: Engineering and Innovation*, 2024, vol. 11, no. 3, pp. 563-576. doi: https://doi.org/10.54287/gujsa.1529271.

Received 02.10.2025
Accepted 10.12.2025
Published 02.05.2026

A. Ahmane[1], *PhD Student,*
D. Sakri [1], *Doctor of Electrotechnical, Professor,*
S.E. Farhi [1,2], *Doctor of Electrotechnical, Professor,*
N. Golea [1], *Doctor of Electrotechnical, Professor,*
[1] Laboratory of Electrical Engineering and Automatic (LGEA), University of Oum El Bouaghi, Algeria,
e-mail: anissa.ah93@gmail.com (Corresponding Author)
[2] Department of Electrical Engineering, University of Souk Ahras, Algeria.

How to cite this article:
Ahmane A., Sakri D., Farhi S.E., Golea N. Three-phase pulse width modulation boost rectifier enhancement direct power control based on super-twisting algorithm. *Electrical Engineering & Electromechanics*, 2026, no. 3, pp. 73-78. doi: https://doi.org/10.20998/2074-272X.2026.3.11

UDC 621.314.5 https://doi.org/10.20998/2074-272X.2026.3.12

O.A.Y. Amran, N.A. Windarko, I. Syarif, T.B.J. Gemilang

Application of the Newton–Raphson algorithm for enhanced harmonic reduction in seven-level packed U-cell multilevel inverters

Introduction. *Recently, multilevel inverters (MLIs) have been widely investigated for industrial and renewable energy systems as they are valuable in applications where they can produce clean, high-fidelity electrical signals that minimize harmonic content and distortion.* ***Problem***. *Among the modulation strategies, selective harmonic elimination pulse width modulation (SHE-PWM) is highly effective, but solving its nonlinear transcendental equations requires accurate numerical methods.* ***Goal***. *To improve the performance of the 7-level packed U-cell (PUC) inverter by applying the Newton–Raphson method to compute optimal switching angles for SHE-PWM, thereby minimizing total harmonic distortion (THD), improving waveform quality, and achieving a more compact and cost-effective design with fewer components.* ***Methodology***. *The Newton–Raphson iterative algorithm was implemented in MATLAB/Simulink to solve the nonlinear equations of SHE-PWM, and a hardware prototype of the 7-level PUC-MLI was fabricated and tested to validate real-world performance.* ***Results***. *The application of the Newton–Raphson algorithm significantly improved the system's performance. After implementation, the THD was reduced to 13.19 % in the simulation and 18.14 % in the hardware prototype, whereas both initially exhibited considerably higher THD levels.* ***Scientific novelty***. *The proposed method demonstrates the capability of the Newton–Raphson algorithm as a reliable numerical solution for selective harmonic elimination in the 7-level PUC MLI, ensuring rapid convergence and precise determination of switching angles.* ***Practical value***. *The study shows that significant harmonic reduction can be achieved without additional hardware or complex circuitry, making the approach applicable to other inverter topologies and suitable for advanced power electronic and renewable energy systems.* References 22, tables 4, figures 9.

Key words: **multilevel inverter, packed U-cell, selective harmonic elimination, Newton–Raphson algorithm, switching angle optimization, total harmonic distortion**.

Вступ. *Останнім часом багаторівневі інвертори (MLI) активно досліджуються для промислових застосувань та систем відновлюваної енергетики, оскільки вони здатні формувати високоякісні електричні сигнали з мінімальним рівнем гармонік і спотворень.* ***Проблема***. *Серед методів модуляції селективне усунення гармонік на основі широтно-імпульсної модуляції (SHE-PWM) є високоефективним, проте розв'язання відповідних нелінійних трансцендентних рівнянь потребує застосування точних чисельних методів.* ***Мета***. *Підвищення ефективності 7-рівневого багаторівневого інвертора з компактною U-коміркою (PUC) шляхом застосування методу Ньютона–Рафсона для визначення оптимальних кутів перемикання в SHE-PWM з метою зменшення сумарного коефіцієнта гармонічних спотворень (THD), покращення форми вихідної напруги та досягнення більш компактної й економічно ефективної конструкції з меншою кількістю компонентів.* ***Методика***. *Ітераційний алгоритм Ньютона–Рафсона реалізовано в середовищі MATLAB/Simulink для розв'язання нелінійних рівнянь SHE-PWM. Для підтвердження працездатності розроблено та експериментально досліджено апаратний прототип 7-рівневого PUC-інвертора.* ***Результати***. *Застосування алгоритму Ньютона–Рафсона суттєво покращило характеристики системи. Після його впровадження значення THD знижено до 13,19 % у моделюванні та до 18,14 % в експериментальному прототипі, тоді як початково ці значення були вищими.* ***Наукова новизна***. *Запропонований підхід демонструє ефективність методу Ньютона–Рафсона як надійного чисельного інструменту для селективного усунення гармонік у 7-рівневому багаторівневому PUC-інверторі, забезпечуючи швидку збіжність і точне визначення кутів перемикання.* ***Практична значимість***. *Показано, що зменшення гармонік може бути досягнуте без ускладнення апаратної частини чи використання додаткових елементів, що робить запропонований підхід придатним для інших топологій інверторів і перспективним для сучасних систем силової електроніки та відновлюваної енергетики.* Бібл. 22, табл. 4, рис. 9.

Ключові слова: **багаторівневий інвертор, компактна U-комірка, селективне усунення гармонік, алгоритм Ньютона-Рафсона, оптимізація кута перемикання, сумарний коефіцієнт гармонічних спотворень.**

Introduction. The rapid expansion of renewable energy systems, electric vehicles, and distributed energy resources has created an increasing demand for highly efficient power conversion systems that ensure reduced losses and improved power quality. Multilevel inverters (MLIs) are widely recognized as promising solutions because they can synthesize nearly sinusoidal voltage waveforms from multiple voltage levels, thereby lowering device stress and suppressing harmonic distortion [1, 2].

These features make MLIs attractive for medium- and high-power applications where grid compliance and reduced electromagnetic interference are critical [3]. Among the existing MLI topologies, the packed U-cell (PUC) inverter offers significant advantages due to its ability to achieve multiple output voltage levels with fewer power electronic components, making it more compact, cost-effective, and modular. Compared to conventional topologies for instance, neutral point clamped (NPC) and cascaded H-bridge (CHB) converter structures, the PUC inverter demonstrates superior scalability, hardware simplicity, and reduced component count while maintaining high-quality output performance [4, 5]. In particular, the 7-level PUC (7-PUC) inverter provides a practical trade-off between hardware complexity and output waveform quality.

However, a major problem arises from its inherent harmonic distortion, especially low-order harmonics, which degrade voltage quality and shorten the lifetime of connected loads [6]. The selective harmonic elimination pulse width modulation (SHE-PWM) is a powerful modulation approach for minimizing harmonics by calculating optimal switching angles. However, solving the SHE nonlinear transcendental equations requires substantial computational effort, particularly for PUC topologies with asymmetric DC sources where the equations become more complex and convergence of numerical methods is less guaranteed [7]. Optimization techniques such as particle swarm optimization, genetic algorithms and ant colony optimization have been applied to SHE metaheuristic solutions for selective harmonic elimination in MLIs [8, 9], but they typically involve high computational costs and are unsuitable for real-time applications. Alternative control strategies have been explored for harmonic suppression. In [10] fuzzy logic control was proposed for harmonic mitigation in power converters, demonstrating effective reduction of low-order harmonics. In [11] was investigated power quality enhancement in inverter-based renewable energy systems through optimized control strategies. However, these approaches either require complex tuning

procedures or involve higher computational overhead compared to analytical methods In contrast, the Newton–Raphson (NR) method offers fast convergence and high accuracy when provided with good initial estimates, and has been effectively used in other inverter topologies such as CHB and NPC [12, 13]. However, the application of NR to 7-PUC inverters with asymmetric voltage sources remains underexplored, which represents a clear research gap.

This study investigates the application of the NR algorithm to the 7-level PUC inverter under asymmetric DC input conditions with a focus on solving the nonlinear switching angle equations of SHE-PWM. The subject of investigation includes the analysis of harmonic performance, algorithm convergence, and total harmonic distortion (THD) reduction in order to evaluate the feasibility and efficiency of this numerical approach for real-time inverter control.

The goal of this work is to improve the performance of the 7-level PUC inverter by applying the Newton–Raphson method to compute optimal switching angles for SHE-PWM, thereby minimizing THD, improving waveform quality, and achieving a more compact and cost-effective design with fewer components.

The main contributions of this study include:

1) formulation of the SHE-PWM problem for 7-PUC under asymmetric DC sources;

2) implementation of the NR algorithm in Simulink and hardware for computing switching angles and evaluating convergence.

This work demonstrates that the NR algorithm provides a computationally efficient solution with reduced processing demand, making it suitable for real-time applications on microcontrollers such as Arduino, based embedded inverter systems.

Methodology of packed U-cell MLI. The employed circuit topology is a compact and efficient MLI topology designed to generate superior output performance waveforms using a reduced number of components. The inverter comprises three cascaded U-cells, each composed of 2 complementary IGBT switches. The entire mechanism functions using six switches and two primary DC voltage sources [14].

The PUC converter was originally proposed by Al-Haddad in earlier studies and later adapted for 7-level configurations [15]. Figure 1 shows a configuration featuring 6 operational switches and 2 DC sources, namely the 1st and 2nd sources. The significant benefit of PUC lies in the total component count relative to other topologies. A reduced number of switches leads to diminished power losses, fewer gate drives and lower costs. The correlation between the quantity of voltage levels attained and the number of sources employed can be formulated as:

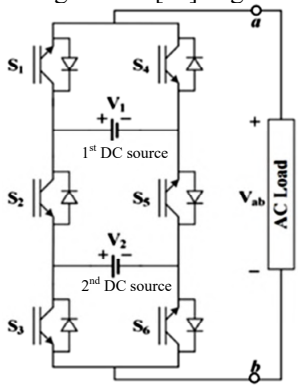

Fig. 1. 7-level PUC inverter

$$N_v = 2^{N_s+1} - 1; \quad (1)$$

$$N_p = 2^{N_s}; \quad (2)$$

where N_v is the number of voltage levels; N_p is the number of power switches; N_s is the number of DC voltage sources.

The PUC configuration achieves elevated voltage generation by reconfiguring the 2nd DC source (V_2) topology, with bottom switches (S_3 and S_6) inverted to suppress unwanted diode conduction. All feasible switching combinations are detailed in Table 2. The inverter produces 7 voltage levels ranging from 0 to 4*E* when V_1 equals $3V_2$. The maximum output voltage of 4*E* results from the series combination of both DC sources.

Table 1

Switching states for 7-PUC inverter

Switching states	S_1	S_2	S_3	S_4	S_5	S_6	Voltages
1	1	0	1	0	1	0	V_1+V_2
2	1	0	0	0	1	1	V_1
3	0	0	1	1	1	0	V_2
4	0	0	0	1	1	1	0
5	1	1	0	0	0	1	$–V_2$
6	0	1	1	1	0	0	$–V_1$
7	0	1	0	1	0	1	$–V_2–V_1$

The study utilizes the SHE-PWM on a 7-PUC inverter to target specific low-order harmonics, primarily the 5th and 7th thereby improving spectral purity by limiting THD. To accomplish this, it is essential to identify 3 switching angles. A notable advantage of the PUC is its utilization of fewer components compared to alternatives such as the CHB, resulting in diminished power losses, reduced gate drive requirements and lower system costs. In this method, 3 switching angles (α_1, α_2, α_3) are determined within the 1st quarter-cycle of the fundamental waveform to shape the stepped output. To ascertain these angles, it is essential to resolve several nonlinear transcendental equations through Fourier analysis. This is subsequently followed by the implementation of the NR method to achieve a prompt and precise solution [16, 17].

The notable advantage of PUC is its reduced component count compared to alternative topologies, such as the CHB, fewer switches result in diminished enhanced efficiency through reduced losses, fewer control circuits, and lower financial investment in the system. The voltage magnitudes produced at the output of the single-phase inverter topology seen in Fig. 1 are enumerated in Table 1. There are 8 possible states, in which S_4, S_5 and S_6 work in reverse with respect to the switches S_1, S_2 and S_3 are controlled in a manner that prevents short circuits across the DC buses. It is important to note that switches S_4, S_5 and S_6 function as complementary pairs to S_1, S_2 and S_3, respectively. As a result, each switch pair (S_1, S_4), (S_2, S_5) and (S_3, S_6) is designed to avoid simultaneous conduction [18]. While the PUC can generate multiple discrete voltage magnitudes from various DC sources, achieving the maximum output voltage V_{ab}. The output voltage V_{ab} can generate 7 distinct levels [19].

Selective harmonic elimination. Various control procedures govern output voltage profiles in converter stages, primarily categorized into 2 types:

- low-frequency switching modulation techniques including phase disposition, phase opposition disposition and SHE;
- high-frequency switching methods employing PWM [20].

SHE decreases switching losses and noise levels, facilitating the use of smaller output filters. It operates by waveform symmetry and advances in a sequentially increasing manner. The design offers a lower number of circuit elements, thereby minimizing power losses and gate drive requirements.

Equation (3) ensures that the switching angles (α_1, α_2, α_3) are properly ordered within one quarter of the output waveform. This constraint maintains the

waveform's symmetry and guarantees correct pulse positioning. It is essential for achieving accurate harmonic elimination using SHE techniques:

$$0 < \alpha_1 < \alpha_2 < \alpha_3 < 90°. \quad (3)$$

Equation (4) defines the modulation index m with respect to the magnitude of the fundamental voltage V_1 relative to the maximum and represents the V_{dc} which is the total direct current supply voltage provided to the inverter:

$$m = \frac{\pi V_1}{4 + 3V_{dc}} =< 3m = \frac{\pi V_1}{4V_{dc}}. \quad (4)$$

Equations (5)–(8) represent the SHE conditions, where the switching angles $\alpha_1 - \alpha_3$ are calculated to achieve the desired modulation index m while eliminating the 3rd, 5th and 7th harmonics from the inverter output voltage:

$$\cos(\alpha_1) + \cos(\alpha_2) + \cos(\alpha_3) = 3m; \quad (5)$$

$$\cos(3\alpha_1) + \cos(3\alpha_2) + \cos(3\alpha_3) = 0; \quad (6)$$

$$\cos(5\alpha_1) + \cos 5(\alpha_2) + \cos(5\alpha_3) = 0; \quad (7)$$

$$\cos(7\alpha_1) + \cos(7\alpha_2) + \cos(7\alpha_3) = 0. \quad (8)$$

The resolution of the SHE equations is a significantly non-linear endeavor, as it produces a transcendental system. Traditional methods, such as sequential and recursive algorithms, particularly the NR method, are frequently favored; however, as inverter levels increase, the task becomes more challenging, necessitating more accurate initial estimates [21].

The Newton–Raphson approach is a commonly employed iterative technique for resolving nonlinear equations. It is especially efficacious when an accurate initial estimate is supplied. The approach relies on the Taylor series expansion and linear approximation of the function in question [22]. The standard formulation of the NR method is expressed as:

$$X_{x+1} = X_n - \frac{f(x_n)}{f'(x_n)}, \quad (9)$$

where X_n is the current approximation; X_{n+1} is the next approximation; $f(x_n)$ is the function value at x_n; $f'(x_n)$ is the derivative of the function at X_n.

In the context of SHE, the target is to find the switching angles that resolve the system of nonlinear mathematical models $f^k(\alpha) = 0$. The NR method requires the computation of the Jacobian matrix $\boldsymbol{J}$ of the equations system, which consists of the partial derivatives of the nonlinear functions corresponding to each switching angle

The proposed NR technique begins by selecting a random initial estimate for the switching angles within the range of 0–90°, where the iteration count is denoted as $\boldsymbol{J}$ and the tolerance as ε. The optimization process for determining the switching angles is structured as follows.

1) *Initialization*. Formulate a preliminary set of estimations for switching angles.

2) *Jacobian calculation*. Determine the parameters for the constraint equations and compute the Jacobian matrix $\boldsymbol{J}$ for the nonlinear system The Jacobian matrix $\boldsymbol{J}$ represents the partial derivatives of the constraint equations $f = [f_1(\alpha), f_2(\alpha),..., f_n(\alpha)]$ with respect to the switching angles $\alpha = [\alpha_1, \alpha_2,..., \alpha_n]$, where $f(\alpha)$ is the system of nonlinear equations for harmonic elimination.

The correction vector $\Delta\boldsymbol{\alpha}$, corresponding to n unknowns in the k-th iteration, is obtained using (10), (11). Here $\boldsymbol{J}^{-1}$ is the inverse of the Jacobian matrix; α^i is the current estimate of switching angles at iteration i, which is then updated as $\alpha^{i+1} = \alpha^i + \Delta\alpha$

$$\boldsymbol{J} = \begin{bmatrix} \frac{\partial f_1}{\partial \alpha_1} & \cdots & \frac{\partial f_1}{\partial \alpha_n} \\ \vdots & \ddots & \vdots \\ \frac{\partial f_m}{\partial \alpha_1} & \cdots & \frac{\partial f_m}{\partial \alpha_m} \end{bmatrix}. \quad (10)$$

$$\Delta\boldsymbol{\alpha} = -\boldsymbol{J}^{-1} \times f(\alpha^i). \quad (11)$$

3) *Convergence check*. Continue the iteration while the tolerance ε remains smaller than $\Delta\boldsymbol{\alpha}$. The process terminates once the tolerance equals or exceeds $\Delta\boldsymbol{\alpha}$.

4) *Angle update*. Update the switching-angle vector $\boldsymbol{\alpha}$ according to (12), then repeat from Step 3 until convergence is achieved .The convergence criterion is defined as $\|\Delta\alpha\| \le \varepsilon$, where $\| \|$ denotes the Euclidean norm and ε is the specified tolerance value.

$$a^{i+1} = a^i + \Delta\alpha. \quad (12)$$

The NR algorithm is employed to determine the optimal switching angles for the SHE-PWM technique through an iterative numerical procedure.

The process begins with an initial estimation of the switching angles, followed by the computation of the Jacobian matrix, which represents the partial derivatives of the nonlinear system equations. A correction vector $\Delta\boldsymbol{\alpha}$ is subsequently calculated and applied to update the switching angles iteratively until the convergence criterion, defined by a specified tolerance ε, is satisfied. Upon convergence, the resulting set of switching angles is considered optimal, effectively minimizing the THD in the inverter output voltage.

The following organizational layout shown in Fig. 2 is intended to utilize the NR technique for solving the mathematical complexity associated with SHE.

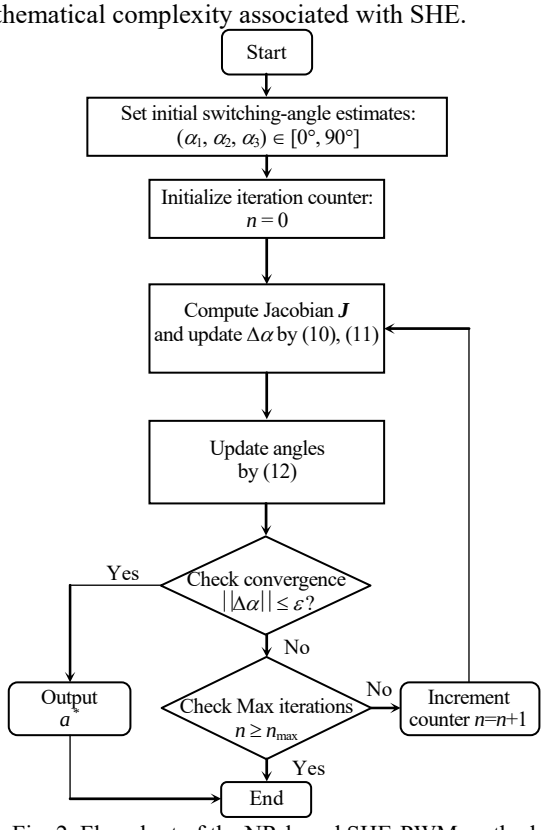

Fig. 2. Flowchart of the NR-based SHE-PWM method

Simulation results. To validate the proposed SHE-NR technique, comprehensive simulations were conducted to evaluate harmonic suppression performance,

switching angle optimization, and THD reduction. The NR method solves the nonlinear equations required to determine optimal switching angles that eliminate specific harmonics while maintaining fundamental voltage across 33 V and 11 V DC links. The following subsections present the detailed analysis and results.

This work utilized the SHE methodology in conjunction with the NR iterative method to ascertain the optimal switching angles for a MLI. The preferred due to its advantages that can easily solve non-linear equations, with special mention of its fast rate of convergence and precision. The following features are essential in the case of the inference of the SHE process, which is nothing but the reduction of lower-order harmonics (for example, the 5th and 7th) from the output voltage waveform by keeping the desired fundamental component. The NR method will, through iterations of an indirect procedure, minimize the discrepancy between the found and the desired harmonic components, and thus the time it takes for convergence to be realized.

Figure 3 and Table 4 present a comprehensive dual-perspective analysis of THD in MLI operation, evaluating performance under varying modulation indices and switching angle configurations. Figure 3 shows an inverse relationship between modulation index (MI) and THD across the range of 0.35 to 1.05, where THD decreases non-linearly from approximately 48 % to 13.91 %, with the steepest reduction occurring below MI = 0.7 and local extrema observed at MI ≈ 0.6 and MI ≈ 0.7 reflecting complex harmonic interactions in PWM strategies. Table 4 illustrates THD variation as a function of 3 independent switching angles (α_1, α_2, α_3) ranging from 11° to 90°, where all 3 parameters exhibit positive correlation with THD, increasing from approximately 13.19 % to 49 %. The SHE-NR optimization algorithm successfully identifies the optimal switching angle combination (α_1 = 12.57°; α_2 = 23.81°; α_3 = 54.33°), achieving minimum THD of 13.19 %, which represents substantial improvement over arbitrary angle selection.

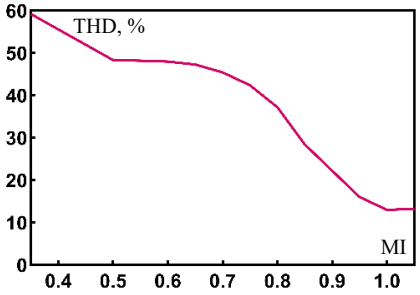

Fig. 3. THD vs modulation index MI

Table 2

SHE-NR switching angles at various MI

Modulation index MI	Switching angles α_1, α_2, α_3		
0.35	46.30	82.37	89.94
0.50	40.77	65.82	89.36
0.55	39.77	62.13	86.57
0.60	39.43	58.58	83.10
0.65	39.39	55.52	78.90
0.70	38.34	53.53	73.96
0.75	34.89	54.46	68.55
0.80	29.24	54.44	64.48
0.85	22.77	49.38	64.56
0.95	13.82	37.19	61.92
1.00	11.68	31.18	58.58
1.05	12.57	23.81	54.33

The parallel upward trajectories in Fig. 3 and the monotonic decrease in Table 4 collectively validate the SHE-NR technique's effectiveness in minimizing harmonic distortion, thereby reducing inverter losses and enhancing output waveform quality for multilevel converter applications. Figure 4 shows the correlation between the MI and the corresponding switching angles. As the MI increases, the inverter strives to deliver higher amplitude of fundamental voltage while maintaining harmonic cancellation, thereby resulting in reduced switching angles.

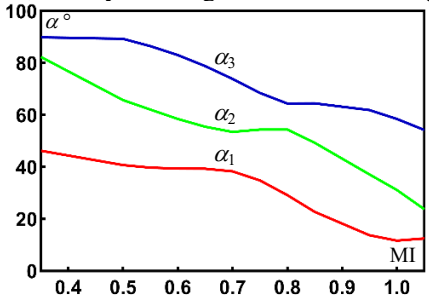

Fig. 4. Switching angles vs modulation index

Figure 5 shows the suppression of low-order harmonics (5th and 7th), with the FFT analysis of THD, which shows a reduction from 59.21 % (MI = 0.35) to 13.19 % (MI = 1.05). The transitory increase in THD to 45.46 % at MI = 0.7 (see Table 2), is associated with the overlapping switching angles. This indicates that SHE-PWM is highly sensitive to the selection of angle. Both outcomes substantiate the notion that the NR method enhances harmonic suppression and waveform fidelity.

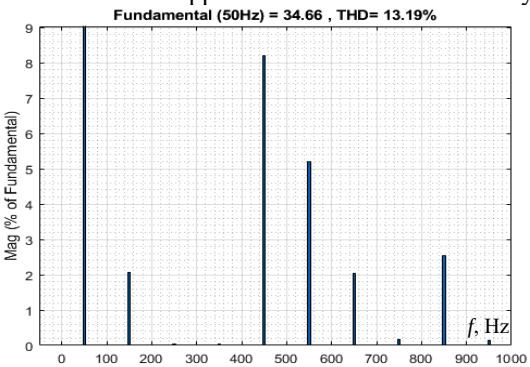

Fig. 5.THD vs switching angle

In Fig. 6, the output waveforms of the topology are shown, obtained using SHE-PWM based on the NR method, where 7-level voltages are produced and harmonic distortion is effectively minimized through selective elimination of low-order harmonics.

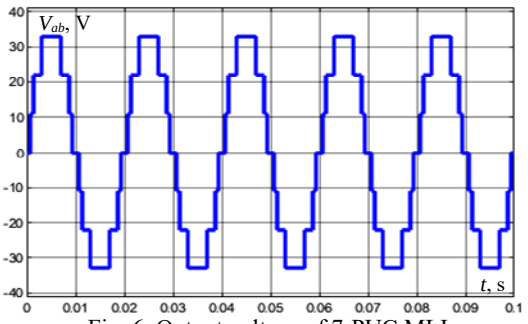

Fig. 6. Output voltage of 7-PUC MLI

As illustrated in Fig. 6, optimal switching angles are iteratively calculated by the NR algorithm to achieve harmonic cancellation, while the desired fundamental component is maintained, resulting in superior power

quality with minimal switching losses suitable for high-power applications.

Hardware testing and practical implementation. The experimental prototype (Fig. 7) consists of a 7-level PUC MLI with 2 DC sources configured in a 3:1 ratio (33 V and 11 V). The power stage includes IGBT switching devices with gate drivers, heat sinks for thermal management, and snubber circuits for protection. An Arduino microcontroller serves as the digital controller, executing pre-calculated SHE-PWM switching angles derived from the NR algorithm. Gate driver circuits with optocouplers provide electrical isolation between control and power stages. The measurement setup includes a GW Instek PSS-3203 programmable DC supply, digital oscilloscope for waveform capture, and FFT analyzer for harmonic spectrum analysis (Table 3).

Table 3

Component list

Components	Specification
Optocoupler	IC FOD 3182
Microcontroller	Arduino
Gate drive power supply	GW Instek PSS-3203, PSW 30-36
IGBT switches	SGL160N60UFD
Converts	Hi link 220V to 12V
Passive heat exchanger	Heat sink

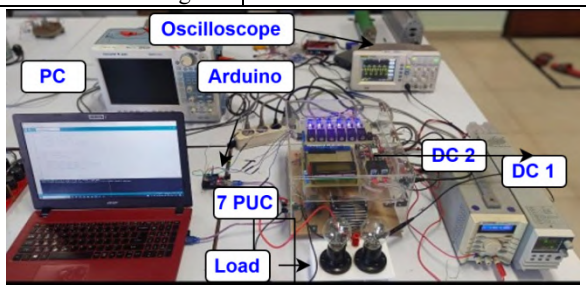

Fig. 7. Experimental setup layout and configuration

The NR algorithm was executed offline in MATLAB to calculate optimal switching angles for harmonic elimination. The computed angles were stored as lookup tables in the Arduino's memory, mapping different modulation indices to their corresponding switching angles. During real-time operation, the Arduino retrieves the appropriate angles based on the desired output voltage and generates precise PWM pulses with microsecond-level timing accuracy. These control signals are processed through gate driver circuits to trigger the IGBT switches at the calculated instants. The PUC topology configuration strategically switches the two DC sources to produce seven distinct voltage levels: 0, ±11 V, ±22 V, ±33 V, ±44 V. This switching sequence synthesizes a stepped quasi-sinusoidal waveform that inherently suppresses the specified 5th and 7th harmonics while retaining the desired fundamental voltage as depicted in Fig. 8.

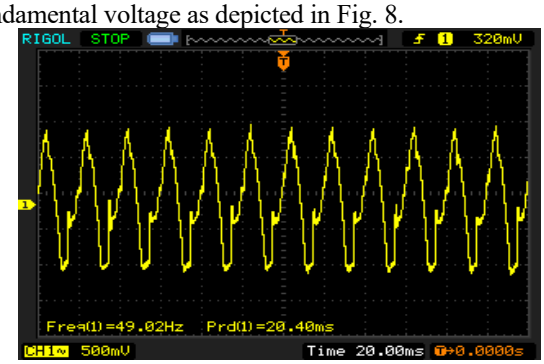

Fig. 8. Experimental output voltage of 7-PUC MLI

Oscilloscope measurements confirm a 7-level stepped waveform with ±44 V peak amplitude and 50 Hz fundamental frequency. The waveform exhibits smooth transitions between voltage levels with symmetric positive and negative half-cycles. FFT analysis reveals the harmonic spectrum with the fundamental component at 100 % reference magnitude as illustrated in Fig. 9. The 5th and 7th harmonics are successfully suppressed to below 3 %, compared to typical values of 15–20 % and 10–15 % in conventional PWM methods. Higher-order harmonics (11th and 13th) remain at approximately 8 % and 6 % respectively, as they were not targeted for elimination in this implementation. The measured THD is 18.14 %, representing a significant improvement over square wave inverters which typically exhibit THD around 45 %, validating the effectiveness of the SHE-PWM approach in reducing low-order harmonics.

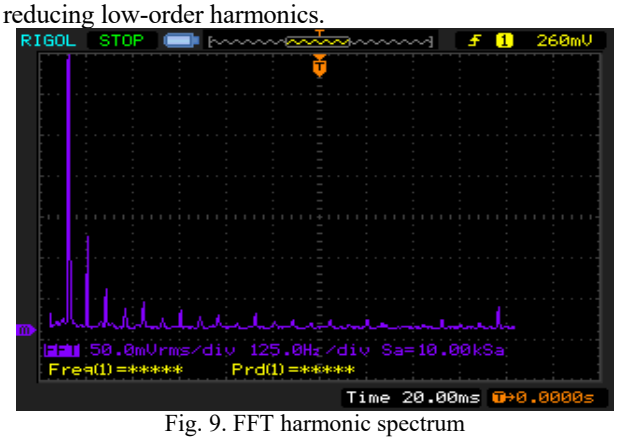

Fig. 9. FFT harmonic spectrum

The experimental results exhibit strong agreement with the theoretical predictions across multiple performance metrics, as presented in Table 4. The voltage levels match the theoretical formula with 100 % accuracy, confirming proper implementation of the PUC topology. Targeted harmonics (5th and 7th) are reduced to below 3 %, validating the NR optimization effectiveness. The measured THD of 18.14 % shows reasonable deviation from theoretical predictions (12–15 %) due to practical non-idealities including switching dead-time (typically 1–2 μs), device voltage drops (≈2–3 V), finite rise/fall times, component tolerances (±5 %), and DC supply ripple (<1 %). The fundamental voltage exhibits linear control with modulation index variation, confirming the expected relationship between control input and output amplitude. These results validate the practical feasibility of SHE-PWM-based harmonic elimination in MLIs using Arduino implementation, demonstrating effective reduction of low-order harmonics while maintaining acceptable power quality for practical applications.

Table 4

Comparison of THD between simulation and hardware results

Type	THD, %
Simulation results	13.19
Hardware results	18.14

Conclusions. The Newton–Raphson algorithm was successfully applied to compute optimal switching angles for selective harmonic elimination pulse width modulation in 7-level packed U-cell MLIs, demonstrating rapid convergence in solving nonlinear transcendental equations and effectively eliminating the 5th and 7th harmonics.

Simulation results achieved a THD of 13.19 % at a modulation index of 1, while hardware testing validated

practical feasibility with a THD of 18.14 %, confirming acceptable power quality for grid-connected applications.

The 7-PUC topology provides significant advantages including reduced component count compared to CHB and NPC configurations, resulting in a more compact and cost-effective design.

The Newton–Raphson method offers a computationally efficient solution suitable for real-time implementation on resource-constrained embedded systems such as Arduino-based microcontrollers, providing a viable path for improving power quality in MLIs.

The proposed approach is applicable for renewable energy integration, with future work recommended to focus on experimental validation under varied operating conditions and extension to higher-level inverter topologies.

Acknowledgments. The authors acknowledge the assistance of Politeknik Elektronika Negeri Surabaya (PENS) for providing the resources and facilities essential for this work. Gratitude is extended to the Renewable Energy Laboratory, the venue for the simulations and analyses performed. The authors acknowledge the contributions of professors, colleagues and others who provided valuable feedback and direction during the course of this study. Special thanks are also extended to the Indonesian Government for awarding the Developing Country Partnership Scholarship (Beasiswa Kemitraan Negara Berkembang – KNB), which made this academic journey possible.

Conflict of interest. The authors declare that they have no conflict of interest.

REFERENCES

1. Rodriguez J., Jih-Sheng Lai, Fang Zheng Peng. Multilevel inverters: a survey of topologies, controls, and applications. *IEEE Transactions on Industrial Electronics*, 2002, vol. 49, no. 4, pp. 724-738. doi: https://doi.org/10.1109/TIE.2002.801052.

2. Kouro S., Malinowski M., Gopakumar K., Pou J., Franquelo L.G., Bin Wu, Rodriguez J., Perez M.A., Leon J.I. Recent Advances and Industrial Applications of Multilevel Converters. *IEEE Transactions on Industrial Electronics*, 2010, vol. 57, no. 8, pp. 2553-2580. doi: https://doi.org/10.1109/TIE.2010.2049719.

3. Shehu G.S., Kunya A.B., Shanono I.H., Yalcinoz T. A Review of Multilevel Inverter Topology and Control Techniques. *Journal of Automation and Control Engineering*, 2016, pp. 233-241. doi: https://doi.org/10.18178/joace.4.3.233-241.

4. Sifat Z., Hussain M.T., Khan M.A., Hussain M.S., Sarwar A., Tariq M., Hasan M. Selective harmonic elimination in PUC-5 multilevel inverter using hybrid IGWO-DE algorithm. *Engineering Reports*, 2024, vol. 6, no. 10, art. no. e12883. doi: https://doi.org/10.1002/eng2.12883.

5. Balal A., Dinkhah S., Shahabi F., Herrera M., Chuang Y.L. A Review on Multilevel Inverter Topologies. *Emerging Science Journal*, 2022, vol. 6, no. 1, pp. 185-200. doi: https://doi.org/10.28991/ESJ-2022-06-01-014.

6. Vahedi H., Sharifzadeh M., Al-Haddad K. Modified Seven-Level Pack U-Cell Inverter for Photovoltaic Applications. *IEEE Journal of Emerging and Selected Topics in Power Electronics*, 2018, vol. 6, no. 3, pp. 1508-1516. doi: https://doi.org/10.1109/JESTPE.2018.2821663.

7. Behbahanifard H., Abazari S., Sadoughi A. New scheme of SHE-PWM technique for cascaded multilevel inverters with regulation of DC voltage sources. *ISA Transactions*, 2020, vol. 97, pp. 44-52. doi: https://doi.org/10.1016/j.isatra.2019.07.015.

8. Ürgün S., Yiğit H., Mirjalili S. Investigation of Recent Metaheuristics Based Selective Harmonic Elimination Problem for Different Levels of Multilevel Inverters. *Electronics*, 2023, vol. 12, no. 4, art. no. 1058. doi: https://doi.org/10.3390/electronics12041058.

9. Mahesh A. A hybrid search space reduction algorithm and Newton–Raphson based selective harmonic elimination for an asymmetric cascade H-bridge multi-level inverter. *International Journal of Emerging Electric Power Systems*, 2025, vol. 26, no. 1, pp. 107-119. doi: https://doi.org/10.1515/ijeeps-2023-0219.

10. Sujatha M.S., Sreelakshmi S., Parimalasundar E., Suresh K. Mitigation of harmonics for five level multilevel inverter with fuzzy logic controller. *Electrical Engineering & Electromechanics*, 2023, no. 4, pp. 52-56. doi: https://doi.org/10.20998/2074-272X.2023.4.08.

11. Parimalasundar E., Kumar N.M.G., Geetha P., Suresh K. Performance investigation of modular multilevel inverter topologies for photovoltaic applications with minimal switches. *Electrical Engineering & Electromechanics*, 2022, no. 6, pp. 28-34. doi: https://doi.org/10.20998/2074-272X.2022.6.05.

12. Marín-Reyes M., Aguayo-Alquicira J., De León-Aldaco S.E. Calculation of Optimal Switching Angles for a Multilevel Inverter Using NR, PSO, and GA- a Comparison. *European Journal of Electrical Engineering*, 2020, vol. 22, no. 4–5, pp. 349-355. doi: https://doi.org/10.18280/ejee.224-506.

13. Manai L., Armi F., Besbes M. Newton-Raphson algorithm–based modified SHE for CHB multilevel inverter control considering capacitor voltage balancing and power factor variation. *International Transactions on Electrical Energy Systems*, 2019, vol. 29, no. 12, art. no. e12126. doi: https://doi.org/10.1002/2050-7038.12126.

14. Biricik S., Komurcugil H. Proportional-Integral and Proportional-Resonant Based Control Strategy for PUC Inverters. *IECON 2018 - 44th Annual Conference of the IEEE Industrial Electronics Society*, 2018, pp. 3369-3373. doi: https://doi.org/10.1109/IECON.2018.8591371.

15. Ait Bellah F., Abouloifa A., Echalih S., Hekss Z., Naftahi K., Lachkar I. Control Design of a Seven-Level Packed U Cell Inverter. *IFAC-PapersOnLine*, 2022, vol. 55, no. 12, pp. 677-682. doi: https://doi.org/10.1016/j.ifacol.2022.07.390.

16. Hiendro A., Yusuf I., Junaidi J., Wigyarianto T.P., Simanjuntak Y.M. Optimization of SHEPWM cascaded multilevel inverter switching patterns. *International Journal of Power Electronics and Drive Systems (IJPEDS)*, 2020, vol. 11, no. 3, pp. 1570-1578. doi: https://doi.org/10.11591/ijpeds.v11.i3.pp1570-1578.

17. Krishnamoorthy U., Pitchaikani U., Rusu E., Fayek H.H. Performance Analysis of Harmonic-Reduced Modified PUC Multi-Level Inverter Based on an MPC Algorithm. *Inventions*, 2023, vol. 8, no. 4, art. no. 90. doi: https://doi.org/10.3390/inventions8040090.

18. Vahedi H., Al-Haddad K. Real-Time Implementation of a Seven-Level Packed U-Cell Inverter with a Low-Switching-Frequency Voltage Regulator. *IEEE Transactions on Power Electronics*, 2016, vol. 31, no. 8, pp. 5967-5973. doi: https://doi.org/10.1109/TPEL.2015.2490221.

19. Ebrahimi F., Wndarko N.A., Gunawan A.I. Wild horse optimization algorithm implementation in 7-level packed U-cell multilevel inverter to mitigate total harmonic distortion. *Electrical Engineering & Electromechanics*, 2024, no. 5, pp. 34-40. doi: https://doi.org/10.20998/2074-272X.2024.5.05.

20. Gajula U., Eragamreddy G. Multicarrier PWM Strategies for Hybrid Symmetrical Multilevel Inverter with Reduced Switch Count. *International Journal of Engineering and Advanced Technology*, 2020, vol. 9, no. 5, pp. 860-866. doi: https://doi.org/10.35940/ijeat.E9792.069520.

21. Buddinni C.D., Usha P. Design of Switched Capacitor Multilevel Inverter with Selective Harmonic Elimination. *IOP Conference Series: Materials Science and Engineering*, 2023, vol. 1295, no. 1, art. no. 012018. doi: https://doi.org/10.1088/1757-899X/1295/1/012018.

22. Krismadinata, Rahim N.A., Ping H.W., Selvaraj J. Elimination of Harmonics in Photovoltaic Seven-level Inverter with Newton-Raphson Optimization. *Procedia Environmental Sciences*, 2013, vol. 17, pp. 519-528. doi: https://doi.org/10.1016/j.proenv.2013.02.067.

Received 30.10.2025
Accepted 13.12.2025
Published 02.05.2026

O.A.Y. Amran[1], *Master of Engineering,*
N.A. Windarko[1], *PhD, Professor,*
I. Syarif[1], *PhD, Professor,*
T.B.J. Gemilang[1], *Bachelor of Engineering,*
[1] Politeknik Elektronika Negeri Surabaya,
Raya ITS Str., Surabaya, 60111, Indonesia,
e-mail: ayub@pens.ac.id (Corresponding Author)

How to cite this article:
Amran O.A.Y., Windarko N.A., Syarif I., Gemilang T.B.J. Application of the Newton–Raphson algorithm for enhanced harmonic reduction in seven-level packed U-cell multilevel inverters. *Electrical Engineering & Electromechanics*, 2026, no. 3, pp. 79-84. doi: https://doi.org/10.20998/2074-272X.2026.3.12

UDC 621.311 https://doi.org/10.20998/2074-272X.2026.3.13

S.A. Alomari, A. Smerat, O.P. Malik, R. Abu Zitar, M. Dehghani, Z. Montazeri

Power system operational optimization using the kakapo optimization algorithm for dynamic economic dispatch

Introduction. *Metaheuristic algorithms are effective for solving complex power system optimization problems characterized by nonlinearity, multimodality, and high dimensionality. Nature-inspired strategies based on adaptive biological behaviors offer significant potential to enhance search efficiency and convergence reliability. The recently published kakapo optimization algorithm (KOA) is employed in this study to address the dynamic economic dispatch (DED) problem over a 24-hour horizon in multi-unit power systems.* ***Problem.*** *The DED problem extends conventional economic load dispatch into a multi-hour planning horizon, considering hourly load variations, generator ramp-rate limits, valve-point effects, and transmission losses. These characteristics render DED highly nonconvex and nonlinear, posing challenges to conventional and metaheuristic techniques. Maintaining a robust balance between global exploration and local exploitation is critical to prevent premature convergence or suboptimal generation schedules.* ***Goal.*** *To apply kakapo optimization algorithm for the dynamic economic dispatch problem, aiming to generate economically optimal and operationally feasible generation schedules over a 24-hour dispatch horizon while preserving population diversity and search stability.* ***Methodology.*** *KOA models two synergistic behavioral phases of the kakapo. Exploration is inspired by lek mating and acoustic signaling, where higher-fitness solutions emit stronger «calls» that probabilistically attract weaker candidates toward promising regions. Exploitation mimics freezing and camouflage strategies, performing fine-grained local adjustments around promising solutions with adaptive step sizes. KOA is applied to a standard five-unit system over 24 hours and benchmarked against nine well-known metaheuristics.* ***Results.*** *KOA achieves the lowest total generation cost, rapid convergence, and high robustness. Statistical performance metrics – including mean, best, worst, standard deviation, and rank – consistently favor KOA, confirming its effectiveness for multi-dimensional, multi-modal DED problems.* ***Scientific novelty.*** *KOA introduces a biologically inspired, self-adaptive search framework that balances exploration and exploitation without external control parameters.* ***Practical value.*** *The algorithm provides a reliable, versatile, and computationally efficient optimization tool for complex power system dispatch problems, with potential applications in renewable integration, multi-objective optimization, and real-time adaptive operations.* References 29, tables 4, figures 2.

Key words: **dynamic economic dispatch, kakapo optimization algorithm, metaheuristic optimization, power system operation, valve-point effects, economic load scheduling.**

Вступ. *Метаевристичні алгоритми є ефективним засобом розв'язання складних задач оптимізації електроенергетичних систем, що характеризуються нелінійністю, мультимодальністю та великою розмірністю. Природоорієнтовані стратегії, засновані на адаптивній біологічній поведінці, мають значний потенціал для підвищення ефективності пошуку та надійності збіжності. У даному дослідженні для розв'язання задачі динамічного економічного розподілу навантаження (DED) у багатогенераторних електроенергетичних системах на 24-годинному інтервалі застосовано нещодавно запропонований алгоритм оптимізації какапо (KOA).* ***Проблема.*** *Задача DED є розширенням класичної задачі економічного розподілу навантаження на багатогодинний часовий горизонт з урахуванням погодинних змін навантаження, обмежень швидкості зміни потужності генераторів, ефектів клапанних точок та втрат у мережі. Ці особливості роблять задачу DED сильно неопуклою та нелінійною, що створює труднощі для традиційних і метаевристичних методів. Для запобігання передчасній збіжності або отриманню неоптимальних графіків генерації необхідно забезпечити надійний баланс між глобальним пошуком і локальним уточненням.* ***Мета.*** *Застосувати алгоритм оптимізації какапо для задачі динамічного економічного розподілу навантаження з метою формування економічно оптимальних і технічно допустимих графіків генерації на 24-годинному інтервалі диспетчеризації зі збереженням різноманітності популяції та стабільності пошуку.* ***Методика.*** *Алгоритм KOA моделює дві взаємодоповнювальні поведінкові фази какапо. Етап дослідження простору пошуку ґрунтується на шлюбній поведінці на токовищі та акустичній сигналізації, за якої розв'язки з вищою пристосованістю генерують сильніші «сигнали», що з певною ймовірністю притягують слабші кандидати до перспективних областей пошуку. Етап уточнення імітує завмирання та маскування, виконуючи локальні коригування перспективних розв'язків за допомогою адаптивних кроків. Алгоритм застосовано до стандартної п'ятиагрегатної системи протягом 24 годин і порівняно з дев'ятьма відомими метаевристичними алгоритмами.* ***Результати.*** *KOA забезпечує найменшу сумарну вартість генерації, швидку збіжність та високу робастність. Статистичні показники ефективності, зокрема середнє значення, найкращий та найгірший результати, стандартне відхилення і ранг, стабільно підтверджують перевагу KOA, що свідчить про його ефективність для багатовимірних і мультимодальних задач DED.* ***Наукова новизна.*** *Алгоритм KOA пропонує біологічно натхнену самоадаптивну пошукову структуру, яка забезпечує баланс між глобальним пошуком і локальним уточненням без використання параметрів зовнішнього керування.* ***Практична значимість.*** *Алгоритм є надійним, універсальним та обчислювально ефективним інструментом оптимізації для складних задач диспетчеризації електроенергетичних систем і має потенціал застосування в задачах інтеграції відновлюваних джерел енергії, багатокритеріальної оптимізації та адаптивного керування в реальному часі..* Бібл. 29, табл. 4, рис. 2.

Ключові слова: **динамічний економічний розподіл навантаження, алгоритм оптимізації какапо, метаевристична оптимізація, функціонування електроенергетичної системи, ефекти клапанних точок, економічне планування навантаження.**

Introduction. Optimization of dynamic economic dispatch (DED) is a fundamental optimization problem in power system operation, aiming to schedule generating units over a multi-hour horizon while minimizing total operating cost and ensuring compliance with system constraints [1]. Unlike the single-period economic load dispatch (ELD), the DED problem incorporates time-coupled characteristics such as ramp-rate limits, valve-point effects, prohibited operating zones, and transmission losses, making it significantly more complex and highly nonlinear [2]. Accurate and efficient DED scheduling is essential for modern power systems, as it ensures economic efficiency, enhances operational security, accommodates fluctuating load patterns, and supports the integration of renewable energy resources. As power systems evolve toward higher penetration of variable renewable energy and increased demand-side management, the importance of robust DED optimization strategies becomes even more pronounced [3].

Given the nonconvex, multimodal, and dynamic structure of the DED problem, deterministic mathematical programming approaches often struggle to provide globally

optimal or computationally feasible solutions. In contrast, metaheuristic algorithms have proven to be powerful tools for solving complex power system optimization problems due to their flexibility, derivative-free search mechanisms, and strong global exploration capabilities [4, 5]. Metaheuristic algorithms are stochastic-based approaches that rely on randomized search processes within the solution space, enabling them to provide high-quality and practically acceptable solutions for complex optimization problems [6–8]. Numerous metaheuristic optimization algorithms – ranging from evolutionary strategies to swarm intelligence and physics-inspired techniques – have been successfully applied to power system applications [9–12]. Recent literature demonstrates the increasing importance of metaheuristic optimization techniques in solving DED problems, particularly due to their strong ability to cope with nonlinearity, nonconvexity, multimodality, and operational constraints. A comprehensive survey of economic and multi-area dispatch confirms the significant expansion of metaheuristic applications in power system optimization and highlights the need for more advanced, adaptive, and robust methods for dispatch problems with dynamic characteristics [13].

Several recent studies have enhanced classical metaheuristics to address the complexities of DED under renewable integration, uncertainty, and practical operating constraints. For instance, an enhanced artificial hummingbird algorithm has been shown to effectively handle DED with uncertain wind power, ramp-rate limits, and valve-point effects, demonstrating strong performance across multiple dynamic test systems [14]. Similarly, the chaotic hippopotamus optimization algorithm (CHOA) has been applied to hybrid renewable power systems involving wind, solar, and electric vehicles, providing improved cost minimization and loss reduction over a 24-hour horizon while satisfying transmission loss and prohibited operating zone constraints [15].

Further improvements have been reported using a cheetah-inspired optimizer, which incorporates demand-side management and pumped-storage operation, achieving measurable cost reductions in renewable-integrated DED environments [16]. Differential evolution (DE) variants have also been adapted for combined heat-and-power DED, introducing migrating variables and constraint-repair mechanisms that significantly enhance feasibility and convergence behavior [17].

Additionally, the improved grey wolf optimizer strengthens exploration–exploitation balance through chaotic initialization and nonlinear convergence mechanisms, achieving superior cost minimization compared with traditional approaches across multi-scale DED systems [18]. Mathematical optimizers have also contributed to DED and ELD improvement; for example, arithmetic optimization algorithm variants using elementary function disturbances provide enhanced global search capability, faster convergence, and improved robustness when addressing nonlinear ELD/DED formulations involving valve-point effects and transmission losses [19].

Despite these advancements, DED remains a challenging problem due to its dynamic constraints, high dimensionality, and susceptibility to premature convergence in existing optimization methods. As highlighted in recent literature, the effectiveness of metaheuristics in solving DED heavily depends on their ability to maintain a proper balance between exploration and exploitation, avoid stagnation in local optima, and adapt their search behavior across the multi-hour dispatch horizon. Consequently, developing novel, robust, and adaptive optimization techniques continues to be an essential research direction in power system studies.

In this context, the present study employs the recently published kakapo optimization algorithm (KOA) to solve the DED problem. KOA is a nature-inspired metaheuristic based on the unique behavioral patterns of the kakapo bird, offering an adaptive, parameter-free, and exploration – exploitation-balanced search mechanism. Its evolutionary dynamics, characterized by probabilistic attraction and fine-tuned local search, make it a promising candidate for addressing the inherent complexities of DED.

The goal of the work is to apply kakapo optimization algorithm for the dynamic economic dispatch problem, aiming to generate economically optimal and operationally feasible generation schedules over a 24-hour dispatch horizon while preserving population diversity and search stability.

The major contributions of this study are summarized as follows. First, a comprehensive DED formulation is considered, incorporating practical system characteristics such as ramp-rate limits, valve-point effects, and time-varying load demands across a 24-hour horizon. Second, the recently developed KOA algorithm is applied to DED for the first time, and its performance is rigorously evaluated. Third, an extensive comparative analysis is performed against nine well-established metaheuristic algorithms to assess robustness, convergence behavior, and cost minimization capability. Fourth, statistical indicators – including mean, best, worst, standard deviation, and rank – are examined to ensure a fair and reliable performance evaluation.

Dynamic economic dispatch problem represents one of the fundamental optimization challenges in modern power system operation, as it extends the traditional single-period dispatch problem into a multi-hour planning horizon. Unlike ELD, where the load demand is assumed to be constant at a single operating point, the DED problem accounts for hourly load variations over a typical 24-hour period. Consequently, its dimensionality becomes significantly higher – specifically, 24 times larger than that of the static ELD – since a separate generation schedule must be determined for each hour of the dispatch interval.

In today's operational environments, system operators face continuously changing demand patterns, technical limitations of generating units, and nonlinearities such as valve-point loading effects. These complexities make the DED problem highly nonconvex and computationally challenging, thereby motivating the use of advanced metaheuristic optimization techniques. The mathematical formulation of the DED problem, including the objective function and its associated operational constraints, is presented in the following subsections.

Objective function. The goal of the DED problem is to minimize the total generation cost over the entire dispatch horizon. The cost of each generator is modeled as a function of its real power output.

The objective function is defined as:

$$\text{Minimize: } F = \sum_{h=1}^{T}\sum_{i=1}^{N_G} F_{ih}\left(P_{ih}\right), \tag{1}$$

where T is the total number of dispatch periods (hours), typically $T = 24$; N_G is the number of committed (online)

generating units; P_{ih} or P_{it} are the real power output (MW) of generator i at hour h (or t); $F_{ih}(P_{it})$ is the fuel cost of generator i during hour h.

For each generator, the fuel cost is approximated by a quadratic function:

$$F_{it}(P_{it}) = a_i P_{it}^2 + b_i P_{it} + c_i , \quad (2)$$

where a_i (\$/MW^2), b_i (\$/MW), c_i (\$) are the cost coefficients of generator i;

Valve-point loading effect. To model nonlinear ripples in fuel cost due to valve-point opening, the cost function becomes:

$$F_{it}(P_{it}) = a_i P_{it}^2 + b_i P_{it} + c_i + \left| e_i \sin\left(f_i \left(P_{it} - P_i^{\min} \right) \right) \right| , \quad (3)$$

where e_i, f_i are the valve-point loading coefficients for generator i; $P_i^{\min}$ is the minimum power output (MW) of generator i. The sinusoidal term creates multiple local minima, significantly increasing the difficulty of the optimization process.

DED constraints. A feasible DED schedule must satisfy several operational constraints related to system balance, generator limits and ramping characteristics.

Power balance constraint. At every hour t, the total power generation must match the system demand plus transmission losses:

$$\sum_{i=1}^{N_G} P_{it} = P_{Dt} + P_{Lt} , \quad (4)$$

where P_{Dt} is the system load demand (MW) at hour t; P_{Lt} is the transmission loss (MW) at hour t.

Transmission losses are computed using the B-coefficient formula:

$$P_{Lt} = \sum_{i=1}^{N_G} \sum_{j=1}^{N_G} P_{it} B_{ij} P_{jt} , \quad (5)$$

where B_{ij} is the loss coefficient (MW^{-1}) relating units i and j.

Generator operating limits. Each generating unit can operate only within its physical minimum and maximum output:

$$P_i^{\min} \le P_{it} \le P_i^{\max}, \quad (6)$$

where $P_i^{\min}$ is the minimum power output limit of generator i; $P_i^{\max}$ is the maximum power output limit of generator i.

Ramp rate limits. Generating units cannot change their power output instantaneously. Their ramp-up and ramp-down capabilities are modeled as:

Generation increase constraint:

$$P_{it} - P_{i(t-1)} \le UR_i. \quad (7)$$

Generation decrease constraint:

$$P_{i(t-1)} - P_{it} \le DR_i, \quad (8)$$

where UR_i is the ramp-up limit (MW/h) of generator i; DR_i is the ramp-down limit (MW/h) of generator i; $P_{i(t-1)}$ is the output of generator i at the previous hour.

These restrictions create a feasible range for the output during hour t:

$$\max(P_i^{\min}, P_{i(t-1)} - DR_i) \le P_{it} \le \min(P_i^{\max}, P_{i(t-1)} + UR_i). \quad (9)$$

Fitness function and constraint handling. A penalty-based fitness evaluation is used to ensure that all equality and inequality constraints are adequately enforced during the optimization process. The fitness function is expressed as:

$$f = \sum_{t=1}^{n} \sum_{i=1}^{N} F_{it}(P_{it}) + \lambda_1 \left(\sum_{t=1}^{n} \sum_{i=1}^{N} P_{it} - P_{Dt} \right)^2 + \lambda_r \left(\sum_{t=1}^{n} \sum_{i=1}^{N} P_{it} - P_r^{\lim} \right)^2 , \quad (10)$$

where n is the number of hours in the scheduling horizon (n=T); N is the number of generating units (N=N_G); λ_1 is the penalty factor for power balance constraint violation; λ_r is the penalty factor for ramp-limit violation.

The adjusted feasible limit $P_r^{\lim}$ is given by:

$$P_r^{\lim} = \begin{cases} P_{i(t-1)} - DR_i , & \text{if } P_{it} < P_{i(t-1)} - DR_i ; \\ P_{i(t-1)} + UR_i , & \text{if } P_{it} > P_{i(t-1)} + UR_i ; \\ P_{it} , & \text{else.} \end{cases} \quad (11)$$

This formulation ensures that solutions violating ramp limits incur a penalty rather than being discarded.

Kakapo optimization algorithm. KOA is a recent bio-inspired metaheuristic method developed based on the ecological and behavioral characteristics of the kakapo (Strigops habroptilus), an endangered nocturnal parrot native to New Zealand. The algorithm, originally proposed in [20], captures the kakapo's distinctive survival, mating, and adaptive strategies, translating them into mathematically structured search operators suitable for solving complex optimization problems. In this research, KOA is employed as the core optimizer for minimizing the DED objective function presented in section «Dynamic economic dispatch problem». To enable a rigorous and transparent application of KOA to the DED problem, this section provides a concise yet fully detailed introduction to the theoretical foundations, mathematical modeling, and computational operators of the algorithm. KOA consists of two synergistic phases, exploration and exploitation, each modeling a different biological aspect of kakapo behavior. Exploration is driven by long-range mating calls and lek-based selection, encouraging global diversification. Exploitation, on the other hand, is inspired by freezing and camouflage strategies, promoting localized refinement of promising solutions. Together, these mechanisms establish a balanced search process capable of avoiding premature convergence while efficiently guiding the population toward high-quality regions of the solution space.

Biological motivation and algorithmic concept. Kakapo exhibits several remarkable behaviors that serve as the conceptual basis of KOA:

- **Lek mating and acoustic signaling (exploration).** Male kakapos construct shallow lek depressions that act as acoustic amplifiers, enabling their booming calls to propagate over large distances. Males emitting stronger calls attract more females. In KOA, this is mapped into a mechanism where candidate solutions with superior fitness generate stronger signals, and weaker individuals are probabilistically guided toward these promising regions.
- **Fitness-based female selection.** Females evaluate multiple males and select the one emitting the most dominant call. Algorithmically, each candidate evaluates a set of superior solutions and moves toward the strongest one, providing directional global search.

• **Freezing and camouflage (exploitation).** When threatened, kakapos avoid movement and rely on camouflage rather than escape. KOA converts this behavior into a local search operator that applies small, adaptive adjustments around the current position, gradually shrinking step size as iterations progress.

Exploration phase: global search via lek mating. The exploration phase is inspired by the kakapo's lek mating system, where males attract females with booming calls. In KOA, the relative quality of candidate solutions determines their booming intensity, which guides exploration:

$$F^n = \begin{cases} \dfrac{f_i - f_{worst}}{\sum_{j=1}^{N_{KOA}} f_j - f_{worst}}, & \text{if } \sum_{j=1}^{N_{KOA}} f_j - f_{worst} \neq 0; \\ \dfrac{1}{N_{KOA}}, & \text{else,} \end{cases} \quad (12)$$

where F^n is the normalized of objective function value; f_i is the objective function value of i^{th} member; N_{KOA} is the number of population members; $f_{worst} = \max\{F_1, F_2, ..., F_{NKOA}\}$ is representing the least fit candidate. This normalization ensures that better solutions emit proportionally stronger signals.

The perceived signal by candidate i from candidate j accounts for distance:

$$V_{i,j} = Voice\left(X_i, X_j\right) = \frac{F^n}{\sqrt{\sum_{d=1}^{m}\left(x_{i,d} - x_{j,d}\right)}}, \quad (13)$$

where the denominator represents the Euclidean distance between solutions X_i and X_j, ensuring that influence diminishes with distance and maintaining population diversity.

Each candidate X_i then selects potential mates from the global best solution X_{best} and all superior candidates:

$$Male_i = \{X_{best} \cup X_k \mid F_k < F_i\}. \quad (14)$$

The dominant mate $Male_i$ is chosen as the individual with the highest received signal. Candidate X_i moves probabilistically toward this selected mate:

$$X_i^{P1} = X_i + 2\sin\left(r\frac{\pi}{2}\right)\cdot\left(Male_i - I\cdot X_i\right), \quad (15)$$

where X_i^{P1} is the proposed new position for i^{th} member based on exploration phase; $r \sim U(0, 1)$ is a uniform random number; $I \in \{1, 2\}$ is a discrete factor controlling attraction intensity. The new position is accepted if it improves the objective value:

$$X_i = \begin{cases} X_i^{P1}, & \text{if } F_i^{P1} \le F_i; \\ X_i, & \text{else.} \end{cases} \quad (16)$$

Exploitation phase: local refinement via camouflage. Local exploitation in KOA is motivated by the kakapo's defensive freezing and camouflage behavior. Once a promising solution is identified, the candidate undergoes small, adaptive adjustments to refine its position:

$$X_i^{P2} = X_i + \left(1 - 2\sin\left(r\frac{\pi}{2}\right)\right)\cdot\left|UB - LB\right|\cdot e^{-t/T}, \quad (17)$$

where X_i^{P2} is the proposed new position for i^{th} member based on exploitation phase; UB, LB are the decision variable bounds; t is the current iteration; T is the maximum number of iterations. The candidate is updated conditionally:

$$X_i = \begin{cases} X_i^{P2}, & \text{if } F_i^{P2} \le F_i; \\ X_i, & \text{else.} \end{cases} \quad (18)$$

This mechanism ensures precise local optimization, stabilizes promising candidates, and promotes convergence toward optima.

In the following section, the DED problem – along with its objective function and full set of constraints – is optimized using the KOA. The performance of KOA is then systematically compared with several other state-of-the-art metaheuristic algorithms to demonstrate its effectiveness and robustness in solving complex dynamic dispatch problems.

Simulation studies and performance analysis of KOA on the DED problem. In this section, the recently proposed KOA is applied to the DED problem to evaluate its performance in optimizing generation scheduling over a 24-hour horizon. The primary goal is to minimize the total generation cost while satisfying system operational constraints, including generation limits, ramp rates and network demand requirements.

Case study: 5 unit power system. The DED study considers a standard 5 unit power system operating over 24 h. The hourly load demand profile and generator-specific parameters are provided as follows: number of load hours – 24; number of generators – 5.

Power demand (MW) over 24 h: 410, 435, 475, 530, 558, 608, 626, 654, 690, 704, 720, 740, 704, 690, 654, 580, 558, 608, 654, 704, 680, 605, 527, 463.

Transmission loss coefficients (B-matrix):

$$B = \begin{bmatrix} 4.9 & 1.4 & 1.5 & 1.5 & 2 \\ 1.4 & 4.5 & 1.6 & 2 & 1.8 \\ 1.5 & 1.6 & 3.9 & 1 & 1.2 \\ 1.5 & 2 & 1 & 4 & 1.4 \\ 2 & 1.8 & 1.2 & 1.4 & 3.5 \end{bmatrix} \times 10^{-5}$$

Generators data (P_{min}, P_{max}, cost coefficients and valve-point effects) are presented in Table 1, while ramp rate and operating zone constraints are provided in Table 2.

Table 1

Generators data

Unit	P_{min}, MW	P_{max} MW	a, \$/MW^2	b, \$/MW	c, \$	e	f
1	10	75	0.008	2	25	100	0.042
2	20	125	0.003	1.8	60	140	0.04
3	30	175	0.0012	2.1	100	160	0.038
4	40	250	0.001	2	120	180	0.037
5	50	300	0.0015	1.8	40	200	0.035

Table 2

Ramp rate and operating zone constraints

Unit	*UR*, MW/h	*DR*, MW/h	Zone1 min	Zone1 max	Zone2 min	Zone2 max
1	30	30	10	10	10	10
2	30	30	20	20	20	20
3	40	40	30	30	30	30
4	50	50	40	40	40	40
5	50	50	50	50	50	50

Implementation of KOA on the DED problem. The KOA algorithm was implemented to optimize the hourly generation schedules of the 5 units over the 24 h dispatch period. The hourly generation results obtained from KOA are shown in Table 3, while the convergence behavior of the algorithm is illustrated in Fig. 1.

Table 3

Hourly generation schedule of generators over the 24-hour dispatch horizon

Hours	Gen. 1	Gen. 2	Gen. 3	Gen. 4	Gen. 5	Demand
1	46.11662	83.52216	83.2277	90.9579	169.3697	473.1941
2	21.4801	87.62952	43.90394	139.9543	157.3372	450.3051
3	51.45117	70.03376	68.21506	128.6201	206.9151	525.2352
4	37.86257	53.29862	74.47033	178.3501	192.3671	536.3487
5	50.12573	72.97188	109.0332	164.1918	168.1146	564.4372
6	29.69906	86.06437	119.7154	176.4838	203.91	615.8726
7	51.04515	84.30845	114.7332	176.0769	208.0255	634.1892
8	51.57515	84.69726	140.8388	172.6809	213.9147	663.7069
9	63.70681	79.63767	129.6526	180.9167	245.129	699.0428
10	54.65936	94.41113	129.6619	225.862	209.4364	714.0308
11	52.49315	80.26212	124.6985	183.1834	251.3803	692.0174
12	59.71101	105.8928	137.3994	169.5833	276.8193	749.4059
13	52.1899	109.967	127.5033	186.7113	239.0105	715.382
14	53.20617	81.67361	116.544	236.5096	211.5443	699.4777
15	51.99971	101.9325	119.3569	186.5427	202.7541	662.5859
16	63.73308	76.59892	82.70339	193.765	168.9226	585.723
17	47.08895	90.25797	114.2526	143.979	190.9772	586.5557
18	53.4963	96.00657	120.3826	169.0987	176.6804	615.6646
19	49.33967	79.86549	137.8555	187.8211	208.9346	663.8163
20	53.54952	91.23786	167.7917	197.979	203.6111	714.1692
21	49.37575	105.1834	139.382	149.2361	246.0384	689.2156
22	50.12384	82.59457	104.1344	180.1852	196.0631	613.1011
23	49.42887	63.509	69.39283	170.916	183.0527	536.2994
24	52.14645	72.6833	30	151.2307	160.9773	467.0377

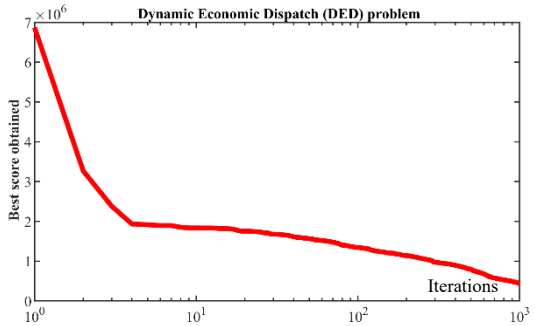

Fig. 1. Convergence curve of KOA performance on the DED problem

The convergence curve in Fig. 1 demonstrates that KOA rapidly approaches near-optimal solutions within the first 100 iterations and gradually refines the total generation cost to a minimal value, confirming the algorithm's stability and efficiency.

Comparative performance analysis. To validate the effectiveness of KOA, its performance was benchmarked against 9 well-known metaheuristic algorithms: genetic algorithm (GA) [21], particle swarm optimization (PSO) [22], gravitational search algorithm (GSA) [23], whale optimization algorithm (WOA) [24], teaching-learning-based optimization (TLBO) [25], multi-verse optimizer (MVO) [26], tunicate swarm algorithm (TSA) [27], grey wolf optimizer (GWO) [28] and marine predators algorithm (MPA) [29].

The statistical results obtained from 30 independent runs of each algorithm are summarized in Table 4, and boxplot distributions of the objective function are depicted in Fig. 2.

The results clearly demonstrate that KOA outperforms all competitor algorithms in terms of mean and best generation cost, achieving the lowest objective value (mean = 437887.2) and securing rank 1 among all tested algorithms. The boxplot analysis in Fig. 2 further highlights the consistency and robustness of KOA, as it exhibits the narrowest interquartile range and minimal variability in solution quality across multiple runs.

Discussion. The superior performance of KOA on the DED problem can be attributed to several factors:

1. **Effective balance between exploration and exploitation.** The lek mating-inspired global search efficiently guides candidate solutions toward promising regions, while the camouflage-driven local refinement ensures precise convergence near optimal solutions.

2. **Preservation of population diversity.** Distance-based signal propagation prevents premature convergence and maintains diverse solution candidates throughout the search process.

3. **Adaptive, stochastic search mechanisms.** Sinusoidal random factors and iteration-based step size reduction provide fine-grained adjustments that enhance solution accuracy.

Overall, the simulation results demonstrate that KOA is highly capable of generating cost-effective and feasible generation schedules for complex, multi-unit DED problems. The algorithm's superior convergence characteristics and robustness compared to GA, PSO, GSA, WOA, TLBO, MVO, TSA, GWO and MPA highlight its potential as a reliable tool for practical power system dispatch applications.

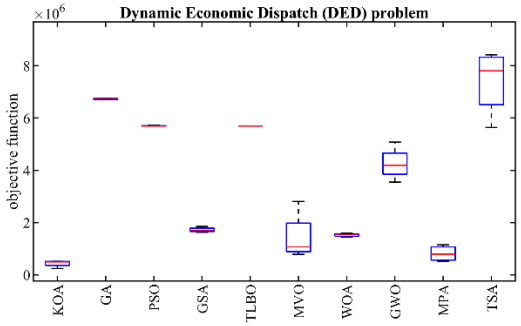

Fig. 2. Boxplot diagrams of KOA and the competitor algorithms on the DED problem

Table 4

Statistical results of KOA and competitor algorithms applied to the DED problem

	KOA	GA	PSO	GSA	TLBO	MVO	WOA	GWO	MPA	TSA
Mean	437887.2	6720657	5698276	1723748	5689705	1434226	1523670	4251127	814578.5	7415002
Best	241032	6697859	5689705	1630110	5689705	783827	1435945	3548498	524603	5636969
Worst	518064.2	6744016	5723987	1852886	5689705	2809419	1592087	5076836	1149721	8413637
Std	132165.5	24865.71	17141.04	94054.47	0	929183.4	65769.13	628895.2	300209.1	1267961
Median	496226.4	6720376	5689705	1705998	5689705	1071828	1533324	4189587	791994.9	7804701
Rank	1	9	8	5	7	3	4	6	2	10

Conclusions. Application of the KOA to the DED problem in a multi-unit power system over a 24 h horizon is investigated. The DED problem, inherently nonconvex and highly nonlinear due to valve-point loading effects, ramp-rate limits, and transmission losses, represents a significant operational challenge for modern power systems. By leveraging KOA's bio-inspired mechanisms, including lek mating-based exploration and camouflage-driven exploitation, the algorithm effectively balances global search diversification with local refinement, enabling the identification of cost-optimal and feasible generation schedules across all dispatch intervals. Simulation results on a standard five-unit system demonstrate that KOA outperforms nine benchmark metaheuristic algorithms in terms of total generation cost, convergence speed, and solution robustness.

The convergence analysis revealed that KOA rapidly reaches near-optimal solutions within the early iterations, while maintaining a stable search process that prevents premature convergence. Statistical performance metrics, including mean, best, worst, standard deviation, and rank, consistently favor KOA, confirming its effectiveness in handling multi-dimensional, multi-modal optimization problems inherent in DED.

The success of KOA in this study can be attributed to three key factors: 1) efficient global exploration through fitness-weighted acoustic signaling and probabilistic attraction, which enables the algorithm to explore diverse solution regions; 2) precise local exploitation inspired by kakapo freezing and camouflage behavior, allowing fine-grained adjustments near promising solutions; 3) adaptive, stochastic search operators that enhance population diversity and robustness against local minima. Collectively, these features render KOA a reliable tool for complex power system dispatch problems, ensuring both economic efficiency and operational feasibility.

For future research, several avenues can be pursued to further enhance the applicability and performance of KOA in DED and related domains:

1. Integration with renewable energy sources such as wind and solar, which introduces additional uncertainty and intermittency in generation profiles.
2. Inclusion of multi-objective criteria, incorporating emission minimization, reliability enhancement, and system security alongside generation cost reduction.
3. Hybridization with other metaheuristics or machine learning techniques to accelerate convergence and improve adaptability to large-scale power systems.
4. Real-time and adaptive implementations, enabling KOA to respond dynamically to sudden load changes or generator outages in practical operational environments.
5. Investigation of scalability and parallelization strategies, to efficiently handle large-scale systems with high-dimensional decision variables and complex network constraints.

Acknowledgment. The authors are grateful to the Deanship of Scientific Research at Jadara University for providing financial support for this publication.

Conflict of interest. The authors declare that they have no conflicts of interest.

REFERENCES

1. Chen X., Zhang Z. Enhanced heap-based optimization algorithm for dynamic economic dispatch considering electric vehicle charging integration. *Energy*, 2025, vol. 324, art. no. 135955. doi: https://doi.org/10.1016/j.energy.2025.135955.

2. Sun L., An W., Chen Y., Zhao P., Ding D. An overview of distributed economic dispatch of microgrids: advances and challenges. *Systems Science & Control Engineering*, 2025, vol. 13, no. 1, art. no. 2467077. doi: https://doi.org/10.1080/21642583.2025.2467077.

3. Marzbani F., Abdelfatah A. Economic Dispatch Optimization Strategies and Problem Formulation: A Comprehensive Review. *Energies*, 2024, vol. 17, no. 3, art. no. 550. doi: https://doi.org/10.3390/en17030550.

4. Xia X., Elaiw A.M. Optimal dynamic economic dispatch of generation: A review. *Electric Power Systems Research*, 2010, vol. 80, no. 8, pp. 975-986. doi: https://doi.org/10.1016/j.epsr.2009.12.012.

5. Qawaqneh H. et al. Pipefish Optimization Algorithm (POA): A Nature-inspired Metaheuristic for Robust and Adaptive Global Optimization. *International Journal of Intelligent Engineering and Systems*, 2025, vol. 18, no. 11, pp. 778-794. doi: https://doi.org/10.22266/ijies2025.1231.48.

6. Matoušová I. et al. Mother optimization algorithm: a new human-based metaheuristic approach for solving engineering optimization. *Scientific Reports*, 2023, vol. 13, no. 1, art. no. 10312. doi: https://doi.org/10.1038/s41598-023-37537-8.

7. Qawaqneh H. et al. Black-breasted Lapwing Algorithm (BBLA): A Novel Nature-inspired Metaheuristic for Solving Constrained Engineering Optimization. *International Journal of Intelligent Engineering and Systems*, 2025, vol. 18, no. 11, pp. 581-597. doi: https://doi.org/10.22266/ijies2025.1231.36.

8. Dinler Ö.B. et al. Blue-eared Hedgehog Optimization (BEHO): A Nature-inspired Metaheuristic for Robust and Efficient Global Optimization. *International Journal of Intelligent Engineering and Systems*, 2025, vol. 18, no. 11, pp. 133-148. doi: https://doi.org/10.22266/ijies2025.1231.08.

9. Manikandan K., Sasikumar S., Arulraj R. A novelty approach to solve an economic dispatch problem for a renewable integrated micro-grid using optimization techniques. *Electrical Engineering & Electromechanics*, 2023, no. 4, pp. 83-89. doi: https://doi.org/10.20998/2074-272X.2023.4.12.

10. Desai J.P. Transmission line planning using global best artificial bee colony method. *Electrical Engineering & Electromechanics*, 2023, no. 5, pp. 83-86. doi: https://doi.org/10.20998/2074-272X.2023.5.12.

11. Bouhadouza B., Sadaoui F. Optimal power flow analysis under photovoltaic and wind power uncertainties using the blood-sucking leech optimizer. *Electrical Engineering & Electromechanics*, 2025, no. 6, pp. 15-26. doi: https://doi.org/10.20998/2074-272X.2025.6.03.

12. Laouafi F. Improved grey wolf optimizer for optimal reactive power dispatch with integration of wind and solar energy. *Electrical Engineering & Electromechanics*, 2025, no. 1, pp. 23-30. doi: https://doi.org/10.20998/2074-272X.2025.1.04.

13. Wang Y., Xiong G. Metaheuristic optimization algorithms for multi-area economic dispatch of power systems: Part I – A comprehensive survey. *Artificial Intelligence Review*, 2025, vol. 58, no. 4, art. no. 98. doi: https://doi.org/10.1007/s10462-024-11070-0.

14. Hassan M.H., Mohamed E.M., Kamel S., Eslami M. Dynamic economic dispatch with uncertain wind power generation using an enhanced artificial hummingbird algorithm. *Neural Computing and Applications*, 2025, vol. 37, no. 10, pp. 7397-7422. doi: https://doi.org/10.1007/s00521-025-10982-4.

15. Mandal B., Roy P.K., Paul C. Dynamic Economic Dispatch Problem in Hybrid Renewable Energy Sources Based Power Systems Using Chaotic Hippopotamus Optimization Algorithm. *Iranian Journal of Science and Technology, Transactions of Electrical Engineering*, 2025. doi: https://doi.org/10.1007/s40998-025-00893-4.

16. Nagarajan K., Rajagopalan A., Bajaj M., Sitharthan R., Dost Mohammadi S.A., Blazek V. Optimizing dynamic economic dispatch through an enhanced Cheetah-inspired algorithm for integrated renewable energy and demand-side management. *Scientific Reports*, 2024, vol. 14, no. 1, art. no. 3091. doi: https://doi.org/10.1038/s41598-024-53688-8.

17. Zou D., Gong D. Differential evolution based on migrating variables for the combined heat and power dynamic economic dispatch.

Energy, 2022, vol. 238, art. no. 121664. doi: https://doi.org/10.1016/j.energy.2021.121664.
18. Yang W., Zhang Y., Zhu X., Li K., Yang Z. Research on Dynamic Economic Dispatch Optimization Problem Based on Improved Grey Wolf Algorithm. *Energies*, 2024, vol. 17, no. 6, art. no. 1491. doi: https://doi.org/10.3390/en17061491.
19. Hao W.-K., Wang J.-S., Li X.-D., Wang M., Zhang M. Arithmetic optimization algorithm based on elementary function disturbance for solving economic load dispatch problem in power system. *Applied Intelligence*, 2022, vol. 52, no. 10, pp. 11846-11872. doi: https://doi.org/10.1007/s10489-021-03125-4.
20. Qawaqneh H. et al. Kakapo Optimization Algorithm (KOA): A Novel Bio-inspired Metaheuristic for Optimization Applications. *International Journal of Intelligent Engineering and Systems*, 2025, vol. 18, no. 11, pp. 913-929. doi: https://doi.org/10.22266/ijies2025.1231.56.
21. Holland J.H. Genetic Algorithms. *Scientific American*, 1992, vol. 267, no. 1, pp. 66-73. Available at: http://www.jstor.org/stable/24939139.
22. Kennedy J., Eberhart R. Particle swarm optimization. *Proceedings of ICNN'95 - International Conference on Neural Networks*, 1995, vol. 4, pp. 1942-1948. doi: https://doi.org/10.1109/ICNN.1995.488968.
23. Rashedi E., Nezamabadi-pour H., Saryazdi S. GSA: A Gravitational Search Algorithm. *Information Sciences*, 2009, vol. 179, no. 13, pp. 2232-2248. doi: https://doi.org/10.1016/j.ins.2009.03.004.
24. Mirjalili S., Lewis A. The Whale Optimization Algorithm. *Advances in Engineering Software*, 2016, vol. 95, pp. 51-67. doi: https://doi.org/10.1016/j.advengsoft.2016.01.008.
25. Rao R.V., Savsani V.J., Vakharia D.P. Teaching–learning-based optimization: A novel method for constrained mechanical design optimization problems. *Computer-Aided Design*, 2011, vol. 43, no. 3, pp. 303-315. doi: https://doi.org/10.1016/j.cad.2010.12.015.
26. Mirjalili S., Mirjalili S.M., Hatamlou A. Multi-Verse Optimizer: a nature-inspired algorithm for global optimization. *Neural Computing and Applications*, 2016, vol. 27, no. 2, pp. 495-513. doi: https://doi.org/10.1007/s00521-015-1870-7.
27. Kaur S., Awasthi L.K., Sangal A.L., Dhiman G. Tunicate Swarm Algorithm: A new bio-inspired based metaheuristic paradigm for global optimization. *Engineering Applications of Artificial Intelligence*, 2020, vol. 90, art. no. 103541. doi: https://doi.org/10.1016/j.engappai.2020.103541.
28. Mirjalili S., Mirjalili S.M., Lewis A. Grey Wolf Optimizer. *Advances in Engineering Software*, 2014, vol. 69, pp. 46-61. doi: https://doi.org/10.1016/j.advengsoft.2013.12.007.
29. Faramarzi A., Heidarinejad M., Mirjalili S., Gandomi A.H. Marine Predators Algorithm: A nature-inspired metaheuristic. *Expert Systems with Applications*, 2020, vol. 152, art. no. 113377. doi: https://doi.org/10.1016/j.eswa.2020.113377.

Received 07.11.2025
Accepted 03.01.2026
Published 02.05.2026

S.A. Alomari [1], *PhD, Associate Professor,*
A. Smerat [2,3], *Candidate PhD, Lecturer,*
O.P. Malik[4], *PhD, Professor,*
R. Abu Zitar [5], *PhD, Professor,*
M. Dehghani [6], *PhD,*
Z. Montazeri [6], *PhD,*
[1] Computer Science Department, Faculty of Information Technology, Jadara University, Irbid 21110, Jordan.
[2] Department of Biosciences, Saveetha School of Engineering, Saveetha Institute of Medical and Technical Sciences, Chennai, 602105, India.
[3] Hourani Center for Applied Scientific Research, Al-Ahliyya Amman University, Amman 19328, Jordan.
[4] Department of Electrical and Software Engineering, University of Calgary, Canada.
[5] College of Engineering and Computing, Liwa University, Abu Dhabi, 41009, United Arab Emirates.
[6] Department of Electrical and Electronics Engineering, Shiraz University of Technology, Iran,
e-mail: adanbax@gmail.com (Corresponding Author)

How to cite this article:
Alomari S.A., Smerat A., Malik O.P., Abu Zitar R., Dehghani M., Montazeri Z. Power system operational optimization using the kakapo optimization algorithm for dynamic economic dispatch. *Electrical Engineering & Electromechanics*, 2026, no. 3, pp. 85-91. doi: https://doi.org/10.20998/2074-272X.2026.3.13

Матеріали приймаються за адресою:
Кафедра "Електричні апарати", НТУ "ХПІ", вул. Кирпичева, 2, м. Харків, 61002, Україна
Електронні варіанти матеріалів по e-mail: a.m.grechko@gmail.com

Довідки за телефонами: +38 067 359 46 96 Гречко Олександр Михайлович

Передплатний індекс: 01216